Conception d'un dispositif de récupération d'énergie vibratoire large bande

Weiqun Liu

UNIVERSITÉ DE GRENOBLE

THÈSE

Pour obtenir le grade de

DOCTEUR DE L'UNIVERSITÉ DE GRENOBLE

Spécialité : **Sciences pour L'ingénieur**

Arrêté ministérial : 7 août 2006

Présentée par

Weiqun Liu

Thèse dirigée par **Fabien Formosa**
et codirigée par **Adrien Badel & Amen Agbossou**

préparée au sein **du Laboratoire SYstème et Matériaux pour la MEcatronique (SYMME)**
et de **l'école doctorale Science et Ingéniérie des Systèmes de l'Environnement et des Organisations (SISEO)**

Conception d'un dispositif de récupération d'energie vibratoire large bande

Thèse soutenue publiquement le **27 octobre 2014**,
devant le jury composé de :

M. Elie, Lefeuvre
Professeur, IEF Paris Sud, Président
M. Einar, Halvorsen
Professeur, Buskerud and Vestfold University College, Rapporteur
M. Zhihua, Feng
Professeur, University of Science and Technology of China, Rapporteur
M. Philippe, Basset
Professeur Associé, ESIEE/ESYCOM Université Paris-Est, Examinateur
M. Mickaël, Lallart
Maître de conférences, INSA Lyon, Examinateur
M. Fabien, Formosa
Maître de conférences, SYMME Université de Savoie, Directeur de thèse
M. Adrien, Badel
Maître de conférences, SYMME Université de Savoie, Co-Directeur de thèse
M. Amen, Agbossou
Professeur, LOCIE Université de Savoie, Co-Encadrant de thèse

Acknowledgments

This thesis summarizes the research work done during my phD between 2011 and 2014 at laboratory SYMME (Systèm et Matériaux pour la Mécatronique), Université de Savoie, France. It is supported by the ANR(Agence Nationale de la Recherche) project REVilaBa (Récupération d'énergie vibratoire large bande). All the work is done under the guiding of my supervisor, Associate Professor Fabien Formosa and my co-supervisors, Associate Professor Adrien Badel and Professor Amen Agbossou.

First of all, I'd like to express my deep thanks to my supervisor Fabien Formosa. Without his careful guidance, enthusiastic encouragement and excellent vision, the work wouldn't be finished so smoothly. His tolerance, understanding and trust make me more confident. I will always keep his warm concern and help in my mind.

I'd also like to give my sincere thanks to my co-supervisor Adrien Badel. His extensive knowledge and abundance of innovative ideas make me feel the happiness of research. His commitment and enthusiasm to outstanding scientific research are precious treasures to me. The perfect atmosphere of free discussions and good cooperations provided by two supervisors is never forgettable.

I'd like to give many thanks to my co-supervisor Amen Agbossou. His recommendation and trust gave me the chance to work with them. He is alway kind and encouraging, making me warm.

I'd like to give my great thanks to Professor Einar Halvorsen and Professor Zhihua Feng for their acceptance to be the reviewers of my thesis. Their expertise and valuable suggestions will be a great help for the improvement of my work. I have to give my special thanks to Professor Zhihua Feng. He is the supervisor of my master study. It's him who opened the door of the research to me and gave me so much encouragement and confidence.

Great acknowledgments to the three examiners of my thesis, Professor Elie Lefeuvre, Associate Professor Philippe Basset and Associate Professor Mickaël Lallart, for their participation and patience. Special thanks to Professor Elie Lefeuvre for accepting to be president of my defence.

A lot of thanks to my partner Yipeng Wu. His help and cooperation make the work get easier.

I'd like to give my deep thanks for all the members of SYMME who have been always friendly and full of passion. I'd like to thank all the friends, especially Yipeng Wu, Zaoli Huang, Ge Li, Chen Yang, Peng He, Haiyang Jiang and many others. We have passed a wonderful time which I will miss all the time.

I'd like to give my deepest thanks to my family whose love has always been the greatest inspiration for me. Special thanks for the great sacrifice of my parents and my wife's parents.

Finally, my sincerest gratitude goes to my beloved wife and my lovely children for their dedicated support.

Contents

Acronyms

BSM	(Buckled-Spring-Mass)
BSMOS	(BSM Oscillator with Stoppers)
DSP	(Digital Signal Processing)
DSSH	(Double Synchronized Switching Harvesting)
ESSH	(Enhanced Synchronized Switching Harvesting)
FIG	(Frequency Increased Generator)
LEO	(Linear Equivalent Oscillator)
MEMS	(Micro Electro-Mechanical System)
NLBO	(Non-Linear Bistable beam Oscillator)
NPBP	(Normalized Power Bandwidth Product)
OSECE	(Optimized Synchronous Electric Charge Extraction)
PKD	(Peak Detector)
PTFE	(PolyeTraFluoroEthylene)
PWM	(Pulse Width Modulation)
RMSHI	(Random Mechanical Switching Harvesting on Inductor)
SECE	(Sychronous Electric Charge Extraction)
SMFE	(Sychronous Magnetic Flux Extraction)
SSHI	(Synchronized Switching Harvesting on Inductor)
VEH	(Vibration Energy Harvester)
WSN	(Wireless Sensor Network)

Résumé

La récupération d'énergie à partir des sources de vibration est une des stratégies développées pour l'alimentation de capteurs autonomes communicants. La variabilité des gisements vibratoires dans l'environnement constitue un défi notable pour l'obtention de performances satisfaisantes et appelle au développement de dispositifs de récupération d'énergie à large bande passante. Les générateurs basés sur des oscillateurs mécaniques non linéaires bistables ont démontré des performances particulièrement intéressantes. Grâce à l'effet de conversion fréquentielle notamment, la plage de fonctionnement est considérablement augmentée.

Une nouvelle architecture de générateur bistable basée sur un oscillateur non linéaire et des composants piézoélectriques est proposé dans la thèse. Ce générateur possède des caractéristiques particulièrement favorables en termes de compacité et de simplicité. Des études théoriques et expérimentales ont été menées. En utilisant les excitations canoniques dans le cas de systèmes dynamiques non linéaires (balayage fréquentiel et bruit blanc), les gains obtenus par rapport à des générateurs linéaires ont été quantifiés. Les performances du générateur proposé sont également supérieures à celles des générateurs bistables de la littérature.

Une attention particulières a été portée à l'étude des réponses dynamiques non linéaires complexes révélant la présence d'attracteurs étranges et l'influence des conditions initiales. Une analyse spectrale est également utilisée pour améliorer la compréhension du comportement du générateur. L'adimensionnement des équations d'équilibres donne à ces analyses une portée générique. Selon le modèle normalisé développé, la performance d'un générateur bistable est liée à quatre paramètres critiques: l'amortissement structurel, le niveau de couplage électromécanique, le niveau de flambement et la fréquence caractéristique. Un facteur de mérite est proposé et constitue un élément de comparaison pertinent entre générateurs.

Une stratégie de conception optimale a été élaborée et mise en œuvre pour la réalisation d'un générateur miniaturisée. Après une caractérisation expérimentale complète utilisant les signaux canoniques, son potentiel d'application à des cas plus proches des environnements réels a été étudié en répliquant en laboratoire l'excitation mesurée sur un véhicule en roulage.

L'association du générateur bistable avec une technique d'extraction d'énergie non linéaire a été réalisée : la technique OSECE (Optimized Synchronous Electric Charge Extraction) est choisie. Les gains de performances obtenus pour différents niveaux de couplage électromécanique dans le cas des excitations canoniques sont étudiés. L'énergie récupérée est considérablement augmentée en cas de faibles couplages électromécaniques. Lorsque celui-ci est plus élevé, les performances sont comparables à celles obtenues avec un simple pont redresseur, mais l'indépendance à l'impédance d'entrée du circuit alimenté dans le cas de la technique OSECE peut être un avantage déterminant pour des applications réelles.

Finalement, compte tenu des gains attendus par l'approche combinée oscillateur bistable et technique OSECE, l'auto-alimentation du circuit actif OSECE est réalisée dans le cas d'un oscillateur bistable par des moyens mécaniques. La complexité du générateur est légèrement augmentée dans la mesure où des butées mécaniques et un système de contacteurs électriques sont ajoutés. Les résultats démontrent le potentiel de l'approche qui capitalise les bénéfices de l'oscillateur bistable et du circuit d'extraction non linéaire.

Abstract

As an emerging technology, energy harvesting has attracted great interests in the past years because of its prospective applications. It offers new possibilities for the development of autonomous sensor networks. Moreover, energy harvesting is consistent with the idea of developing green and clear energy. Since scavenging the energy from the vibration sources has the wide adaptability and the easy feasibility of integration with other sources, it becomes one of the hottest topic in the energy harvesting field. The variability of the environmental vibrations introduces a challenge to the conventional linear harvesters and calls for the development of wideband vibration generators. Plenty of approaches have been proposed, such as resonance tuning structures, multi-modal oscillators, frequency-up-conversion mechanisms, monostable hardening or softening generators, bistable structures etc.. Among them, bistable generators have shown some of the best properties of the frequency-up-conversion effect at the low frequency range and the bandwidth increase from the nonlinear backbone response.

A novel bistable generator with a BSM (Buckled-Spring-Mass) architecture is proposed in the thesis. This BSM generator possesses some especially desired properties of compactness and simplicity. Utilizing the chirp and noise excitations, experimental and numerical investigations have shown that it effectively extends the operation bandwidth compared with linear generators. The performance is also demonstrated to be better than most of the reported bistable generators. The complex nonlinear dynamics have been studied, including the strange attractor and the influence of the initial condition. A spectrum method is also used to give more details about the motion of the BSM generator.

According to the developed normalized model, the BSM generator's performance is related to four critical parameters: structural damping, electromechanical coupling level, buckled position and characteristic frequency. Applying the concluded optimization and design procedures, a miniaturized BSM generator of the millimeter scale has been produced and tested. The application potential is further investigated with a replicated realistic excitation from the wheel of a driving car. Moreover, a wireless demonstration platform has been constructed to exhibit the wideband operation ability.A figure of merit is proposed to make fair comparisons between the literature nonlinear wideband generator and the BSM generators.

Chapter 4 presents a novel energy harvesting solution which combines the BSM generator with a nonlinear extraction technique: the OSECE (Optimized Synchronous Electric Charge Extraction) technique is used along with the BSM bistable generator.The performances of the proposed solution for different levels of electromechanical coupling coefficients in the cases of chirp and noise excitations are compared against the performance of the BSM generator with the standard technique. It is shown that the harvested energy is drastically increased for all excitations in the case of low electromechanical coupling coefficients. When the electromechanical coupling coefficient is high, the performance of the OSECE technique is not as good as the standard circuit for forward sweeps, but superior for the reverse sweep and band-limited noise cases in the tested range.

Finally, a self-powered approach for the combination of the BSM generator and the OSECE circuit is realized by replacing the electronic switches with mechanical switches and introducing additional stoppers. It allows wideband harvesting capability, high harvested power and autonomous features. A model of this novel generator is detailed and experimentally validated. Discussions and optimizations are performed to find the optimal parameters and fully investigate the performance of the proposed generator. It shows that introducing the stoppers and the self-powered OSECE circuit using mechanical switches

can substantially enhance the harvested power with moderate additional complexity.

0

Résumé étendu en Français

Contents

0.1 Contexte et état de l'art

0.1.1 Introduction

Des progrès énormes ont été réalisés en micro-électronique et capteurs au cours des dernières décennies. Les dispositifs et les composants sont de plus petites dimensions et leurs consommations sont minimes. La demande de technologies sans fil est de plus en plus grande et omniprésente, en particulier pour les réseaux de capteurs sans fil. Ils permettraient d'offrir de nouveaux bénéfices et opportunités dans de nombreuses applications : surveillance de la dégradation des structures mécaniques, traçabilité dans l'industrie alimentaire et agricole, surveillance de l'environnement, monitoring de santé humaine, etc..

Les composants de mesure et de traitement de l'information sont aujourd'hui miniaturisés et bien maitrisés. Mais la taille des nœuds de capteurs composant les réseaux de capteurs sans fil est imposée par les batteries nécessaires à l'alimentation énergétique. L'autonomie est limitée par l'énergie totale de la source de la batterie et donc son volume. Pour s'affranchir de cette limitation, la récupération d'énergie, puisant dans les sources d'énergie ambiante pour alimenter le nœud de capteurs sans fil est une solution prometteuse.

Certains avantages spécifiques et souhaitables inhérents à la stratégie de récupération d'énergie peuvent être énoncés : durée de vie « infinie », diminution des coûts de maintenance, capacité de travailler dans des environnements dangereux en continu, protection de l'environnement.

De nombreuses sources d'énergie sont disponibles dans notre environnement qu'il soit naturel, urbain ou industriel. Ces sources d'énergie sont principalement classées en quatre types: lumière, chaleur, vibrations et ondes radio. Par rapport aux autres sources, les vibrations présentent une densité de puissance intéressante et moins de contraintes quant à leur exploitation. Tant que les sources de vibrations existent, le générateur peut toujours fonctionner. De nombreux travaux de recherche sont focalisés sur ce type de source. C'est le cas de ce travail de thèse.

0.1.2 Récupération d'énergie vibratoire (Vibration Energy Harvester)

Comme le montre la figure 1, un VEH (Vibration Energy Harvester) est souvent constitué de trois parties: l'oscillateur mécanique, le transducteur électromécanique et le circuit d'extraction et de stockage d'énergie. La combinaison de l'oscillateur mécanique et du convertisseur électromécanique est souvent désigné par « le générateur ». C'est lui qui produit l'énergie électrique à partir de la source vibratoire. Les générateurs sont souvent classés selon le mécanisme de conversion utilisé : les générateurs piézo-électriques, les générateurs électromagnétiques, les générateurs électrostatiques, etc..

La sélection du type de conversion est fonction des applications. Dans le cas des générateurs piézoélectriques et électromagnétiques, une approche unifiée a été proposée dans la thèse d'Emmanuelle Arroyo au laboratoire SYMME [1]. Elle permet d'effectuer une comparaison immédiate entre ces deux approches. Les générateurs électrostatiques ont largement été développés à l'échelle de MEMS. Dans cette thèse, seules les conversions piézoélectriques et électromagnétiques sont abordées.

Pour améliorer les performances d'un VEH, les chercheurs explorent principalement deux aspects: (1) les circuits d'interface pour l'extraction et le stockage de l'énergie; (2)

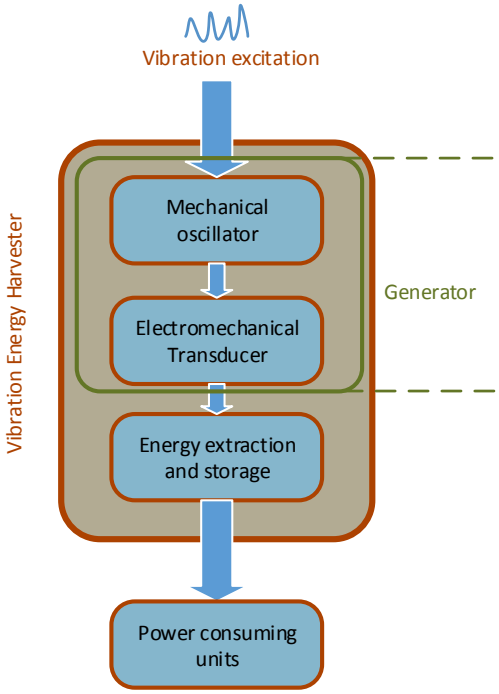

Figure 1: Vibration energy harvester.

les structures électromécaniques oscillantes (générateur).

De nombreuses techniques et circuits non linéaires d'extraction d'énergie ont été mises au point pour augmenter la puissance [2, 3, 4, 5, 6, 7]. Mais la plupart des générateurs utilisés sont conçus à partir d'oscillateurs linéaires.

Toutefois, les spectres de fréquences de vibrations réelles sont souvent à large bande et aléatoires. Lorsque la fréquence propre d'un oscillateur linéaire n'est pas à l'intérieur de l'intervalle favorable de l'excitation comme le montre la figure 2 (au temps 2), la puissance récupérée est très faible. Cela signifie que l'énergie récoltée n'est peut être pas suffisante pour assurer le fonctionnement normal du nœud de capteur autonome. Pour avoir une puissance de sortie stable et durable, un générateur qui présente une caractéristique de réponse fréquentielle à large bande est une nécessité (figure 2).

0.1.3 Générateur large bande (Wideband vibration generator)

Puisque la majorité des excitations dans les environnements sont variables et à large bande, il est essentiel d'avoir un générateur dont le comportement est compatible avec ces environnements d'applications complexes. De nombreuses réalisations démontrant des performances remarquables ont été présentées dans les dernières années [8, 9]. La synthèse des stratégies développées est faite ici.

Ajustement de résonance (resonance tuning)

Les performances des générateurs linéaires sont conditionnées à la connaissance du spectre de fréquence de l'excitation. La fréquence de résonance du générateur conçu devra

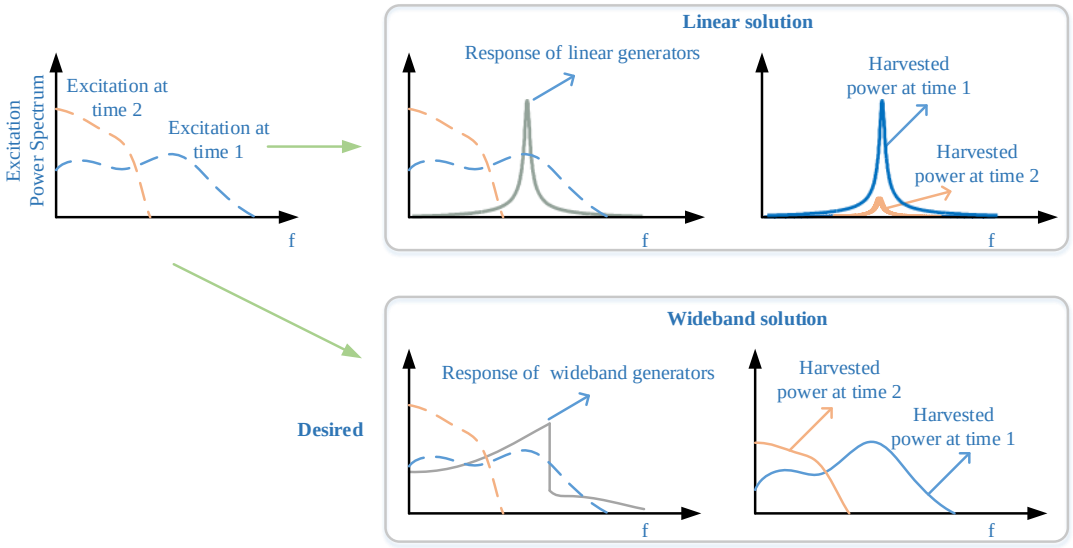

Figure 2: Les avantages des générateurs large bande.

coïncider avec la fréquence de la source pour laquelle la densité spectrale de puissance est maximale. Si cette fréquence d'excitation dérive dans le temps, les performances du générateur sont globalement très faibles. Par conséquent, des générateurs dont la fréquence de résonance est ajustable sont proposés. La démarche habituelle consiste à changer la raideur ou la masse effective en ajoutant des structures ou systèmes auxiliaires [10, 11, 12].

Selon les modes d'opération du réglage, les générateurs peuvent être divisés en deux classes: passifs et actifs. Pour les premiers, la fréquence de résonance est ajustée et fixée in-situ préalablement au fonctionnement. Pour les générateurs appartenant à la deuxième classe, la fréquence peut être adaptée à l'excitation en temps réel avec des composants actifs.

En faisant correspondre la fréquence de résonance avec l'excitation, ces générateurs présentent des performances supérieures aux générateurs linéaires. Cependant, il existe certaines limitations: d'abord, la stratégie de contrôle complexe de la fonction de réglage actif induit un retard pour le suivi de la fréquence d'excitation ; d'autre part, une grande quantité d'énergie est consommée pendant l'opération de réglage de telle sorte qu'un temps de fonctionnement sans ajustement est nécessaire. Ces deux aspects peuvent induire la perte du suivi de la fréquence optimale notamment en cas de dérive rapide. De plus, la plage de réglage est généralement limitée autour de la fréquence de résonance initiale. Par conséquent, cette approche n'est pas adaptée pour les applications dans lesquelles le spectre d'excitation varie dans une gamme très large ou trop rapidement.

Oscillateur multimodal (Multimodal oscillator)

La réalisation d'un générateur linéaire est basée sur une structure mécanique dont le comportement fréquentiel est riche. Ainsi, si, dans une bande de fréquence donnée, le comportement peut être réduit à une seul mode de résonance, cela signifie que les réponses des autres modes sont négligeables. Cependant, la réponse de la structure peut être plus complexe et le générateur voir ses performances améliorées si plusieurs modes à des fréquences différentes peuvent être exploités efficacement et simultanément.

La première façon de construire un oscillateur multimodal est d'avoir un certain nom-

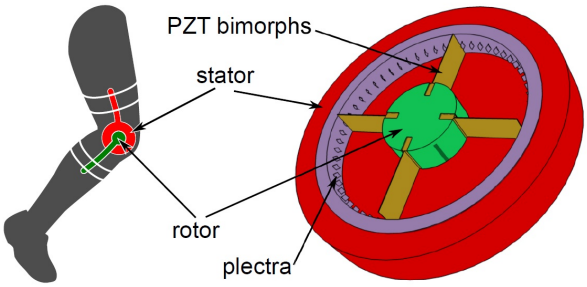

Figure 3: Générateur piézoélectrique à cordes pincées [16].

bre d'oscillateurs mono-fréquence utilisés conjointement mais de manière découplée [13, 14]. Un système hybride est également une solution pour la réalisation d'un générateur multimodal[15]. Dans ce cas, deux ou plusieurs dispositifs de transduction différents à des fréquences de résonance différentes sont intégrés sur un même générateur.

Les générateurs multimodaux sont capables d'obtenir des réponses à large bande sans réglage. Dans le même temps, la puissance de sortie est accrue. Néanmoins, la densité de puissance totale est réduite dans la mesure où le générateur au complet occupe beaucoup d'espace alors qu'un seul de ses sous-ensembles travaille à sa fréquence optimale. En outre, les propriétés électriques sont complexes de sorte que les difficultés pour la conception des circuits sont augmentées.

Conversion de fréquence (frequency up-conversion)

Dans de nombreux cas, la majeure partie de la puissance d'excitation peut se trouver dans une plage de fréquences basses. Pour disposer d'un générateur linéaire à basse fréquence, la solution est d'avoir soit une masse importante soit une faible rigidité, soit les deux. Cependant, la taille réduite des générateurs est souvent une des caractéristiques imposées par le cahier des charges de l'application visée. Comme la taille des générateurs devient plus petite, la masse est réduite en raison de la restriction de volume tandis que la rigidité est augmentée en raison de l'effet d'échelle. Par conséquent, la fréquence de résonance se déplace généralement à des valeurs plus élevées. De plus, pour récupérer l'énergie des basses fréquences, la grande course de déplacement nécessaire est difficile à satisfaire dans un volume réduit. Par conséquent, une méthode de conversion de fréquence est proposée pour transférer l'énergie disponible à basses fréquences à la gamme des hautes fréquences qui peut alors être exploitée par le générateur.

Un procédé courant consiste à utiliser une conception à deux étages de structures mécaniques. L'excitation de basse fréquence est captée par une structure de faible raideur, qui applique la force au générateur de haute fréquence positionné dans sa trajectoire de mouvement. Une grande déformation de la structure haute fréquence est alors obtenue. À la deuxième étape, le générateur est libéré et commence à vibrer librement sur sa fréquence propre. L'énergie de déformation transférée au cours de la première étape est dissipée dans l'amortissement mécanique et convertie en énergie électrique.

L'une des applications potentielles est la récupération d'énergie des mouvements du corps humain. Figure 3 donne un exemple développé par Pozzi et al [16]. pour la récupération de l'énergie au niveau des articulations des genoux. Toutefois, une conception fine est nécessaire pour réduire la perte d'énergie à la première étape et ainsi conserver des niveaux de performances acceptables.

Oscillateur non linéaire (Nonlinear oscillators)

Pour répondre à la question de la bande passante étroite des générateurs linéaires, l'exploitation des non-linéarités de structures mécaniques est considérée comme une solution efficace [17, 8, 9, 18]. En raison de leurs réponses spécifiques, les générateurs à structures mécaniques non linéaires offrent la possibilité d'augmenter l'énergie extraite sur une large bande de fréquences par rapport à des générateurs linéaires.

générateurs monostables

Pour les générateurs monostables, une seule position d'équilibre stable existe en l'absence de sollicitations extérieures. L'exemple le plus courant est l'oscillateur Duffing:

$$F_M = M\ddot{x} + (\mu_m(x) + \mu_e(x))\dot{x} + ax + bx^3 \tag{1}$$

Dans le cas où $a > 0$. En fonction de la valeur de b, l'équation précédente peut décrire un comportement raidissant ($b > 0$) ou assouplissant ($b < 0$) ou encore un simple oscillateur linéaire ($b = 0$).

Un autre type de structures monostables souvent utilisé est l'oscillateur linéaire par morceaux. Généralement, la courbe de réponse quasi-statique force-déplacement est constituée de plusieurs segments de droites de pentes (raideur) différentes.

Dans le cas de générateurs non linéaires monostables, la bande passante peut être améliorée. Toutefois, cet avantage est obtenu principalement pour les réponses de « haute énergie » autour de la fréquence caractéristique du système. Par conséquent, une question importante est de garantir cette réponse spécifique. Par ailleurs, il est intéressant de constater que certains des générateurs à ajustement de fréquence présentent également les caractéristiques des générateurs monostables.

Générateurs bistables/multi-stables

Lorsque plus d'une position d'équilibre existe dans la structure, les générateurs sont dits bistables ou multi-stables. Etant donné la complexité d'étude et de réalisation des générateurs à plus de deux positions stables, très peu de générateurs multi-stables sont développés. Par conséquent, dans cette section, les analyses se concentrent principalement sur les générateurs bistables.

Parmi les solutions à large bande introduites, le générateur bistable est considéré comme un des plus prometteurs en raison de ses caractéristiques uniques. Les sauts d'une position d'équilibre à une autre pour des grandes amplitudes d'excitation, induisent de grandes amplitudes de mouvements et augmentent donc considérablement la production d'électricité. L'effet de la conversion de fréquence (après un saut, la structure oscille autour de ses positions stables à haute fréquence) et la réponse non linéaire peuvent améliorer de façon significative la puissance produite et la bande de fonctionnement.

Bien qu'il existe un grand nombre de générateurs bistables publiés [19, 20], la plupart d'entre eux peuvent être classés en deux catégories dépendantes du mécanisme induisant la bistabilité : flambement et interaction magnétique.

a. Flambement. Le flambement est un moyen très courant de créer des structures bistables. Il est issu de l'instabilité mécanique dans le cas de fortes contraintes de compression. Un exemple représentatif est la poutre déformée, comme représenté sur la figure 4. Lorsque la force axiale est supérieure à la charge critique de flambage P_{cr}, la structure devient instable a sa position d'origine et se courbe dans une des configurations symétriques (b1) ou (b2).

b. Interaction magnétique. En raison des forces magnétiques à distance et sans contact,

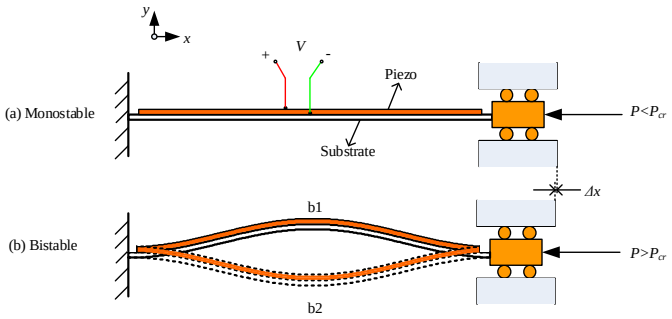

Figure 4: Poutre encastrée-encastrée avec charge axiale: (a) Monostable; (b) bistable.

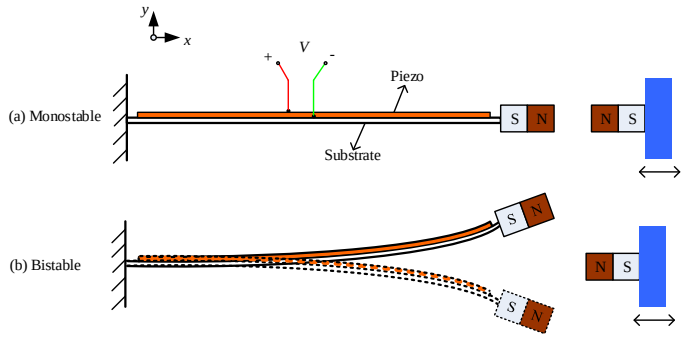

Figure 5: Poutre cantilever avec aimants : (a) cas Monostable; (b) cas bistable.

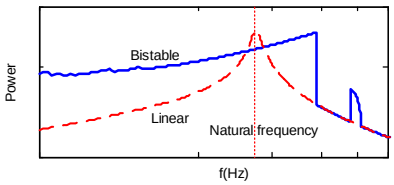

Figure 6: Réponses électriques typiques d'un générateur bistable et de son générateur linéaire équivalent.

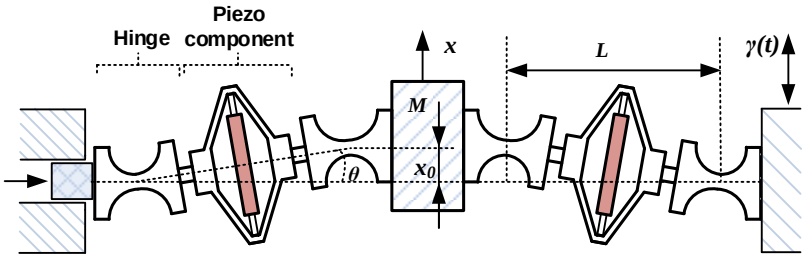

Figure 7: Principe du générateur BSM proposé.

l'interaction magnétique fournit une méthode simple et pratique pour obtenir un oscillateur bistable. Une configuration très fréquente est une poutre en porte à faux équipée d'un aimant à son extrémité libre se déplaçant devant un deuxième aimant statique. Ces deux aimants ont une polarité opposée comme le montre la figure 5. Si les aimants sont suffisamment rapprochés, la force répulsive génère une position instable à l'horizontal et deux positions stables de part et d'autre.

En raison de la particularité de la courbe de potentiel énergétique, le générateur bistable est en mesure d'obtenir de meilleures réponses à plus basses fréquences que le générateur monostable (linéaire ou non linéaire). La figure 6 représente une réponse fréquentielle typique de la puissance d'un générateur bistable soumis à une excitation de type balayage fréquentiel croissant. Les performances du générateur bistable sont supérieures à celles d'un générateur linéaire équivalent sur une large bande de fréquences.

0.2 Proposition du générateur BSM (Bistable-Spring-Mass)

0.2.1 Modèle

Un nouveau générateur piézoélectrique bistable conforme avec le mécanisme de l'effet de flambage est présenté sur la figure 7. En comparaison avec les oscillateurs bistables de la littérature, la nouvelle architecture proposée est compacte et relativement simple. Basé sur un système ressort-masse bi-encastré, il est composé de deux éléments piézoélectriques et d'une masse inertielle centrale. Des liaisons souples sont utilisées pour relier les parties ensemble ainsi qu'au châssis qui est soumis à l'accélération de l'environnement vibratoire ambiant $\gamma(t)$. La structure est symétrique de telle sorte que la masse se déplace seulement le long de la direction x.

En utilisant l'approche d'Euler-Lagrange, l'équation régissant le comportement dynamique peut être écrite comme:

$$\begin{cases} M\gamma = M\ddot{x} - \dfrac{Kx_0^2}{2L^2}x + \dfrac{Kx^3}{2L^3} + \mu\dot{x} + \alpha V_p \dfrac{x}{L} \\ I = \alpha\dfrac{x\dot{x}}{L} - C_0\dot{V}_p \end{cases} \tag{2}$$

Avec

$$x_0 = \sqrt{l_0^2 - L^2 - \frac{8K_\theta}{K}} \tag{3}$$

L'équation mécanique (3) montre que la rigidité des liaisons influe sur le niveau de flambage initial x_0. Si la rigidité de rotation est telle que $K_\theta > (l_0^2 - L^2)K/8$, la structure BSM se comporte comme un oscillateur monostable à comportement durcissant avec une seule position d'équilibre en $x = 0$. Cet effet souligne le rôle essentiel de K_θ pour la structure BSM.

En normalisant les équations, on obtient:

$$\begin{cases} \bar{\gamma} = \ddot{\bar{x}} - \dfrac{1}{2}\omega_0^2\bar{x} + \dfrac{1}{2}\dfrac{\omega_0^2}{\epsilon^2}\bar{x}^3 + 2\xi\omega_0\dot{\bar{x}} + \dfrac{k^2}{1-k^2}\dfrac{\omega_0^2\bar{x}}{\epsilon}\bar{V} \\ \bar{I} = \dfrac{\bar{x}\dot{\bar{x}}}{\epsilon} - \dot{\bar{V}} \end{cases} \tag{4}$$

Les paramètres de la structure sont donnés dans les tableaux 2.1 et 2.2.

Le choix de l'expression normalisée est conforme à l'approche unifiée citée précédemment. Elle souligne quatre paramètres caractéristiques : ω_0 la pulsation caractéristique, k^2 le coefficient de couplage électromécanique, ξ l'amortissement mécanique et, pour le système bistable, un paramètre sans dimension supplémentaire ϵ associé au niveau de flambage.

0.2.2 L'analyse du balance harmonique

Avant d'entreprendre les études numériques et expérimentales du générateur BSM, une analyse harmonique est utilisée pour explorer les différentes réponses dynamiques, en particulier pour les mouvements inter-puits (entre les positions stables) lors d'excitations harmoniques.

Dans la mesure où le mouvement périodique du générateur bistable possède une composante fondamentale dominante semblable à un signal sinusoïdal, la solution des équations d'équilibre dynamique du générateur de BSM est supposée être:

$$\bar{x} = c(t) + a\sin\omega t + b\cos\omega t \tag{5}$$

$$\dot{\bar{x}} = \dot{c} + (\dot{a} - b\omega)\sin\omega t + (\dot{b} + a\omega)\cos\omega t \tag{6}$$

$$\ddot{\bar{x}} = (2\dot{a} - b\omega)\omega\cos\omega t - (\dot{b} + 2a\omega)\sin\omega t \tag{7}$$

L'amplitude du mouvement est supposée varier lentement dans le temps, de sorte que les dérivées d'ordre deux ou supérieur sont négligées. On note $c(t)$ la composante continue du mouvement. Sa valeur est nulle pour le mouvement inter-puits.

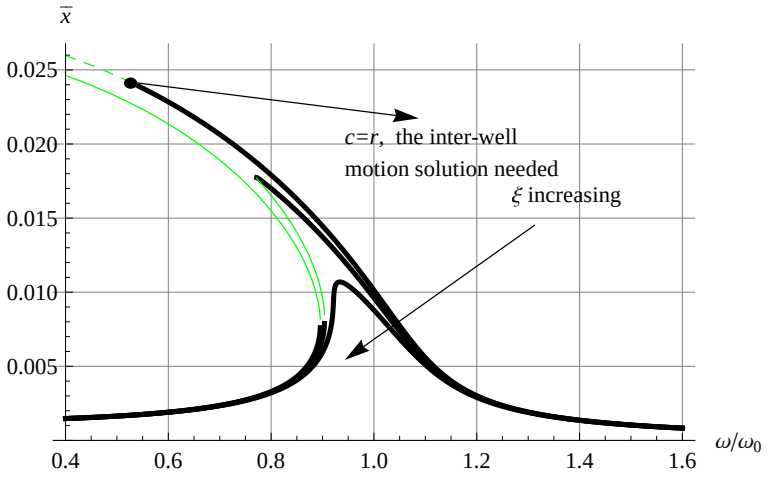

Figure 8: Réponses de déplacements intra-puits pour différents cas d'amortissement. Solutions stables (courbes en trait gras); solutions instables (courbes en trait fins).

Mouvement intra-puits

La figure 8 représente les réponses de déplacements intra-puits pour différents niveaux d'amortissement. Le générateur BSM se comporte comme un oscillateur de Duffing assouplissant tandis que l'effet des non linéarités diminue à mesure que le coefficient d'amortissement augmente.

La composante continue $c(t)$ pour le mouvement intra-puits est liée à l'amplitude, car le système dans le cas monostable n'est pas symétrique par rapport à la position d'équilibre. Lorsque l'amplitude augmente, $c(t)$ va dériver vers la position $x = 0$. Cependant, il est à noter que l'amplitude r du mouvement intra-puits doit satisfaire à la relation $r < c$. Sinon, le mouvement du générateur est tel que le potentiel critique est franchi $(c - r < 0)$ et qu'il doit donc être analysé comme un mouvement inter-puits.

Mouvement inter-puits

La figure 9 montre une réponse en fréquence inter-puits pour un générateur BSM donné. La courbe supérieure en trait gras représente la solution inter-puits stable tandis que les deux courbes rouges sont les solutions instables. Les orbites intra-puits de faible énergie stables (courbes inférieures en trait gras) et instable (courbes vertes) sont représentées afin de proposer une description complète des réponses potentielles. Il est clair que pour la même excitation, le mouvement inter-puits constitue une réponse plus favorable en termes de puissance récupérable que le cas monostable. Les droites en pointillés sont utilisées pour indiquer la position des sauts entre l'orbite de haute énergie et de basse énergie. Les directions des sauts sont liées aux réponses selon que l'excitation soit un balayage fréquentiel croissant ou décroissant. Les phénomènes d'hystérésis caractéristiques de la réponse de ce système non linéaire sont facilement déduits des positions des sauts.

Pour mieux comprendre les propriétés du générateur BSM, l'influence des paramètres sur la réponse inter-puits a été étudiée. Les conditions préférables pour maximiser la puissance et la bande passante ont été identifiées : faible coefficient d'amortissement, valeur optimale de la charge électrique, niveau élevé de couplage électromécanique et niveau d'excitation propre à générer les mouvements inter-puits.

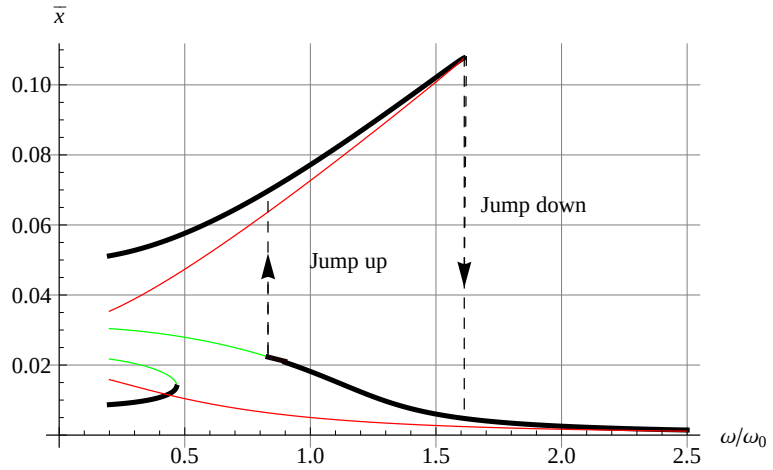

Figure 9: Réponses de déplacements inter-puits d'un générateur BSM.

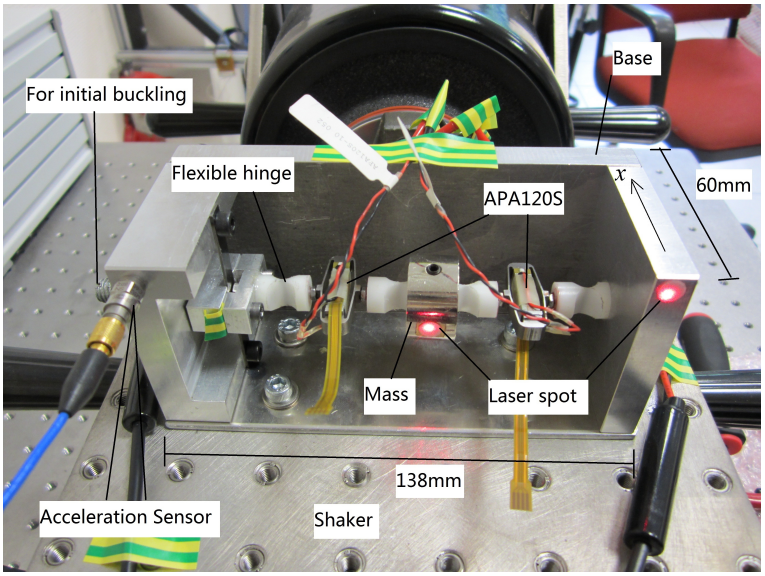

Figure 10: Prototype du générateur BSM.

0.2.3 Etudes numériques et expérimentales sur le générateur BSM

Montage expérimental

Pour confirmer le comportement du générateur BSM, un prototype expérimental a été réalisé (figure 10). Il comprend une masse inertielle, deux transducteurs piézoélectriques (APA120S, CEDRAT Technologies©) et quatre liaisons souples réalisées en PTFE. Les deux composants piézoélectriques sont connectés en parallèle.

Excitation harmonique

Pour étudier les performances et les propriétés concernant la bande passante du générateur BSM, les études utilisant des excitations classiques à fréquence fixe ne conviennent plus. L'analyse des réponses lorsque le système est soumis à des excitations de type « chirp » est capables de fournir de plus amples informations sur les propriétés.

Les réponses expérimentales sont présentées sur la figure 11. On peut voir que, pour une faible excitation, le générateur se comporte comme son oscillateur linéaire équivalent.

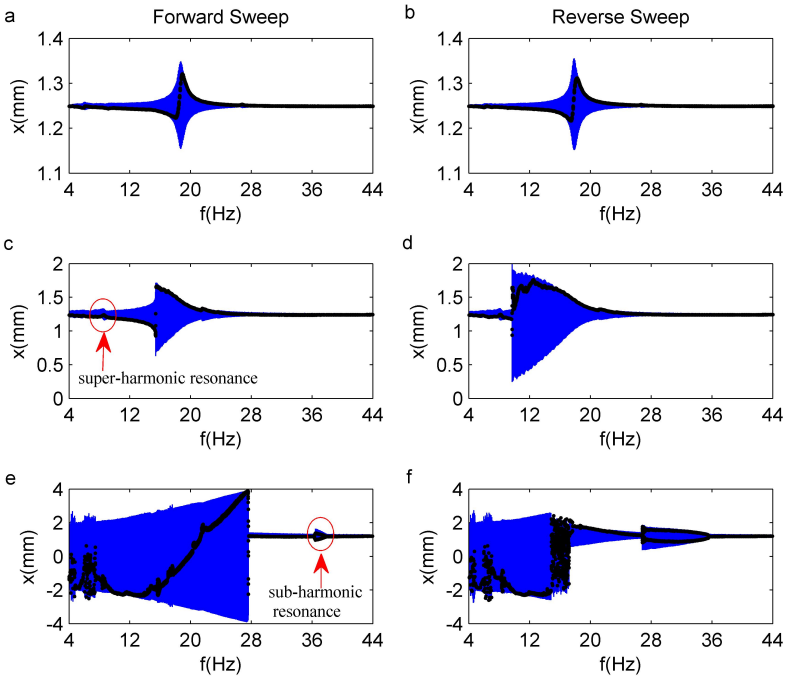

Figure 11: Déplacement expérimental (courbe bleue) et section de Poincaré (points noirs) de la masse pour des balayages fréquentiels croissants et décroissants: 0.075 m/s^2 *(a,b),* 0.5 m/s^2 *(c,d),* 3 m/s^2 *(e,f).*

Lorsque l'amplitude d'excitation est augmentée à 0.5 m/s^2, des réponses intra-puits non linéaires apparaissent.

Dans le cas de la plus haute amplitude d'excitation (3 m/s^2), la masse franchit périodiquement la position centrale et les propriétés du comportement inter-puits peuvent être déduites. Ces mouvements apparaissent pour des fréquences de 4 Hz à 27 Hz pour le balayage à fréquences croissantes et de 18 Hz à 4 Hz pour le balayage décroissant. Des oscillations périodiques sont visibles pendant la majeure partie du processus de balayage, alors que le mouvement chaotique se produit autour de 5 Hz et 7.5Hz quelques soit le sens du balayage fréquentiel. Les sections de Poincaré qui se présentent sous la forme de points noirs alignés pour les oscillations périodiques et des points noirs distribués pour les oscillations chaotiques soulignent clairement ces phénomènes. Pour le balayage inverse, il existe une bande de fréquence supplémentaire de 16 à 18Hz où le mouvement chaotique existe.

Les puissances théorique et expérimentale correspondantes au générateur BSM sont présentées dans la figure 12. A des fins de comparaison, la puissance disponible déduit du modèle équivalent linéaire est également tracée pour la même excitation. Les résultats expérimentaux sont en bon accord avec la théorie.

Lorsque l'amplitude d'excitation atteint 3 m/s^2, la puissance disponible maximale est évaluée à 12mW pour le générateur équivalent linéaire avec une largeur de bande de 1Hz. Le générateur bistable, qui présente des mouvements inter-puits, délivre une puissance maximale de 13mW (balayage à fréquences croissantes) et plus de 5 mW de 18Hz à 27Hz. Même pour le cas moins favorable de l'excitation avec un balayage fréquentiel décroissant, la puissance maximale disponible est encore de 1.8mW et plus de 0.4mW peut être obtenue à partir de 15 Hz et jusqu'à 5 Hz. Ces résultats confirment que le générateur bistable

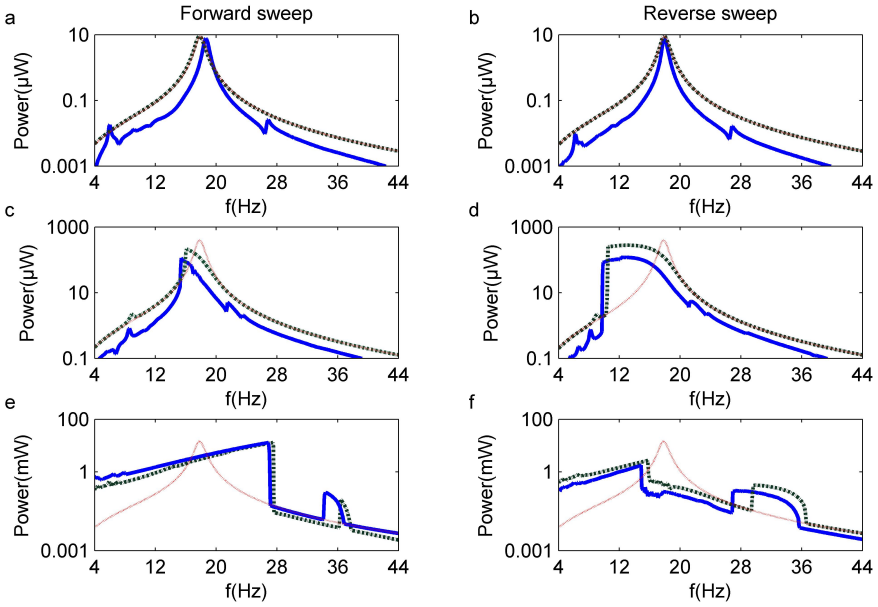

Figure 12: Réponses en puissance théoriques (trait gras, pointillés) et expérimentales (trait gras) pour des signaux modulés en fréquence et des amplitudes d'excitations variées : $0.075\ \mathrm{m/s^2}$ *(a,b),* $0.5\ \mathrm{m/s^2}$ *(c,d),* $3\ \mathrm{m/s^2}$ *(e,f). La ligne rouge en pointillés représente la puissance que fournirait le générateur linéaire équivalent.*

proposé est supérieure à un générateur linéaire équivalent en ce qui concerne la largeur de bande.

En général, pour les systèmes non-linéaires possédants des solutions multiples, la réponse correspondante aux déplacements les plus élevés est souhaitable pour maximiser l'énergie. Cependant, celle-ci est dépendante des conditions initiales qui ne sont pas maitrisables. Il est alors intéressant de trouver une méthode pour permettre à l'oscillateur non linéaire le saut de l'orbite basse énergie à l'orbite de haute énergie. Une solution possible consiste à appliquer une forte excitation brève grâce à une structure active additionnelle au prix d'une complexité accrue et d'une puissance consommée supplémentaire. Masuda et al [21] ont théoriquement étudié la méthode de commutation entre la charge électrique et une charge résistive négative (circuit actif) pour déclencher le passage à l'orbite de haute énergie. Une autre approche possible consiste à modifier la barrière de potentiel en fonction du niveau d'excitation.

Excitation de type bruit

Le comportement de l'oscillateur bistable dans le cas des excitations arbitraires ne peut être déduit directement de l'analyse précédente. Les spectres de vibrations correspondants à des environnements réalistes sont généralement non stationnaires et possèdent une certaine richesse fréquentielle. Le comportement du générateur dans le cas d'un bruit blanc à bande limitée est ainsi également étudié pour confirmer ses propriétés vis-à-vis de sa bande passante.

Tout d'abord, un bruit à bande limitée à une fréquence de coupure de 40 Hz est utilisé pour la simulation numérique. Cette excitation est obtenue en utilisant un bruit blanc standard filtré à l'aide d'un filtre passe-bas (Butterworth du quatrième ordre). La figure 13 montre les spectres en tension du générateur BSM et de son équivalent linéaire. Comme nous pouvons le voir, le BSM a des bonnes performances sur toute la plage des basses

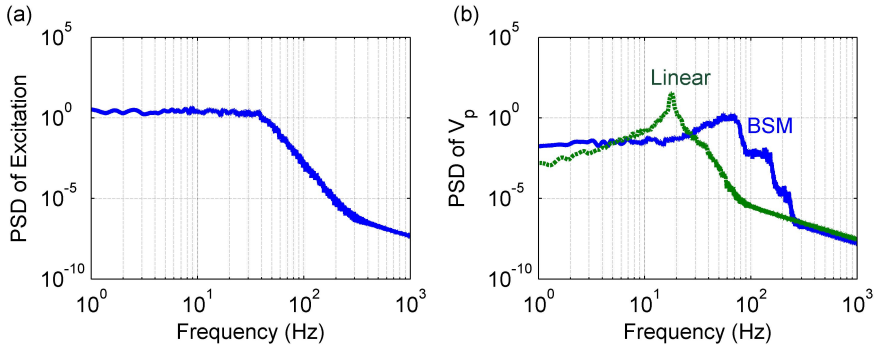

Figure 13: (a) Densité spectrale de puissance d'une excitation de type bruit à bande limitée; (b) Densité spectrale de puissance de la tension piézoélectrique.

fréquences. Par ailleurs, les meilleurs résultats sont également obtenus par le générateur BSM à des fréquences supérieures à la fréquence de résonance du générateur linéaire équivalent. Ceci est une conséquence du doublement de la fréquence de la tension lorsque la masse franchit la position horizontale.

Pour préciser les capacités d'adaptation du générateur BSM pour différentes excitations, des bruits blancs à bande limitée avec des fréquences de coupure différentes sont utilisés. Afin d'effectuer une comparaison significative, ces signaux d'excitation sont pondérés pour présenter la même valeur RMS quelles que soient leurs fréquences de coupure, comme le montre la figure 14(a).

Dans ces conditions, les puissances issues des résultats de simulation et expérimentaux sont donnés dans la figure 14(b) pour une accélération RMS de 2m/s^2 · La puissance issue du modèle équivalent linéaire est également donnée. Il est clairement démontré que la récupération d'énergie bistable est capable de récupérer efficacement de l'énergie à partir d'un bruit limité en fréquence à chaque fois que la fréquence de coupure est inférieure à f_0, fréquence propre du générateur linéaire équivalent. Cependant, si la fréquence f_0 est comprise dans la bande de fréquence de l'excitation, le générateur linéaire équivalent et le générateur bistable produisent théoriquement une puissance quasiment identique.

0.3 Optimisation et conception du générateur BSM

Les générateurs bistables démontrent plus d'avantages par rapport aux approches linéaires lorsque les excitations sont suffisamment élevées pour induire le mouvement inter-puits. Pour obtenir de bonnes performances, il est alors nécessaire de s'assurer que le générateur BSM opère en mode « inter-puits ». Toutefois, le choix d'une faible barrière de potentiel conduirait à un comportement linéaire. En conséquence, les paramètres du système doivent être optimisés pour obtenir les propriétés souhaitées.

0.3.1 Stratégie d'optimisation pour le générateur de BSM

Comme il est indiqué dans l'analyse harmonique, une meilleure performance est obtenue pour un faible amortissement mécanique et un niveau de couplage élevé. Considérant que k^2 est habituellement fixé pour un composant piézoélectrique sélectionné et que l'amortissement ξ est liée à la structure et aux matériaux, l'optimisation peut être effectuée sur les paramètres ω_0 et ϵ. Dans la mesure où les réponses du système sont fortement dépendantes de la nature

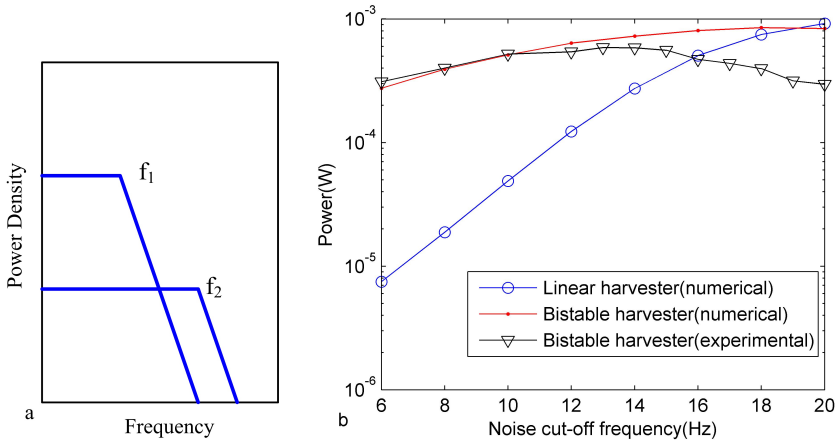

Figure 14: (a) Spectre schématique des signaux de bruit blanc à fréquences de coupure différentes et valeurs RMS constantes. (b) Comparaison de la puissance entre un générateur linéaire et bistable pour une excitation de type bruit blanc à bande limitée avec une valeur RMS constante (2$\mathrm{m/s^2}$ *).*

de l'excitation, il est impossible d'obtenir le même générateur optimal pour des situations différentes. L'optimisation doit donc être faite pour des exigences spécifiques. Par conséquent, certaines conditions prédéfinies et les critères d'optimisation doivent être choisis et précisés préalablement.

Avec le modèle, les conditions prédéfinies et les critères confirmés, une stratégie d'optimisation est ensuite proposée : L'excitation γ est déterminée par l'application visée alors que le niveau de couplage est lié à l'élément piézoélectrique choisi pour assurer une génération de puissance suffisante. En considérant que le volume peut être un des éléments défini par le cahier des charges de l'application visée, une valeur d'essai de L est choisie permettant l'estimation d'un volume initial. Ces paramètres sont utilisés comme entrée dans le modèle normalisé qui est simulé dans Matlab/ Simulink.

En faisant varier ω_0 et ϵ, une valeur extrême de la fonction d'optimisation f_{op} (la densité de puissance) est trouvée et comparée à la valeur de densité de puissance cible. Si cette valeur optimisée est conforme à l'exigence, nous pouvons déterminer les paramètres optimaux initiaux et passer à l'étape suivante de la conception; sinon, une autre valeur d'essai de L est choisie. S'il est impossible de satisfaire aux exigences, les paramètres d'entrée doivent être modifiés soit en relâchant la contrainte de volume, soit en changeant les matériaux piézoélectriques ou encore en diminuant la densité de puissance cible.

A l'issu de la détermination des paramètres optimaux, l'étape suivante de conception peut être entamée. Elle se déroule comme suit:

- Selon les valeurs sélectionnées de ϵ et ω_0, un choix initial de M et K peut être déterminé pour satisfaite aux exigences de volume. Si le volume est convenable, M et K sont utilisés. .
- Ensuite, un modèle d'analyse de la liaison souple est utilisé pour déterminer les paramètres de conception. La raideur en rotation des liaisons souples K_θ en particulier doit être évaluée. De plus, la limite élastique des matériaux peut contraindre fortement la conception.
- Finalement, une solution est trouvée. En cas de non satisfaction des critères, le processus d'optimisation doit être repris en relâchant certaines contraintes.

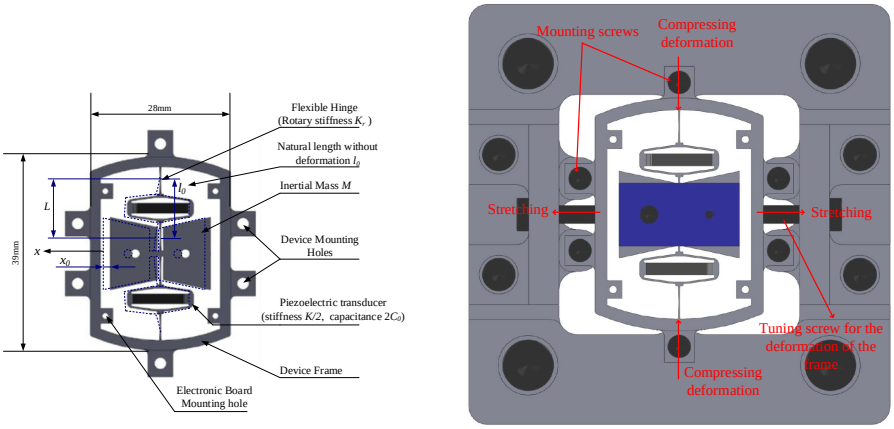

(a) (b)

Figure 15: (a) Générateur BSM monobloc miniaturisé; (b) Plate-forme de montage permettant le réglage du flambement initial.

0.3.2 Conception mono-bloc d'un générateur BSM miniaturisé

Avec la stratégie utilisée et les contraintes prises en compte, un générateur BSM monobloc miniaturisé a été conçu et fabriqué grâce au savoir-faire technique de CEDRAT Technologies©.

Principe de conception

La CAO du générateur ainsi que sa plate-forme de montage sont représentées sur la figure 15. L'architecture est basée sur le schéma de principe du générateur BSM avec une conception monobloc, ce qui permet d'améliorer la compacité et la fiabilité.

Quatre poutres sont utilisées comme liaisons souples. En comparaison du premier prototype, les liaisons ainsi réalisées présentent une rigidité axiale supérieure. Les sections rectangulaires offrent une raideur en rotation K_θ inférieure et un angle de rotation maximal plus élevée. En outre, la structure de poutre simplifie les fabrications.

Une masse inertielle est reliée aux liaisons. L'écart entre les ces deux parties est choisi pour éviter le choc durant les mouvements et pour maximiser la masse. Les deux formes elliptiques amplifient les forces exercées sur les matériaux piézoélectriques qui sont précontraints. Le flambement maximal de la structure est alors limité par la valeur de cette précontrainte. Les électrodes des empilements piézo-électriques sont interdigitées et connectées respectivement aux pôles positif et négatif.

La procédure de flambement est décrite ci-après: Avant les opérations, les vis dans les trous de fixation sont desserrées et le dispositif est dans des conditions libres. La plate-forme de montage permet la déformation du cadre par l'action de traction de deux vis dédiées, comme représenté sur la figure 15(b). La déformation du cadre induit la compression des liaisons souples et des éléments piézoélectriques le long de leur axe. En conséquence, le dispositif est réglé de façon statique à une position choisie. La masse atteint une nouvelle position d'équilibre, comme indiqué par la ligne en pointillés sur la figure 15(a). Enfin, les six vis dans les trous de fixation sont serrées pour maintenir la déformation du cadre constante pendant le fonctionnement. Les vis de réglage peuvent ensuite être retirées.Le dispositif fabriqué est illustré à la figure 16.

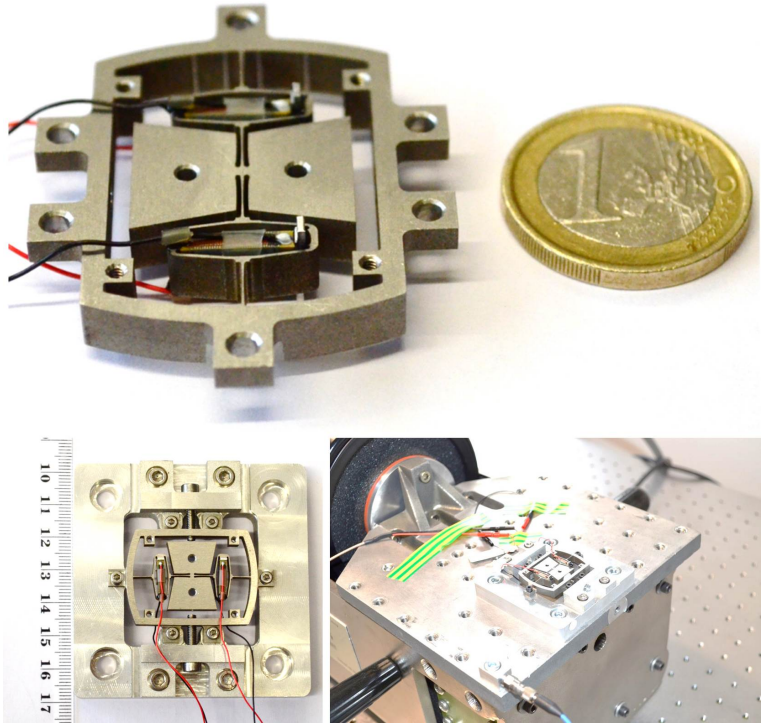

Figure 16: Générateur monobloc fabriqué et montage sur pot vibrant.

Etude des performances

Le volume total du dispositif est de $5,46\ \text{cm}^3$. Pour étudier les propriétés de bande passante et de puissance, une excitation de type « chirp » (amplitude 6 m/s^2, 15Hz-66Hz, 0,05 Hz/s) est appliquée au dispositif. Les réponses théoriques et expérimentales de déplacement sont cohérentes comme le montre la figure 17.

Les courbes rouges en pointillés représentent le déplacement maximal admissible de la masse centrale (1,2 mm). Il est déterminé par la limite élastique du matériau utilisé. Selon la figure 18, une puissance maximale de 2,64mW est obtenue à 66Hz pour le balayage fréquentiel croissant. La densité de puissance correspondante est de $0,483\ \text{mW/c}^3\text{m}$.

Une excitation de type bruit blanc à bande limitée (fréquence de coupure 40Hz, RMS 4,5 m/s^2) a été également utilisée pour évaluer les performances. Pour étudier l'influence du niveau de flambement x_0 sur les performances, les puissances moyennes produites pour différentes valeurs de $x - 0$ sont présentées. Les résultats de la figure 19 sont conformes aux valeurs attendues lors de l'optimisation.

Pour donner une perspective d'application éventuelle du dispositif BSM miniaturisé dans un environnement réel, un signal d'accélération correspondant à celui enregistré au niveau d'une roue de voiture [22] (laboratoire de NiPS, Université de Pérouse) est reproduit par le pot vibrant. Les formes d'ondes de tension et de déplacement sont indiquées sur la figure 20. Une puissance moyenne de 0,056mW est obtenue avec une valeur d'accélération RMS de 0,7 g. Les spectres sont représentés dans la figure 21.

0.3.3 Comparaison avec les générateurs de la littérature

Pour faire des comparaisons avec les autres générateurs non linéaires pour la récupération d'énergie à large bande dans la littérature, un facteur de mérite doit être proposé. Sans aucun doute, les propriétés les plus importantes des générateurs non linéaires sont la

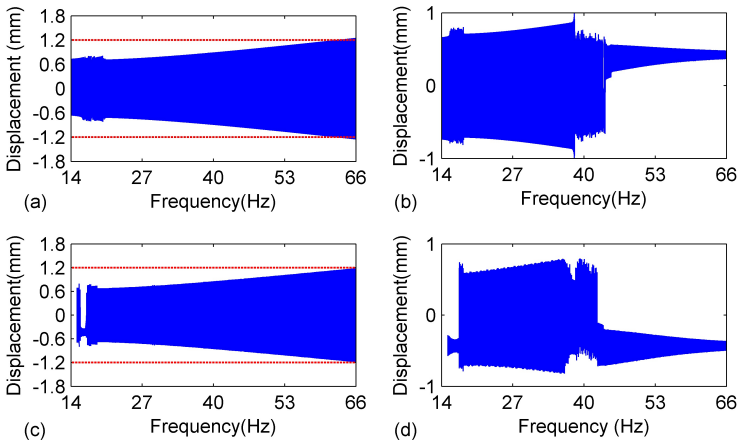

Figure 17: Réponses de déplacement du générateur de BSM mono-bloc: (a) balayage fréquentiel croissant théorique; (b) balayage décroissant théorique; (c) balayage fréquentiel croissant expérimental; (d) balayage décroissant expérimental.

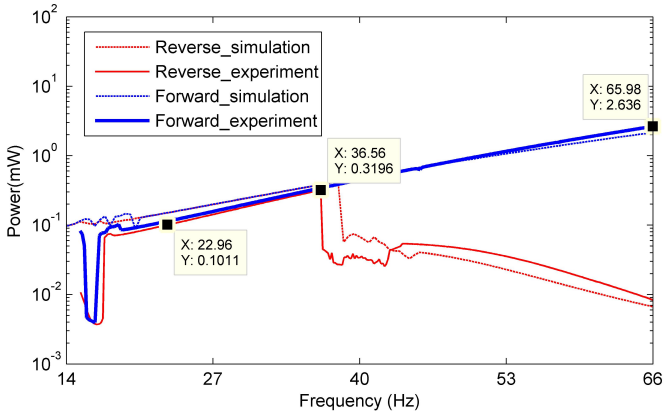

Figure 18: Réponses en puissance du générateur BSM monobloc.

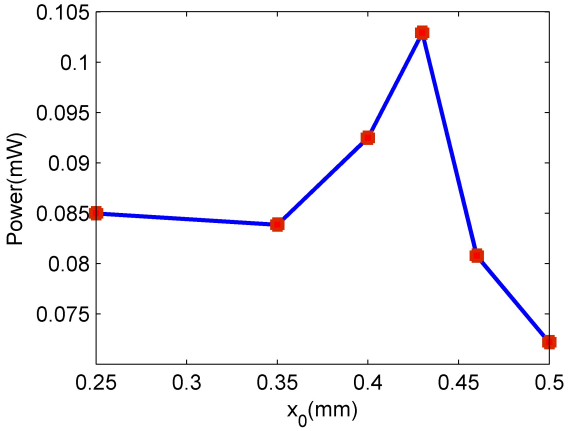

Figure 19: Puissance récupérée en fonction du niveau de flambement.

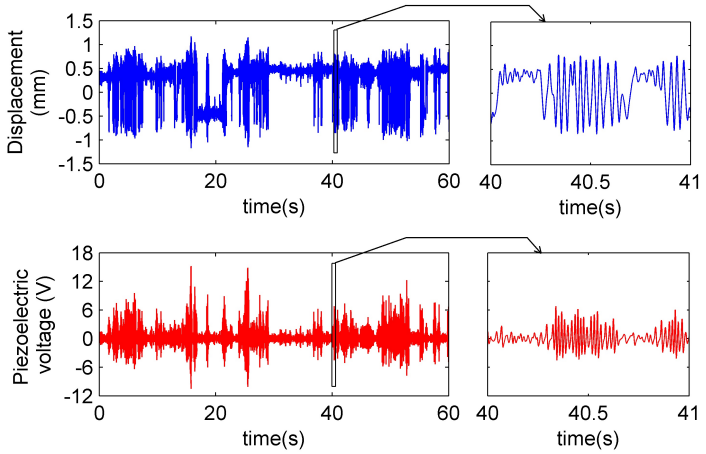

Figure 20: Formes d'ondes des déplacements et des tensions pour le signal d'excitation provenant d'une voiture.

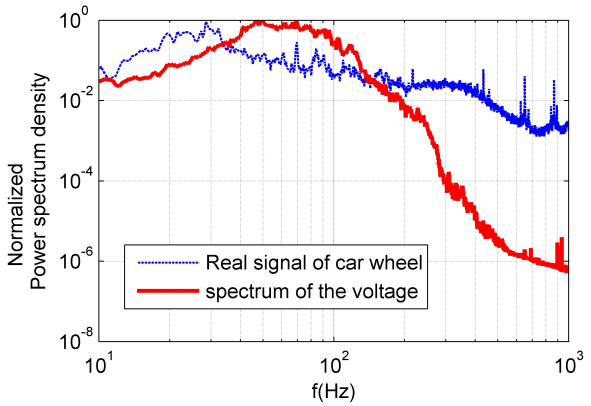

Figure 21: Spectres de l'excitation provenant d'une voiture et de la tension du générateur BSM monobloc.

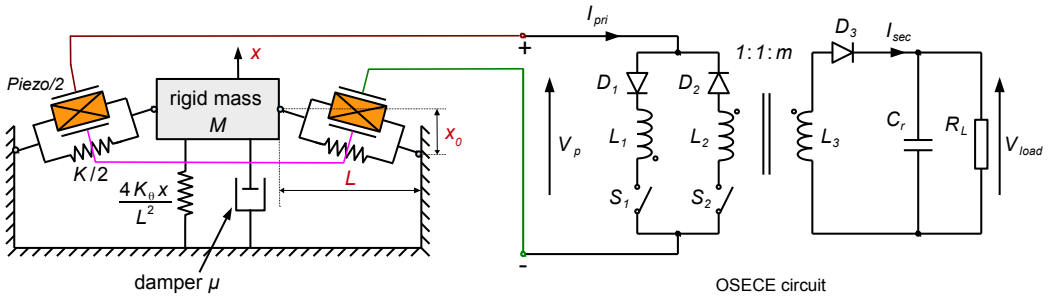

Figure 22: Générateur BSM avec circuit OSECE.

bande passante et la puissance disponible. La figure de mérite proposée doit tenir compte des différentes conditions d'essai et des masses utilisées pour fournir des évaluations justes. Par conséquent, le NPBP (Normalized Power Bandwidth Product) suivant est suggéré:

$$NPBP = \frac{P_{av}}{P_{lim}}\frac{\Delta f}{f_c}Q_m = \frac{P_{av}}{\frac{M\gamma^2 Q_m f_c}{2\pi f_c}}\frac{\Delta f}{f_c}Q_m = \frac{2\pi\Delta f P_{av}}{M\gamma^2} \tag{8}$$

où P_{av} représente la puissance moyenne sur la bande de fréquences effective Δf, f_c est la fréquence centrale, M est la masse inertielle du générateur, γ est l'amplitude de l'accélération, Q_m est le facteur de qualité. P_{lim} est la puissance maximale pouvant être récupérée dans le cas d'un générateur linéaire qui serait sujet à la même excitation, avec les mêmes fréquence centrale, masse et facteur de qualité mécanique.

Le chiffre NPBP contient un triple point de vue : puissance normalisée, bande passante normalisée et facteur de qualité. Il donne l'indication qu'un bon générateur doit être conçu pour maximiser la synthèse de ces trois aspects.

0.4 Générateur BSM avec OSECE

La figure 22 montre le modèle du générateur de BSM utilisé conjointement avec le circuit OSECE (Optimized Synchronous Electric Charge Extraction). Les composants piézoélectriques sont connectés en série. Ceci permet notamment de doubler la tension piézoélectrique de telle sorte que les pertes d'énergie dans les diodes sont diminuées.

Les formes d'onde théoriques du générateur et du circuit sont tracées sur la figure 23. Les interrupteurs sont toujours dans des états complémentaires, et sont commutés aux passages de V_p par des extrema. Ils sont maintenus dans leur état jusqu'au prochain extremum. Il est intéressant de noter que les interrupteurs sont commutés quatre fois par période de mouvement inter-puits. En effet, la période de contrainte est la moitié de la période de déplacement ce qui est une particularité par rapport au cas linéaire habituel.

Le but de ce travail est d'étudier les meilleures performances atteignables en utilisant la combinaison du circuit OSECE et du générateur bistable pour différents cas de couplage électromécanique et d'excitations. En connectant un condensateur supplémentaire Ca en série avec les éléments piézoélectriques, le coefficient de couplage électromécanique peut être abaissé à la valeur désirée. En ce qui concerne les excitations, les balayages fréquentiels croissant et décroissant ainsi que le bruit à bande limitée ont été utilisés pour les tests. Les performances du générateur BSM avec circuit standard sont également étudiées à des fins de comparaison. Dans la mesure où un dispositif avec un haut niveau de couplage est nécessaire ici, le premier prototype macroscopique ($k^2 = 0.0684$) est exploité.

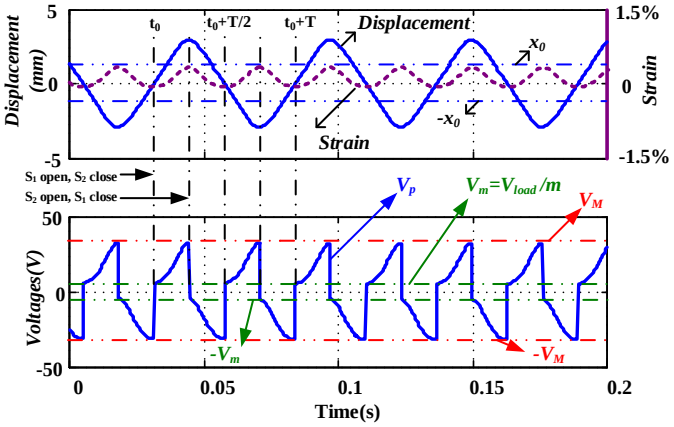

Figure 23: Forme d'onde théorique pour le générateur BSM + OSECE.

Le signal de balayage fréquentiel avec une amplitude de 4m/s^2 et un taux de variation fréquentiel de 0,05 Hz/s est utilisé. Ces paramètres sont choisis pour obtenir des mouvements inter-puits périodiques pour tous les cas testés.

La figure 24 montre les puissances théoriques et expérimentales dans le cas d'un couplage faible ($k^2 = 0,0137$). Plus de puissance est produite à l'aide du circuit OSECE sur toute la gamme de fréquences, à l'exception d'une petite zone. Pour celle-ci, l'effet d'amortissement plus fort induit pas le circuit OSECE limite les amplitudes de déplacement. Lorsque la réponse n'est pas sensible à l'effet d'amortissement du circuit OSECE, plus de puissance est extraite et exploitée par le circuit. Cependant, lorsque la fréquence croît et se rapproche de la fréquence naturelle, l'amortissement dû aux performances du circuit OSECE empêche le mouvement d'augmenter encore. Par conséquent, la réponse en puissance du générateur BSM chute plus tôt pour le circuit OSECE que pour le circuit standard.

Dans le cas d'un couplage élevé, l'effet d'amortissement du circuit OSECE est d'autant plus évident que k^2 est élevé. La réponse en déplacement représentée sur la figure 25 montre clairement cet effet d'amortissement qui augmente avec le coefficient de couplage. Pour un balayage vers l'avant, le mouvement inter-puits se termine à une fréquence beaucoup plus basse de 19Hz ($k^2 = 0,0684$) par rapport au 38Hz pour un couplage faible ($k^2 = 0,0137$).

Les tests ont été effectués à nouveau pour plusieurs valeurs de kr, les puissances moyennes sont représentées sur la figure 26. Il est clair que le circuit OSECE montre de bien meilleures performances pour le cas des faibles couplages. L'effet d'amélioration de puissance du circuit OSECE est supérieur à son effet d'amortissement. Lorsque k^2 augmente, le circuit OSECE induit des effets d'amortissement qui peuvent dépasser la valeur optimale. Cette valeur est fonction de l'amortissement mécanique ξ. Dans ces situations, le mouvement du générateur BSM est plus amorti. Par conséquent, le circuit standard obtient plus de puissance pour les excitations à fréquences croissantes lorsque k^2 est assez élevé.

Un autre cas typique d'excitation est le bruit blanc à bande limitée. Le bruit à bande limitée est défini ici comme un bruit blanc idéal filtré pour conserver une bande 4Hz-20Hz (filtre passe bande Butterworth du second ordre) avec une amplitude efficace de $3,5\ \text{m/s}^2$. Pour comprendre l'influence du coefficient de couplage, les puissances moyennes expérimentales et théoriques sont obtenues pour plusieurs valeurs de k^2 comme le montre

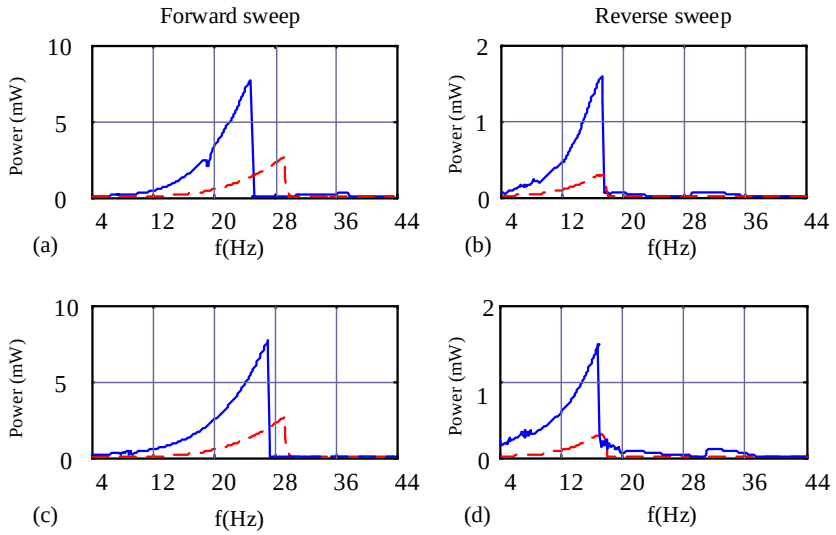

Figure 24: Puissances expérimentale (a, b) et théorique (c, d) pour $k^2 = 0.0137$. *Ligne continue: circuit OSECE; Ligne pointillée: circuit standard.*

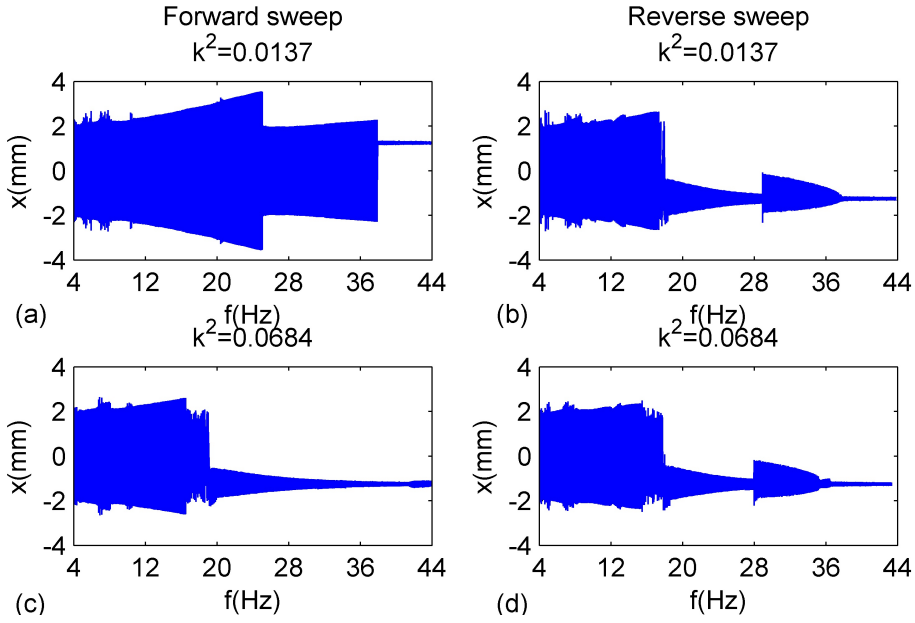

Figure 25: Déplacements expérimentaux du générateur BSM avec le circuit OSECE pour $k^2 = 0.0137$ *et* $k^2 = 0.0684$.

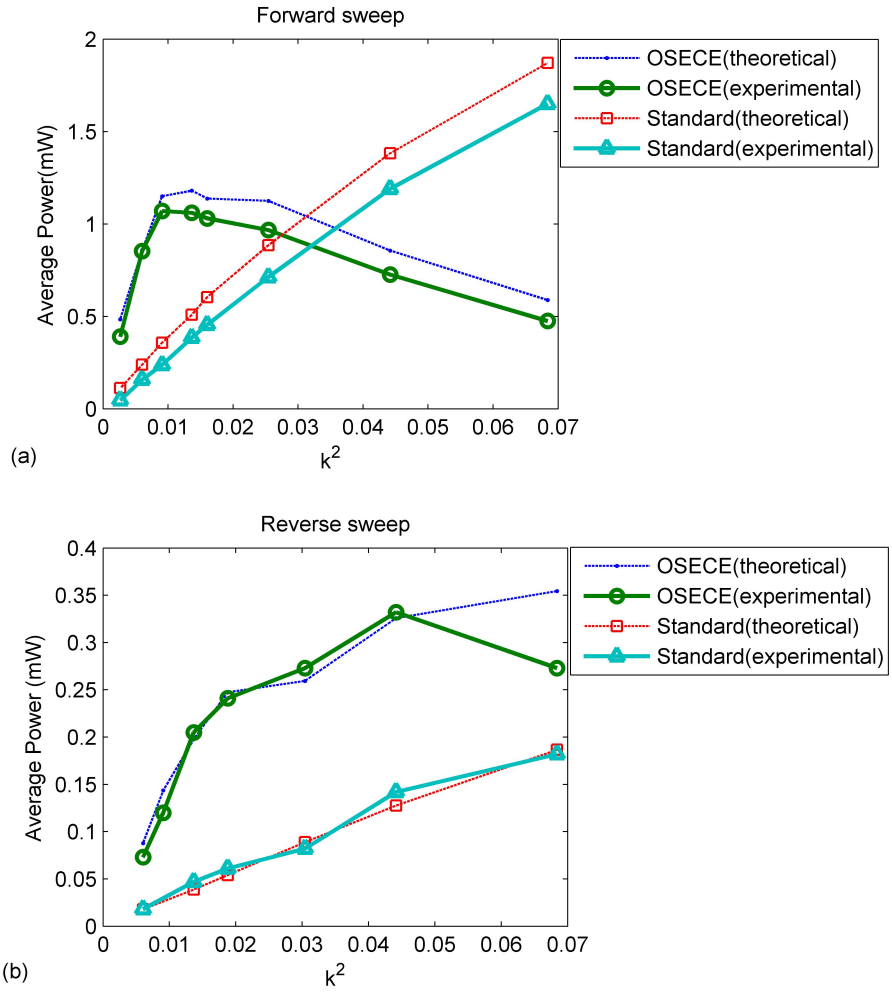

Figure 26: Puissance moyenne en fonction de k^2 pour balayage fréquentiel ($4\mathrm{m/s}^2$, 4-44Hz, 0.05Hz/s) (a) balayage croissant; (b) balayage décroissant.

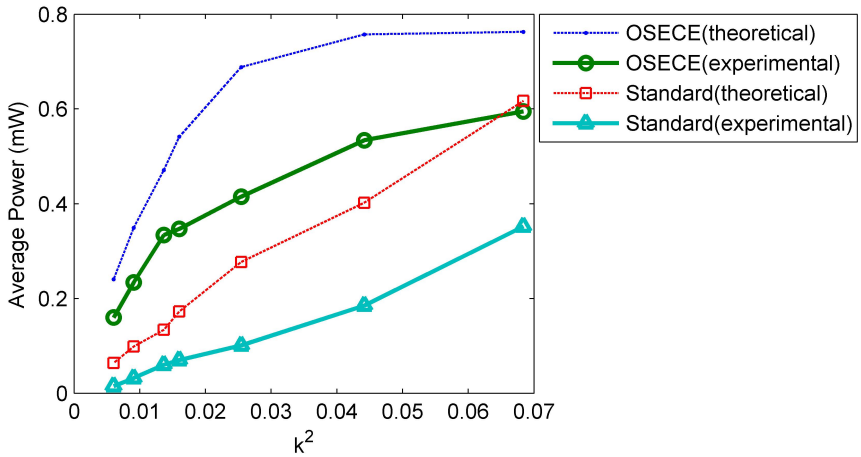

Figure 27: Puissances moyennes pour le circuit OSECE et le circuit standard pour une excitation de type bruit à bande limitée.

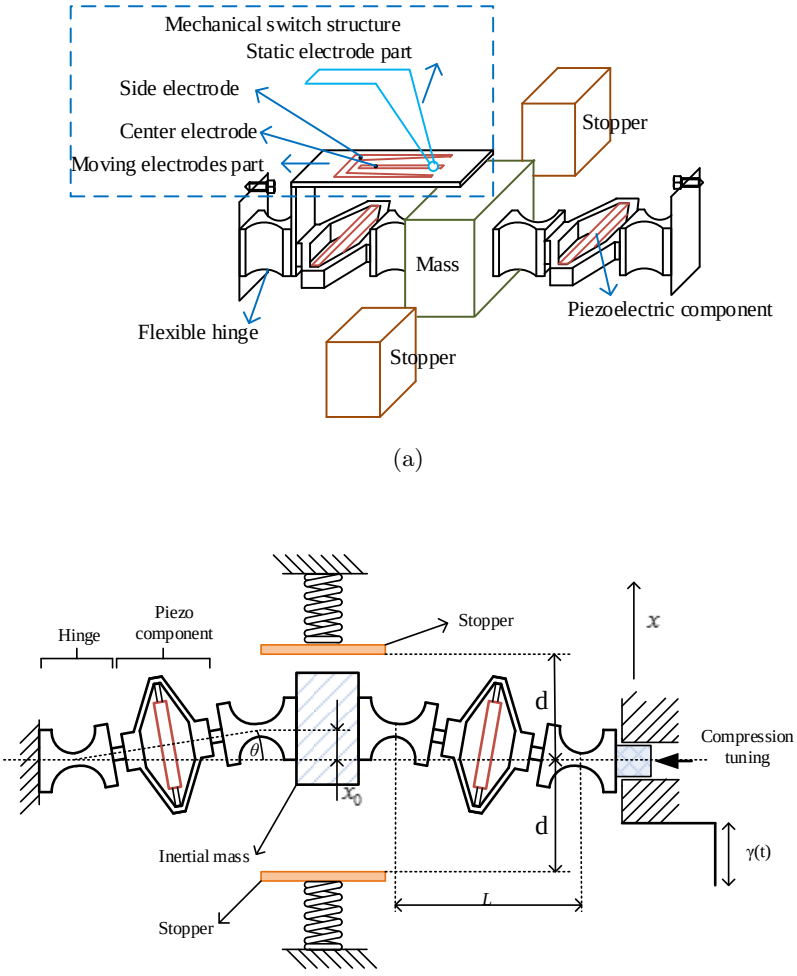

Figure 28: Structure du BSMOS : (a) Représentation schématique 3D (avec des interrupteurs mécaniques). (b) vue schématique 2D (sans les interrupteurs mécaniques).

la figure 27. La technique OSECE semble être supérieure à la technique standard pour tous les cas, ce qui est un résultat similaire à ce qui précède. Le gain en puissance de la technique OSECE est plus important que les effets d'amortissement induits.

0.5 Circuit autoalimenté OSECE avec des interrupteurs mécaniques pour le générateur BSM

La stratégie de commutation de la technique OSECE est simple ce qui permet d'envisager le remplacement de l'approche électronique par une approche mécanique. L'utilisation de commutateurs mécaniques permet d'optimiser la perte d'énergie dans les composants électroniques. Cette approche autoalimentée est appliquée à une nouvelle structure : BSMOS (BSM Oscillator with Stoppers).

Comme le montre la figure 28, la structure BSMOS proposée comprend trois parties : un oscillateur bistable, une structure de commutateur mécanique et deux butées élastiques. Pour réaliser un générateur autonome, une structure de commutateur mécanique est introduite dans l'oscillateur BSM. La structure BSMOS vise à combiner les avantages des

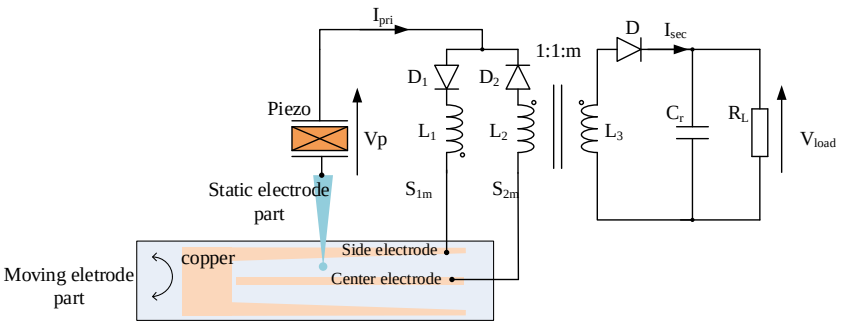

Figure 29: Circuit OSECE autoalimenté avec la structure de commutateur mécanique.

deux techniques non linéaires (bistabilité et butée élastique). Les objectifs de ces butées élastiques sont doubles : obtenir une bande passante plus large que l'oscillateur BSM seul et permettre l'auto-alimentation de la technique OSECE.

Un support d'électrode est fixé entre la liaison souple et l'un des composants piézoélectriques de sorte qu'il suive le mouvement de rotation de ce dernier. Deux électrodes de cuivre séparées (l'électrode centrale et l'électrode de côté) sont gravées. Lorsque les électrodes de la partie mobile se déplacent avec la liaison, la partie d'électrode fixe est connectée électriquement à l'électrode centrale en mouvement lorsque la masse traverse la position centrale et à l'électrode du côté mobile quand la masse arrive à une position maximale donnée. En faisant cela, la connexion électrique est effectuée alternativement et les électrodes agissent comme des commutateurs synchrones. En outre, deux butées élastiques identiques sont disposées symétriquement sur les deux côtés de la masse. Lorsque le déplacement est suffisamment grand pour permettre le contact de la masse avec une butée, la rigidité supplémentaire engendre un effet de durcissement plus prononcé que pour l'oscillateur bistable seul. Ainsi, la bande passante peut être augmentée dans certains cas d'excitation. La figure 29 présente le circuit OSECE autoalimenté avec la structure de commutateur mécanique pour être utilisé avec la structure BSMOS.

Lorsque les mouvements sont suffisamment grands pour que la masse centrale entre en contact avec les butées, le déplacement est limité à une valeur pratiquement constante ce qui simplifie le fonctionnement des interrupteurs mécaniques.

La figure 30 montre les courbes expérimentales issues du générateur autoalimenté BSMOS à 12.3Hz avec d=2mm.

Un gain de puissance est obtenu comme représenté sur la figure 31. La puissance moyenne sur l'ensemble de l'excitation (balayage fréquentiel croissant) est de 0,235mW pour le générateur BSMOS autoalimenté alors qu'elle n'est que de 0,156mW pour le circuit standard dans les mêmes conditions d'amortissement.

0.6 Conclusion

L'objet du développement de récupérateurs d'énergie vibratoire large bande est d'améliorer l'adéquation avec les conditions réelles dans lesquelles les fréquences sont variables. Ainsi, la pertinence de l'utilisation de générateurs linéaires est discutable pour des applications concrètes. L'étude bibliographique permet de dégager plusieurs approches typiques pour élargir la bande passante de fonctionnement : structures avec ajustement de fréquence, oscillateurs multimodaux, mécanismes de type « frequency up-conversion » et systèmes non linéaires.

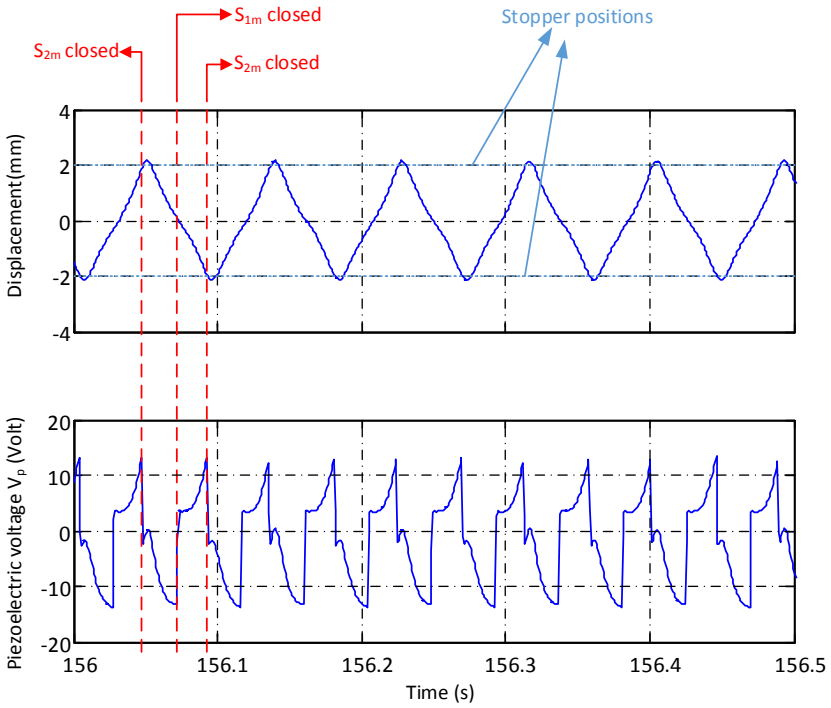

Figure 30: Forme d'onde expérimentale du générateur BSMOS autoalimenté ($d = 2mm$).

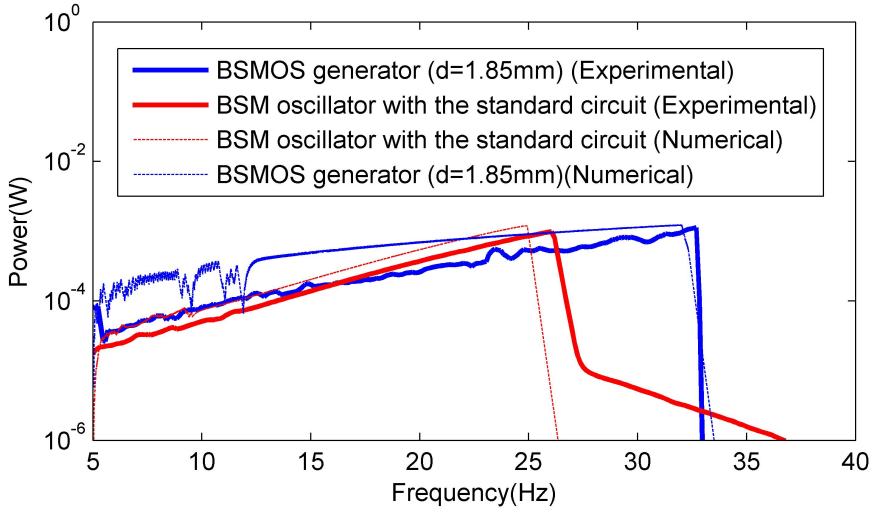

Figure 31: Comparaison de la puissance du générateur BSMOS autoalimenté ($d = 1,85mm$) et du générateur BSM avec le circuit standard.

Un nouveau concept de générateur bistable présentant une architecture ressort-masse est proposé, étudié et optimisé. Il est simple et compact avec deux transducteurs piézoélectriques, une masse inertielle et quatre liaisons flexibles. Avec le modèle élaboré et normalisé, une méthode de résolution approchée harmonique est mise en œuvre pour obtenir une première analyse des relations existantes entre les performances et les paramètres. Un prototype bistable à échelle centimétrique a été fabriqué et testé. Les études des réponses expérimentales lorsque celui-ci est soumis à des excitations de type balayage fréquentiel et bruit blanc confortent les bons résultats de simulations. Des comparaisons sont faites entre le prototype BSM et certains générateurs de la littérature. La densité de puissance obtenue compte parmi les meilleures reportées.

En suivant une procédure d'optimisation globale, un générateur BSM monobloc miniaturisé a été fabriqué. Les performances ont été évaluées en utilisant les excitations canoniques de balayage fréquentiel et de bruit blanc à bande limitée. De plus, une excitation issue de mesures réelles a été testée dans les conditions expérimentales du laboratoire. Le bon potentiel de ce générateur est confirmé par les tests.

Une plateforme de démonstration de réseau de capteurs sans fil autonome a été développée au laboratoire et vise à montrer la capacité de l'alimenter à partir de vibrations large bande. En outre, une figure de mérite NPBP est proposée pour faire des comparaisons équitables entre les différents générateurs large bande. La puissance, la largeur de bande et le facteur de qualité sont inclus dans un indice unique qui facilite la comparaison.

Du point de vue du circuit électronique d'extraction d'énergie, le circuit OSECE a été choisi pour être interfacé avec le générateur BSM. Les performances sont étudiées pour différents niveaux de couplage électromécaniques avec différents types d'excitations. Le compromis entre l'augmentation de la puissance extraite et l'amortissement induit par le circuit d'extraction est analysé en détail. Lorsque le circuit d'interface exerce peu d'amortissement sur le générateur (cas de couplage faible), la puissance récupérée est toujours supérieure pour la nouvelle approche (BSM+OSECE). Ceci est particulièrement évident dans la plage des basses fréquences lorsque le générateur BSM est peu sensible à l'amortissement. C'est également le cas pour le balayage inverse et dans le cas de bruits à bande limitée.

Finalement, un système de commutateurs mécaniques et butées élastiques a été ajouté à la structure du BSM pour l'autoalimentation du circuit OSECE. Les résultats obtenus démontrent la pertinence de cette approche.

1

Background and literature review

Contents

1.1 Background

1.1.1 Wireless sensor networks

Enormous advancements have been achieved about the micro electronics and systems during the past decades. The devices and components are getting smaller with less power required at the same time. Technique improvements provide the feasibilities for the portable devices such as mobile phones, pad computers, micro calculation unit etc.. Until now, a lot of devices are capable of working with the power of dozens of micro watt [23].

Meanwhile, the desire of release from the constraint of wires and free mobility is growing rapidly [24]. Wireless technologies are entering a new phase under the drive of the technologies and the demand, especially for the WSNs (Wireless Sensor Networks). Each sensor node in the pervasive WSNs can be viewed as a platform in which mobile computing and communication elements converge with the sensor unit. Compared to the wired solutions, the WSN allows the portability and reduces the installation costs. As one of the most significant technologies, WSNs offer great convenience and benefits in many applications, such as structure health monitoring [25], food and agriculture industry [26], environment monitoring [27], human health care [28], and so on.

Structures including buildings, bridges, dams, aircrafts, etc. are common and essential for human life. Although they are usually well designed with the account of safety and reliability, hash loading scenarios which are not anticipated during the design often happens with long-term damages accumulated. As a result, it is likely to bring potential danger threat for the human life without proper surveillance. Sometimes, it is difficult to place the wires for powering the sensors of the necessary monitoring network which are spread over the whole building. With the WSN proposed as a solution of substitution, the status of the structures can be collected and analyzed in real time by the distributed sensor nodes [29]. Timely alarming and processing are possible so that the safety can be secured. Figure 1.1 presents a general wireless structural monitoring system.

For a long time, health care refers to short-term treatments rather than long-term body monitoring and prevention [30]. The modern medical science reveals that effective treatments according to the timely updated biological information such as blood pressure, insulin, heart rate etc. can significantly improve the condition of patients [31] and even save more lives. These kinds of information are easily collected with the wearable and implantable sensors [32]. The low power consumption and miniaturized volume make the devices compatible for human life and mobility. Hopefully, the WSN will play a more and more important role in the health care field.

Moreover, the WSN is intensely investigated to contribute to the development of the food and agriculture industry. With the acquired water, temperature information etc. from the WSN in the food and agriculture background, the production can be improved by proper interactions. For both the environment protection against the pollution and the construction of smart towns and cities, the WSN show large benefits too.

1.1.2 Motivation for energy harvesting

Due to advanced information and chip technologies, the measuring and process components could be tiny. Meanwhile, the power source is the heart of the wireless sensor nodes. So far, most of the wireless devices rely on batteries for which less performance improvements have been obtained these years [34]. As a result, the size of a wireless node

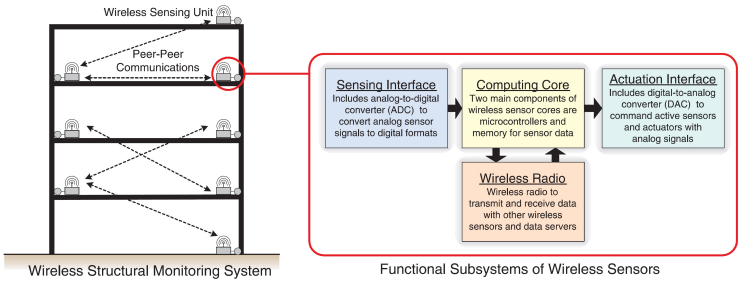

Figure 1.1: General wireless structural monitoring system [33].

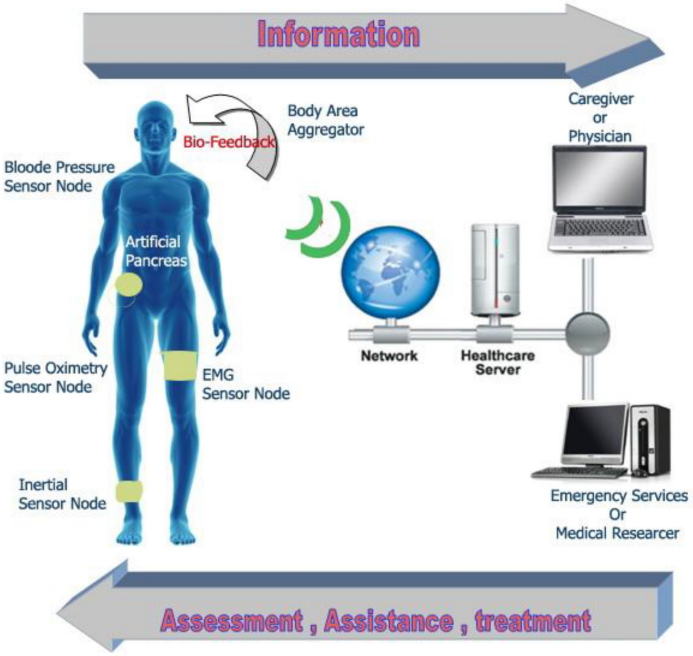

Figure 1.2: Wireless body area network [32].

is dominated by the required large batteries to support long-time operations. However, the lifetime is still limited by the total energy of the battery source.

To get rid of this restriction, one way is to develop high energy density sources to extend the lifetime such as fuel cells while another possible way is to find a sustainable power source without time limitations instead. In this context, energy harvesting comes up as a most promising solution which uses the ambient energy sources to power the wireless sensor node.

P. D. Mitchson had investigated the feasibility of the energy harvesting solution by an example [35]: With the STLM20 temperature sensor from ST Micro.©, the reported ADC developed by Sauerbrey et al. [36] and the IEEE 802.15.4a standard-compliant ultra-wide-band transmitter from IMEC together, the wireless sensor node can work under a low data rate condition with the power consumption of a few micro watt. Considering the volume to be restricted to less than 1 cm^3, the desired power density is about 10 $\mu W/cm^3$ which has been achieved by a lot of reported generators [37].

Despite the application for the WSN, new interests about large scale energy harvesting are on the way [38]. Significant energy is to be harvested from car regenerative brakes and absorbers, civil structures, railway tracks and so on, ranging from 1 W to 100 kW or more. Actually, the utilizations of hydro, solar and wind plants can be also regarded as some kind of energy harvesting.

Compared with the solutions with the power from batteries or wires, there are some special features for the energy harvesting technique:

- Less dependency on battery power. Harvested ambient energy may be sufficient to eliminate battery completely. The device can be powered only from by the harvester and rely on internal energy storage to smooth out variations in available ambient energy.
- Decreased installation costs. The wire arrangement wouldn't be a problem any more.
- Minimized maintenance costs. The devices are always on and there is no need to replace batteries.
- Capability of working in hazardous environments continuously.
- Long-term solutions available. As long as the ambient energy is available, it can continue working, thus perfectly suited for long-term applications.
- Protection of environment. Energy harvesting provides clean and renewable energy while eliminating the need for millions of batteries and energy costs of battery replacements.

All these provide a hopeful prospect for the energy demanding future.

1.1.3 Potential ambient energy sources

In the natural or human environments, there are a lot of energy sources which are not well utilized. Taking the car as an instance, only a few percents of the fuel energy is converted to the drive force while a considerable part of energy is dissipated in the form of heat or vibration. Most of the wasted energy can be utilized in a regenerative way by

Figure 1.3: Potential available energy sources. [39].

recovering the heat and vibration, including the braking and the shock absorbing energy [38]. The efficiency can then be improved.

Figure 1.3 presents some of the possible energy sources which can be harvested from human activities or the environment. These energy sources are mainly classified into four types: light, heat, vibration and radio wave.

- Light (Solar) energy: According to Roundy's investigations, about 100 mW/cm^2 is available for the outdoor solar energy at midday on a sunny day [40]. With the single crystal silicon used, a conversion efficiency of 15%-20% can be achieved, corresponding to a power density of 15 mW/cm^2 or more. For the indoor application, the usable light energy is decreased to about 10 $\mu W/cm^2$.

- Heat: The electricity is generated with the Seebeck effect whenever there is a temperature difference [41]. Some wearable applications have already been developed such as the Seiko wrist watch [34].

- Radio wave: The development of the mobile communication makes the radio wave exists almost everywhere in human environments. The available maximum power density is 0.26 $\mu W/cm^2$ for an electric field of 1 V/m [42].

- Vibration energy: Vibration energy is spread widely in our daily life. Table 1.1 gives some ambient vibration sources for which the spectrum ranges from several Hertz to several hundred Hertz [40, 43]. In addition, the human body motion can be considered as special vibration energy. Depending on the application environment, vibration can provide considerable power density. As long as the vibration sources exist, the generator can always work. Hence, it attracts much attention for the wide application possibilities. In this thesis, the work will be focused on this form of energy harvesting.

In many situations, the environments possess more than one kind of energy sources such as the buildings, which provide all the four sources at the same time. Moreover, these energy forms can be converted into each other. Recently, O. Puscasu used flexible bimetal

Vibration source	Peak Acceleration (m/s^2)	Peak frequency (Hz)
Car engine	12	200
Base of 5 HP 3-axis machine tool with 36" bed	10	70
Kitchen blender casing	6.4	121
Clothes dryer	3.5	121
Door frame just after door closes	3	125
Small microwave oven	2.25	121
HVAC vents in office building	0.2–1.5	60
Wooden deck with people walking	1.3	385
Breadmaker	1.03	121
External windows (size 2 ft × 3 ft) next to a busy street	0.7	100
Notebook computer while CD is being read	0.6	75
Washing Machine	0.5	109
Second story floor of a wood frame office building	0.2	100
Refrigerator	0.1	240
Railroad	1.5	5-20
Highway Traffic	0.01	5-100
Bridge	0.01-0.1	5-20

Table 1.1: Typical vibration sources. [40, 43]

to convert heat energy into vibration energy which is then harvested by a piezoelectric beam [44]. With a shape memory alloy-piezoelectric hybrid transducer, Avirovik et al. successfully converted the remote light energy into vibration energy for harvesting [45]. Meanwhile, other energy sources may not be included in these four types such as wind, flowing fluid, sound and so on. However, it is possible to convert these energy sources into vibrations with proper structures as investigated for the fluid by A. Erturk [46] and the wind by Pan et al. [47].

1.2 Vibration energy harvesting

As shown in figure 1.4, a VEH (Vibration Energy Harvester) is often constituted of three parts: the mechanical oscillator, the electromechanical transducer and the energy extraction and storage circuit.

The mechanical oscillator is the receptor of external vibration energy from the environment. Generally, the mechanical structure is required to be optimized to achieve high response so that the generator can capture the vibration energy as much as possible. A very common way is to have a resonance-based oscillator whose natural frequency is de-

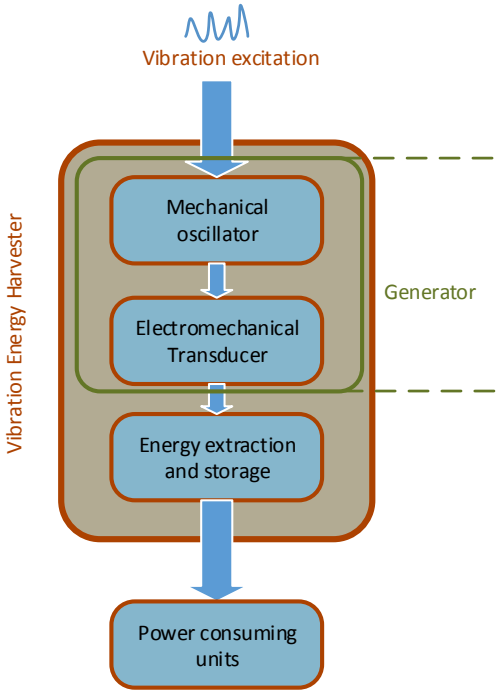

Figure 1.4: General vibration energy harvester architecture.

signed to match the excitation frequency. Subsequently, a transducer is used to convert the mechanical energy into electric energy which is usable for the power consuming units, usually the sensor and the transmission components. As the structural part of the VEH, the combination of the mechanical oscillator and the electromechanical transducer is often called as the generator which produces the desired electric energy from the environment vibration.

After that, an interface circuit is needed to extract electric energy from the generator and store it in a battery, a capacitor or a super capacitor. The energy is then transferred to the wireless sensor node to support the normal measurements and transmissions as a final step.

1.2.1 Conventional generators

To reclaim the energy from the vibrations, an electromechanical transducer is the essential part which turns the mechanical vibrations into electricity. According to the conversion mechanism, the generators can be classified as follows: piezoelectric generators, electromechanical generators, electrostatic generators and others.

Piezoelectric generators

The mechanical strain in the piezoelectric materials induces the electric polarization with charge produced on the surface of the materials. With this effect used in energy harvesting, the piezoelectric generator converts the vibration to forces which are applied to the piezoelectric materials to obtain the electric energy. Figure 1.5 shows a cantilever structure with piezoelectric materials attached to the top and bottom. As a typical piezoelectric generator structure, the cantilever provides low resonance frequency which is well

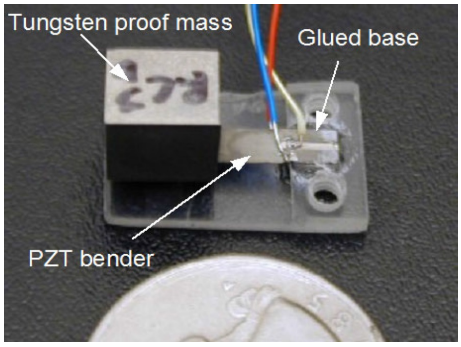

Figure 1.5: Piezoelectric cantilever generator [48].

suited for vibration energy harvesting. A basic analysis was performed by Roundy et al [48] while more detailed investigations were provided by A. Erturk et al. [49] in 2009. For the rectangular beam structure, the strain distribution in the piezoelectric materials is not even so that the total coupling level is sometimes decreased by the less deformed area. To figure out this issue, Glynne-Jones et al. [50] proposed a taped beam design while Guan et al. [51] suggested the utilization of an H-shape proof mass. Xu et al. [52] proposed a right angle cantilever to improve the harvesting efficiency. Under the driving of the pursuit of miniaturization, some micro-machined silicon cantilevers were also fabricated with the surface [53] or interdigitated electrodes [54] while Liu et al. [55] proposed a new S-shaped cantilever for low frequency energy harvesting at the MEMS (micro electromechanical system) scale.

Apart from the cantilever structure, some other common structures for piezoelectric energy harvesting were summarized by Cook-Chennault [56], including rainbow structures, multilayer structures, moonie structures and cymbal structures etc.. Moreover, some special generators were developed for body energy harvesting applications such as the piezoelectric dimorph [57], the micro-fiber composite actuator [58], the piezoelectric shoe insole [59] and so on. Recently, a flexible wearable harvester with a piezoelectric polymer PVDF in-shell structure was demonstrated to be able to generate high power from the human motions [60].

The piezoelectric generators are capable of directly converting force into electricity with no additional requirements. Therefore, the structures are usually simple and compact. High produced voltage and good compatibilities with MEMS techniques are important advantages too while the shortcoming is that the performance and the lifetime are usually limited by the mechanical properties. With the number of the working cycle increases, the induced fatigue in the materials will lead to the performance decrease or the device damage [61].

Electromagnetic generators

The electromagnetic generators take advantages of the Faraday's law which states that the electricity is produced in a closed-loop conductor as the passed magnetic flux is varying. When used for vibration energy harvesting, the closed-loop conductor typically takes the form of a coil in series with the load while the variation of the magnet flux is realized by the relative motion between the coil and a permanent magnet driven by the external vibrations.

In 1996, William et al. [62] analyzed the feasibilities of a micro generator while Shearwood et al. [63] fabricated a prototype at millimeter scale in 2001, obtaining a power of 0.3 μW. Since then, a lot of work has been performed on the electromagnetic generators.

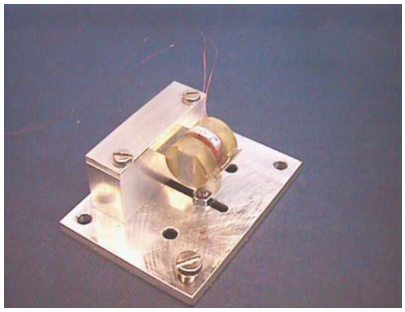

(a) Developed by Glynne-Jones et al. [64]

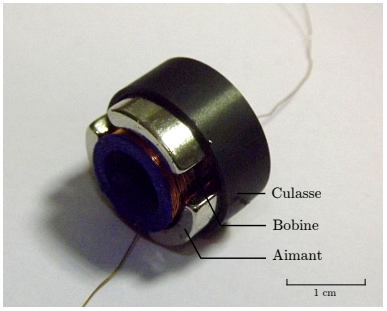

(b) Developed by Arroyo et al. [65]

Figure 1.6: Electromagnetic generators.

Figure 1.6(a) shows a generator developed by Glynne-Jones et al. [64]. In this work, it was shown that the generator was capable of obtaining an average power value of 157µW and a peak of 3.9mW when subjected to a car engine.

By making comparison between several electromagnetic coupling architecture without ferroelectric materials, Spreemann et al. [66] concluded that the max voltage point and power point did not coincide for a determined configuration. To improve the coupling for enhancing the output voltage and the power density, optimizations on the structures have been lasted for years. Pan et al. developed a rotary electromagnetic generator with a residual induction of 1.44T achieved [67]. Marioli et al. [68] proposed a new structure with a planar coil while Arroyo et al. [65] recently presented an optimized generator as shown in figure 1.6(b). Moreover, the miniaturization and integration with the MEMS technique are continually investigated [69].

Since the electromagnetic generators have no requirements of intelligent materials, many common materials are usable to construct the structures for the desired properties. Meanwhile, strong coupling level is easily achieved since high performance magnets are readily available. However, the performance at the micro scale is limited because of the poor properties of planar magnets [37] and the difficulties of integration.

Electrostatic generators

To take one movable electrode of a charged capacitor away from the other, some mechanical work is required to overcome the electrostatic force. In this process, the electric energy stored in the capacitor is increased. Applying this scheme, the electrostatic generator comes up as another typical method to convert the vibration into electricity.

The first electrostatic generator in the literature was proposed by Chandrakasan's group [70] in 2001 as shown in figure 1.7. In this work, the authors described and compared two working ways of the electrostatic generator: constant charge cycle and constant voltage cycle. The investigations concluded that the constant voltage cycles presented better performance with the same voltage and capacitance ratio constraints. The same group utilized the electrostatic generator to power a DSP chip in 2004 [71].

Roundy studied the methods of varying the capacitance and categorized the generators into three types: in-plane overlap varying, in-plane gap closing and out-of-plane gap closing [40]. It was stated that the in-plane gap closing generator had the best performance of the three with 100 $\mu W/cm^3$ produced for an optimized design.

Since the work cycles of the electrostatic generator need to be charged and discharged

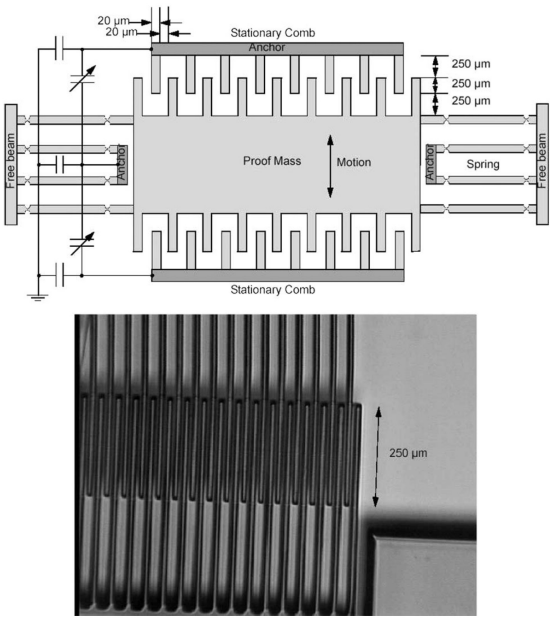

Figure 1.7: Electrostatic generator from MIT [70].

alternatively, a battery is usually required for assistance. To get rid of the limitation of the charging and discharging process, electrostatic generators with electrets were proposed by Sterken et al. [72] and further investigated by Arakawa [73] and Peano [74].

The electrostatic generators have good compatibility with MEMS technology and the facility of improving the energy by decreasing the capacitance gap. These features make them suitable for miniaturizations but the high voltage output and pre-charging work cycle require complex circuit design.

Except the three methods above, other transduction mechanisms have been developed such as the magnetostrictive materials which deforms under magnetic field. When used for energy harvesting, the magnetostrictive materials are usually used with the piezoelectric materials [75]. Recently, a new mechanism which utilizes triboelectric effect has been investigated a lot [76, 77].

A proper method is to be selected when a vibration generator is designed according to the applications. For an overall idea about these common methods, both advantages and disadvantages of each method have been concluded and compared in Arroyo' thesis [1]. Since the electrostatic generator is mainly used at the MEMS scale with similar structures, the piezoelectric and electromagnetic generators are more considered in this thesis.

1.2.2 VEH Optimizations

To improve the performance of a VEH, researchers mainly explore two aspects: (1) Interface circuit for energy extraction and storage; (2) Mechanical oscillating structure with transducers.

Interface circuit for energy extraction and storage

For piezoelectric energy harvesting applications, a common way, known as standard circuit, is a full-bridge rectifier and a smoothing capacitor [78]. However, in this case, the resulting performance is dependent on the load and the electromechanical coupling coefficient. The latter is usually related to the amount of piezoelectric materials used in

the structure. When the former is away from its optimal value or when the amount of piezoelectric material is restricted, the harvested power may be very low [2].

To increase the harvested power, many nonlinear switching harvesting techniques are developed, such as the parallel SSHI (Synchronized Switching Harvesting on an Inductor) and series SSHI [2, 3, 4]. It is well known that SSHI circuits can significantly increase the harvested power compared to the standard circuit, especially in the case of low electromechanical coupling coefficient [2, 79, 80, 81]. However, for SSHI, the harvested power is still dependent on the load impedance [2]. To overcome this shortcoming, a SECE (Synchronous Electric Charge Extraction) technique was proposed by Lefeuvre et al. [5]. Although the theoretical harvested power is not as high as SSHI circuit, it is independent on the load. For SECE, the switching time is to be very precisely controlled to get the maximum power which makes this circuit difficult to be operated correctly. Some similar techniques are developed to improve the harvested power, such as the DSSH (Double Synchronized Switch Harvesting) technique [6], the ESSH (Enhanced Synchronized Switch Harvesting) technique [82] and the Initial Energy Injection technique [83]. The switching strategies of these circuits are even more complicated than for the SECE technique. As a result, it hinders the concrete applications of these techniques.

An OSECE (Optimized Synchronous Electric Charge Extraction) technique has been proposed by us at SYMME [7] recently. In this new circuit, the switching strategy is much simpler than for SECE while providing higher performance and preserving the weak impedance dependence property for a wide load range. Only one diode between the piezoelectric element and the primary inductor is required which reduces energy losses whereas a single common ground in the circuit facilitates the self-power capability.

For the electromagnetic generators, investigations about the interface circuits did not attract as much attention as the piezoelectric generators because of the low output impedance and good compatibilities with common power electronics. However, investigations on improving the harvesting power have been substantially performed to some extent. In 2007, Mitcheson et al. [84] studied the power processing circuits for different kinds of generators including the electromagnetic ones while Cao et al. developed a foward-feedthrough and feedback DC-DC PWM boost converter [85]. Applying the similar strategy of the SECE circuit, Arroyo et al. [86] developed a nonlinear SMFE (Synchronous Magnetic Flux Extraction) technique which presented much better performance compared with the rectifier method, especially in the case of low output voltage.

After its extraction from the generator, the electric energy is usually required to be regulated and saved in a storage element, mostly a super capacitor or a battery. Moreover, the power managing strategy should be optimized to schedule the energy usage for the best. Further details can be found in the book of Beeby and White [87].

Mechanical oscillating structure with transducers

Thus far, most of the reported conventional generators are designed with linear oscillators. It can be usually described with the spring-mass-damper model as shown in figure 1.8.

The dynamic equation is expressed as:

$$F_M = M\ddot{u} + (\mu_m + \mu_e)\dot{u} + Ku \tag{1.1}$$

Here, μ_m is the intrinsic damping of the structure and μ_e is the damping induced by energy harvesting. When subjected to a sinusoidal excitation $F_M = \gamma_M \cos \omega t$, the max

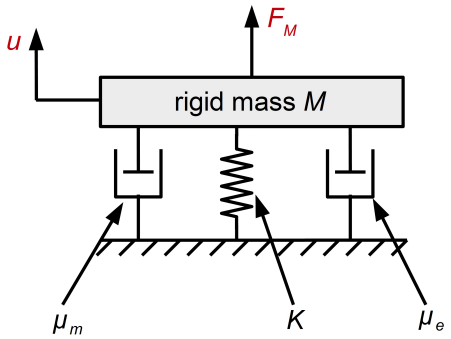

Figure 1.8: Generic model of linear generators

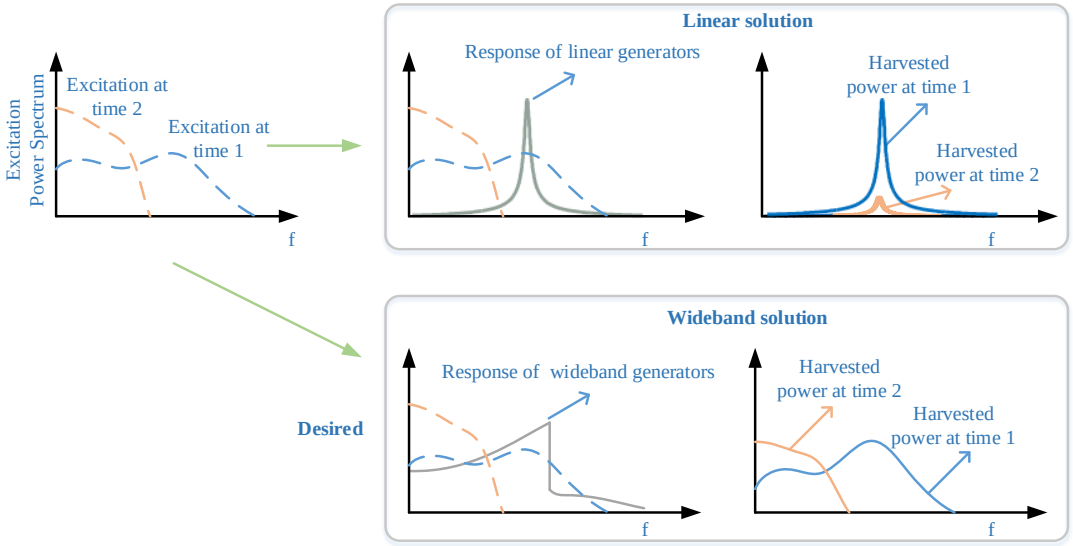

Figure 1.9: Schematic figure: benefits of wideband generators.

available power is obtained with the structure natural frequency $\omega_0 = \sqrt{K/M} = \omega$ and $\mu_m = \mu_e$ [88, 89]:

$$P_{max} = \frac{F_M^2}{8\mu_m} = \frac{M\gamma_M^2 Q_m}{8\omega_0} \tag{1.2}$$

where Q_m is the quality factor of the structure. Therefore, the optimization for the VEHs with linear oscillators are focused on increasing Q_m and the mass M as possible while satisfying the design requirements.

However, the realistic vibration frequency spectrums are often broadband and varying from time to time. When the natural frequency of the linear oscillator is not inside the favorable range of the excitation as shown in figure 1.9 (at time 2), the harvested power is very poor. It means that the harvested energy is not enough to support the normal work of the autonomous sensor node sometimes. To have stable and sustainable power output, a generator with wideband responses is desired as shown in figure 1.9.

1.3 Wideband vibration generator

Since the majority of the excitations in the environments are variable and broadband, it is critical to have a wideband vibration generator adaptable for complex application environments. Great achievements have been obtained in the recent years [8, 9]. In this section, several common ways to broaden the bandwidth are introduced.

1.3.1 Resonance tuning

The basis for the good performance of the linear generators is to know the excitation frequency spectrum first and therefore let the frequency of maximum power density coincide with the resonance frequency. As this favorable excitation frequency is varied from time to time, the performance of the generator might be poor. So, the resonance-tunable generators are proposed to follow the change of the excitations.

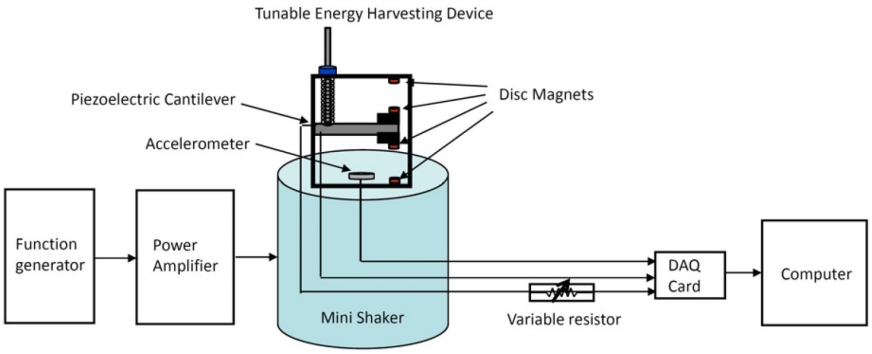

(a) Passive resonance tuning generator with magnets [12].

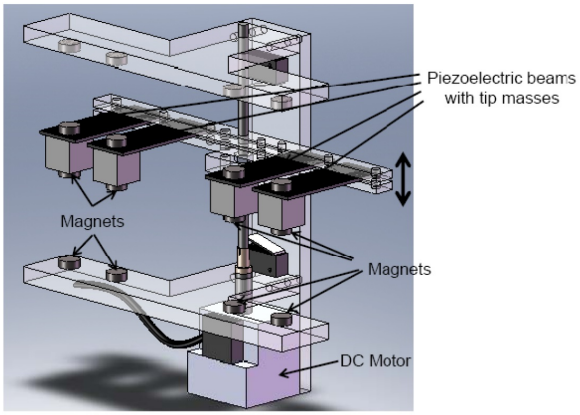

(b) Active resonance tuning generator with a DC motor driving structure [90].

Figure 1.10: Resonance tuning generators.

According to the tuning operation modes, the generators can be divided into two classes: passive and active. For the former, the resonance frequency is tuned before the generator gets to work. In 2006, Leland et al. [10] presented a clamped beam with an axial compression preload which changed the stiffness of the beam thus the resonance frequency. A variation of the resonace frequency from 200Hz to 250Hz was obtained with this method. With the similar strategy applied to a cantilever beam, Eichhorn et al. [91] achieved to shift the resonance frequency from 380Hz to 292Hz. Another example was demonstrated

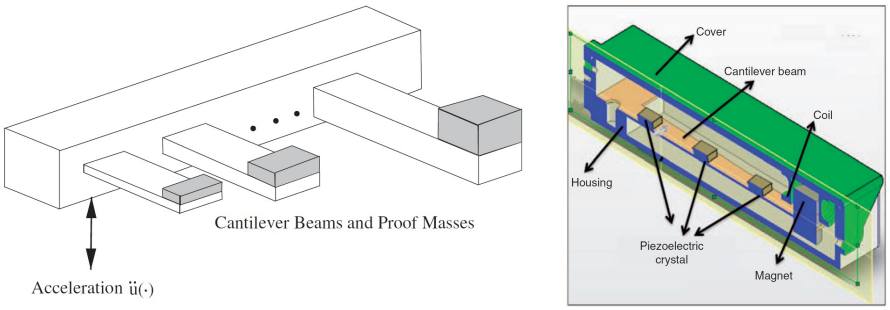

(a) Array of linear generators [13]. (b) Hybrid generator [15].

Figure 1.11: Multimodal generators.

by Challa et al. [12] with the magnetic force as shown in figure 1.10(a). By tuning the space between two fixed permanent magnets and the piezoelectric beam with two small magnets at the tip, the resonance frequency is varied because of the stress induced from the magnetic interaction. However, the resonance frequency is not automatically changeable even though the excitation frequency shifted away for the passive operation mode. Consequently, the self-tunable generators with active components to change the resonance frequency are developed. The first example was presented by Roundy and Zhang who split the piezoelectric materials on the beam into two parts: one for harvesting and the other for tuning [11]. As an improvement for the proposed passive solution, Eichhorn et al suggested a self-sufficient frequency tunable cantilever beam with two tuning piezoelectric arms at the two sides. The resonance frequency is automatically tunable between 150Hz and 190Hz with a time space requirement larger than 10s between two adjustments. The group of Challa also presented an self-tunable solution instead of the passive one (figure 1.10(a)) as shown in 1.10(b) [90]. The beams are driven by a DC motor to the desired positions. The resonance frequency is altered from 13Hz to 22Hz while a minimal recovery time of 88 minutes is required for the next tuning operation.

By matching the resonance frequency with the excitation, the self-tunable generators are capable of providing the benefits of the performance improvement. However, there are some limitations to be noted: First, the complex control strategy of the active tuning function takes a long time to find the optimal excitation frequency; Second, a lot of energy is consumed during the tuning operation so that a long recovery time is required. These two points make the generator lose the pace of the excitation in some cases, leading to the fail of the tuning mechanism. Moreover, the tuning range is usually restricted around the initial resonance frequency. As a result, the resonance tuning generators are not suitable for those applications in which the excitation spectrum varied in a very wide range or too fast.

1.3.2 Multimodal oscillator

A linear generator is usually the simplified single-mode model of the device in which other high-order modes are not in the interested excitation range. However, the useful bandwidth can be extended if a generator has good performance at multiple modes with different frequencies close to each other.

The first way to achieve a multimodal oscillator is to have many single-mode oscillators with different resonance frequencies together. Figure 1.11(a) presents a generator which comprises multiple piezoelectric cantilevers with different lengths and masses [13]. Each cantilever has a distinct resonance frequency. All these generators are connected to a

single common base. In a covered frequency range, there is always some generator which is excited around its resonance frequency. The performance as a whole device presents the desired wideband properties. Another generator with an array of piezoelectric beams of different thicknesses was developed by Xue et al. [14]. It was found that the bandwidth was improved from 6Hz to 28Hz with higher power compared to the single beam. With a similar generator as shown in figure 1.11(a), Ferrari et al. demonstrated that the array is capable of providing more stable performance over a larger frequency when used for powering a wireless transmission node [92]. Recently, Lien et al. [93] investigated the performance of the interface circuit for the array generators with the equivalent impedance strategy.

Hybrid harvesting scheme is also a solution of realizing a multimodal generator. In this generator, two or more different transduction mechanisms of energy harvesting are integrated with different resonance frequencies. An example developed by Tadesse et al [15] is shown in figure 1.11(b). The piezoelectric and electromagnetic harvesting principles are combined together. Similar work has been performed by Challa et al. [94]. Another kind of multimodal generator is to use coupled oscillators as done by Yang et al. [95]. Two piezoelectric beams with different resonance frequencies are connected through a spring so that the motions are coupled into each other. When the two resonance frequencies are close, the useful band is enlarged by connecting them together.

The multimodal generators are capable of obtaining wideband responses without tuning. At the same time, the power output is enlarged. Nevertheless, the total power density is decreased since the generator array occupies a lot of space while only one part works at the optimal frequency. Moreover, the electrical properties are complex so that the challenges for designing the circuits are increased.

1.3.3 Frequency-up-conversion method

In many cases, most of the excitation power may reside in the low frequency range. To have a resonance-based linear generator at some low frequency, the only solution is to have large mass or low stiffness or both. However, the generators are frequently required to be restricted to a small volume. As the size of the generators gets smaller, the mass is decreased because of the volume restriction while the stiffness is increased simultaneously due to the scaling effect. Consequently, the resonance frequency usually shifts to higher values in the opposite direction of the desired. Moreover, to harvest the low frequency energy, the necessary large displacement stroke is difficult to be satisfied within a constraint volume. Therefore, the frequency-up-conversion method is proposed to transfer the low frequency energy to the high frequency range which can be harvested by the high resonance frequency generator.

A common way is to use a two stage design of mechanical gear structures. At the first stage, the low frequency excitation is captured by a low stiffness structure which applies the force to the high frequency generator in its motion path. A large deformation of the generator is then obtained in this quasi static process. At the second stage, the high resonance generator is released and begins to vibrate freely. The stored strain energy in the deformation during the first stage is then dissipated in two forms: structural damping and energy harvesting. As a result, the low frequency energy is converted to the generator's resonance point.

Figure 1.12 presents a frequency-up-conversion electromagnetic generator proposed by Galchev et al. [96]. An inertial mass is alternatively attached to and detached from two FIGs (Frequency Increased Generators) under the low frequency excitations. At the splitting moments, the FIG which has deformed considerably under the action of the inertial

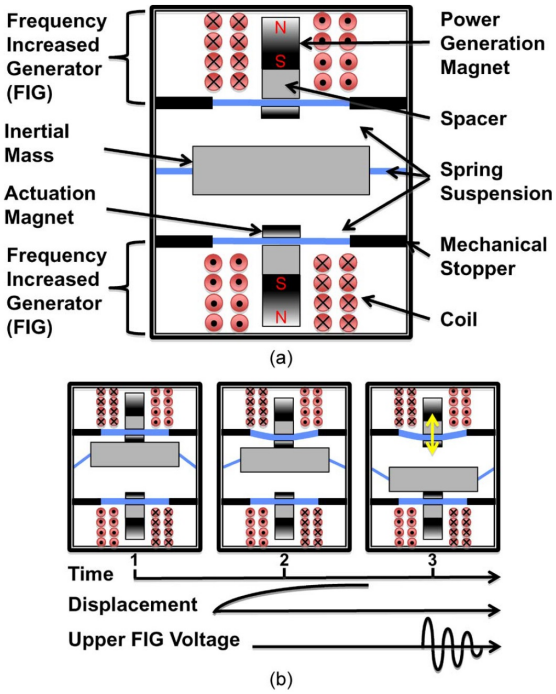

Figure 1.12: Frequency-increased generator developed by Galchev [96]: (a) Architecture; (b) Illustration of the method of operation.

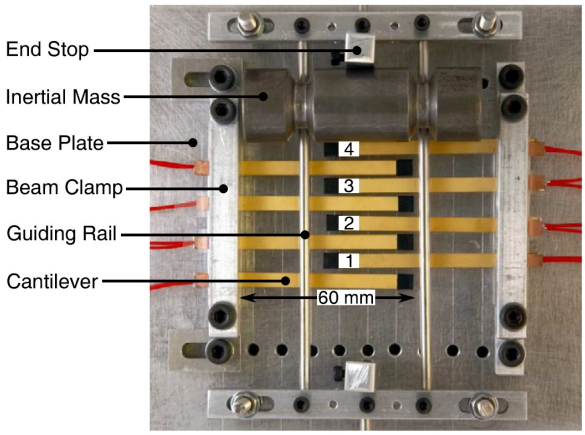

(a) Prototype.

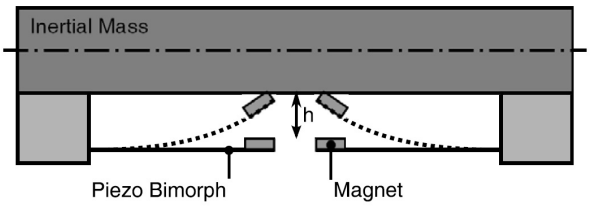

(b) Illustration of the beam bending process.

Figure 1.13: Scalable impulse excited harvester proposed by Pillastch et al. [97]

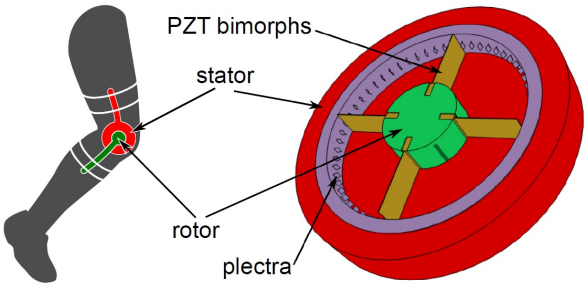

Figure 1.14: Plucked knee-joints piezoelectric generator [16].

mass begins to vibrate at its high frequency resonance point. More detailed investigations are provided in [98] for an electromagnetic generator and in [99] for a piezoelectric generator with this design. A different structure with the similar strategy is developed by Tang et al. [100]. In this new structure, two FIGs are not separated from the inertial magnet mass and placed at the two sides. As the mass crosses the center position, the FIGs are excited with an impulse excitation and start to oscillate subsequently. With a compliant beam of low resonance frequency and two high resonance frequency beams placed at the upper and bottom sides, Gu et al. demonstrated a power increase of 4.8 times due to the frequency-up-conversion mechanism of this new structure. [101].

Pillatsch et al. proposed a scalable impulse excited design as shown in figure 1.13 [97]. When excited by the low-frequency impulses, the circular rod mass rolls forward and backward on the guiding rail. The cantilever is attracted upward because of the magnetic force when the mass is getting close. As the mass moves to other positions, the beam returns to its original place with free oscillations.

The frequency-up-conversion method is especially useful at the micro scale. In 2007, Lee et al. [102] presented a structure composed of a micro piezoelectric bimorph beam with a tip microprobe and a micro comb slider with a ridge. The piezoelectric beam is force and freed alternatively when the probe slides on the moving ridge. Another example is demonstrated by Najafi et al. which stated that 0.5 μJ is obtained in a second for the up-conversion generator [103]. The harvested energy is much larger than the available 6.8 nJ per second for the traditional linear method.

Considering that the frequency-up-conversion method presents significant improvements on the performance of low-frequency energy harvesting, one of the best applications is human motion energy harvesting. Figure 1.14 gives an example developed by Pozzi et al. [16]. This plucked piezoelectric beam is designed to harvest the energy from human knee-joints. Moreover, some other generators devoted to human walking energy harvesting are proposed by Moro et al. [104], Renaud et al. [105] and so on. However, for the frequency-up-conversion method, careful design is required to reduce the loss at the first stage for the high energy conversion efficiency.

1.3.4 Nonlinear oscillator

To figure out the narrow bandwidth issue of linear generators, bringing nonlinearities into the mechanical and/or electromechanical structure is considered as an effective solution [17, 8, 9, 18]. Because of the special backbone responses, nonlinear structures provide the ability of improving the generated energy over the broad frequency band when compared with linear generators.

Generally, two possible ways are used for the generator to include the nonlinearities:

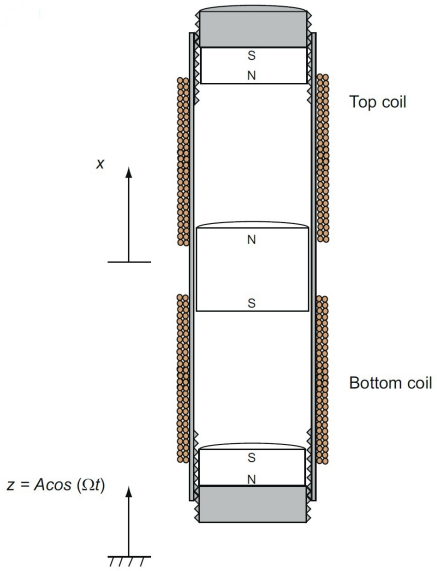

(a) Schematic of the generator.

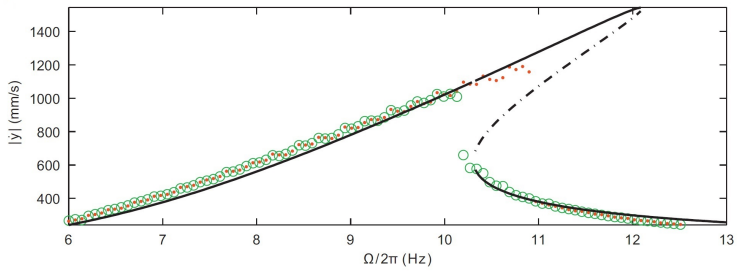

(b) Frequency response for the chirp excitation of 8.4 m/s^2 (line: theoretical results; dots: forward sweep; circles: reverse sweep).

Figure 1.15: The monostable hardening generator realized with magnet levitation [108].

nonlinear stiffness and nonlinear coupling. For the latter, the nonlinear effects of the piezoelectric coupling have been studied by Triplett et al. [106] and Stanton et al. [107]. Since the nonlinear coupling effect are relatively small, realizing nonlinear stiffness is the mostly used method.

With some simplifications, many nonlinear oscillators are usually described by the equation:

$$F_M = M\ddot{x} + (\mu_m(x) + \mu_e(x))\dot{x} + f(x) \tag{1.3}$$

where $f(x)$ is the restoring force of the structure which contains high order components, $\mu_m(x)$ is the damping coefficient which can be approximated to be constant or variable and $\mu_e(x)$ is the damping induced by the harvesting transduction mechanism. According to the stable equilibrium positions obtained from equation (1.3), the nonlinear generators can be divided into two types: mono-stable and bistable/multi-stable.

Mono-stable generators

For the mono-stable generators, only one stable equilibrium position exists in the structure under free conditions. A most common example is the Duffing oscillator:

$$F_M = M\ddot{x} + (\mu_m(x) + \mu_e(x))\dot{x} + ax + bx^3 \tag{1.4}$$

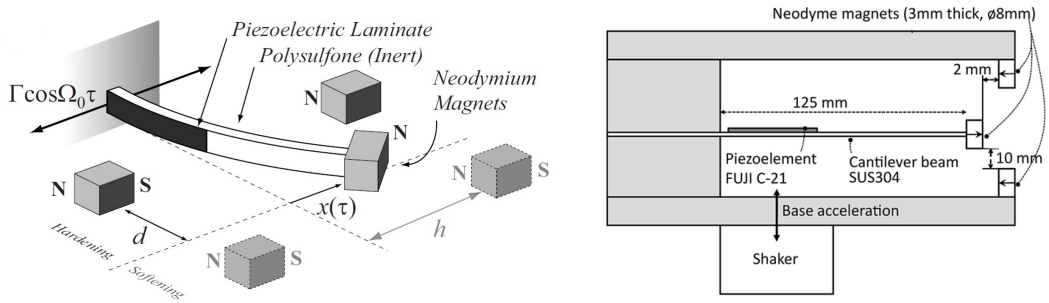

(a) Cantilever beam using magnets for hardening or softening configuration [109].

(b) Cantilever beam with three magnets [110].

Figure 1.16: Nonlinear piezoelectric cantilever generators.

in the case of $a > 0$. Depending on the value of b, it can be a hardening oscillator ($b > 0$) or a softening oscillator ($b < 0$) or a linear oscillator ($b = 0$).

Figure 1.15 shows a hardening oscillator implemented with magnet levitation by Mann and Sims [108]. Two static magnets are placed at the two ends of the tube while an inertial magnet mass moves between them. The varying magnetic flux density induces the electric current in the coil which is used for harvesting the vibration energy. The restoring force provided by the magnetic interaction is getting stronger as the center magnet approaches any of the two static magnets, presenting a stiffness hardening effect. Band broadening effect is clearly observed from the forward frequency sweep response.

Stanton et al. [109] proposed a cantilever generator with a tip magnet and two fixed magnets as shown in figure 1.16(a). By changing the positions of two static magnets, either the hardening or the softening effects on the stiffness can be imposed. With a similar configuration in figure 1.16(b), Sebald et al. theoretically [111] and experimentally [110] investigated the band increasing performance of this hardening cantilever beam. The results showed that a decrease of 60% at the max power point and a band increase of 450% were observed compared with the linear cantilever. Moreover, a cantilever generator using the interaction between two tip magnets and an iron coil is also studied by Barton et al. [112] with both random and periodic excitations.

Without magnets, other solutions such as pre-stress and nonlinear spring structures are frequently utilized to construct a mono-stable generator. Hajati and Kim [113] utilized the stretching strain in double clamped beams to induce hardening stiffness in a piezoelectric harvester while Nguyen et al. [114] realized a softening MEMS electrostatic generator with four bent beams.

Another kind of often used mono-stable generators is the piece-wise generator. Figure 1.17 presents an example developed by Soliman et al. [115]. When the displacement of the beam is not large enough to touch the stopper, it works just as a linear generator. Once the stopper is reached by the beam, the beam part at the left side of the stopper is restricted while the right part continues vibrating as a shortened beam clamped at the stopper position. A sudden stiffness change happens for the beam when contacting the stopper. As a result, a hardening generator is obtained while the stiffness curve is connected with two straight line segments of different slopes. With the similar strategy, the performance of a MEMS piezoelectric generator with stoppers is detailed by Liu et al. [116]. The frequency-up-conversion effect of this structure is also presented by Ashraf et al. [117] and Liu et al. [118]. Recently, Dhakar et al. [119] proposed an improved structure with an additional extended polymer beam.

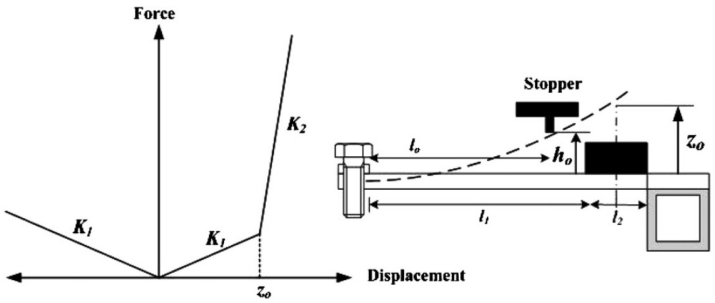

Figure 1.17: A piecewise generator realized with a stopper [115].

Due to the special backbone responses, the bandwidth can be improved with the mono-stable nonlinear generators. However, the benefits are mainly presented for the high-energy attractor around the characteristic frequency. Therefore, an important issue is to keep the generator working in this state. Besides, it is interesting to find that some of the resonance-tuning generators are mono-stable nonlinear generators at the same time.

Bistable/Multi-stable generators

When more than one equilibrium positions exist in the structure, the generators are bistable or multi-stable. Since the complexities of the multi-stable generators are much higher than the mono-stable cases and the bistable cases, very few generators are developed. Therefore, in this section, the investigations are mainly focused on the bistable generators.

Among the introduced wideband solutions, the bistable generator is considered as a most promising one because of its unique features. The snap-through mechanism in the case of large excitations makes it to transit from one equilibrium position to another, which induces large motion amplitude and dramatically increased power generation. The frequency-up-conversion effect for the low frequency excitation and the nonlinear wideband response can significantly enhance the harvested power and the operation band.

Although there are a lot of bistable generators published [19, 20], most of them can be classified into two categories according to the formative mechanism of the bi-stabilities: buckling effect and magnetic interaction.

a. Buckling effect. It is a very common way to create bistable structures which utilizes the mechanical instability in the case of high compression stress. A representative example is the buckled beam as shown in figure 1.18 . As the axial load exceeds the critical buckling load P_{cr}, the beam becomes unstable at the original position and bends into the buckled symmetrical configurations (b1) or (b2).

As a classical bistable structure, the potential for energy harvesting applications has been discussed by many literatures. Masana and Daqaq [120] investigated the performance of the clamped-clamped beam in monostable and bistable cases for sweep excitations. The beam with axial compression load showed the characteristics of a hardening oscillator in the monostable case and the special features of a bistable Duffing oscillator after buckled. Moreover, the shape of the potential function of the post buckled beam plays an important part on the harvested power. Cottone et al. [121] studied a post buckling beam for random vibration energy harvesting while Sneller et al. [122] investigated a post-buckled piezoelectric beam with an attached center mass to scavenge energy from the chirp excitations. Blarigan et al. proposed a new structure with a piezoelectric bimorph and a single layer aluminum beam bonded together [123] as shown in figure 1.19. When applied with axial

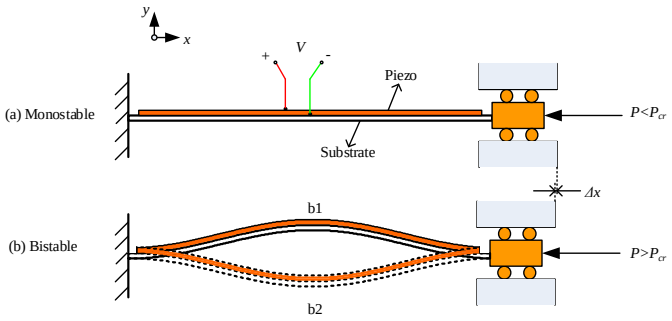

Figure 1.18: Clamped-clamped beam with axial load: (a) Monostable; (b) Bistable (Buckled).

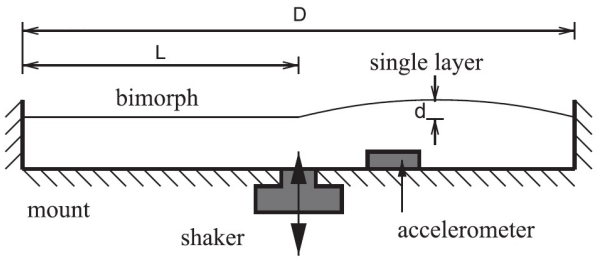

Figure 1.19: Bistable generator composed of two beams with one buckled and the other unbuckled [123].

load, the single layer beam is slightly buckled. Experimental tests showed that a useful band of 150Hz-200Hz which was much larger than the corresponding linear cantilever was obtained.

Except the buckled beam, the curved composite bistable plate which has two asymmetric stable positions, as shown in figure 1.20, is also proposed for energy harvesting by Arrieta et al. [124]. The design of bistable oscillators based on buckled beams and plates presents good potential for energy harvesting purpose, especially because of their compactness leading to larger power density.

b. Magnetic interaction. Because of the special no-contact and concentrated poling effects, magnetic interaction provides an easy and convenient method to construct a bistable oscillator. A very common configuration is a cantilever beam equipped with a magnet at its free end moving in front of a static second magnet whose polarity is in the opposite di-

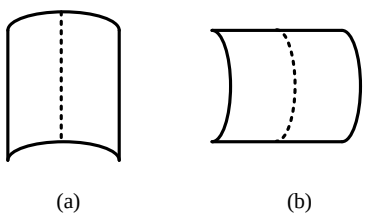

Figure 1.20: Buckled plate: (a) Stable position 1; (b) Stable position 2.

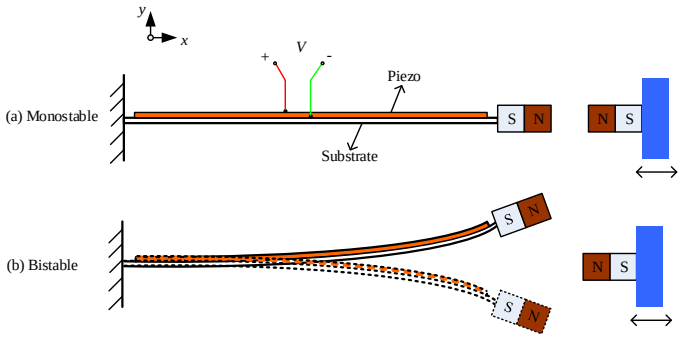

Figure 1.21: Cantilever beam with tip magnets: (a) Monostable case; (b) Bistable case.

rection as shown in figure 1.21. As the two magnets get closer, the repulsive force between the two magnets generates a potential saddle at the original equilibrium position and two symmetric stable positions.

Cottone et al. firstly demonstrated that a power gain of 400%-600% was obtained from a bistable oscillator of this type compared to a linear one for band-limited noise excitations [125]. Subsequently, Ferrari et al. [126] studied the performance using white noise excitations while Stanton et al [127] theoretically and experimentally investigated the nonlinear dynamics for sweep excitations. Instead of the repulsive interaction, Erturk and Inman utilized the attractive force of two magnets placed above and below the steel beam to obtain a bistable oscillator [128]. Broadband energy harvesting on high-energy orbits of this bistable cantilever beam was discussed for harmonic signals. A bistable piezoelectric harvester utilizing the attracting force of the two poles of a single magnet is also discussed by Ferrari et al. [129]. Ando et al. presented the investigations of this nonlinear bistable mechanism used in a MEMS generator [130]. Using the magnetic repelling interaction, a two dimensional generator was constructed by Ando et al. [131] when putting two cantilever beams together with their face orthogonal and the tip magnet of each beam pointing to the other.

Apart from these bistable cantilever beam structures, a bistable electromagnetic harvester (figure 1.21) driven by non-contact magnetic repulsion was discussed by Mann et al. for chirp excitations [132]. In this work, a max power of 210 mW was obtained for a volume of 130 cm^3 and an excitation of 10 m/s^2.

Along with the increasing interests in the bistable generators, different kinds of new bistable structures are developed. Some of them have novel mechanisms which do not belong to the two catalogs, such as the hair bundle structures [133]. Recently, Harne et al. developed a coupled generator composed of a bistable generator and an auxiliary linear oscillator [134].

Generally, the benefits of the bistable generators come from two aspects: the frequency-up-conversion effect and the nonlinear wideband response. For the normal linear generators, the response at the low frequency which is away from the resonance frequency is very low and the harvested energy is poor. The special snap-through mechanism of the bistable generator is capable of converting the low excitation frequency to the high frequency range around the resonance point. This resonance point is the natural frequency for each of the two potential wells. Cohen et al. [135] investigated the slow-fast response about the frequency-up-conversion effect of a bistable generator as shown in figure 1.23.

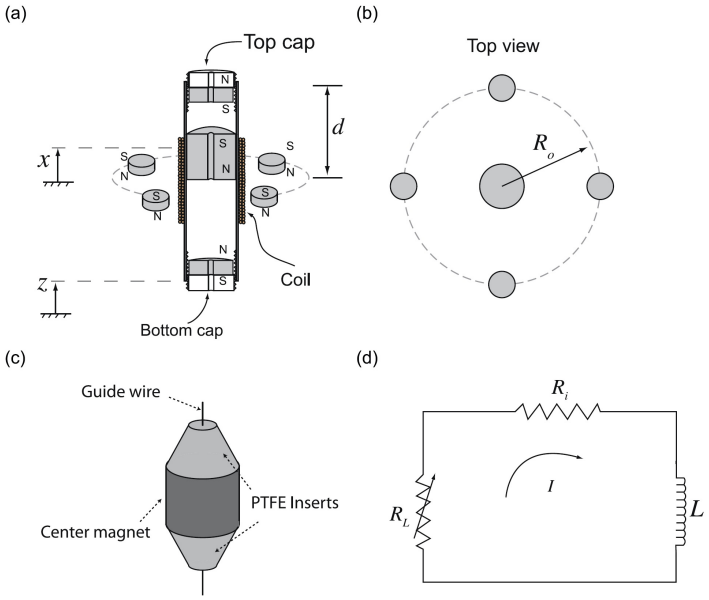

Figure 1.22: Illustrations of a bistable electromagnetic generator with a magnet insert [132].

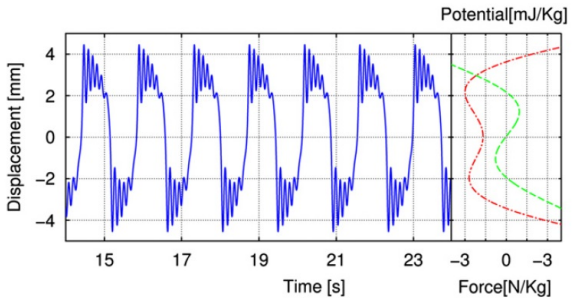

(a) Waveform.

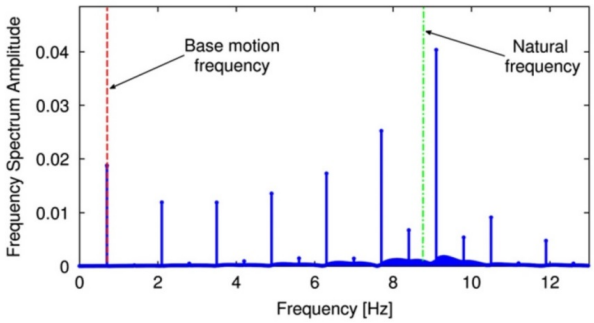

(b) Spectrum.

Figure 1.23: Frequency up-conversion effect of the bistable generator [135].

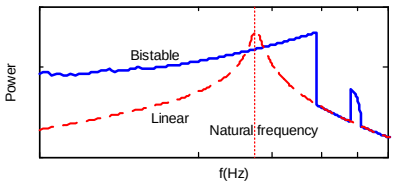

Figure 1.24: Typical power responses of a bistable generator and its equivalent linear one.

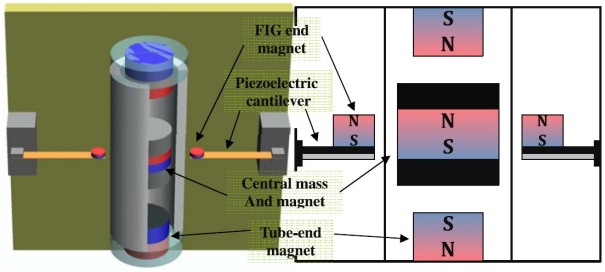

Figure 1.25: 3D schematic (left) and structural layout (right) of the frequency-up-conversion piezoelectric energy harvester developed by Tang et al. [100].

When the low-frequency excitation is large enough to let the bistable generator transit from one equilibrium position to another (figure 1.23(a)), a large initial velocity is imposed to the oscillator which is made to vibrate freely at the new equilibrium position with the frequency near the resonance point as revealed in figure 1.23(b). In this way, the energy of the low-frequency excitation is transferred to the range around the resonance point which improves the harvested energy greatly. This mechanism was also used by Tang et al. [100] and Galcheve et al. [98] for low-frequency energy harvesting as discussed before.

Because of the special feature of two potential wells, the bistable generator is able to obtain better responses over low-frequency range than the monostable generator (linear or nonlinear). Meanwhile, the nonlinear hardening effect promises wideband and high power output. Figure 1.24 shows a typical power response of a bistable generator compared to a linear equivalent one for the forward sweep excitation. The performance of the bistable generator is enhanced over a large frequency band. However, as pointed out by Halvorsen, the performance of the bistable generator is not necessarily better than the linear oscillator, especially in the noise excitation case [136].

On behalf of the snap-through effects, a new bistable structure which is composed of two buckled bridges and four cantilever beams at the center position was developed for realizing the frequency-up-conversion effect by Jung and Yun [137]. Another bistable frequency-up-conversion structure was proposed by Tang et al. [100] as shown in figure 1.25. The bistable structures with magnetic interaction are able to enhance the harvested power and improve the operation band as discussed in the section of the frequency-up-conversion method.

1.4 Conclusion

In this chapter, the motivations and the advantages of the energy harvesting technology are presented. Lots of energy sources which surround the human life can be utilized such as light, heat, RF, and vibration energy. Among them, vibration energy attracts great interests due to the mostly wide existence and feasibilities. Several usual mechanisms such

as piezoelectric, electromagnetic, electrostatic, triboelectric and magnetostrictive effects have been introduced for harvesting the energy while new transduction mechanisms are to be developed.

The undergoing researches about vibration energy harvesting are devoted to two issues: interface circuits and mechanical oscillating structures of the generators. For the former, the aim is to develop an optimal circuit which scavenges energy from the generator as much as possible and manages the power utilization efficiently; For the latter, the aim is to capture and convert the most mechanical energy into the electric energy. Generally, these two aspects are required to be considered as a whole unit to get the optimal performance.

Nevertheless, a big challenge for the vibration energy harvesting is that real excitation signals are wideband. Thus, an important subject is to develop a generator adapted to the complex environments in which the vibrations are frequency-varying or closed to noises. A number of available solutions are proposed such as resonance tuning structures, multi-modal oscillators, frequency-up-conversion mechanisms or nonlinear oscillators. As a special branch of the nonlinear oscillators, the bistable generators present the desired features of frequency-up-conversion effect and nonlinear wideband frequency response. The developed bistable generators have been mainly classified into two catalogs according to the mechanisms. Followed investigations are focused on this promising solution with a novel architecture.

2

Proposition of a BSM bistable generator

Contents

2.1 Introduction

In view of the good characteristics of the bistable generators, it is meaningful to develop a desired one on which detailed investigations can be performed for wideband energy harvesting. Before getting started, careful considerations between two ways of constructing a bistable generator have to be made.

The architecture with magnetic interactions is easy to realize, whereas the main drawback is the relatively bulk volume. The presence of the magnets decreases the available power density and makes the architecture difficult for micro fabrications. Moreover, experimental results are usually not consistent with simulations because of the difficulties to properly model complex magnetic interactions. The lack of predictive models hinders the optimization of the devices.

For the buckling effect way, the structures are usually compact and suitable for miniaturization. A representative example of this kind of generators is the buckled beam. On this basis, the double buckled beam with an inertial center mass in figure 2.1 was initially thought to be a good choice. A multi-modal analytical model was derived while experimental tests were performed on a fabricated monolithic prototype for validations. Detailed investigations can be found in appendix A. However, because of the complexities of the model, the fabrication flaws and the imperfect assembly, it is difficult to get consistent results for the simulations and experiments on the fabricated device and thus impossible to optimize devices for different application environments. Therefore, a better wideband generator is expected for high power density and easy feasibilities of optimizations.

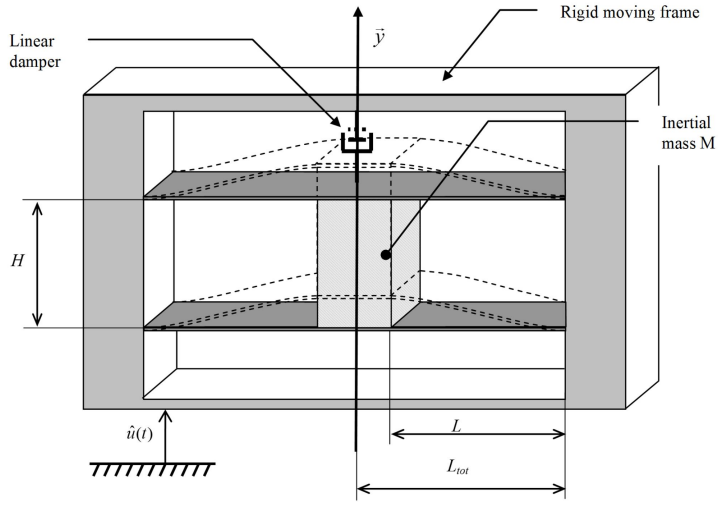

Figure 2.1: General scheme of the double buckled beam with an inertial mass.

2.2 BSM generator

A novel piezoelectric bistable harvester complying with the buckling effect mechanism is presented in figure 2.2. Compared to many reported bistable oscillators, the proposed new architecture is relatively compact and simple. Based on a buckled spring-mass system, it is composed of two piezoelectric components and a central inertial mass. Flexible hinges are used to connect those parts together and with the frame which is subjected to the ambient acceleration $\gamma(t)$. The structure is highly symmetric so that the mass moves along the x direction with other freedoms neglectable.

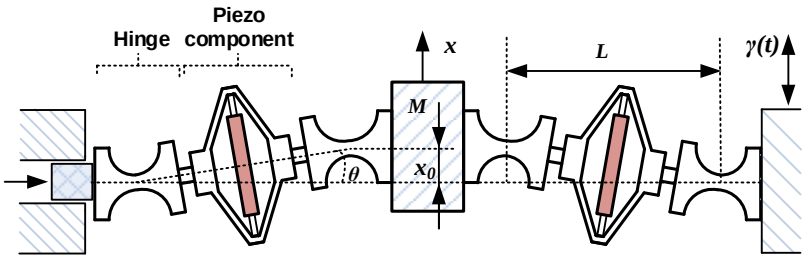

Figure 2.2: Scheme of the proposed BSM generator.

The main features of the architectures are presented as follows:

- First, the inertial mass M is selected to dominate the whole system mass so that the sum dynamic mass of the hinges and the piezoelectric elements can be neglected. As a result, the kinetic energy of the whole structure is governed by M. This also increases the power density because all the mass is efficiently used.
- Second, the piezoelectric components are chosen from the APA devices (CEDRAT Technologies©). The amplified elliptical structure allows large displacement and relatively small stiffness so that significant initial buckling level x_0 is possibly obtained. Moreover, the piezoelectric devices are placed at positions of enduring the maximum stress, thus produce the maximum electric energy. The two APA transducers are electrically connected in parallel or series.
- Finally, flexible hinges are used to avoid dry friction and lash. However, their rotational stiffness is to be taken into account because of their effect on the initial buckling level x_0, as shown later.

2.3 Modeling

In the BSM generator, the mass is supposed to be initially at the position $x = 0$ while the natural longitudinal length between the rotary centers of two adjacent flexible hinges is denoted l_0. With a small tunable displacement applied at the tuning end, the buckling happens and the mass moves to a new equilibrium position. The parameters definitions of the structure are shown in figure 2.2 and given in Table 2.1.

As a classical method, the Euler-Lagrange approach is used to deduce the governing equation of the structure. Ignoring the mass of the piezoelectric springs and the hinges, the kinetic energy of the system is:

$$T = \frac{1}{2} M \dot{x}^2 \tag{2.1}$$

The potential energy of the piezoelectric springs is written as:

$$U_1 = \frac{K}{2} \Delta l^2 = \frac{K}{2} (l_0 - \sqrt{L^2 + x^2})^2 \tag{2.2}$$

In addition, the potential energy of the hinges is calculated as (assuming that the mass slightly deviates from the zero position ($x << L$) during operation):

$$U_2 = 4 \times \frac{K_\theta \theta^2}{2} = 2K_\theta (\arctan(\frac{x}{L}))^2 \approx 2K_\theta \frac{x^2}{L^2} \tag{2.3}$$

Definition of Parameters	Symbol
Mass	M
Horizontal Distance between two adjacent rotary centers	L
Stiffness of one piezoelectric spring	$K/2$
Damping coefficient	μ
Capacitance	C_0
Piezoelectric force factor	α
Rotational stiffness of the hinge	K_θ
Initial buckled position	x_0
Load resistance	R

Table 2.1: Numerical and Experimental parameter definitions.

From equation (2.1)-(2.3), we can write the Euler-Lagrange equation as:

$$\frac{d}{dt}\left(\frac{\partial \Pi}{\partial \dot{x}}\right) - \frac{\partial \Pi}{\partial x} = M\ddot{x} + K\left(1 - \frac{l_0}{\sqrt{L^2+x^2}}\right)x + 4K_\theta\frac{x^2}{L^2} = M\gamma - \alpha V_p \sin\theta - \mu\dot{x} \quad (2.4)$$

where $\Pi = T - U_1 - U_2$ is the Lagrangian function, V_p is the piezoelectric voltage, α is the piezoelectric force factor and the last term is the damping force.

Considering the electric charge balance, we have:

$$I = -\alpha\Delta\dot{l} - C_0\dot{V}_p = \alpha\frac{x\dot{x}}{\sqrt{L^2+x^2}} - C_0\dot{V}_p \quad (2.5)$$

where I is the current and V_p is the piezoelectric voltage.

Combining equation (2.4) and equation (2.5) , the overall electromechanical equations can be obtained (assuming $x << L$):

$$\begin{cases} M\gamma = M\ddot{x} - \dfrac{K}{2L^2}(l_0^2 - L^2 - \dfrac{8K_\theta}{K})x + \dfrac{Kx^3}{2L^2} + \mu\dot{x} + \alpha V_p\dfrac{x}{L} \\ I = \alpha\dfrac{x\dot{x}}{L} - C_0\dot{V}_p \end{cases} \quad (2.6)$$

With $K_\theta < (l_0^2 - L^2)K/8$ satisfied, the BSM generator has two stable equilibrium positions $x = x_0$ and $x = -x_0$ and one unstable equilibrium position $x = 0$. The stable positions are found by setting the differential terms and V_p equal to zero:

$$x = \pm\sqrt{l_0^2 - L^2 - \frac{8K_\theta}{K}} \quad (2.7)$$

Equation (2.7) shows that the rotational stiffness of the hinges affects the initial buckling level x_0. If the rotational stiffness fails to satisfy the condition that $K_\theta < (l_0^2 - L^2)K/8$, it is found that the BSM structure becomes a monostable hardening Duffing oscillator with only one equilibrium position $x = 0$. Then the BSM structure can be expressed by the simplified model in figure 2.3(b). This degeneration effect underlines that K_θ is critical for the BSM structure.

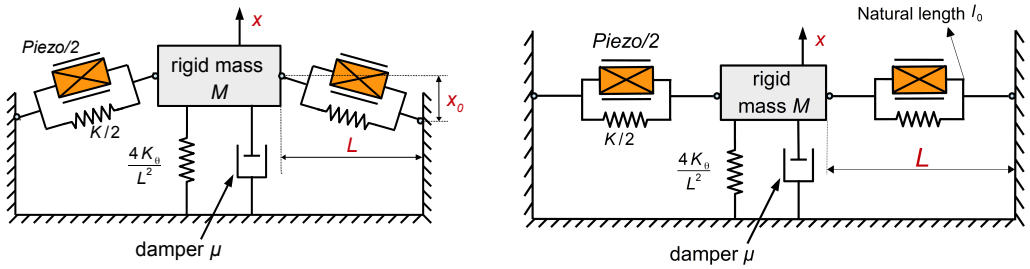

(a) Bistable case. (b) Monostable case.

Figure 2.3: Simplified Model for the BSM generator.

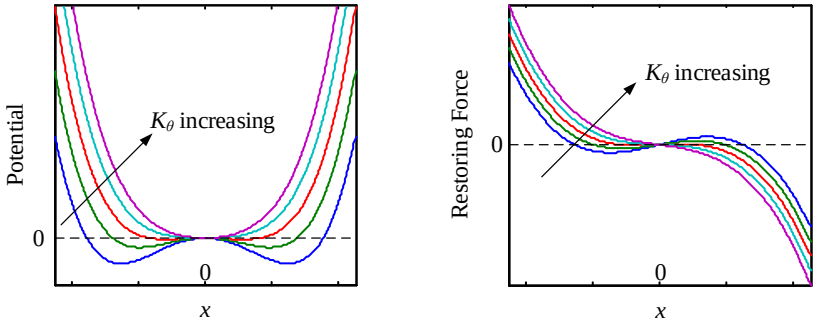

(a) Potential vs K_θ. (b) Force vs K_θ.

Figure 2.4: Potential and restoring force curves for different hinge stiffness.

To better explicate the influence of the rotation stiffness, figure 2.4 shows the potential function and the restoring force curve for different values of K_θ. It is obvious that the BSM potential saddle at the zero position decreases to zero as K_θ increases, leading to a monostable structure.

With only the interesting bistable cases considered and equation (2.7) used, equation (2.6) can then be written again as:

$$\begin{cases} M\gamma = M\ddot{x} - \dfrac{Kx_0^2}{2L^2}x + \dfrac{Kx^3}{2L^3} + \mu\dot{x} + \alpha V_p \dfrac{x}{L} \\ I = \alpha\dfrac{x\dot{x}}{L} - C_0\dot{V}_p \end{cases} \tag{2.8}$$

For the purpose of using the model in a wider scope and making a comparison with the linear generator, normalization is performed. With the new parameters defined in Table 2.2, equation (2.8) can be written as:

$$\begin{cases} \bar{\gamma} = \ddot{\bar{x}} - \dfrac{1}{2}\omega_0^2\bar{x} + \dfrac{1}{2}\dfrac{\omega_0^2}{\epsilon^2}\bar{x}^3 + 2\xi\omega_0\dot{\bar{x}} + \dfrac{k^2}{1-k^2}\dfrac{\omega_0^2\bar{x}}{\epsilon}\bar{V} \\ \bar{I} = \dfrac{\bar{x}\dot{\bar{x}}}{\epsilon} - \dot{\bar{V}} \end{cases} \tag{2.9}$$

The choice of the normalized groups allows this model to be in line with the standard vibration energy harvester model [88] that underlines three critical parameters: ω_0 the

Normalized parameters and variables	Symbol	Definition
Buckling level	ϵ	x_0/L
Electromechanical coupling coefficient	k^2	$\alpha^2/(\alpha^2+KC_0)$
Mechanical damping coefficient	ξ	$\mu/(2\epsilon\sqrt{KM})$
Characteristic angular frequency	ω_0	$\epsilon\sqrt{K/M}$
Normalized displacement	$\bar{L}$	x/L
Normalized excitation	$\bar{\gamma}$	γ/L
Normalized voltage	$\bar{V}$	$V_p/(\alpha x_0/C_0)$
Normalized current	$\bar{I}$	$I/(\alpha x_0)$
Normalized power	$\bar{P}$	$P/(ML^2)$

Table 2.2: Normalized parameters and variables.

characteristic pulsation, k^2 the electromechanical coupling coefficient and ξ the mechanical damping. For the bistable system, an additional dimensionless parameter ϵ relative to the buckling level is brought to light. Equation (2.9) provides a generic and scalable model for the feasibilities of both design and optimization.

With the normalized parameters, the power output can be written in the followed form:

$$P = V_p I = \frac{\alpha^2 x_0^2}{C_0}\bar{V}\bar{I} = \frac{k^2 K L^2 \epsilon^2}{1-k^2}\bar{V}\bar{I} = ML^2\bar{V}\bar{I}\frac{k^2\omega_0^2}{1-k^2} = ML^2\bar{P} \tag{2.10}$$

which is shown to be logically proportional to the mass.

When examining the normalizing parameters, it is interesting to find that the coupling coefficient k^2 is not affected by the additional stiffness K_θ due to the hinges. By comparing the resonance frequency under the short and open circuit conditions or calculating the electric and mechanical energy increment in the case of small excitations around one equilibrium position, it is also validated that k^2 keeps constant and does not rely on ϵ which is related to K_θ. However, the power depends both k^2 and ϵ.

As an important step toward the development of the nonlinear harvesting approach, the comparison of the bistable dynamic behavior with a linear oscillator is capable of providing valuable information about the two approaches. Therefore, a rigorous linearization strategy is proposed to define a reference linear oscillator allowing fair comparisons.

If the excitation is large enough to let the generator have the dynamic vibrations between two potential wells, we call the motion as inter-well motion. When the generator is restricted in one potential well, the motion around one equilibrium position is usually called intra-well motion. Considering this intra-well vibration around ϵ, we set $\bar{x} = \epsilon + \bar{u}$. Equation (2.9) can then be written as:

$$\begin{cases} \bar{\gamma} = \ddot{\bar{u}} + \omega_0^2\bar{u} + \dfrac{3\omega_0^2\bar{u}^2}{2\epsilon} + \dfrac{1}{2}\dfrac{\omega_0^2}{\epsilon^2}\bar{u}^3 + 2\xi\omega_0\dot{\bar{u}} + \dfrac{k^2\omega_0^2}{1-k^2}\bar{V} \\ \bar{I} = \dot{\bar{u}} - \dot{\bar{V}} \end{cases} \tag{2.11}$$

Equation (2.11) exhibits both quadratic and cubic terms. According to the nonlinear oscillator theory, super-harmonic resonances are then to be expected at half and one-third the resonant frequency.

For small excitation cases ($\bar{u} << \epsilon$), the nonlinear terms can be neglected leading to the following linearized equivalent equation:

$$\begin{cases} \bar{\gamma} = \ddot{\bar{u}} + \omega_0^2 \bar{u} + 2\xi\omega_0 \dot{\bar{u}} + \dfrac{k^2\omega_0^2}{1-k^2}\bar{V} \\ \bar{I} = \dot{\bar{u}} - \dot{\bar{V}} \end{cases} \tag{2.12}$$

which is the LEO (Linear Equivalent Oscillator) model for the proposed bistable model in the case of small vibrations around one of the two equilibrium positions. The same expression was used to characterize linear piezoelectric energy harvesters by Arroyo et al. [88]. It can be inferred that the LEO model represents the comparable linear oscillator of the bistable oscillator. Therefore, comparison between the two models is helpful for better understanding the performance of the proposed bistable system over linear systems. It is worthy of note that for any linear model, there is a variety of bistable oscillators with same parameters ω_0, k^2 and ξ which can be constructed with different values of ϵ according to the real application.

2.4 Harmonic balance analysis

Prior to numerical or experimental investigations of the BSM generator, harmonic balance analysis is used to study the dynamic responses, especially for the inter-well motions under external harmonic excitations. This analytical method is valuable for characterizing the dynamic properties of the BSM generator for different parameter variations and providing important guiding information for design and tests [138]. It also provides a rapid and convenient solution of initial optimizations and evaluations.

Considering the simplest situation of the electrical load for the normalized model described by equation (2.9), a resistor R is directly connected to the piezoelectric components. Then equation (2.9) can be written as:

$$\begin{cases} \bar{\gamma}\cos\omega t = \ddot{\bar{x}} - \dfrac{1}{2}\omega_0^2\bar{x} + \dfrac{1}{2}\dfrac{\omega_0^2}{\epsilon^2}\bar{x}^3 + 2\xi\omega_0\dot{\bar{x}} + \dfrac{k^2}{1-k^2}\dfrac{\omega_0^2\bar{x}}{\epsilon}\bar{V} \\ \omega_r\bar{V} = \dfrac{\bar{x}\dot{\bar{x}}}{\epsilon} - \dot{\bar{V}} \end{cases} \tag{2.13}$$

where $\omega_r = 1/(RC_0)$ represents the electric load and the harmonic excitation is $\bar{\gamma}\cos\omega t$.

It is well known that the periodic response for a harmonic excitation can be approximated by a truncated Fourier series. The accuracy is usually determined by the number of the preserved terms. Since it is shown in [135] that the periodic motion of the bistable generator has a dominant fundamental frequency component, the displacement solution of the BSM generator is assumed as:

$$\bar{x} = c(t) + a\sin\omega t + b\cos\omega t \tag{2.14}$$

$$\dot{\bar{x}} = \dot{c} + (\dot{a} - b\omega)\sin\omega t + (\dot{b} + a\omega)\cos\omega t \tag{2.15}$$

$$\ddot{\bar{x}} = (2\dot{a} - b\omega)\omega\cos\omega t - (\dot{b} + 2a\omega)\sin\omega t \tag{2.16}$$

The amplitude of the motion is supposed to vary slowly so that the second or higher derivatives are neglected. $c(t)$ is the DC component of the intra-well motion and the value is zero for the inter-well motion.

2.4.1 Intra-well motion

When the generator vibrates around the equilibrium position of this well, the piezoelectric voltage is expressed as:

$$\bar{V} = p\sin\omega t + q\cos\omega t \tag{2.17}$$

$$\dot{\bar{V}} = (\dot{p} - q\omega)\sin\omega t + (\dot{q} + p\omega)\cos\omega t \tag{2.18}$$

Only the fundamental frequency which is the same as the excitation frequency is preserved in the equations.

Substituting equations(2.14-2.16) and equations (2.17-2.18) into equation (2.13), removing the high-order harmonic terms and balancing the items for DC , $\sin\omega t$ and $cos\omega t$ components, five equations can be obtained:

$$\frac{-c\omega_0^2}{2} + \frac{(3a^2+3b^2+2c^2)c\omega_0^2}{4\epsilon^2} + \frac{(ap+bq)k^2\omega_0^2}{2\epsilon(1-k^2)} + 2\dot{c}\xi\omega_0 = 0 \tag{2.19}$$

$$-b\omega^2 - \frac{b\omega_0^2}{2} + \frac{(3a^2+3b^2+12c^2)b\omega_0^2}{8\epsilon^2} + \frac{ck^2\omega_0^2 q}{\epsilon(1-k^2)} + 2a\xi\omega\omega_0 + 2\dot{a}\omega + 2\dot{b}\xi\omega_0 = \bar{\gamma} \tag{2.20}$$

$$-a\omega^2 - \frac{a\omega_0^2}{2} + \frac{(3a^2+3b^2+12c^2)a\omega_0^2}{8\epsilon^2} + \frac{ck^2\omega_0^2 p}{\epsilon(1-k^2)} - 2b\xi\omega\omega_0 - 2\dot{b}\omega + 2\dot{a}\xi\omega_0 = 0 \tag{2.21}$$

$$\frac{ac\omega}{\epsilon} - p\omega - q\omega_r + \frac{\dot{b}c}{\epsilon} + \frac{b\dot{c}}{\epsilon} - \dot{q} = 0 \tag{2.22}$$

$$\frac{bc\omega}{\epsilon} - q\omega + p\omega_r - \frac{\dot{a}c}{\epsilon} - \frac{a\dot{c}}{\epsilon} + \dot{p} = 0 \tag{2.23}$$

In steady states, all the derivatives approach zero, then equations (2.19-2.23) becomes:

$$\frac{-c\omega_0^2}{2} + \frac{(3a^2+3b^2+2c^2)c\omega_0^2}{4\epsilon^2} + \frac{(ap+bq)k^2\omega_0^2}{2\epsilon(1-k^2)} = 0 \tag{2.24}$$

$$-b\omega^2 - \frac{b\omega_0^2}{2} + \frac{(3a^2+3b^2+12c^2)b\omega_0^2}{8\epsilon^2} + \frac{ck^2\omega_0^2 q}{\epsilon(1-k^2)} + 2a\xi\omega\omega_0 = \bar{\gamma} \tag{2.25}$$

$$-a\omega^2 - \frac{a\omega_0^2}{2} + \frac{(3a^2+3b^2+12c^2)a\omega_0^2}{8\epsilon^2} + \frac{ck^2\omega_0^2 p}{\epsilon(1-k^2)} - 2b\xi\omega\omega_0 = 0 \tag{2.26}$$

$$\frac{ac\omega}{\epsilon} - p\omega - q\omega_r = 0 \tag{2.27}$$

$$\frac{bc\omega}{\epsilon} - q\omega + p\omega_r = 0 \tag{2.28}$$

With $r = (a^2+b^2)^{1/2}$ and $r_v = (p^2+q^2)^{1/2}$ separately represent the amplitude of the displacement and the voltage, the equation group (2.24-2.28) can be simplified as:

$$c = (\epsilon^2 - \frac{3}{2}r^2 - \frac{k^2\omega^2 r^2}{(1-k^2)(\omega^2+\omega_r^2)})^{1/2} \tag{2.29}$$

$$r = \frac{\bar{\gamma}}{(M_a^2+M_b^2)^{1/2}} \tag{2.30}$$

$$r_v = \frac{cr\omega}{\epsilon(\omega^2+\omega_r^2)^{1/2}} \tag{2.31}$$

where

$$M_a = -\omega^2 - \frac{\omega_0^2}{2} + \frac{3r^2\omega_0^2}{8\epsilon^2} + \frac{3c^2\omega_0^2}{2\epsilon^2} + \frac{c^2k^2\omega_0^2\omega^2}{\epsilon^2(1-k^2)(\omega^2+\omega_r^2)} \tag{2.32}$$

$$M_b = \frac{c^2k^2\omega_0^2\omega\omega_r}{\epsilon^2(1-k^2)(\omega^2+\omega_r^2)} + 2\xi\omega\omega_0 \tag{2.33}$$

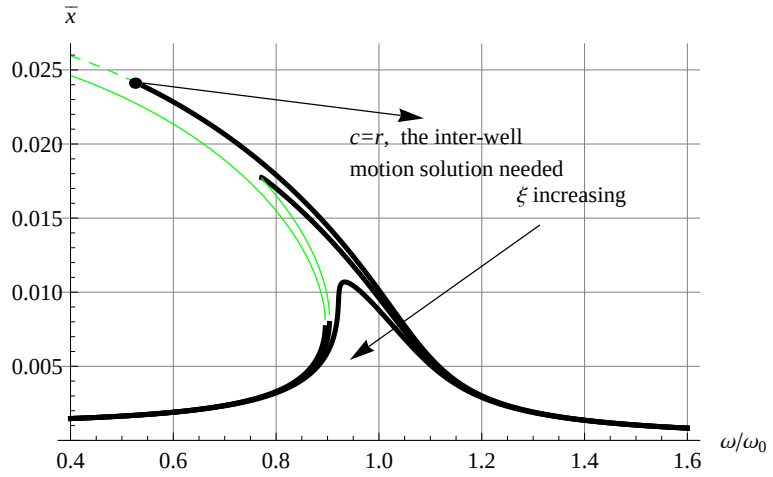

Figure 2.5: Intra-well displacement responses for different damping coefficients ($\bar{\gamma} = 15.2$ s $^{-2}$,$\omega_0 = 110$ rad/s , $\omega_r = \omega_0$, $k^2 = 0.07$, $\xi = \{0.0156, 0.03, 0.045\}$). Thick lines, stable solutions; Thin lines, unstable solutions.

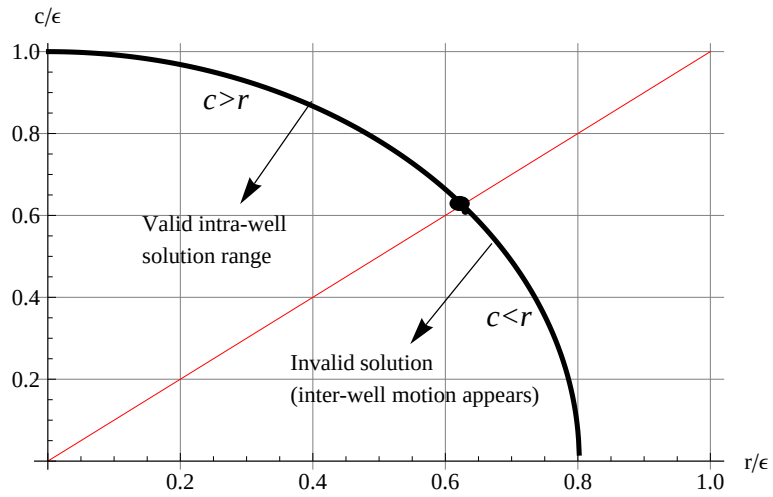

Figure 2.6: DC component c versus the displacement response amplitude r ($\omega_r = \omega_0 = 110$ rad/s , $k^2 = 0.07$).

Then the frequency response of the BSM generator can be determined by finding the real roots of equations (2.29-2.31). Figure 2.5 depicts the intra-well displacements responses for different damping cases. The thick lines represent stable solutions while the thin lines are unstable solutions. The stability of the solution is determined using the perturbation method [139]. For a given solution $s(a_0, b_0, c_0, p_0, q_0)$, a small perturbation $\Delta s(\Delta a, \Delta b, \Delta c, \Delta p, \Delta q)$ is applied so that we have the $s + \Delta s$. Substituting this perturbed solution into equation 2.19 and linearizing it for Δs, we have a new differential equation group about Δs. Depending the eigenvalue of the coefficient matrix, the stability of the solution s is determined: stable if all the eigenvalues have negative real parts; unstable if there is any positive real parts. This stability determination is also applied for the followed inter-well solution.

As it is seen in the figure, the BSM generator behaves like a softening Duffing oscillator while the nonlinear effect decreases as the damping coefficient increases in this monostable case with intra-well motions.

The DC component c for the intra-well motion is related to the amplitude because the

system in the monostable case is not symmetrical for the equilibrium position. As the amplitude increases, c will drift towards the position $\bar{x} = 0$. The relationship between c and r is pictured in figure 2.6. As the displacement amplitude r goes to 0.8ϵ, c gets close the zero position. However, it is notified that the amplitude r for the intra-well motion needs to be less than c. Otherwise, the motion of the generator has crossed the potential saddle ($c - r < 0$) and should be analyzed as the inter-well motion case. The transition point is indicated by the converged point of the thin line and the thick line in the figure. The intra-well solutions are valid at the left range of the critical point. When the amplitude goes to the right side, the inter-well solutions are required to be used. An example of the transition from the intra-well motion to the inter-well motion is demonstrated in figure 2.5 for $\xi = 0.0156$. The amplitude responses which are higher than the indicated critical point in the figure are not longer valid as stable solutions.

2.4.2 Inter-well motion

Since the most desired properties come from the inter-well motion of the bistable generator, main efforts are focused on the solution in this case. With the same displacement solution assumed as equation (2.14), the voltage solution for the inter-well motion is slightly different. Looking at the scheme of the BSM generator in figure 2.2, the deformation of the piezoelectric components is symmetric about the position $\bar{x} = 0$ while the piezoelectric voltage is determined by the deformation. Then in a period of the harmonic inter-well motion, the piezoelectric voltage has the identical waveforms for the $\bar{x} > 0$ and $\bar{x} < 0$ range. It means the voltage frequency is two times the displacement frequency in the inter-well case. As a result, the voltage solution is assumed as:

$$\bar{V} = p \sin 2\omega t + q \cos 2\omega t \tag{2.34}$$

$$\dot{\bar{V}} = (\dot{p} - 2q\omega) \sin 2\omega t + (\dot{q} + 2p\omega) \cos 2\omega t \tag{2.35}$$

With the same operations as for the intra-well motion, the equation group for solving the steady states is:

$$c = 0 \tag{2.36}$$

$$-b\omega^2 - \frac{b\omega_0^2}{2} + \frac{(3a^2 + 3b^2 + 12c^2)b\omega_0^2}{8\epsilon^2} + \frac{k^2\omega_0^2(ap + bq)}{2\epsilon(1 - k^2)} + 2a\xi\omega\omega_0 = \bar{\gamma} \tag{2.37}$$

$$-a\omega^2 - \frac{a\omega_0^2}{2} + \frac{(3a^2 + 3b^2 + 12c^2)a\omega_0^2}{8\epsilon^2} + \frac{k^2\omega_0^2(aq + bp)}{2\epsilon(1 - k^2)} - 2b\xi\omega\omega_0 = 0 \tag{2.38}$$

$$\frac{ab\omega}{\epsilon} - 2p\omega - q\omega_r = 0 \tag{2.39}$$

$$\frac{(a^2 - b^2)\omega}{2\epsilon} + 2q\omega - p\omega_r = 0 \tag{2.40}$$

After simplifications, we have the final equations:

$$c = 0 \tag{2.41}$$

$$r = \frac{\bar{\gamma}}{(M_p^2 + M_q^2)^{1/2}} \tag{2.42}$$

$$r_v = \frac{r^2\omega}{2\epsilon(4\omega^2 + \omega_r^2)^{1/2}} \tag{2.43}$$

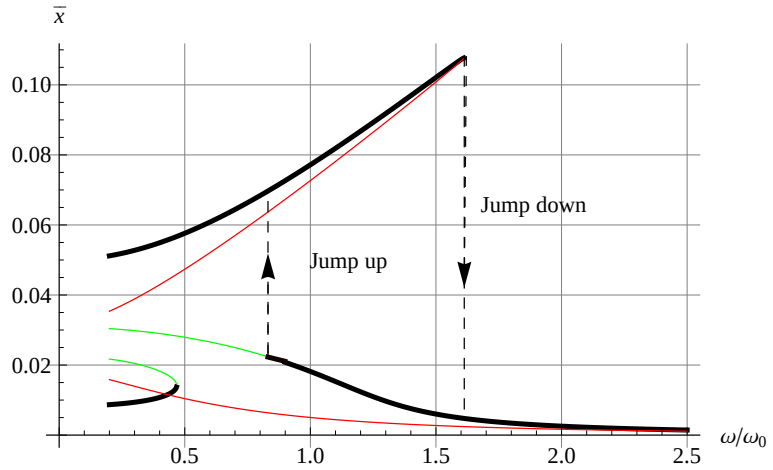

Figure 2.7: Inter-well displacement responses of a BSM generator ($\bar{\gamma} = 91$ s $^{-2}$,$\omega_0 = 110$ rad/s , $\omega_r = \omega_0$, $k^2 = 0.07$, $\xi = 0.0156$). Thick lines, stable solutions; Thin lines, unstable solutions.

where

$$M_p = -\omega^2 - \frac{\omega_0^2}{2} + \frac{3r^2\omega_0^2}{8\epsilon^2} + \frac{r^2k^2\omega_0^2\omega^2}{2\epsilon^2(1-k^2)(4\omega^2+\omega_r^2)} \tag{2.44}$$

$$M_q = \frac{r^2k^2\omega_0^2\omega\omega_r}{4\epsilon^2(1-k^2)(4\omega^2+\omega_r^2)} + 2\xi\omega\omega_0 \tag{2.45}$$

Figure 2.7 shows an inter-well frequency response for a given BSM generator by solving equations (2.41-2.43). The top thick line represents the stable inter-well solution while two red thin lines are the unstable solutions.

Since equations (2.41-2.43) gives only the high-energy inter-well orbits, it is necessary to use the equations (2.29-2.31) to obtain the low-energy intra-well orbits as shown by the two thick lines (stable) below and the green thin line (unstable) for the purpose of the complete solutions. It is clear that for the same excitation, the inter-well motion has a much better responses than the monostable case, thus more power to be harvested. The dashed lines with arrows are used to indicate the jump position between the high-energy orbit and the low energy orbit. The jump-up and jump-down arrows are separately related to the responses for forward and reverse harmonic sweeps while the arrow direction represent the jump direction. The special hysteresis phenomena of the nonlinear system response are clearly seen from the jump indications.

2.4.3 Influence of the parameters on the inter-well motion

To better understand the properties of the BSM generator, it is interesting to investigate the influence of the parameters on the desired inter-well response.

As an important system parameter, the damping coefficient ξ is studied first. Figure 2.8 shows the inter-well responses for increasing damping coefficients. To ensure the inter-well motion for the damping cases, a higher excitation than the one used for figure 2.7 is assumed ($\bar{\gamma} = 152\text{s}^{-2}$). The thick lines represent the stable solutions while the dotted lines are the unstable solutions. The arrows on the dashed lines indicate the jumps between the high-energy stable orbits to low-energy stable orbits. As can be seen, the BSM generator jumps from the high-energy orbit to the low-energy orbit earlier for higher damping cases. Nevertheless, the influence of the increasing damping on the low-energy orbits and the

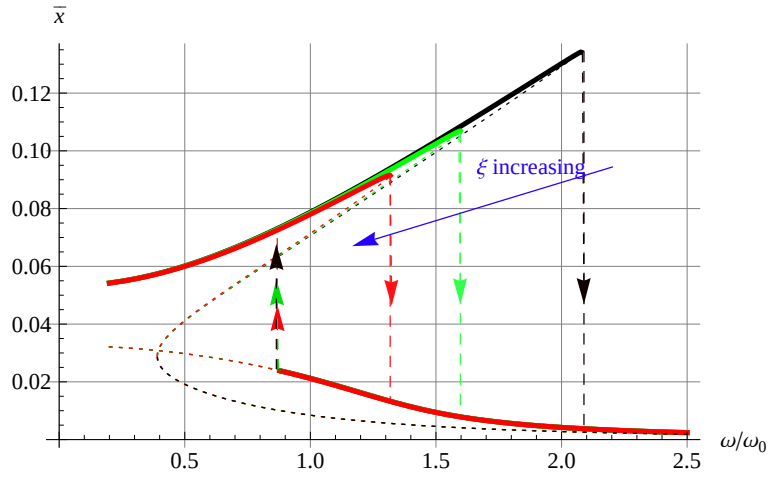

Figure 2.8: Stable inter-well displacement responses for different damping coefficients ($\bar{\gamma} =$ 152 s $^{-2}$,$\omega_0 = 110$ rad/s , $\omega_r = \omega_0$, $k^2 = 0.07$, $\xi = \{0.0156, 0.03, 0.045\}$).

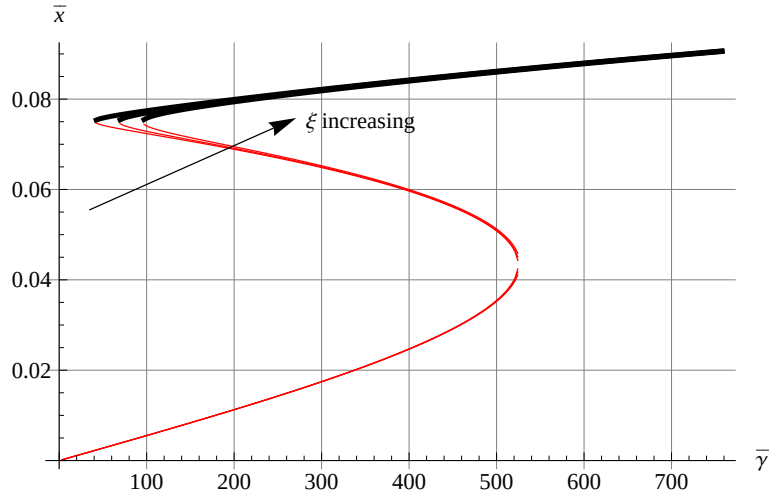

Figure 2.9: Inter-well responses versus the excitation amplitude at a specific frequency and different damping levels ($\omega_0 = 110$ rad/s , $\omega = \omega_r = \omega_0$, $k^2 = 0.07$, $\xi = \{0.0156, 0.03, 0.045\}$). Thick lines, stable solutions; Thin lines, unstable solutions.

high-energy orbits at the left of the jump positions is not so obvious. The responses at these positions are almost identical. The jump positions from the low-energy orbit to the high-energy orbit are not affected either. Clearly, to have a wider band and higher power output, it is always preferred to have low damping systems.

It is also evident in the figure 2.9 which depicts the evolution of the inter-well motion amplitude versus the excitation level at a selected single frequency point. To get the stable inter-well motions, a certain excitation amplitude should be ensured while the increasing damping increases the minimum excitation threshold as indicated by the arrow. As the excitation is much larger than the threshold, the response amplitude hardly changes for different damping values. In this situation, it is similar to the case of vibration with constant displacement amplitude.

Another important normalized parameter is the electric load related frequency $\omega_r = 1/(RC_0)$, which affects the harvested power and the dynamic displacement responses. According to equation (2.10), the average normalized power of the generator in one period is

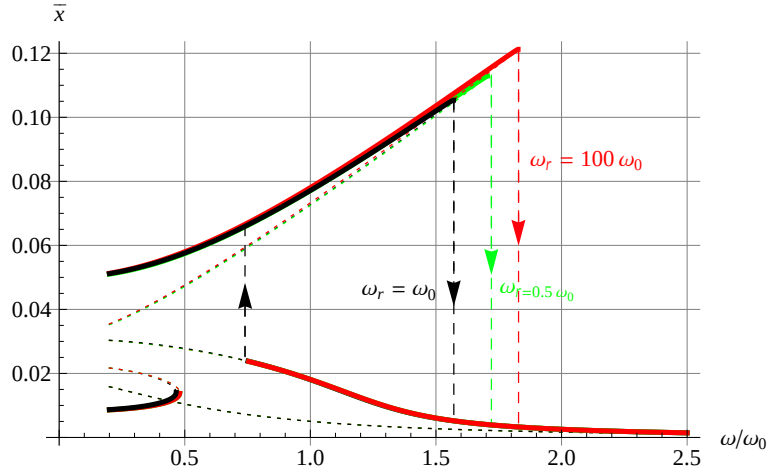

(a) Displacement responses versus load .

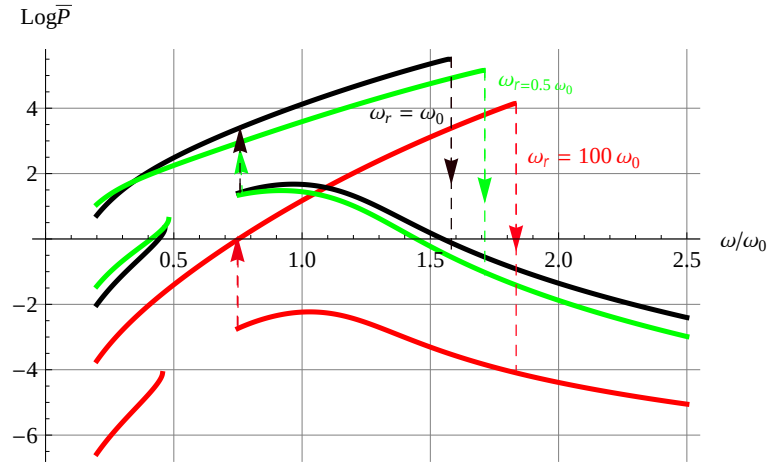

(b) Power responses versus load.

Figure 2.10: Inter-well displacement and power responses for different resistor values ($\bar{\gamma} =$ 91 s $^{-2}$,$\omega_0 = 110$ rad/s , $\omega_r = \{0.5, 1, 100\}\omega_0$, $k^2 = 0.07$, $\xi = 0.0156$).

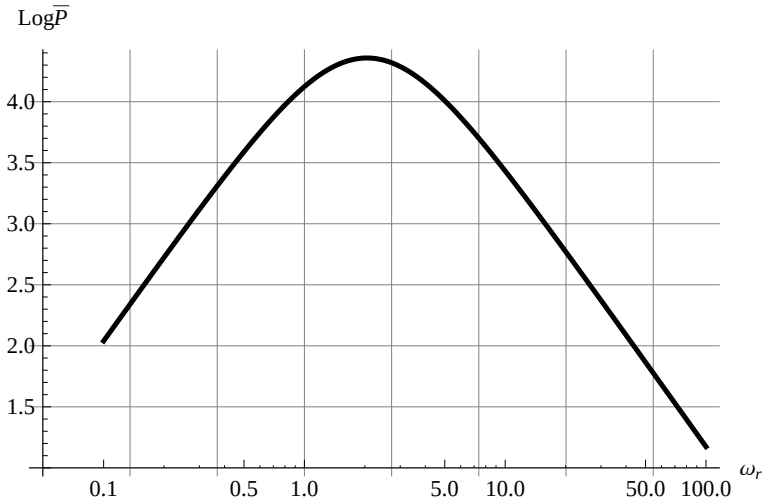

Figure 2.11: Harvested power versus the load ($\bar{\gamma} = 91$ s $^{-2}$,$\omega_0 = 110$ rad/s , $\omega = \omega_0$, $k^2 = 0.07$, $\xi = 0.0156$).

expressed as:

$$\bar{P} = \frac{1}{T}\int_0^T \frac{k^2\omega_0^2}{1-k^2}\bar{V}\bar{I}dt = \frac{k^2\omega_0^2\omega_r r_v^2}{2(1-k^2)} \tag{2.46}$$

which is based on the sinusoidal assumption equation (2.34).

Figure 2.10(a) and 2.10(b) shows the inter-well displacement responses and the corresponding power responses for different resistor values (C_0 is fixed). For the power responses, only the stable solutions are considered here. It is interesting to find that the inter-well motion range first decreases then increases with the increasing ω_r ($\omega_r = 0.5\omega_0 \rightarrow \omega_r = \omega_0$). The jump position from the high-energy orbit to the low-energy orbit moves from the higher frequency (indicated by the green arrow) to the lower frequency (indicated by the black arrow). However, the harvested power is increased as seen by comparing the power curves for these two ω_r cases. As ω_r continues increasing to $100\omega_0$, the jump-down position shifts back to a much higher frequency while the power is decreased sharply at the same time. Looking back at the influence of the damping on the system responses, it shows that the power consumed on the load acts as a special electrical damping for the generator motion.

Moreover, from the power response trends for three selected different load conditions, it can be inferred that there is an optimal value of the load resistor to get the maximum total harvested power over a specific frequency range. The compromise between the harvested energy and the operation band has also to be taken into consideration.

To get the clear relationship between the harvested power and the load value, investigation is done at a selected frequency ($\omega = \omega_0$) with varied ω_r values as shown in figure 2.11 with only inter-well motion considered. The power has a peak around $\omega_r/\omega = 2$ which means the matching impedance at 2ω. This is due to the frequency doubling effect of the BSM generator for the voltage response in the case of inter-well motion. It is to be further shown later. Nevertheless, the power is not changed much for a considerable load range.

Beside the load resistor, the harvested power is related to the electromechanical coupling level. Figure 2.12(a) pictures the available power at a selected frequency with the load matched. The power is rapidly increasing with k^2 when it is small. It is because the displacement amplitude decreases very slowly with the increasing coupling level as

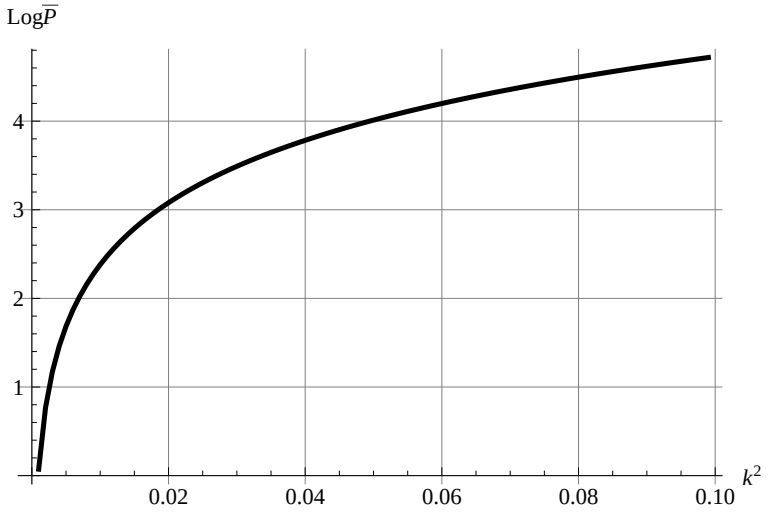

(a) Power responses versus k^2.

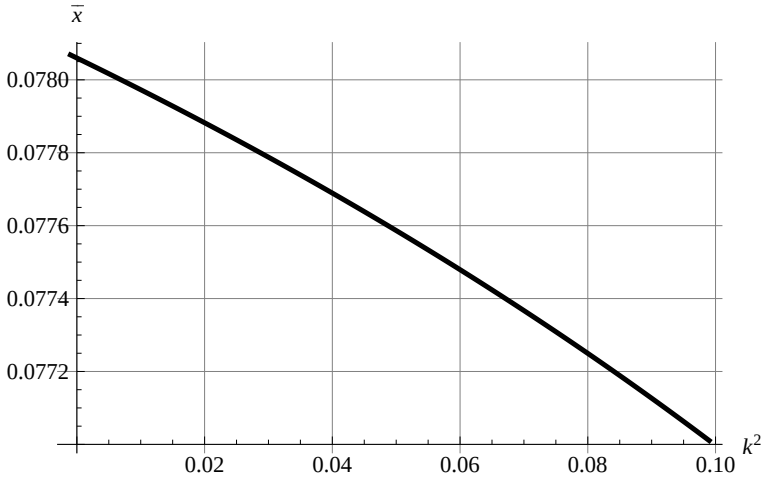

(b) Displacement responses versus k^2.

Figure 2.12: Inter-well displacement and power responses for different k^2 values ($\bar{\gamma} = 91$ s $^{-2}$,$\omega_0 = 110$ rad/s , $\omega_r = 2\omega_0$, $\omega_0 = 110$, $\xi = 0.0156$).

shown in figure 2.12(b) when the damping from the energy harvesting is not obvious. This is consistent with the results in figure 2.9 that the displacement response keeps almost constant for different damping levels if the excitation is large enough. As the coupling level keeps increasing, it brings more damping in the form of harvested energy so that the displacement amplitude decrease is not to be neglected. As a result, the power increase lessens.

From the discussion above, it is inferred that to get more harvested power and wider operation band, the following conditions are preferred: low damping coefficient, optimal load value, high electromechanical coupling level and proper excitation level to maintain the inter-well motions.

2.5 Numerical and experimental investigations

After the analytical studies of the BSM generator, numerical and experimental investigations are performed to get the detailed properties and performance. Unlike linear generators, the nonlinear bistable generators have multiple solutions for the same excitation as shown by the harmonic balance discussion. Even with only stable solutions considered, it has still usually more than one possibilities. As a result, the research about the bistable generator is more complicated than about the linear one.

According to the nonlinear dynamic theory, the final motion status is dependent on the initial conditions when the nonlinear oscillator has multiple solutions. With varying initial velocity or displacement, the oscillator may stay at the inter-well orbit or the intra-well orbit or even the chaotic orbit [128]. For a chirp excitation, the responses are very different related to the sweep directions, showing a special hysteresis characteristic [127]. Therefore, it is necessary to do many tests for different kinds of excitations to have a full view of the properties.

In this section, the realized BSM generator is driven by two typical kinds of excitations: chirp (forward and reverse sweeps) and noise signals. The performance for different excitation strengths is also investigated. Comparisons are done for the numerical and experimental results in order to validate the developed model.

2.5.1 Experimental set-up

BSM prototype generator

To confirm the behavior of the BSM generator, an experimental prototype has been realized as shown in figure 2.13(a). It comprises an inertial mass, two piezoelectric transducers (APA120S, CEDRAT Technologies©) and four flexible hinges. The two piezoelectric components are connected in parallel to supply the harvested power.

When assembling the device, the mass is placed at the zero position $x = 0$ and the piezoelectric elements are at their natural unconstrained length l_0. At the left end of the structure, a screw connected to a vertical beam structure is used for tuning the initial buckling level. This deformable beam structure is capable of supplying the desired displacement and stopping the rotation of the components. After a small tunable static displacement is applied, the buckling happens and the mass moves to a new equilibrium position. Meanwhile, the flexible hinges effectively suppress other movements except translation along the x direction.

As discussed in the modeling section, a necessary condition which allows the buckling condition to happen is that the rotary stiffness of the hinges K_θ is less than $(l_0^2 - L^2)K/8$.

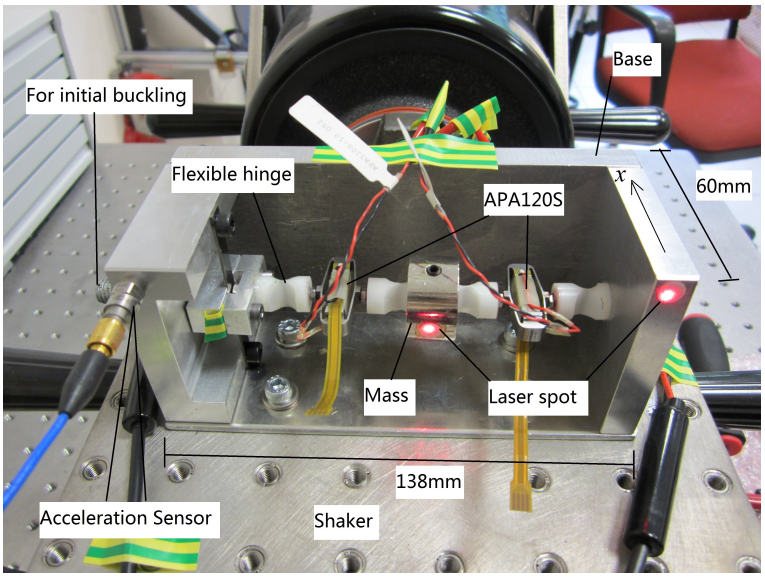

(a) BSM prototype generator.

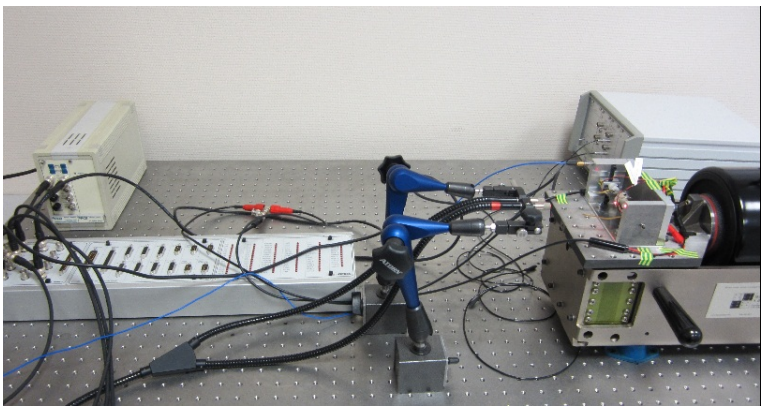

(b) BSM testing bench.

Figure 2.13: Experimental system for the BSM generator.

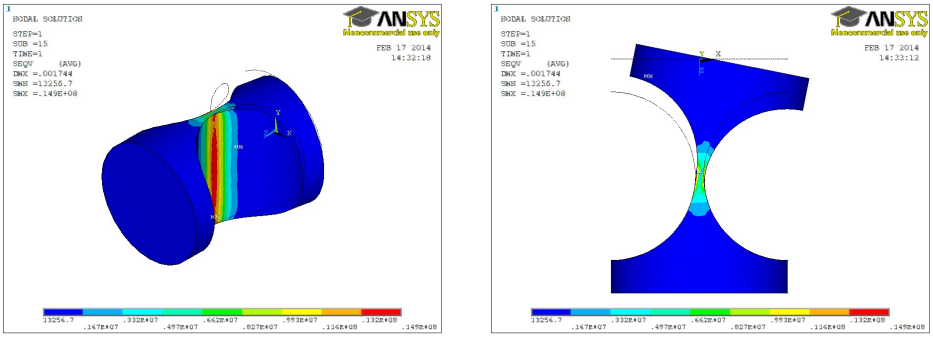

(a) Oblique view.

(b) Top view.

Figure 2.14: Strength verification of the flexible hinges.

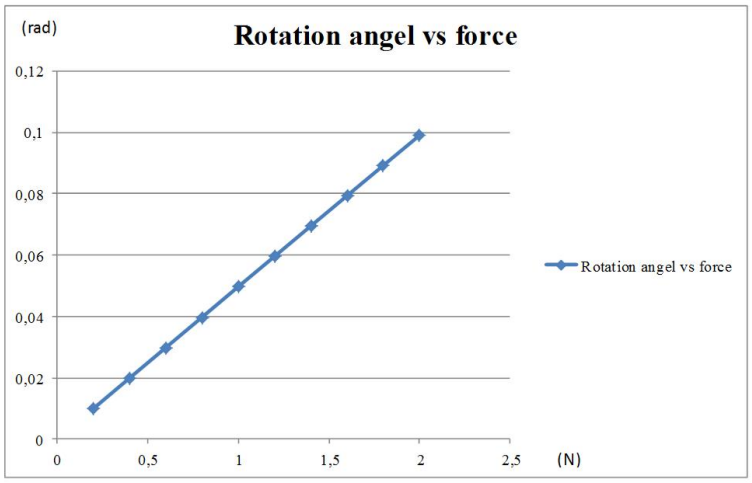

Figure 2.15: Rotation angle of the flexible hinge versus the force at the tip.

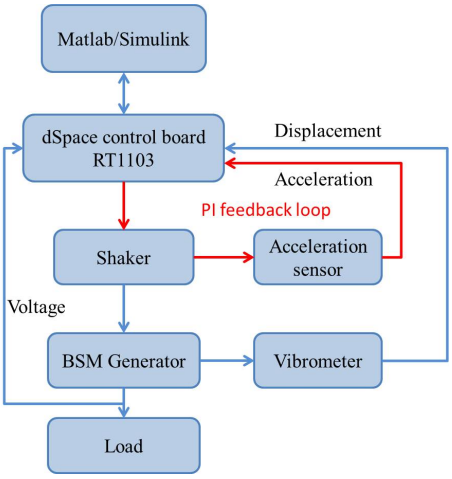

Figure 2.16: Control principle of the experimental platform.

At the same time, the maximum rotation angle of the hinges is expected to be big enough to obtain large displacement without breaking the device. Therefore, it is critical to select the proper material for the hinges. In this prototype, Polytetrafluoroethylene (PTFE) is selected for low tensile modulus (300-800 MPa) and high tensile strength (40 MPa).

The strength of the designed hinge has been checked with the ANSYS software prior to experimental investigations as shown in figure 2.14. For a maximum stress of 15 MPa located at the center of the hinge, the rotation angle is 0.185 rad which is considered large enough for the desired high displacement response. The rotation angle is almost proportional to the force at the tip (the moment can be evaluated by the force multiplied with the distance from the center to the end) as the ANSYS results show in figure 2.15.

Experimental environment and identification

The experimental platform is shown in figure 2.13(b). The BSM generator is fixed on a shaker (2075E-HT, The Modal Shop©) which moves along the horizontal direction (x direction) to avoid the gravity effect. A Matlab©dedicated program is used to produce the desired excitation signals and interfaces the real-time control board (RTI1103, dSpace©). The shaker is driven in a PI feedback loop with the accelerometer (M352C68, PCB©) as an input to ensure constant acceleration amplitude. The displacement of the central mass

Parameter	Value	Parameter	Value
M(g)	45.8	L(mm)	33
K(N/m)	3.9e5	x_0(mm)	1.25
C_0(µF)	2.3	α(N/m)	0.26
μ(N/(m/s))	0.16	R(kΩ)	3.84
K_θ (Nm/rad)	0.03		

Table 2.3: Parameters for the BSM generator.

is measured using a differential optical vibrometer (OFV-552 and OFV-5000, Polytec©). The control principle of the system test platform is shown in figure 2.16.

Experimental parameters were identified as shown in table 2.3. With the capacitance (two transducers parallel connected), the mass and the initial buckled position x_0 measured directly, the stiffness K and the piezoelectric coefficient α were obtained in the case of a small signal chirp excitation (to ensure linear response) in short-circuit and open-circuit conditions. In the open-circuit case, the current I in the equation (2.5) is set to zero. Then we have:

$$\frac{\alpha x_0 \dot{x}}{L} - C_0 \dot{V}_p = 0 \tag{2.47}$$

α is calculated as $C_0 V_p L/x_0$ from the displacement and voltage responses for the same excitation. The damping coefficient μ was estimated by the small signal bandwidth method in a short-circuit condition. It is worthy of note that the stiffness and the piezoelectric coefficient of the APA120S are slightly different from the datasheet because of the longitudinal stiffness of the hinges. Based on the linear properties shown by the ANSYS analysis in figure 2.15, the rotational stiffness is obtained from the resonance frequency through an additional dynamic test with a mass attached to one hinge's end.

Following a classical strategy for linear harvesters, the electrical load is selected to match the piezoelectric elements impedance at the resonant frequency of the LEO:

$$R = \frac{1}{C_0 \omega_0} \tag{2.48}$$

Another impedance matching strategy called "adaptive impedance matching" is later tested in next section.

2.5.2 Harmonic excitation

To study the performance and wideband properties of the BSM generator, the investigations with conventional single frequency excitations is no longer suitable. Instead, chirp excitations are capable of providing more information over an interested wide frequency range. With three different amplitudes (0.075m/s^2 , 0.5m/s^2 , 3m/s^2), the properties for both intra-well and inter-well cases are studied. Forward and reverse sweeps with a rate of 0.025Hz/s are considered to obtain the stable responses accounting for the hysteresis phenomena.

Displacement responses

The experimental displacement responses are shown in figure 2.17. From figure 2.17(a, b), it can be seen that for the small excitation of 0.075m/s^2 , the bistable harvester be-

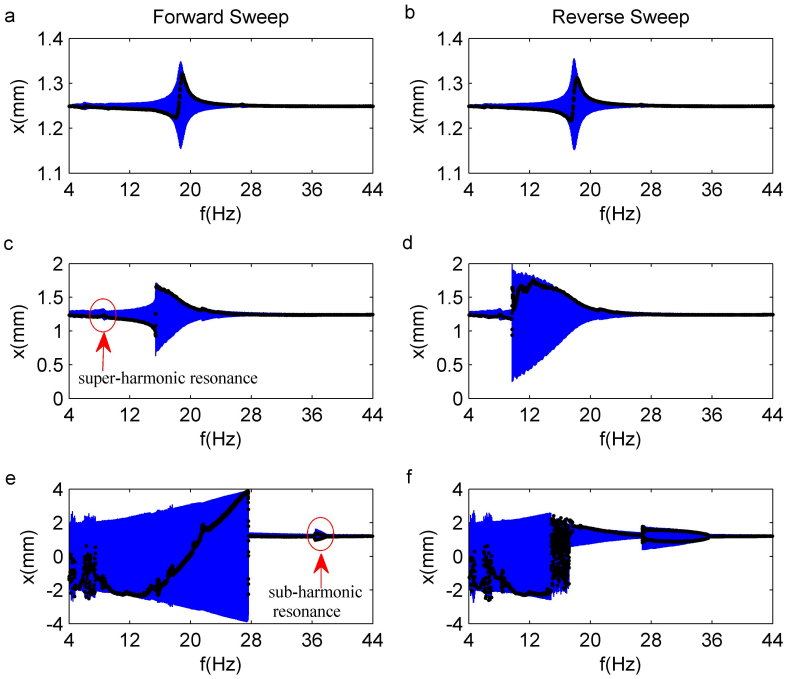

Figure 2.17: Experimental displacement responses (blue lines) and Poincaré sections (black dots) of the BSM generator for chirp excitations: 0.075$\mathrm{m/s^2}$ *(a,b), 0.5*$\mathrm{m/s^2}$ *(c,d), 3*$\mathrm{m/s^2}$ *(e,f).*

haves like its derived LEO, which is consistent with the modeling of the proposed architecture. The experimental resonant frequencies are 18.3Hz and 17.9Hz for forward and reverse sweeps respectively. The small 1.7% resonant frequency discrepancy means that the 0.025Hz/s chirp rate and the 0.075$\mathrm{m/s^2}$ excitation amplitude are small enough to get the quasi-static response of the system.

When the excitation amplitude is increased to 0.5$\mathrm{m/s^2}$, the bistable harvester exhibits strong intra-well nonlinear characteristics. As expected from equation (1.4), the super-harmonic resonance can be observed in figure 2.17(c, d). However, only the super-harmonic resonance at half the resonant frequency can be clearly distinguished while the super-harmonic resonance at one-third the resonant frequency is hard to detect because the quadratic term has more influence than the cubic term for the bistable structures.

In the case of the highest excitation 3$\mathrm{m/s^2}$, the mass periodically crosses the local potential maximum, and inter-well motions are exhibited. These inter-well motions happen from 4 Hz to 27 Hz for the forward sweep and from 18 Hz to 4 Hz for the reverse sweep. Periodic oscillations are exhibited during most of the sweep process, whereas chaotic motion can be found in the vicinity of 5Hz and 7.5Hz for both forward sweep and reverse sweeps, as can be inferred from the Poincaré sections which are lines connected by black dots for periodic oscillations and distributed black dots for chaotic oscillations. For reverse sweep, there is another frequency band of 16-18Hz where chaotic motion exists. Sub-harmonic resonance is also observed around 35Hz. According to the Poincaré sections in figure 2.17(e, f), the period of motion around the sub-harmonic resonance point is twice the period of excitation.

In order to validate the developed model of the BSM generator, the experimental displacement amplitude for the inter-well motions obtained in the case of 3$\mathrm{m/s^2}$ excitation

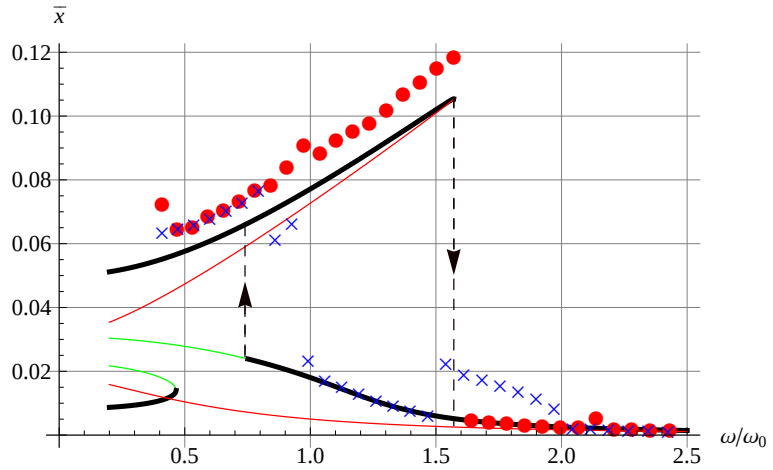

Figure 2.18: Analytical results vs experimental results for the chirp excitations of 3 m/s^2. *Circles: Experimental results for the forward sweep; Crosses: Experimental results for the reverse sweep; Lines: Analytical results.*

is first compared with the analytical results from the harmonic balance method as presented in figure 2.18. The solid circles represent the forward sweep experimental responses and the crosses represent the reverse sweep response while the solid lines represent the analytical solutions. For the experimental chaotic motions, the amplitude is accounted for by the half of the peak-peak displacement.

It shows that the experimental results are very close to the theoretical results. However, the chaotic motion cannot be analyzed with the harmonic balance method with the periodic motion assumptions. Moreover, since the harmonic balance method takes only the fundamental frequency component into consideration, the super-harmonic and sub-harmonic resonances are not included unless include high-order terms. The model might become more complex if high-order terms were to be added for a better description.

Because of the limited information from the harmonic analysis and the desire for more accurate and full results, numerical simulations are performed using the parameters given in table 2.3 with the Matlab ODE45 (Dormand-Prince) variable step solver and Simulink tools. From the results in 2.19, the Poincaré sections indicating the motion type (chaotic or periodic) and the sub-harmonic and super-harmonic resonances are clearly seen. Better consistence is found between the experimental and numerical results than the one between the analytical and experimental results. Therefore, numerical methods are chosen for comparing with experimental results and the optimizations of the generator in the following chapters.

Voltage response

Since the deformation of the piezoelectric components is not proportional to the displacement due to the nonlinearity of the BSM generator, it is interesting to investigate the voltage response.

Figure 2.20(a, b) and figure 2.21(a, b) represent the voltage responses in the case of small excitation 0.075 m/s^2, in which the BSM generator is similar to its LEO. With the same responses as for the LEO case obtained, comparison between the linear and the BSM generators becomes feasible. To detail the performance comparison of the BSM generator with a linear one, the available voltage of both linear and nonlinear harvesters is compared in figure 2.20(c, d) for the excitation of 0.5 m/s^2. Using the linear characteristics, the

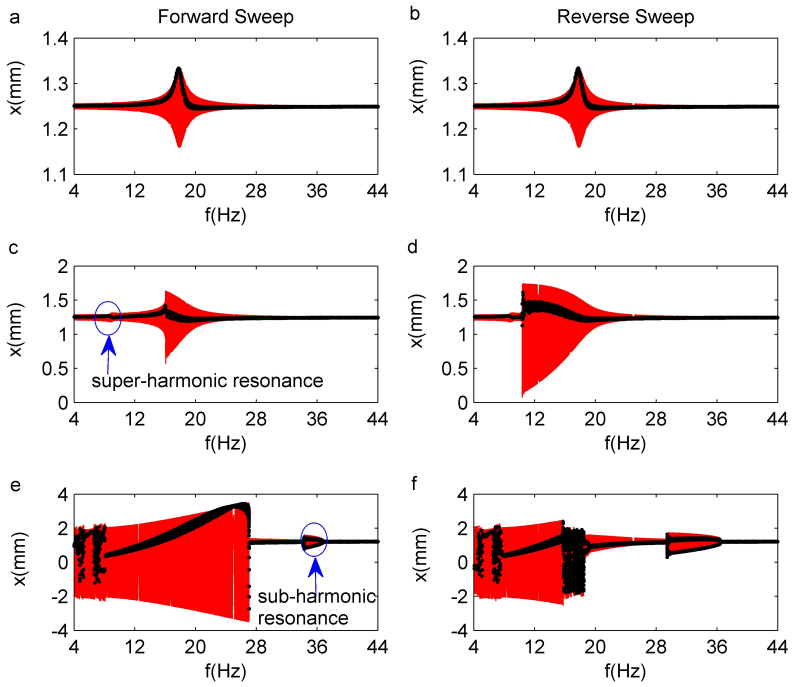

Figure 2.19: Simulation displacement responses (red lines) and Poincaré sections (black dots) of the BSM generator for chirp excitations: 0.075$\mathrm{m/s^2}$ *(a,b),* $\mathrm{m/s^2}$ *(c,d),* $\mathrm{m/s^2}$ *(e,f).*

dashed line is the available voltage amplitude derived from figure 2.20(a, b) for the LEO harvester with the ratio of $0.5/0.075 = 6.67$. It appears that the voltage response is slightly poorer for forward sweep but much better for reverse sweep.

When the excitation $3\mathrm{m/s^2}$ is strong enough to make the inter-well motions happen as shown in figure 2.17(e, f), it brings great benefits to the bistable harvester which scavenges more energy. This is obvious in figure 2.20(e, f). Both periodic and chaotic motions produce higher voltage than the LEO case. Better performance is obtained in the low frequency range below the resonant frequency for both forward and backward sweeps. Especially for forward sweep signal, the BSM generator is superior to the LEO for almost the whole frequency range except for the narrow band around the resonance frequency.

Although the reverse sweep response is not as good as the forward sweep response, it still shows advantages below the resonant frequency and around the sub-harmonic resonance band from 30 to 36 Hz. Considering the average performance for the forward and reverse sweeps, the BSM generator still outperforms the LEO case over a much wider band.

Moreover, an interesting phenomenon that the voltage response is not symmetric about zero is observed in figure 2.21 and 2.20. This is due to the asymmetry about the compression and elongation deformation of the piezoelectric components in the BSM structure. Especially for the inter-well motions, the strain gets the negative apex value at the zero position and then changes for stretching along both displacement directions. Therefore, the negative voltage extreme related to the compression strain is always less than the positive one. Since the voltage has the same waveform for the positive and negative displacement half-period in a inter-well motion period, its frequency is two times the excitation frequency as discussed in the harmonic balance analysis and validated in figure 2.22.

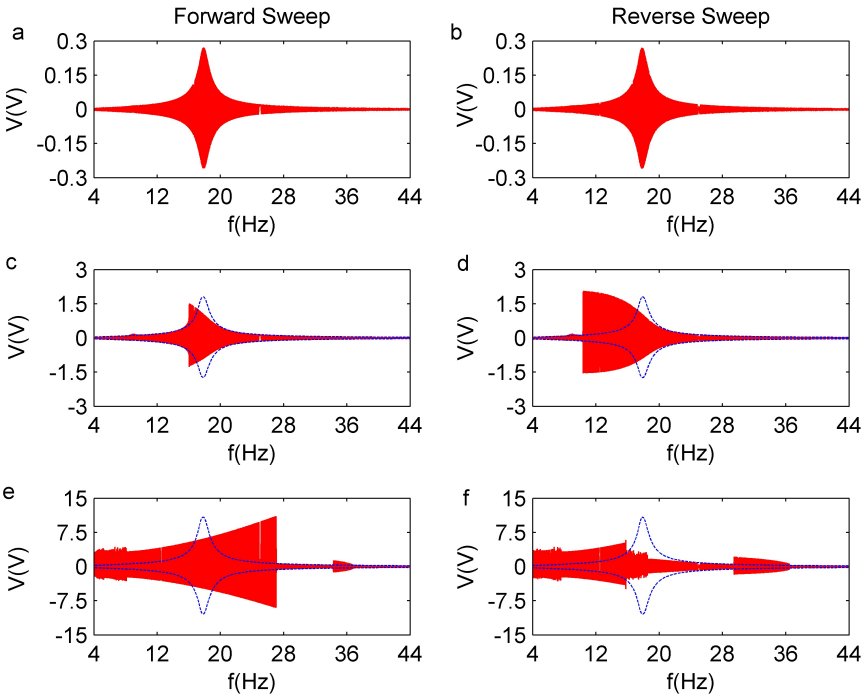

Figure 2.20: Simulation voltage of piezo elements for chirp excitations: 0.075$\mathrm{m/s^2}$ *(a, b), 0.5*$\mathrm{m/s^2}$ *(c, d), 3*$\mathrm{m/s^2}$ *(e, f). The red lines represent the voltage responses and the blue dashed lines represent the available voltage responses of the LEO harvester with the same excitation.*

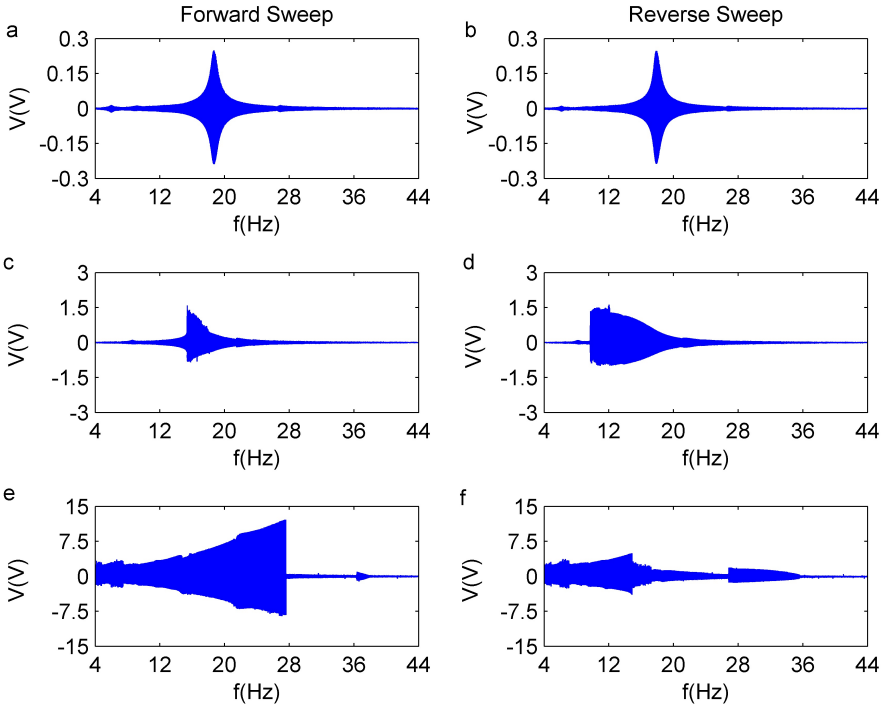

Figure 2.21: Experimental voltage of piezo elements for chirp excitations: 0.075$\mathrm{m/s^2}$ *(a, b), 0.5*$\mathrm{m/s^2}$ *(c, d), 3*$\mathrm{m/s^2}$ *(e, f).*

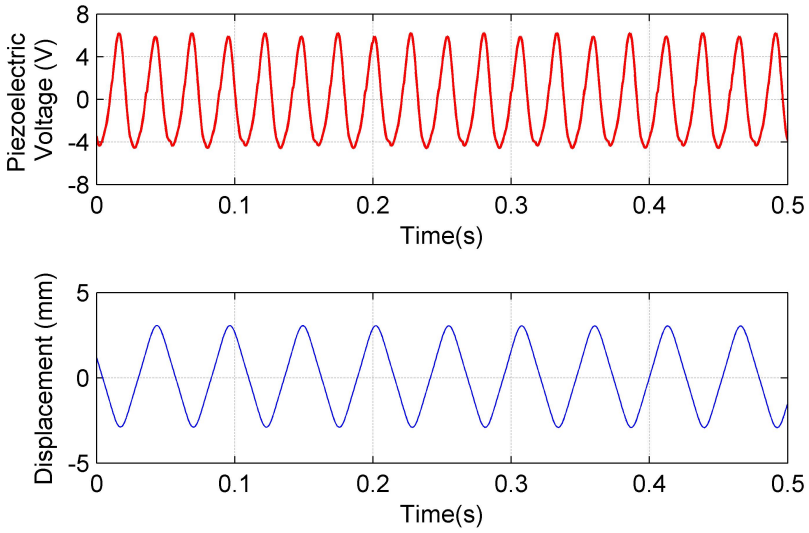

Figure 2.22: Experimental voltage and displacement waveforms at the frequency 18.5Hz with an excitation of 3 m/s^2.

Power

The corresponding numerical and experimental harvested power values of the BSM generator are both presented in figure 2.23. For comparison purpose, the available power inferred from the LEO model is also plotted with the same excitation. It is clear that the experimental results are in good accordance with the theory as it has been already exhibited for the displacement and voltage responses.

In the case of intrawell linear motions for the small excitation $0.075m/s^2$, the maximum available power at the resonant frequency is 7.5µW and the bandwidth is less than 1Hz as shown in figure 2.23(a).

As the excitation increased to $0.5m/s^2$, the maximal power is slightly less than the one for the LEO for the intra-well nonlinear motions. However, a broader bandwidth can be obtained for the backward sweep as shown in figure 2.23(d). This case corresponds to a typical softening Duffing oscillator due to the quadratic term and does not provide significant advantage compared to the LEO.

When the excitation amplitude reaches $3m/s^2$, the maximal available power is evaluated to be 12mW for the LEO with a bandwidth of 1Hz. Nevertheless, the bistable harvester, which exhibits inter-well motions, presents a maximal power of 13mW (forward sweep) and more than 5mW from 18Hz to 27Hz as can be seen in figure 2.23(e). Even for the less favorable reverse sweep case (figure 2.23(f)), the maximum available power is still 1.8mW and more than 0.4mW can be obtained from 15Hz to 5Hz. These results confirm that the proposed bistable harvester is superior to the LEO regarding the bandwidth.

Adaptive impedance matching strategy

To investigate the influence of the electric load on the harvested power, another strategy called adaptive impedance matching is performed. The load impedance which exactly matches the excitation frequency ω is expressed as equation (2.49):

$$R_a = \frac{1}{C_0 \omega} \tag{2.49}$$

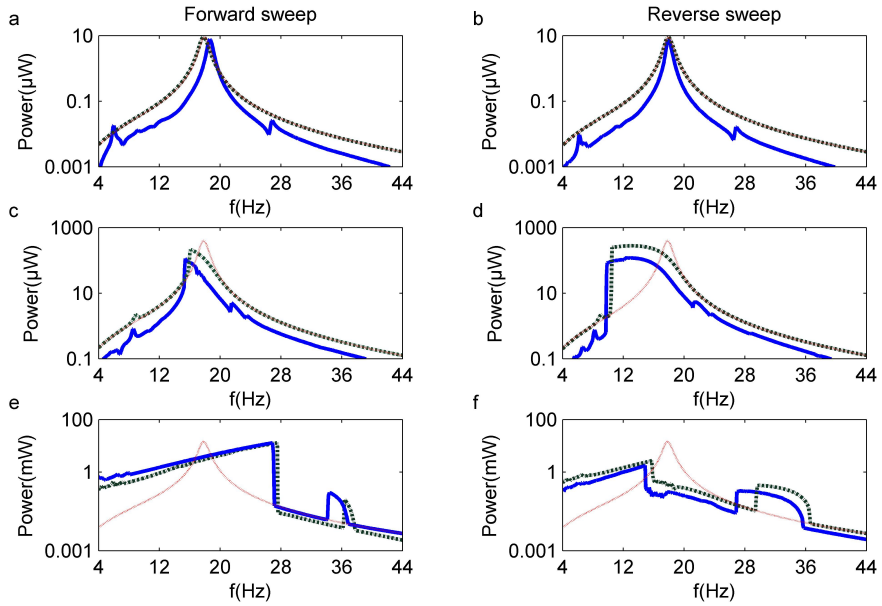

Figure 2.23: Numerical (thick dashed lines) and experimental (thick solid lines) harvested power of the BSM harvester for chirp excitations: 0.075$\mathrm{m/s^2}$ *(a, b), 0.5*$\mathrm{m/s^2}$ *(c, d), 3*$\mathrm{m/s^2}$ *(e, f). The thin dashed lines represent the available power of the LEO harvester.*

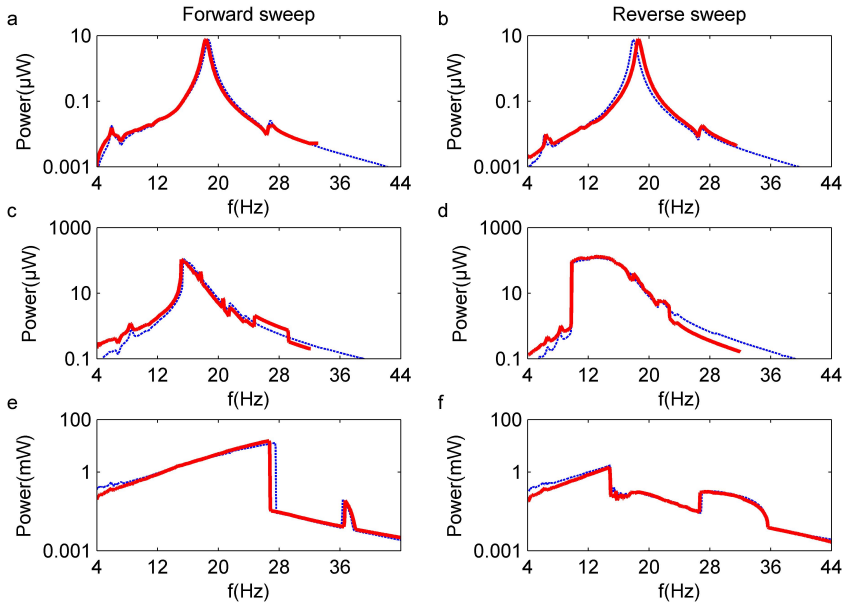

Figure 2.24: Power comparison between classical (dashed lines) and adaptive impedance matching strategies (solid lines) for chirp excitations: 0.075$\mathrm{m/s^2}$ *(a, b), 0.5*$\mathrm{m/s^2}$ *(c, d), 3*$\mathrm{m/s^2}$ *(e, f).*

Reference generators	Input excitation	Volume (cm^3)	Power (mW)	Power density (mW/cm^3)	Normalized power density (mW/cm^3)
BSM generator (This work)	Chirp $3m/s^2$	48	16	0.33	3.7
[132]	Chirp $10m/s^2$	130.7	105	0.8	0.8
[127]	Chirp $10m/s^2$	19	0.36	0.019	0.019
[120]	Chirp $14m/s^2$	9.9	0.56	0.059	0.03
[100]	Single freq. 10Hz $10\ m/s^2$	1.67	0.0141	0.0084	0.0084
[124]	Chirp $20m/s^2$	40	34	0.675	0.17

Table 2.4: Power density of several bistable harvesters.

The experimental available power in this case is shown by the solid lines in figure 2.24 while the dashed lines represent the power for the classical approach. The two impedance matching strategies lead to similar harvested power except for the frequencies lower than about 10Hz. It is because the resistor value range (17.3kΩ to 1.6kΩ) is too small to drastically affect the harvested power in the studied frequency band.

However, in the case of the $3m/s^2$ forward sweep shown in figure2.24(e), the harvested power with the adaptive impedance matching strategy reaches 16mW at 26.5Hz, a little higher than 13mW at 27Hz in the case of impedance with resonant frequency matching strategy. The inter-well motion also disappears at 26.5Hz, slightly before 27Hz. This result further validates that in some conditions, the damping effect of the energy harvesting circuit exerts impact on the bistable harvester motion as analyzed with the harmonic balance method.

Power density

To evaluate the performance of a generator, power density which is defined by the obtained power divided by the occupied volume is often used as an important criterion. Before starting, it is proposed that the power density should be calculated based on the overall volume required for the harvester to work normally [35, 140]. The considered volume includes not only the volume of the functional parts but also the volume swept during operation. A power density of $0.33mW/cm^3$ is then obtained for the maximum harvested power 16mW. The maximum power densities p of several bistable harvesters from the literature are estimated and given in table 2.4. It is noted that the maximum average power given is calculated from the maximum transient power divided by 2 for the reference with the assumption of sinusoidal motions [132, 127, 120].

Because the different bistable devices in the literature are operated at various acceleration amplitudes, a normalized power is suggested for fair comparison. Considering that, in the linear case, the power is proportional to the square of the acceleration γ [88] at a determined frequency, a normalized power density is calculated as the power density that would be harvested at $10m/s^2$ if the system was linear, as shown in equation (2.50). Of course the proposed normalized power density is questionable since the real power density at $10m/s^2$ cannot be simply evaluated because of the nonlinear behavior of the harvesters.

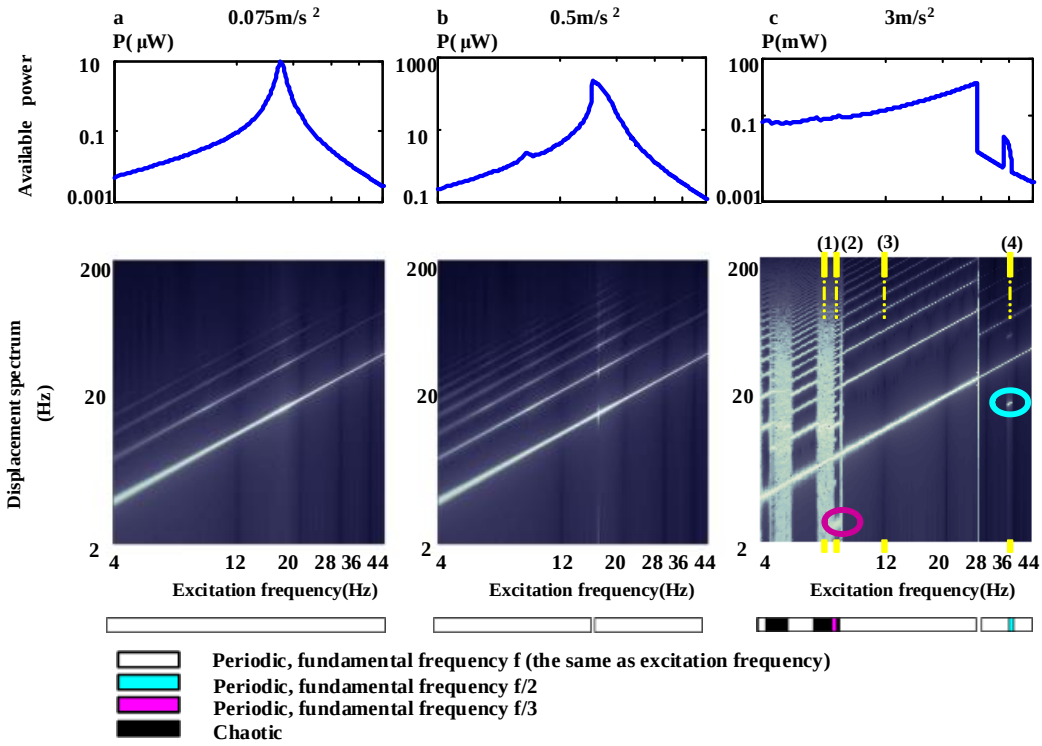

Figure 2.25: Simulated harvested power and the corresponding spectrum of the harvester motion for forward sweep excitations: 0.075$\mathrm{m/s^2}$ *(a), 0.5*$\mathrm{m/s^2}$ *(b), 3*$\mathrm{m/s^2}$ *(c).*

It is however thought as a fair figure of merit for comparison purpose.

$$\bar{p} = p\frac{10^2}{\gamma^2} \tag{2.50}$$

It is shown that the proposed device exhibits very good performances since it has the best normalized power density, corresponding to one of the highest power density for the lowest acceleration.

Spectrum analysis

The Poincaré sections in figure 2.17 and figure 2.19 provide some insights about whether the motion is chaotic or periodic. However, other information is not given, such as the presence of high-order harmonic components. A spectrum plot representing the displacement spectral density as a function of the excitation frequency is then proposed in figure 2.25 to allow a full analysis of the motion frequency characteristic. It is plotted together with the numerical harvested power for the forward sweep excitation cases.

At low acceleration, the parallel white lines shown in figure 2.25(a) indicate the fundamental frequency (bottom line) and the high-order harmonic components. Although the displacement response in 2.19(a) suggests that the bistable harvester behaves like the LEO harvester, the spectrum plot highlights that there still exist weak nonlinear effects.

When the excitation is increased, high-order components are more important, as shown in figure 2.25(b). The additional vertical white line at 14 Hz represents the sharp amplitude jump associated to the nonlinear softening effect.

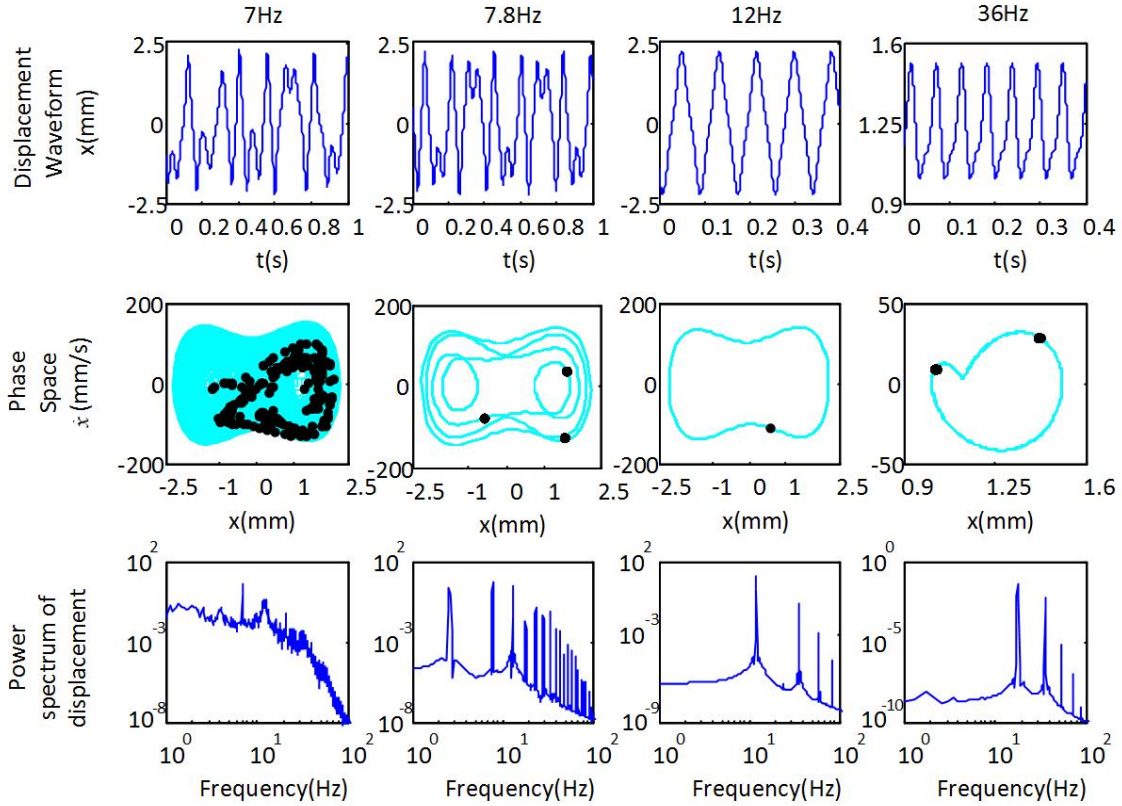

Figure 2.26: Waveforms, phase spaces with Poincaré sections and motion power density spectrum for four selected frequencies: 7Hz, 7.8Hz, 12Hz and 36Hz.

As the excitation amplitude is increased to 3m/s^2 (figure 2.25(c)), a more complex pattern appears, featuring two different types of motions:

- Periodic nonlinear motions (white lines). Most of the time, periodic motions at the excitation frequency are exhibited. Periodic motions at half (sub-harmonic resonance, highlighted in blue) and one third (highlighted in purple) of the excitation frequency can however also be found.
- Chaotic motions (white vertical stripes).The spectrum of the chaotic motion is not a line spectrum and includes frequency components from 2Hz to 200Hz.

Plotting the harvested power in the same figure allows seeing that the chaotic motion does not generate more energy than the periodic nonlinear motion.

From figure 2.25(c) four different frequencies are selected and analyzed in a more classical manner. They are respectively: (1) chaotic motion at 7Hz; (2) periodic motion at one third of the excitation frequency at 7.8Hz; (3) periodic motion at the excitation frequency at 12Hz and (4) periodic motion at half the excitation frequency at 36Hz. These selected cases are pointed out by the four yellow dashed lines in figure 2.25(c). The respective simulated displacement waveform, phase space with Poincaré section and motion power density are then plotted in figure 2.26 and confirm that the spectrum plot proposed in figure 2.25 provides accurate and concise description of the system motion.

Strange attractor and the effect of the initial condition

As a feature of the nonlinear oscillator, the strange attractor represents a special status that the excitation and the initial condition is sufficient for the requirement of crossing the

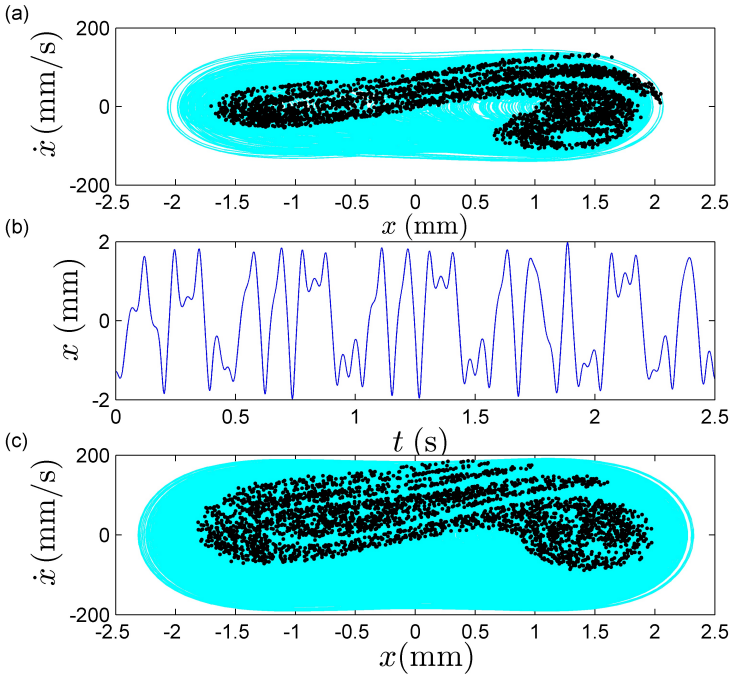

Figure 2.27: (a) Phase space (line) and strange attractor (black dots) observed by experiment; (b) Cut-out experimental displacement waveform; (c) Phase space and strange attractor by simulation.

potential barrier but not enough to obtain the inter-well motion in the form of limit cycles. Figure 2.27(a) shows the experimentally observed strange attractor with a single frequency excitation at 17Hz. The excitation is 3m/s^2 while the initial conditions are:

$$x_{t=0} = x_0; \dot{x}_{t=0} = 0; V_p = 0 \tag{2.51}$$

The waveform in figure 2.27(b) is chaotic while the strange attractor reveals that the motion follows an intrinsic law. The simulated result is plotted in figure 2.27(c). The consistency validates the accuracy of the model again. All the results in this figure are obtained without load connected.

As we can see from figure 2.19(e, f), the BSM generator exhibits a limit cycle motion for the forward sweep and chaotic motion for the reverse sweep at 17Hz. It means the BSM generator has multiple solutions at this position for the same excitation. The only difference is the initial condition which determines the oscillator going to the limit cycle or the chaotic motion. Figure 2.28(a, b) shows an example of the different displacement responses for the same excitation with varied initial conditions at 17Hz by simulation. It is also applicable for the case of the coexistence of inter-well and intra-well motion at 23Hz as indicated in figure 2.28(c, d). With the initial condition changed, the BSM generator stays at the high-energy inter-well orbit instead of the low-energy intra-well orbit. The initial conditions for these four cases are shown as follows:

$$x_{t=0} = x_0; \dot{x}_{t=0} = 0; V_p = 0 \ for \ (a) \tag{2.52}$$
$$x_{t=0} = x_0; \dot{x}_{t=0} = 0.1m/s; V_p = 0 \ for \ (b) \tag{2.53}$$
$$x_{t=0} = x_0; \dot{x}_{t=0} = 0; V_p = 0 \ for \ (c) \tag{2.54}$$
$$x_{t=0} = x_0; \dot{x}_{t=0} = 1m/s; V_p = 0 \ for \ (d) \tag{2.55}$$

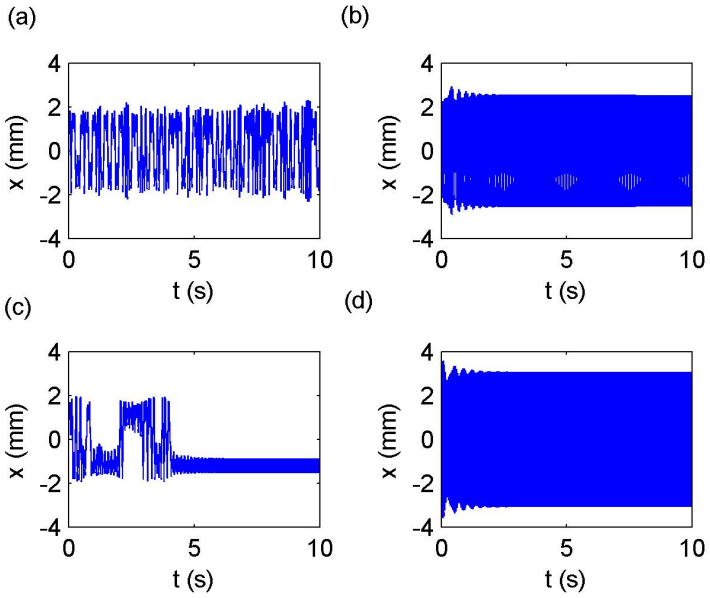

Figure 2.28: Simulation displacement responses for different initial conditions with the same excitation 3$\mathrm{m/s^2}$ *: (a) chaotic motion at 17Hz; (b) Inter-well limit cycle at 17Hz; (c) Intra-well limit cycle at 23Hz; (d) Inter-well limit cycle at 23Hz.*

Generally, for the nonlinear systems with multiple dynamic solutions, the one with the highest displacement response is desired for the purpose of maximum harvested energy. However, the initial conditions are not satisfied to have the good solution in many cases as shown for the cases of figure 2.28(a,c). It is interesting to find a method to let the nonlinear oscillator jump from the low-energy orbit to the high-energy one. A possible way is to apply a transient strong excitation [128] through an additional active structure which increases the complexity and the consumed power. Masuda et al. [21] theoretically investigated the method of switching between a passive resistive load and an active negative load to trigger the motion for high-energy orbit. Another potential approach is to change the potential barrier corresponding to the excitations.

2.5.3 Noise excitation

The behavior of the bistable oscillator in the case of arbitrary excitations cannot be inferred from the previous chirp analysis since it is a nonlinear system. Usual vibrations generally present non-stationary and wide-range vibrations components. The proposed bistable harvester behavior in the case of band-limited noise is then also to be studied to confirm its wideband characteristic. The load is selected to be matched at the characteristic frequency $R = 1/(\omega_0 C)$.

First, a band-limited noise (RMS 2 $\mathrm{m/s^2}$) with a cut-off frequency of 40Hz is used for numerical simulation. This band-limited noise is obtained by a standard white noise passing through a fourth order Butterworth low-pass filter. Figure 2.29 shows the voltage power spectrum responses of the BSM generator and its LEO. As we can see, the BSM has good performance over the low frequency range for the noise excitation as for the chirp excitation. Moreover, better results are also found for the BSM generator at the frequency higher than the LEO resonance frequency. It is considered to be induced by the feature that the voltage frequency is doubled when the mass crosses the potential barrier.

To detail the adaptive performance of the BSM generator for different noise excitations, the band-limited noises with varying cut-off frequencies are used for testing. In order to

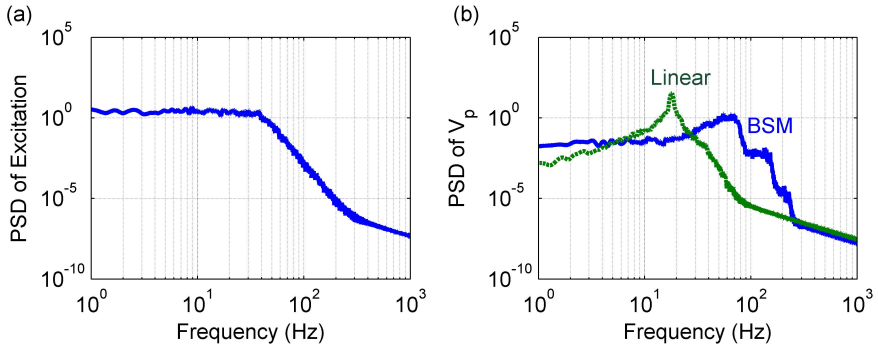

Figure 2.29: (a) PSD (Power Spectrum Density) of the bandlimited noise excitation for the simulation; (b) PSD of the piezoelectric voltage obtained from the simulation.

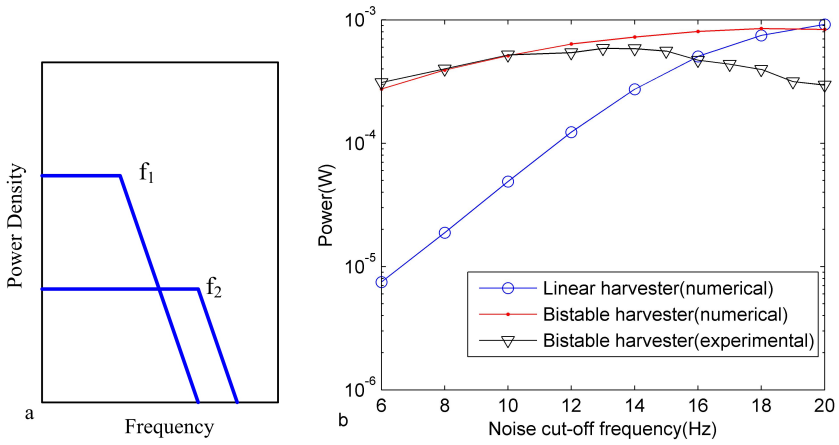

Figure 2.30: (a) Schematic figure of band-limited noise signals with varied cut-off frequency and constant RMS value. (b) Harvested power comparison between linear and bistable harvester for band-limited noise with constant RMS value (2$\mathrm{m/s^2}$ *).*

perform meaningful comparison, these excitation signals are weighted to present the same RMS value whatever their cut-off frequencies, as shown in figure 2.30(a).

In these conditions, numerical and experimental harvested power using the bistable harvester are given in figure 2.30(b) for a $2\mathrm{m/s^2}$ RMS acceleration. For comparison purpose, the harvested power from the LEO model is also given. It is clearly shown that the bistable harvester is able to efficiently scavenge power from the band-limited noise whenever the cut-off frequency is below f_0, the natural frequency of the LEO. However, if the noise band includes f_0, the LEO theoretically generates almost the same or even better power than the proposed bistable generator. It is in accordance with Halvorsen's results [136]. A good agreement between the experimental and simulation results is found again, even if discrepancies are exhibited at higher frequencies due to the additional filtering of the input signal by the shaker.

These results confirm the wideband characteristic of the proposed bistable harvester, especially for frequencies lower than the resonant frequency. It is useful for the cases in which the excitation spectrum varies a lot. The resonance frequency is not always inside the noise band.

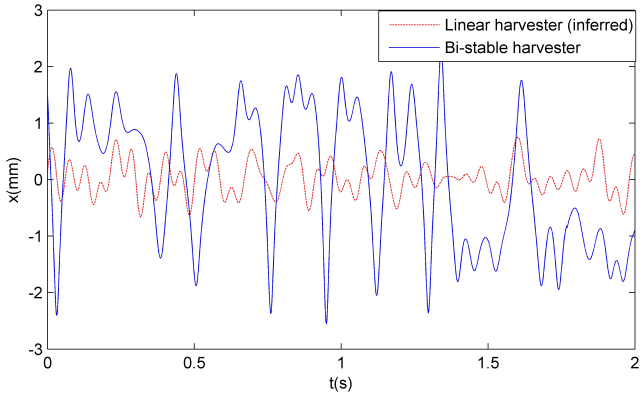

Figure 2.31: Displacement waveforms for a band-limited noise excitation with a cut-off frequency of 6 Hz.

The frequency-up conversion effect is also observed for the low-frequency noise excitations. Figure 2.31 shows the experimental displacement waveform from a band-limited noise excitation with a cut-off frequency of 6 Hz. The corresponding waveform of the LEO is also plotted for comparison. As we can see, much better response is obtained for the BSM generator. Especially, the jumps from one equilibrium position to the other bring higher voltage and the accompanied oscillations at the resonance frequency. As a result, much better performance is obtained.

2.6 Conclusion

Based on the buckling effect, a new BSM generator which is simple and compact has been proposed. With normalization performed for the developed analytical model, it is found to be only related to four dimensionless parameters (ω_0, k^2, ξ and ϵ) when geometry size L is determined. In order to get a quick and convenient tool for the initial understanding and evaluation of the BSM generator, harmonic balance analysis is performed to obtain the analytical solution. The influence of the parameters on the performance of the BSM generator is studied, providing important information for the subsequent numerical and experimental investigations.

A prototype of the proposed BSM generator has been realized and tested. Both chirp and band-limited noise excitations were used to investigate its performance and to compare it with the linear case. Numerical and experimental results show that it exhibits both large bandwidth and high power density. A maximum power of 16mW is obtained for a 0.3g chirp excitation and the corresponding power density is 0.33mW/cm^3 · This result is higher than most of the previously proposed bistable harvesters in the literature.

Experimental results are in good accordance with simulations. This agreement proves that the proposed model can be efficiently used as a predictive tool. A strange attractor of this BSM generator is observed during the experiment. It is found to be in accordance with the simulation. The effect of the initial condition on the final dynamic solution of the BSM generator is studied with the possible solutions discussed to obtain high-energy orbits.

3

Optimization and design of the BSM generator

Contents

3.1 Introduction

The BSM generator shows more benefits over linear approaches when the excitations are high enough to trigger the inter-well motion, which has been testified by previous studies with the chirp and noise excitations. To obtain good performance, it is then necessary to keep the BSM generator working within the inter-well dynamics. However, choosing a small energy potential saddle would tend to an ordinary mono-stable generator behavior while a high potential barrier would restrict the generator in a single well. As a result, the system parameters have to be optimized to get the desired properties.

Meanwhile, there are many constraints when a generator is to be designed for a specific application environment. For instance, the volume and the mass are usually limited in the case that the generator is used for body health monitoring. Another example is the strain or stress safety requirements which are important for those application environments in which very strong excitations may occur occasionally.

Considering that the model is able to provide accurate predictions of the BSM generator's dynamics, it hints that theoretical fundamentals have been prepared for the optimization. Therefore, an optimization strategy of the BSM generator parameters to achieve best performance is introduced and discussed in this chapter. The optimizing procedure is demonstrated for both chirp and noise excitations. Design considerations including the constraints are introduced for further investigations.

Due to the advancements of the MEMS technologies and the demand of portability and compactness, miniaturization of the sensing devices and components has become an important trend. It is a critical step for enhancing autonomous human mobility, monitoring and communication. As a potential power supplying solution for these applications, the same miniaturization requirement is applicable to energy harvesting devices. Consequently, developing a miniaturized generator with high power density and large operation band is a demanding issue.

For the autonomous wireless sensors, the power requirement is mainly driven by the consumption of the wireless transmitter. Depending on the application and the transmission rate, 10-100μW might be enough for most cases. Meanwhile, the available power of the generator decreases with the volume reduction. On one side, when the generator is designed at the MEMS scale (less than 1mm), its power output usually achieves the order of micro-watt which is sufficient for a lot of sensors integrated inside the same chip with low power requirements; On the other side, in many cases, it is more convenient if the generator can be used as an independent power source which is capable of interfacing with different devices. The realizations as standalone sources have good adaptabilities for different applications such as wearable devices, environment and health monitoring etc. Moreover, if the power is achieved at the order of milliwatt while the size is restricted in the centimeter scale as exhibited by many commercial products, it may provide more possibilities for many applications. Our goal is then to realize a miniaturized generator of this type.

3.2 Necessity for the optimization

With a given application environment or excitation, the performance of the generator is determined by different structure parameters, such as size, mass, coupling level, stiffness and so on. For linear generators, three critical normalized parameters can be concluded: the resonance frequency ω_0, the coupling level k^2 and the damping coefficient ξ [88]. Besides, the electric load is also necessary to be included with the harvesting interface circuits

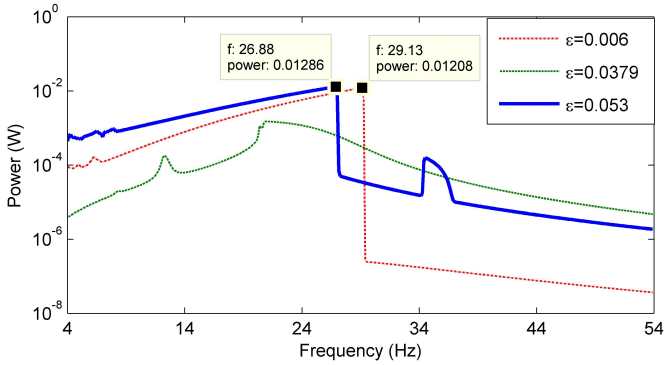

Figure 3.1: Numerical power responses of the macro BSM generator for different buckling levels.

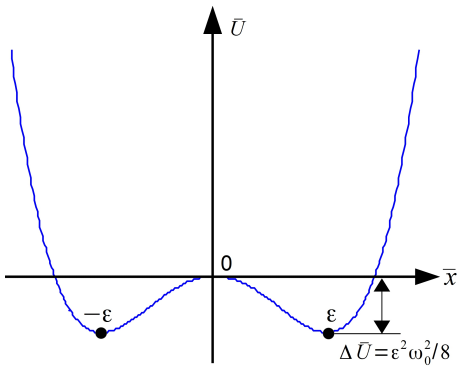

Figure 3.2: Potential curve of the normalized model of the BSM generator.

considered. When subjected to various applications, the normalized model can be scaled according to the specific size and mass.

Other than the parameters similar to the linear generators, the bistable generator has an additional one, the initial equilibrium position. For the BSM generator, it refers to the initial buckling level ϵ. Figure 3.1 shows the numerical power responses of the BSM generator prototype in chapter 2 for several values of ϵ with other parameters constant. The results are obtained for the applied forward sweep excitation (3m/s^2 , 4Hz-54Hz, 0.05Hz/s).

The optimal power response in figure 3.1 is obtained for a buckling level of $\epsilon = 0.0379$. As ϵ is tuned to a higher value, the potential barrier is too large to have the inter-well motions. In this situation, the BSM generator behaves as a softening oscillator while the power performance is poor for the forward excitation. When ϵ is tuned to a smaller value, the potential barrier is so small that the BSM generator is similar to a hardening oscillator. Although the maximum power is not decreased obviously in this case, the power response over the low-frequency range is getting worse, leading to weakened wideband properties.

Through this example, it is found that the performance of the BSM generator has strong dependence on the buckling level. This kind of dependence is also shown for the other critical parameters (ω_0, ξ, k^2). Thus, optimization on the BSM generator is necessary and meaningful.

3.3 Optimization strategy for the BSM generator

3.3.1 Critical parameters of the BSM generator

To provide a generic solution for the optimization, it is preferred to use the normalized model expressed by equation (2.9) and equation (2.10) which show that the power normalized by the mass is only related to four parameters for a determined excitation:

- Characteristic frequency ω_0 (natural resonance frequency for small excitation);
- Electromechanical coupling coefficient k^2;
- Mechanical damping ξ;
- Buckling level $\epsilon = x_0/L$;

As indicated in the harmonic balance analysis, better performance is obtained for lower mechanical damping and higher coupling level. Considering that k^2 is usually fixed for a selected piezoelectric component while ξ is related to the structure and the materials, the optimization is focused on ω_0 and ϵ with high-quality factor structures and high coupling piezoelectric materials assumed.

According to equation (2.9), we can write the normalized energetic potential expression as follows:

$$\bar{U} = -\frac{1}{4}\omega_0^2\bar{x}^2 + \frac{\omega_0^2}{8\epsilon^2}\bar{x}^4 \tag{3.1}$$

with the potential barrier calculated to be:

$$\Delta\bar{U} = \frac{1}{8}\epsilon^2\omega_0^2 \tag{3.2}$$

From the potential curve of the normalized model in figure 3.2, it is inferred that ϵ determines the distance of two potential wells while the potential barrier is related to the combined action of ω_0 and ϵ. The optimization of the parameters ω_0 and ϵ is to find the optimal potential curve for the generator.

3.3.2 Preset conditions

Since the excitations are variable, it is impossible to get a universal optimal generator for different situations. Optimizations have to be done for some specific requirements. Hence, some preset conditions have to be made as a start:

- First, the application environment is determined so that the optimization is feasible for a specific excitation.
- Second, the piezoelectric component is pre-selected according to the application requirements. As the optimization is focused on ω_0 and ϵ, a fixed electromechanical coupling level is a precondition.
- Third, the size L of the BSM generator is confined by the suitable volume for the application.

With all these predefined conditions, it is possible to approach a feasible and optimal generator.

3.3.3 Criteria

Before starting the optimization, a proper target needs to be selected. The target of the optimization may differ for different applications, especially for those with special requirements about transient peak power or voltage amplitude. One of the most used criteria is the power density which represents the available power per unit volume. In this work, this criterion is used with the optimization function expressed as:

$$f_{op} = \frac{1}{Power\ density} = f_{op}(power, Volume) = f_{op}(\epsilon, \omega_0) \tag{3.3}$$

The aim is to find the proper values of ϵ and ω_0 satisfying the power density requirement $f_{op} < f_{targ}$.

3.3.4 Procedure

With the model, the preset conditions and the criteria confirmed, an optimization strategy is then proposed. Figure 3.3 explicates the procedure. The excitation $\gamma(t)$ is determined by the specific application while the coupling level is related to the piezoelectric component selected to ensure the sufficient power output. According to the volume requirement, a trial value of L is chosen and an initial volume is estimated with the method introduced for the power density calculation last chapter. These parameters are used as the input to the normalized model which is constructed in the Matlab/Simulink platform to calculate the power performance.

By varying ω_0 and ϵ in a range related to the excitation spectrum, a minimal value of the optimization function $f_{op}(\epsilon, \omega_0)$ is found and compared with the target power density value. If this optimized value conforms to the requirement, we can determine the initial optimal parameters and step next to the design consideration; otherwise, another trial value of L is applied to start the optimization procedure again. When it is impossible to find the proper result to satisfy the requirements in some cases, the input parameters are to be modified by releasing the volume constraint or changing the materials (piezoelectric or structural) or decreasing the power density target.

3.4 Optimizations for two typical excitations

To have a sound idea about the influence of parameters on the performance, optimization is performed for two typical excitations: chirp and noise signals. With the absence of a specific application, the target of the power density is not clear in this case. Instead, a goal of finding the parameter configurations to get the largest harvested power is proposed for a given L. For simplification, the piezoelectric component is directly chosen from the transducers from the CEDRAT-Technologies© company. The APA50XS transducer ($k^2 = 0.169$) is considered as a good option to have a miniaturized generator of centimeter scale as the design object while L is selected to be 15mm. This size is determined for the purpose of providing the necessary space for the hinges while keeping the volume as small as possible. The specific design requirements of the hinges are to be explicated later.

3.4.1 Chirp excitation

With the preset L and piezoelectric component, investigations are firstly performed for a chirp signal (1g, 40Hz-120Hz). For an easy understanding, the optimization starts from a fixed ϵ but varied ω_0. Figure 3.4 shows the power responses for two selected buckling level $\epsilon = 0.018$ and $\epsilon = 0.033$ while $f_0 = \omega_0/2\pi$ changes from 20Hz to 120Hz. This selected

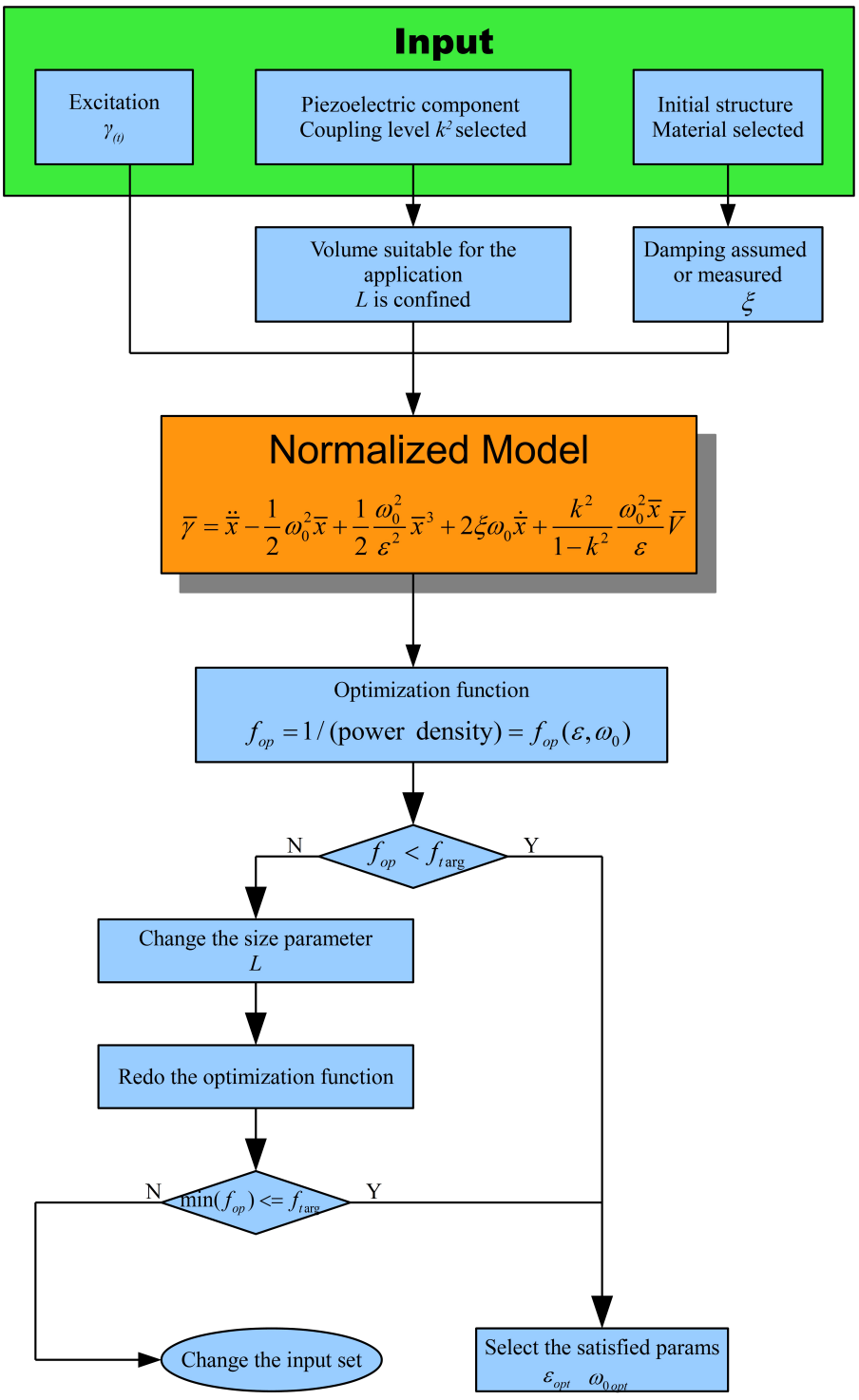

Figure 3.3: Optimization procedure of the BSM generator.

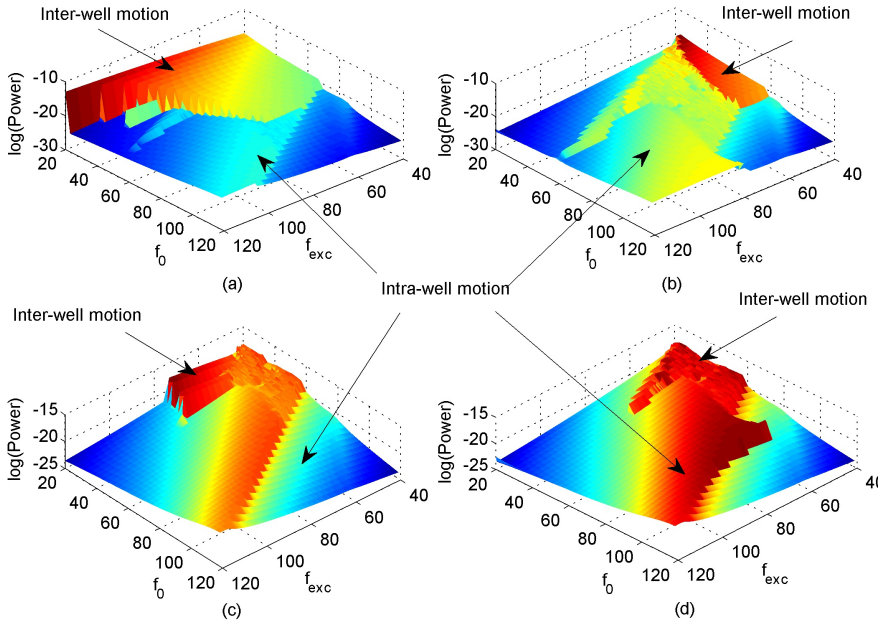

Figure 3.4: Power responses (unit: mW) in the case of 1g chirp excitation for a fixed ϵ and varied f_0 : (a) Forward sweep, $\epsilon = 0.018$; (b). Reverse sweep,$\epsilon = 0.018$; (c) Forward sweep, $\epsilon = 0.033$; (d) Reverse sweep, $\epsilon = 0.033$.

range is expected to include the possible favorable f_0 values corresponding to the excitation spectrum. According to the expression $\omega_0 = \epsilon\sqrt{K/M}$, the characteristic frequency can be changed by the mass M since K is determined by the piezoelectric component for a fixed buckling level. In the figure, f_{exc} represents the excitation frequency of the chirp signal.

As indicated by the forward sweep response in figure 3.4(a) for $\epsilon = 0.018$, the favorable results come from the inter-well motion area in the case of small f_0 values due to smaller potential barriers defined by equation (3.2) and larger mass. Along the simultaneous increase of f_0 and the potential barrier, the inter-well motion range is getting smaller. However, for the backward sweep response shown in figure 3.5(b) , there is an optimal f_0. Below this value, the inter-well motion range decreases with f_0 because of the nonlinear hysteresis property. Since the power response is much smaller for the reverse sweep, the performance optimization is mainly accounted for the forward sweep which determines the final average power value of the two cases.

When turning to figure 3.4(c)(d) for a buckling level of $\epsilon = 0.033$, it is found that the inter-well motion range shrinks dramatically. Higher ϵ constructs a larger barrier which limits the available inter-well dynamics. As can be seen in figure 3.4, whenever the oscillator is restricted to one of the two potential wells, the wideband properties is not as good as the case with inter-well motions. Therefore, a proper potential barrier needs to be chosen.

To overcome the potential barrier for the desired inter-well motions, another way is to increase the excitation amplitude. The power responses are presented in figure 3.5 with the same buckling levels but a higher excitation amplitude of $2g$. It is clear that the inter-well motion range is enlarged for all cases. Especially for the forward sweep case of $\epsilon = 0.018$ in figure 3.5(a), the inter-well motions are obtained for most of the f_0 and f_{exc} values. In this case, it is easy for the generator to cross the potential barrier. By comparing figure 3.5 (a) and (c), it is found that the power response for $\epsilon = 0.033$ is better in the case of low f_0 values than the one for $\epsilon = 0.018$, which suggests that a higher potential barrier is

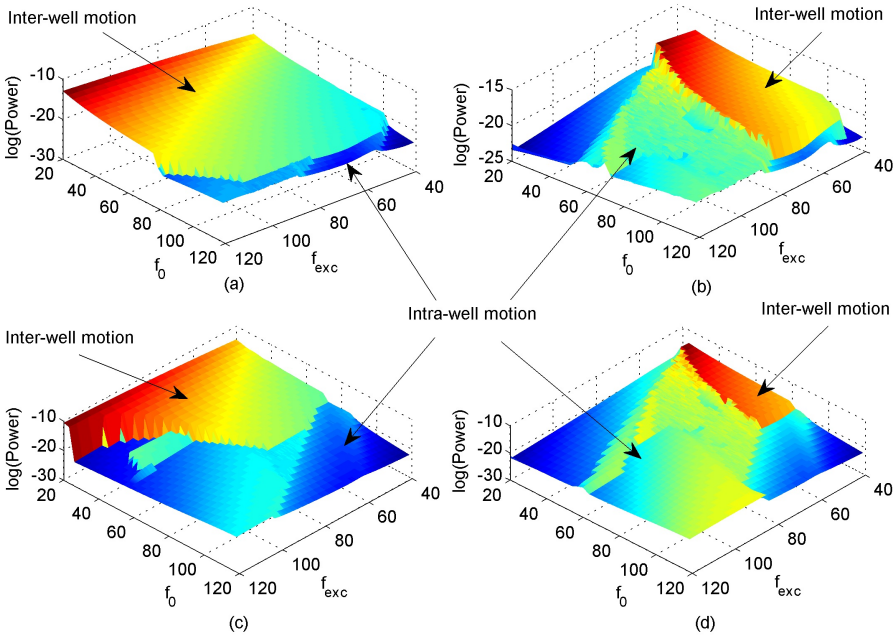

Figure 3.5: Power responses (unit: mW) in the case of 2g chirp excitation for a fixed ϵ and varied f_0 : (a) Forward sweep, $\epsilon = 0.018$; (b). Reverse sweep,$\epsilon = 0.018$; (c) Forward sweep, $\epsilon = 0.033$; (d) Reverse sweep, $\epsilon = 0.033$.

more suitable for the increased excitation.

The investigations are further performed for both ϵ (0 – 0.08) and f_0 (20Hz – 120Hz) to search an optimal configuration. The concerned range is selected for the feasibilities of a bistable generator. Outside this range, the constraint requirements are likely not to be satisfied. For instance, the mass is usually too large or too small to be installed or the displacement exceeds the value related to the maximum allowable deformation of the piezoelectric components and the hinge materials.

The average power over the total excitation frequency range is used for the performance merit figure. Figure 3.6 shows the average power over the total excitation frequency range for the chirp excitations of $1g$ and $2g$ in the case of a forward and reverse sweep respectively. It is found that the optimal parameters always lie at the lowest f_0 for the forward sweep and shift towards higher buckling level with the increased excitations. It is induced by the hardening effect of the bistable generator with inter-well dynamics. The lower f_0 promises a wider inter-well motion frequency range. In spite of this, the potential barrier requires to be well tuned by the buckling level ϵ together to get the best performance. For the reverse sweep, it is quite different and the optimal configuration is actually obtained when the BSM generator resides in one of the two potential wells. In this case, it can be considered as a mono-stable softening generator which has the favorable response for the reverse sweep. However, the dominant performance comes from the forward sweep as inferred by the optimal values of these two cases.

The optimization results in figure 3.6 are obtained with a fixed K and varied M. As we know from equation (2.10), the power is proportional to M so that the fairness is questionable. To exclude the effect of the mass, the average power normalized by the mass is shown in figure 3.7. Similar results are obtained.

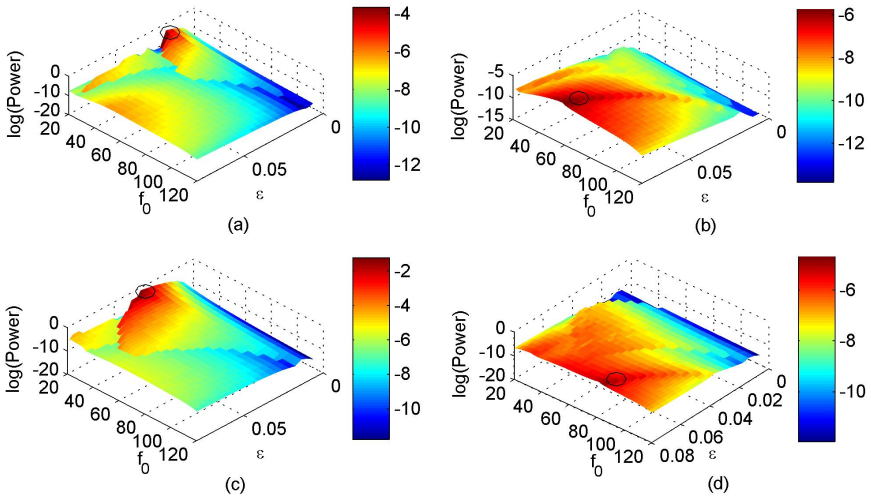

Figure 3.6: Average power (unit: mW) over the frequency range (40Hz-120Hz) for different ϵ and f_0 : (a) Forward sweep, 1g; (b). Reverse sweep, 1g; (c) Forward sweep, 2g; (d) Reverse sweep, 2g.

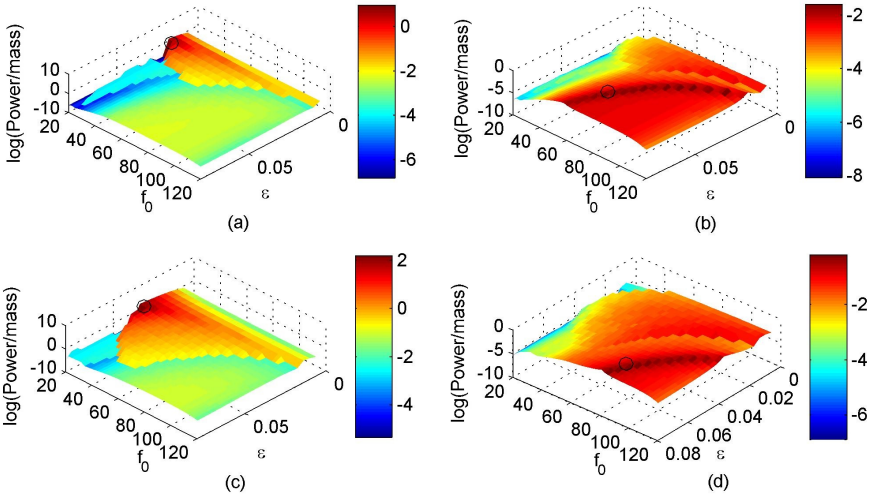

Figure 3.7: Average power normalized by mass (unit: mW/kg): a) Forward sweep, 1g; (b). Reverse sweep, 1g; (c) Forward sweep, 2g; (d) Reverse sweep, 2g.

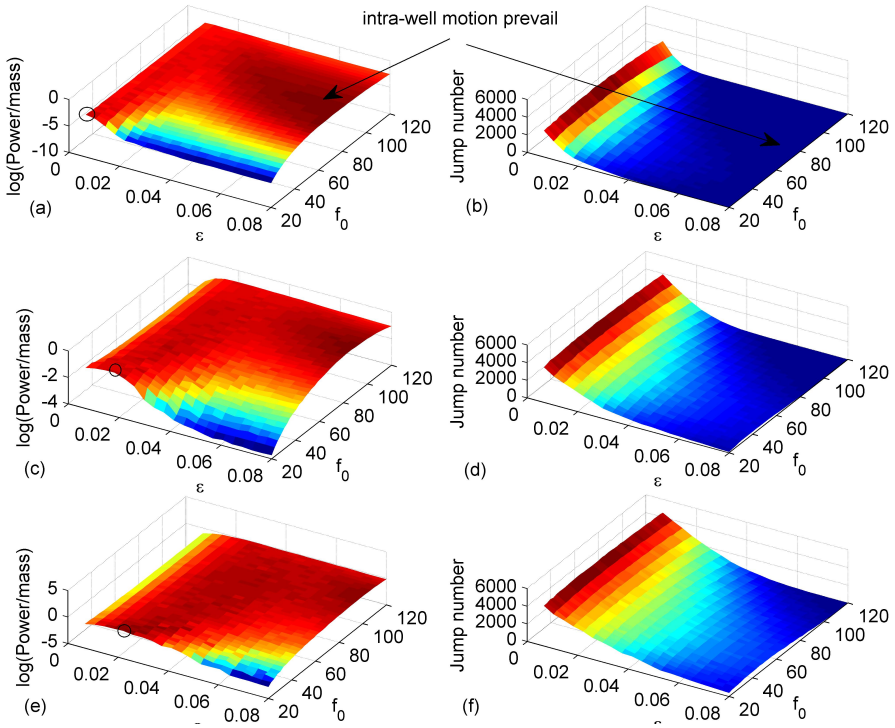

Figure 3.8: Average power normalized by the mass (unit: mW/kg) and the jump number for three different noise excitations: (a)(b) RMS 1g; (c) (d) RMS 2g; (e)(f) RMS 3g.

3.4.2 Noise excitation

The performance optimization about the noise excitations are also performed as shown in figure 3.8. Three different noise excitations are used with RMS values of $1g$, $2g$, $3g$ and the same band of 40–120Hz (white noise passing through two four-order Butterworth filters, 40Hz high-pass plus 120Hz low-pass). In the figure, only the average power normalized by mass is plotted for fairness consideration. The interesting information about the jump number between two wells is also presented in a duration of 50s.

Unlike the chirp cases, the performance of the bistable generators is relatively flat for the noise excitations. However, the optimal parameters are still located around relatively low f_0 values. The same trends as the chirp excitations are found that the optimal buckling level increases with the excitation amplitude.

Besides the optimal point at the left corner in figure 3.8(a), there is another high performance area corresponding to the intra-well motion prevailing cases, which can be distinguished from the jump number plot at the right. Only a few jumps are found in this area. Similar results are observed for figure 3.8(c) and (e). It has been discussed in [136] and chapter 2 that the linear generator with the resonance frequency inside the noise band shows better performance than the bistable generator. Considering that the inter-well motion is what we desire for the wideband response, the optimal points are determined in the areas with numerous inter-well motions.

It is noted that the performance decreases rapidly as the buckling level increases in the range of low f_0 values. The reason is that the increasing potential barrier limits the generator in a single well while f_0 is not in the excitation frequency range (40-120Hz). The benefits of the intra-well case as a softening generator do not take effect under this situation.

As expected and indicated in figure 3.8(b)(d) and (f), the jump number increases with the excitation strength. It is worthwhile to find that the inter-well jump number is more affected by ϵ than by f_0.

3.5 Design considerations about the BSM generator

3.5.1 Procedure with design constraints

With the optimal parameters defined from the optimization procedure, the generator gets to be designed. However, there are some considerations to be taken into account:

- The first one comes from the buckled condition. From equation (2.7), the equilibrium position can be rewritten as:

$$x_0 \approx \sqrt{2\Delta l' L - \frac{8K_\theta}{K}} \tag{3.4}$$

  in which $\Delta l' = l_0 - L$ represents the compressed deformation of the piezoelectric element at $x = 0$. Generally, it should be less than the maximum allowed value Δl_{max} of the component which is related to the allowable stress or strain. Equation (3.4) implies that the buckled condition is only satisfied when $2\Delta l' L - 8K_\theta/K > 0$ and $\Delta l' < \Delta l_{max}$. It means that K_θ has to be limited under the value $K\Delta l_{max} L/4$.

- The second constraint to be accounted for is the safety requirement. When subjected to excitations, the induced max stress in the hinges should be less than the security stress. Then we have

$$\sigma_{max} < \sigma_{safe} \tag{3.5}$$

  The displacement response of the generator is then restricted inside this stress range. Otherwise, the generator would be damaged.

- In addition, the volume requirement mentioned before is another important issue to be checked.

- Finally, other special requirements determined by the applications may have to be included.

Thus, an additional procedure after the process in figure 3.3 is compulsory to contain the design constraints. The output of the optimization requires to be verified in the subsequent process shown in figure 3.9 .

The process goes as follows:

- After optimization, the parameters which meet the power density requirement are selected.

- According to the selected values of ϵ and ω_0, an initial shot of M and K can be determined for the verification of the volume requirement. If the volume is suitable, M and K are used for other constraints under which the possible K_θ values are given.

- Then an analytical model of the flexible hinge is used to determine the design parameters under the safety stress constraint. When there is any satisfied design, the final K_θ values are used in the model for check again. If there is no design available or the check fails, other possible values of ϵ and ω_0 are tried with the same process.

- In the end, a desired design is found; otherwise, the input set of the optimization needs to be reconsidered to get a converged solution.

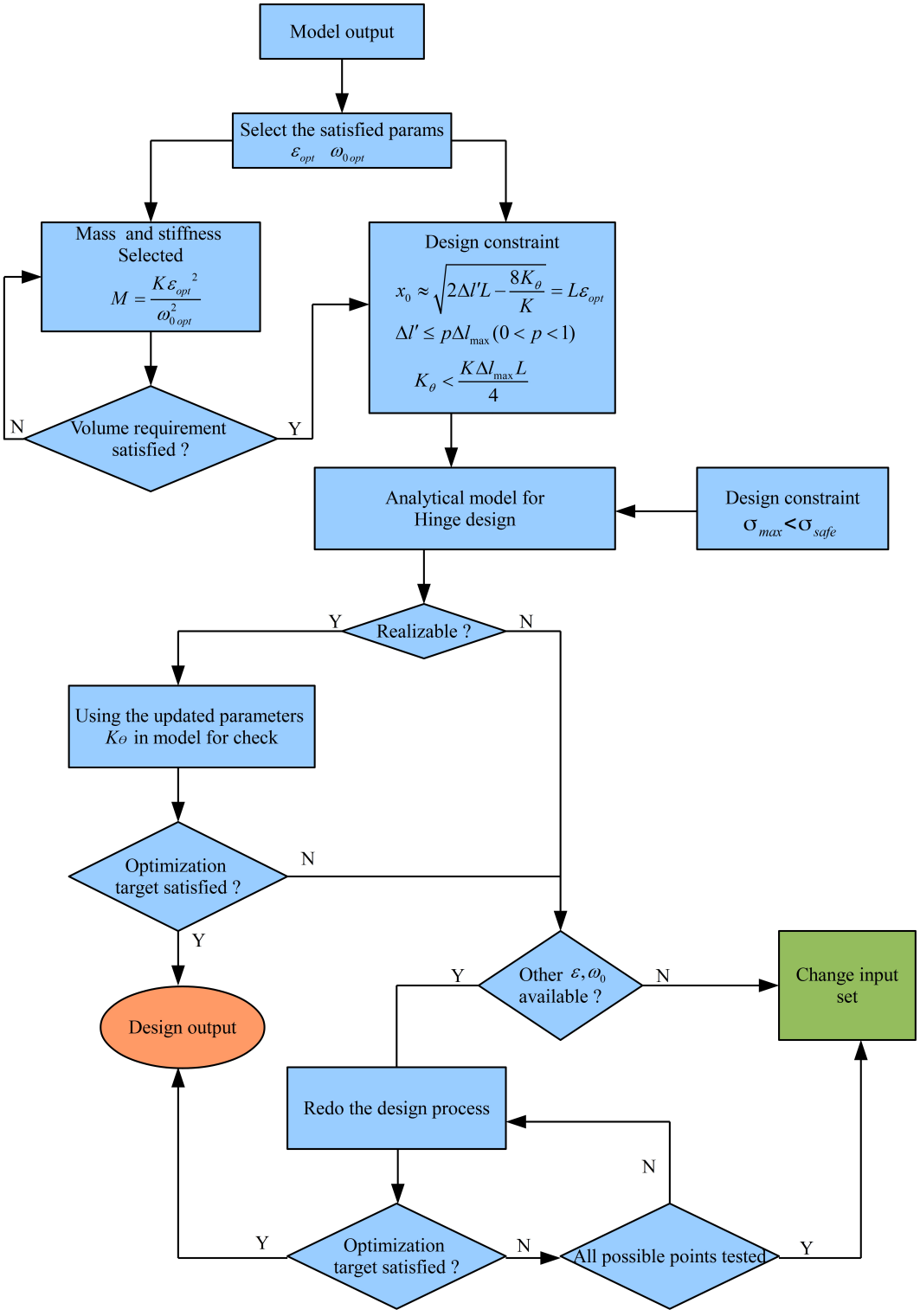

Figure 3.9: Complement design process after the optimization.

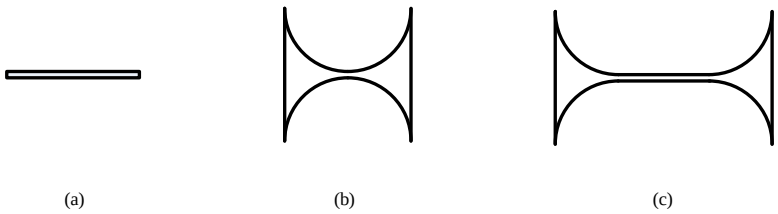

Figure 3.10: Three usual flexible hinge types: (a) Rectangular; (b) Circular; (c) Corner-filleted.

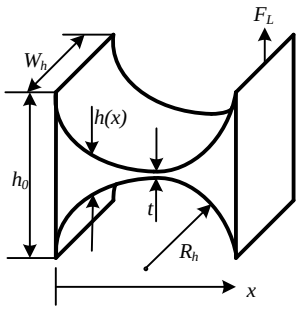

Figure 3.11: 3D plot of the hinge and its design parameters.

3.5.2 Hinge design

From the discussions above, it is found that the hinge plays an important role in the design of the BSM generator. As the safety requirement indicates, the hinge rotation angle is limited by the allowed stress of the hinge materials, and then we have:

$$\theta \approx \frac{x}{L} \leqslant \theta_{safe}(\sigma_{safe}) \tag{3.6}$$

Obviously, the maximum displacement is limited by the available rotation angle which is related to the allowed stress of the material. A reliable hinge with qualified stiffness is necessary and critical for the performance.

Some of the usual flexible hinge structures are shown in figure 3.10. The simplest one is the rectangular hinge in the form of a beam. The second one is the circular hinge with the cross rectangular section. This type has been used for the prototype in chapter 2 with a circular cross section which is not the usual case. Another one is the corner-filleted hinge which is the combination of the former two types.

The circular type is further investigated while the rectangular and corner-filleted type can be analyzed in a similar way. The parameters are shown in figure 3.11 where F_L represents the load force and L_h is the length of the hinge. The thickness of the hinge $h(x)$ is expressed as:

$$h(x) = 2\sqrt{R_h^2 - (x - L_h/2)^2} + t \ (0 \leqslant x \leqslant L_h = 2\sqrt{R_h(h_0 - t) - (h_0 - t)^2/4}) \tag{3.7}$$

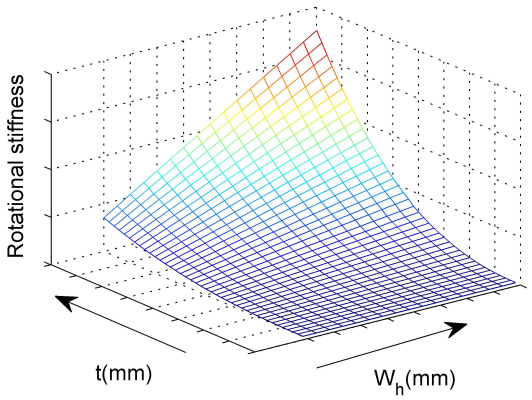

Figure 3.12: Rotational stiffness versus t and W_h.

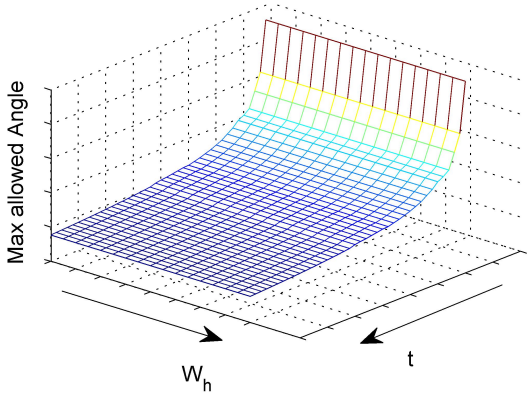

Figure 3.13: Max allowed angle versus t and W_h.

Then the static equilibrium equation is written as:

$$\frac{E_h W_h}{12}\frac{d^2}{dx^2}(h(x)^3\frac{d^2y}{dx^2}) = 0 \tag{3.8}$$

$$\frac{d}{dx}(h(x)^3\frac{d^2y}{dx^2})\mid_{x=L_h} = F_L, y(0) = 0, \frac{dy(0)}{dx} = 0 \tag{3.9}$$

in which $y(x)$ is the deflection of the hinge.

It is assumed that the rotary center is located at the thinnest position $x = L_h/2$ and the angle of rotation θ is linearly related to the moment $M_h = L_h F_L/2$. As a result, the rotational stiffness can be calculated by:

$$K_\theta = \frac{F_L L_h}{2\theta} = \frac{F_L L_h^2}{y(L_h)} \tag{3.10}$$

with the equations (3.8-3.9) solved for the given F_L. Since R_h and h_0 are usually fixed for the size requirements of the hinges, it is more interesting to investigate the influence of the width and the thickness at the rotation center. Figure 3.12 shows the evolution of the rotational stiffness versus t and W_h. The arrows in the figure indicate the increasing direction of the parameters. It is logical to find that low K_θ is obtained for small thickness and width.

Since the largest deformation is situated at the rotary center $x = L_h/2$, the corresponding maximum stress in the hinge can be estimated with the thickness t and the moment

M_h:

$$\sigma_{max} = \frac{M_h t}{2(W_h t^3/12)} \tag{3.11}$$

which requires to satisfy equation (3.5).Then with the given safety stress of the material, the applicable maximum moment is determined and so is the allowable rotation angle as present in figure 3.13. It is seen that the max allowed angle is only related to t and not dependent on W_h. The thinner is the hinge, the larger is the allowed angle.

With the developed model for the hinge, it is possible to select the proper parameters for the required design. Moreover, when used in the BSM generator, it is worth noting that the axial stiffness of the hinge should not be neglected in the case that its stiffness is comparable with the piezoelectric transducer. It is especially important for the hinges made of soft materials. This effect has been pointed out for the BSM prototype device in chapter 2. In addition, a final stress validation of the design is proposed to be performed with the FEM (Finite Element Method) software.

3.5.3 A design and optimization example

An example of the optimization with design constraints contained is introduced to explicate the design procedure. The assumed requirements and conditions are listed to be:

- External excitation: Forward and Reverse sweep; Amplitude 1g; Frequency range 40-100Hz.
- Maximal volume: 5 cm^3.

With the same approach explicated in section 3.3, the transducer APA50XS (Length: 12.8mm, Height: 4.7mm, Width: 9mm, $k^2 = 0.169$) [141] has been chosen as it matches the volume requirement while L is still selected to be 15mm. According to former testing results, the damping factor ξ is assumed to be 0.025. Stainless steel material is used for the hinges and the mass. The circular hinge structure with a rectangular cross section is assumed here.

As an output of the optimization process, the power density (average value for both forward and reverse sweeps) for different parameters is plotted in figure 3.14. It is obtained without any constraints. With volume and stress constraints added in the complement process, the power density for those points which do not satisfy the volume and safety requirements is set to zero. When all constraints are met, the optimal parameters (x_0=0.35mm and M=4.76g) are obtained to get the maximum power density as indicated in figure 3.14(c). The maximum average power density is 0.436mW/cm^3 for a total volume of 4 cm^3. The corresponding average power is 1.75mW which is an applicable value for a lot of wireless sensor nodes.

3.6 Design of the miniaturized mono-block BSM generator

With the optimization strategy used and the design constraints taken into consideration, an optimized BSM generator which uses the design for the independent power source utilization is fabricated from a mono-block steel material with the knowhow of the CEDRAT Technologies© company. However, because of the real design limitations from the fabrication and materials, the obtained generator is slightly different from the optimization results presented in last section.

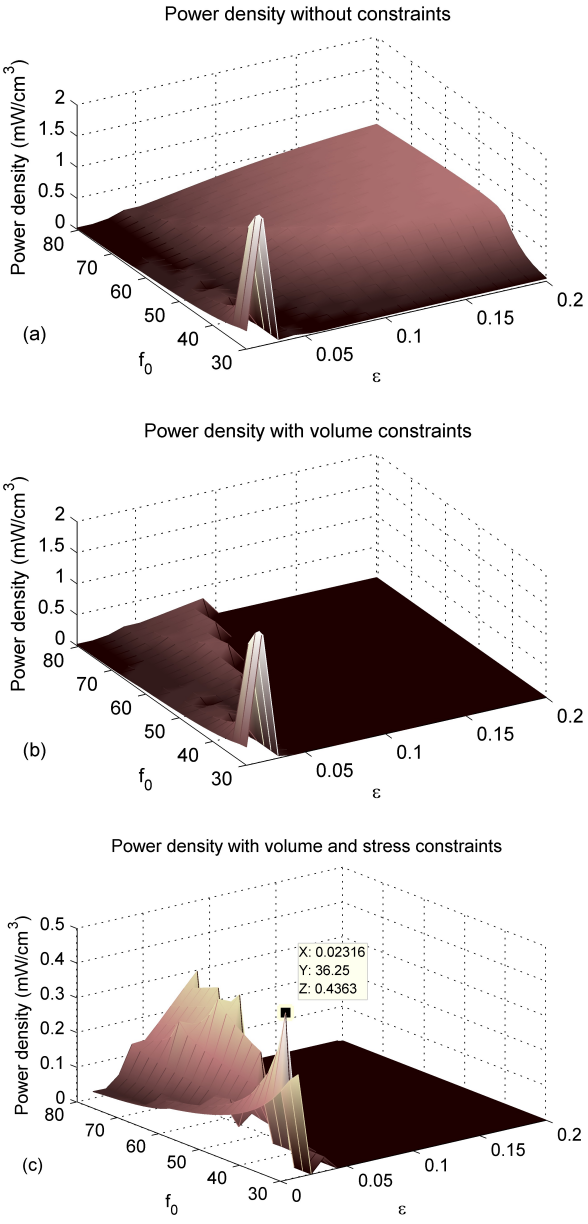

Figure 3.14: Available power density: (a) No constraint; (b) Volume constraints included; (c) Volume and stress constraints included.

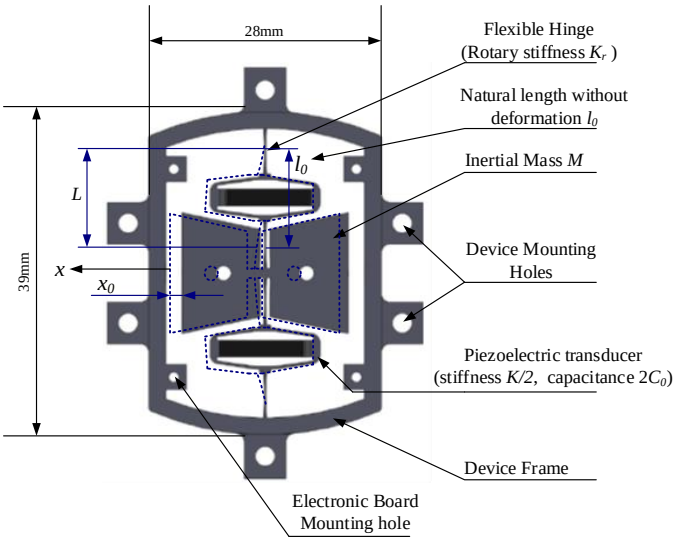

(a)

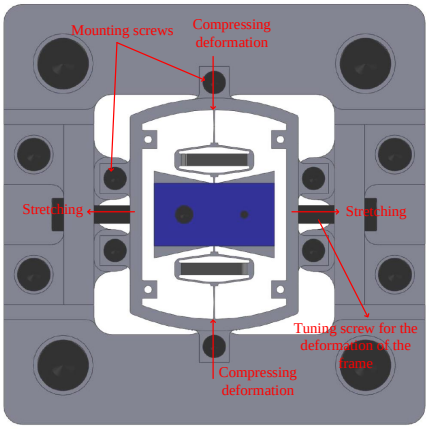

(b)

Figure 3.15: (a) Miniaturized mono-block BSM generator; (b) Assemble platform for initial buckling position tuning and clamping.

3.6.1 Design principle

The CAD plots of the developed miniaturized design and its assembly platform are shown in figure 3.15. It is based on the BSM generator scheme with a unique mono-block design which allows the compactness and reliabilities to be optimized.

Four circular flexible hinges with a large radius of 34.5mm are used instead of the ones with a small radius in the first prototype. This large radius value makes the circular hinges look like rectangular beams. The hinge design is to satisfy the requirements of safety and low stiffness analyzed before and to provide higher allowed rotational angle with the same thinnest thickness at the rotation center. Consequently, the beam-like hinges promise higher displacement responses than the ones with a small radius before getting damaged.

An inertial mass is connected to the hinges with a narrow joint at the center position of maximum displacement. The gap between the two parts is selected to avoid the shock during the motions and maximize the mass. Two elliptical shapes in the structure are

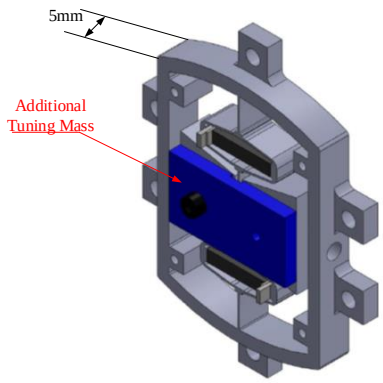

Figure 3.16: 3D CAD plot of the mono-block generator.

used to amplify the force on the piezoelectric stacks which are mounted under a pre-stress condition. The allowed compress deformation of the piezoelectric transducer is then limited by the pre-stress value. As usual piezoelectric stacks, the interdigitated electrodes are separately connected to the positive and negative poles.

The buckling procedure is described hereafter: Before operations, the screws in the mounting holes are loose and the device is under free conditions. The assembly platform allows the deformation of the frame to be tuned by the pulling action of two dedicated screws as shown in figure 3.15(b). The stretching deformation along the tuning screws induces the compressing deformation perpendicularly. As a result, the device is statically set to a chosen buckled position and the mass then moves from the center position to a new equilibrium position as indicated by the dashed line in figure 3.15(a). Finally, six screws in the mounting holes are tightened to keep the frame deformation unvaried during operation. The tuning screws can then be removed. Although the mono-block BSM generator shown in figure 3.15 is mounted on the assembling platform, it could be fixed directly to the application surface with a redesigned assembling platform whose inner square hole could be enlarged. The mono-block BSM generator could then be placed totally inside. After tuning and fixing the generator on the application surface, the assembling platform could then be removed.

3.6.2 Auxiliary considerations

Besides the realization of the most important functions for a BSM generator, some complement points about the design are also to be noted:

- First, four electronic board mounting holes are drilled on the generator for easy future integration with the interface circuit;
- Second, after the buckled position is fixed by the mounting screws, the tuning screw positions can be utilized by either elastic stoppers to protect the device from excessive displacement responses or guiding screws to prevent undesired mode;
- Finally, since the harvested power is proportional to the mass, the power level can be improved with additional weight as shown in figure 3.16.

3.6.3 Modal analysis

To investigate the possible modes of the mono-block generator, analysis is performed with the CAD software tool Solidworks©. First, the static buckling modes of the first

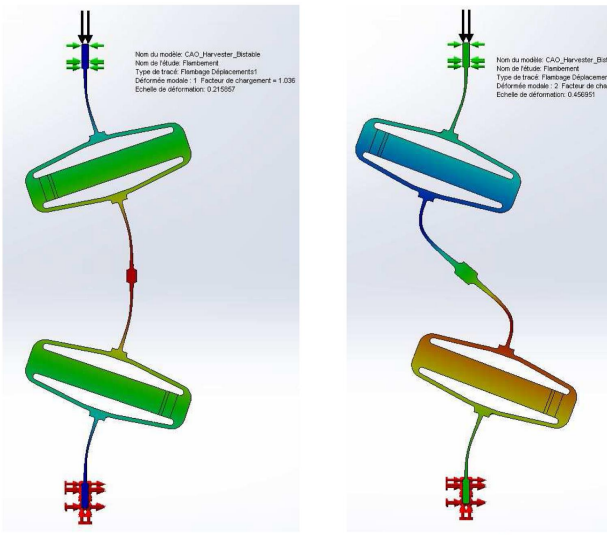

(a) (b)

Figure 3.17: Buckling modes: (a) The first buckling mode (similar shape of the transversal vibration mode); (b) The second buckling mode (similar shape of the rotation vibration mode).

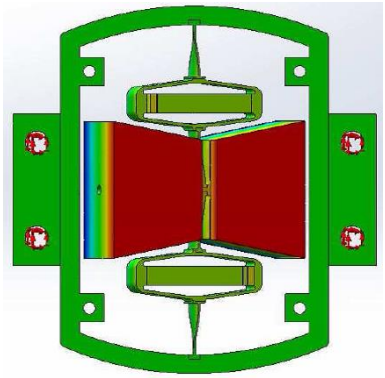

Figure 3.18: Out-of-plane mode.

two orders are investigated as shown figure 3.17. According to the analysis in [142], the critical load for the occurrence of the first buckling mode is much less than high-order buckling modes. Meanwhile, the first buckling mode of desire is stable while the second one is unstable [142]. It is more likely for us to have the desired buckling configuration.

To some extent, these two static buckling modes have the similar shapes of the possible post-buckling in-plane vibration modes of the structure, which we call the transversal mode and the rotation mode respectively. Beside, another out-of-plane vibration mode is demonstrated in figure 3.18.

For the desired transversal vibration mode in figure 3.17(a) , the mass vibrates in phase with the piezoelectric transducers. Identical strain is produced in the stacks, leading to the same voltage.

Regarding the rotation mode in figure 3.17(b), two piezoelectric components are out-of-phase. It is worth noting that in this mode, the mass always approaches close to the two transducers, possibly inducing a shock easily because of the narrow space between them. Generally, the existence of this mode is low with the excitation in the transversal direction and with characteristic frequency of this mode much higher than the excitation spectrum.

Parameter	Value	Parameter	Value
M(g)	9	L(mm)	11.17
K(N/m)	4.6e5	x_0(mm)	0.43
C_0(µF)	0.104	α(N/m)	0.041
μ(N/(m/s))	0.071	R(kΩ)	34
K_θ (Nm/rad)	0.016		

Table 3.1: Parameters for the mono-block BSM generator.

However, since the hinges are soft with low rotational stiffness while the joint between the mass and the hinges is narrow, it is likely to be excited in some cases, especially when the excitation deviates from the assumed direction or the structure is not very symmetric. Anyway, it is necessary to avoid this rotation.

Another mode needed to be restricted is the out-of-plane rotation as explicated in figure 3.18. In most cases, the out-of-plane rotation is suppressed by the hinge's high torsion stiffness. Nevertheless, it is still easy to be excited if the mass is not balanced. Because the pursuit of low rotation stiffness makes the hinges extremely thin but lowers the torsion stiffness simultaneously, the out-of-plane rotation mode frequency may fall into the interested frequency range. Therefore, much care is required for balancing the additional mass.

3.6.4 Performance investigation

According to the design principle, a mono-block generator is fabricated as shown in figure 3.19 . The total volume of the device is calculated to be 5.46cm^3 with the dimension annotated in figure 3.15 and figure 3.16 (39mm×28mm×5mm).

The generator is firstly tuned to the desired buckled position and then fixed. After that, the generator is placed on the shaker for tests. The two piezoelectric transducers in the structure are serially connected to increase the output voltage. The total capacitance C_0 is measured to be 0.104µF while the inertial mass M is calculated to be 9 grams. With x_0 tuned to 0.43mm, the piezoelectric force factor α (0.041N/m) corresponding to coupling coefficient $k^2 = 0.034$ and the stiffness of the transducers K (46000 N/m) are estimated in the open-circuit and short-circuit cases for small harmonic excitations. For simple characterization, a pure resistor is used as the load. According to the measured characteristic frequency $\omega_0 = 283.4$ rad/s, the value of the load resistor is selected to be $R = 1/(C_0\omega_0)$=34 kΩ. The parameters are listed in table 3.1.

Chirp excitations

To investigate the wideband properties and the harvesting performance, a chirp excitation (amplitude 6m/s^2 , 15Hz-66Hz, rate 0.05Hz/s) is applied to the mono-block device. The numerical and experimental displacement responses are consistent as shown in figure 3.20. A little disagreement at the low frequency range is found that the generator resides inside one potential well. It is induced by the slight asymmetry of the structure with the effect of the wires and the imperfect tuning. The two stable position are not perfectly symmetric.

The red dashed lines in the figure represent the allowed maximum displacement response (1.2mm) which is determined by the safety stress of the steel materials used for the

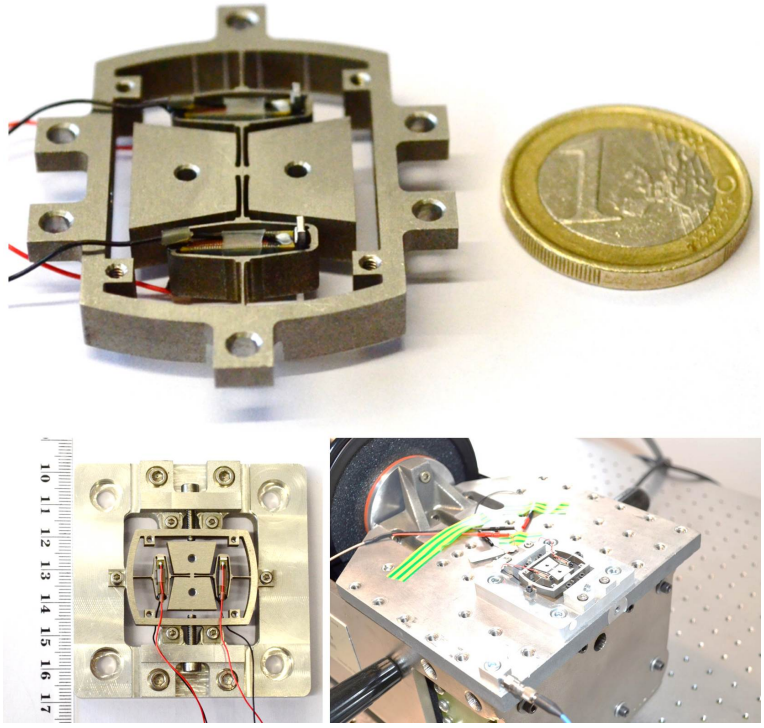

Figure 3.19: Fabricated mono-block generator and the assembly platform.

hinges. Hence, the displacement response has to be restricted inside the range between the two red lines. Otherwise, the hinges are inclined to be damaged. It is always satisfied for the reverse sweep responses in figure 3.20 (b) and (d). However, this value is approached as the forward sweep excitation is close to 66Hz. The test is then stopped for safety purpose as indicated in figure 3.20(c). For real applications, protective elastic stoppers are suggested to be added using the tuning screw location when removed so that the generator can be used for much larger excitations and higher sweep excitation frequencies.

From the corresponding power responses presented in figure 3.21, a maximum power of 2.64mW is obtained at 66Hz for the forward sweep. Using the calculated volume, the corresponding power density is 0.483 mW/cm^3. With the excitation normalized to $10m/s^2$ as performed in chapter 2, the value is $1.34mW/cm^3$, which is much higher than both the linear piezoelectric generators reported in [37] and most of the bistable generators. However, it is less than the first prototype for the coupling level k^2 of the miniaturized prototype is much less. It is interesting to find that the experimental power is getting higher than the numerical results at the high frequency end. This is probably due to the imperfect pre-stress condition of the piezoelectric stack. As the strain increases, the coupling level k^2 is increased since the piezoelectric components are well deformed.

Meanwhile, the wideband properties of the device are also validated as the average power for the forward sweep is more than 0.32mW over a frequency range of 30Hz as shown by the results in figure 3.21. Regarding the backward sweep, a maximum power of 0.32mW is harvested and more than 0.10mW is obtained over a frequency range of 13.6Hz.

Band-limited noise

A band-limited noise excitation has been also used to evaluate the performance of the generator. The selected excitation is generated using a Butterworth low pass filter with a cut-off frequency of 40Hz with the RMS value of 4.5 m/s^2. Figure 3.22 shows the excitation

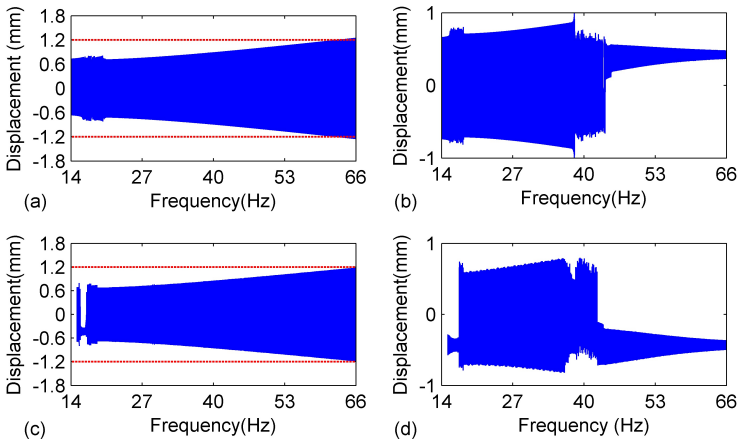

Figure 3.20: Displacement responses of the mono-block BSM generator for a 6$\mathrm{m/s^2}$ *chirp excitation: (a) Forward sweep, simulation; (b) Reverse sweep, simulation; (c) Forward sweep, experiment; (d) Reverse sweep, experiment.*

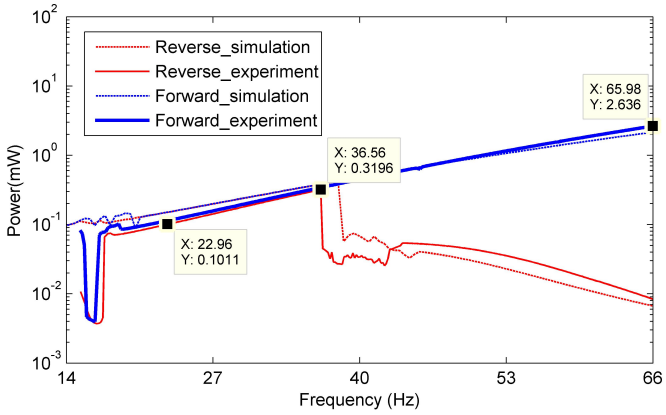

Figure 3.21: Power responses of the mono-block BSM generator for a 6$\mathrm{m/s^2}$ *chirp excitation.*

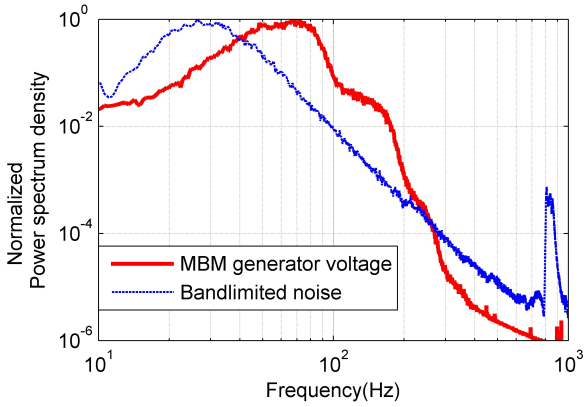

Figure 3.22: Spectrum of the noise and the ensuing mono-block BSM generator voltage.

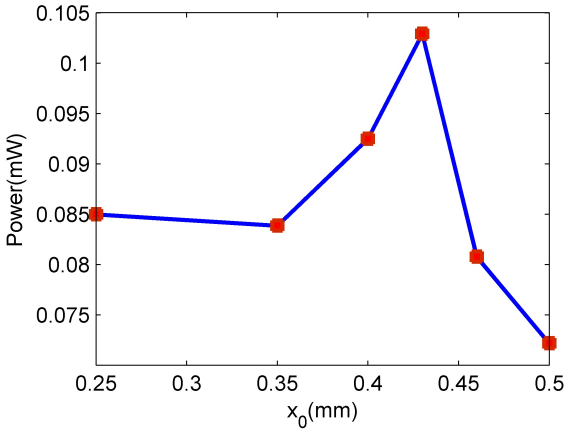

Figure 3.23: Power versus the buckling level.

spectrum and the voltage power spectrum density underlining the wideband response of the device. An average power of 0.103mW is obtained for this noise excitation.

To investigate the influence of the buckling level x_0 on the performance, the average harvested power for different x_0 values is presented for the same band-limited noise excitations. The results in figure 3.23 display an optimal value of the buckling level. It is in accordance with the optimization analysis. Small values of x_0 do not allow the advantages of the bistable generator to be exploited and the results are close to a non-optimized linear generator; Too large values of x_0 cancel the benefits of the bistable structure which has less chance to exhibit the inter-well motion.

Real excitations from the wheel of a driving car

To give further insights into the potential application of the miniaturized BSM device in a real environment, an acceleration signal acquired from a driving car wheel (figure 3.24) [22] (authorized from the NiPS lab, University of Perugia) is replicated by the shaker. For this real excitation signal, an optimal buckled position also exists as shown in figure 3.25. From figure 3.23 and figure 3.25, it is inferred that proper buckled position needs to be tuned to have the optimal performance for a determined excitation.

The displacement and voltage waveforms are shown in 3.26. As can be seen in the figure, the snap-through jumps between two equilibrium positions bring higher voltage, which enhances the harvested power. This feature also enlarges the operation bandwidth

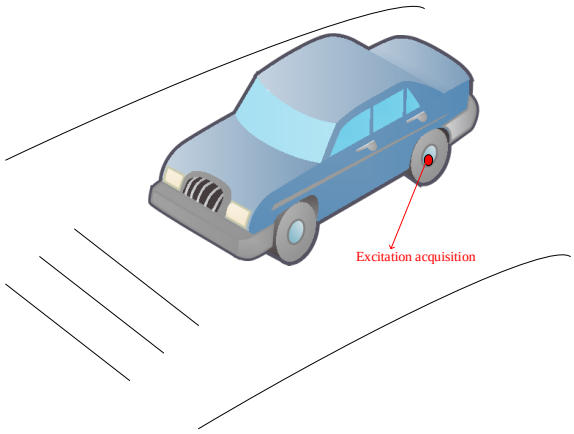

Figure 3.24: Excitation acquisition from the wheel of a driving car.

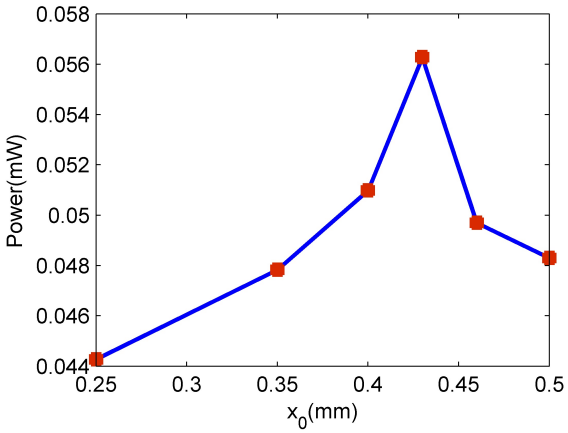

Figure 3.25: Power versus the buckled position for the excitation of the car wheel.

as indicated by the spectrum of the excitation and the piezoelectric voltage (x_0=0.43mm) in figure 3.27. Comparing figure 3.22 and figure 3.27, it is clear that the "real excitation" of the car wheel is spread over a much wider frequency range than the band-limited noise used previously. Therefore, the potential energy located in the high frequency range, which exceeds the frequency range of the mono-block BSM device cannot be harvested. However, the wideband characteristics are still obvious and an average power of 0.056mW is obtained with an RMS acceleration value of 0.7g, corresponding to a power density of 10.2 $\mu W/cm^3$. It is capable of providing the needed power for low-power sensors such as the ones presented in [143].

Future improvements

During the testing operations of the mono-block BSM generator, some problems are observed:

- Out-of-plane rotations are found when the additional mass is only added to the top of the original mass. Since the mass balance is broken in the case of low torsion stiffness, this undesired effect is induced. It increases the threshold for the inter-well motions. Fortunately, the phenomenon disappears with the mass rebalanced.

- In-plane rotations exist in some cases, leading to the contact between the mass and

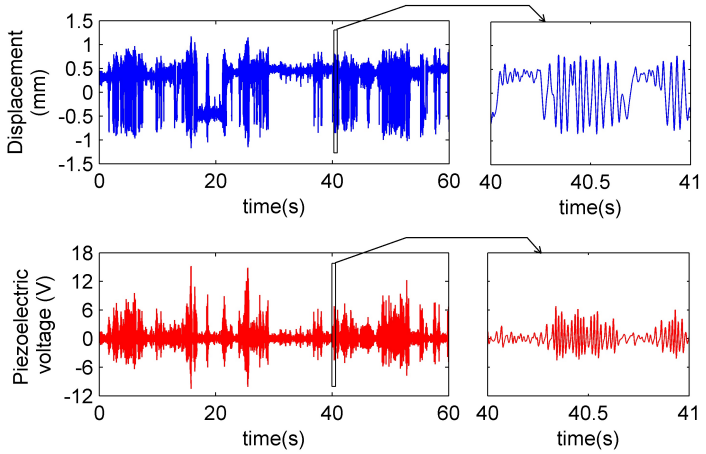

Figure 3.26: Displacement and voltage waveforms for the car excitation signal.

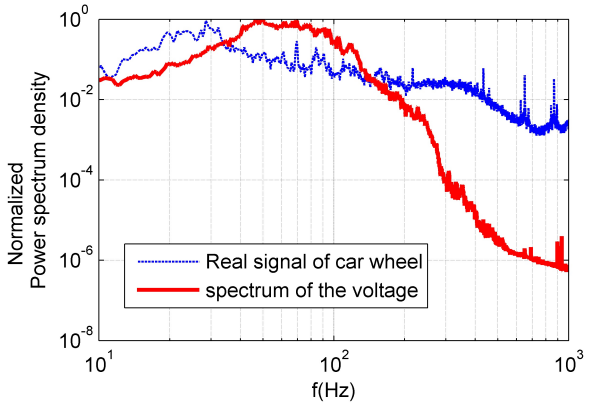

Figure 3.27: Spectrum of the replicated car excitation and the ensuing mono-block BSM generator's voltage.

the piezoelectric components. As a result, the inter-well motion ends earlier than expected. Improvements about the symmetry may fix the problem.

- The coupling level k^2 is lower than the designed value due to the imperfect pre-stress condition.

With the concerned problems overcome, better performances are expected, including higher power output and more stable inter-well dynamics.

3.6.5 Demonstration with an autonomous sensor node

Considering that the final aim of energy harvesting is to be used as a substitutive and sustainable power source, it is interesting to study the performance of the proposed mono-block generator when used in an autonomous sensor node. A demonstration platform of the wireless sensor network is then developed.

Power conditioning unit

To provide the harvested energy of the generator for an autonomous device, the power conditioning unit acts essentially as an interface. Generally, it contains two parts: the interface circuit and the voltage regulation.

The interface circuit which has been discussed in chapter 1 with some typical techniques is used to convert the alternative energy to DC energy. The nonlinear circuit is strongly recommended when the figure of merit k^2Q_m is much less than unit [7]. As k^2Q_m approaches one, investigations show that the standard circuit provides similar or even better performance than nonlinear approaches. Here, the value of k^2Q_m is calculated to be 1.13. Therefore, the standard interface circuit is selected.

The output of the interface circuit varies for different vibration level, thus possibly higher or lower than the designed load voltage in most cases. To provide a stable voltage supply so that the node can work normally, a regulation unit is required to adapt the output of the interface circuit to the load. Obviously, a good power conditioning unit is important for utilizing the harvested energy efficiently and enhancing the performance of autonomous system. Due to the increasing attention on the energy harvesting technique, a lot of commercial products for power conditioning are now available. LTC3588-1 from Linear Technology©is a good choice among them. As shown in figure 3.28, it includes a standard rectifier and a DC-DC buck block to convert the high voltage (required to be less than 20V) to a desired fixed low voltage (1.8V, 2.5V, 3.3V, 3.6V) .

In order to stand the fluctuations of the stored voltage, a special hysteresis loop is designed for the output voltage: The output is initially enabled as the stored voltage exceeds a certain high threshold and then disabled as the stored voltage drops below a certain low threshold. The power supply is immune to small variations of vibration level. In this demonstration platform, LTC3588-1 is selected as the power manage unit for the mono-block generator.

All the other components can be classified as the power consuming unit. Generally, it contains one or more sensors, a wireless communication module and a micro-controller. The tri-axial acceleration sensor (BMA222, Bosch©) and the wireless module (MRF49XA, Microchip©) are used. Both of them are operated by a micro-controller (PIC18LF14K50, Microchip©) which integrates the temperature and the voltage sensors itself. The work loop of the micro-controller is shown in figure 3.29. The output voltage of LTC3588-1 is set to 2.5V to satisfy the requirements of the chips and decrease the power consumption as much as possible.

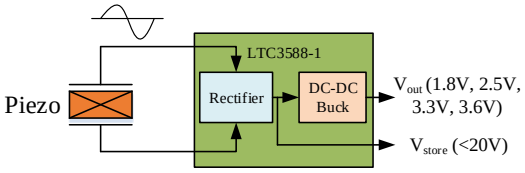

Figure 3.28: Schematic plot of the power conditioning chip LTC3588-1.

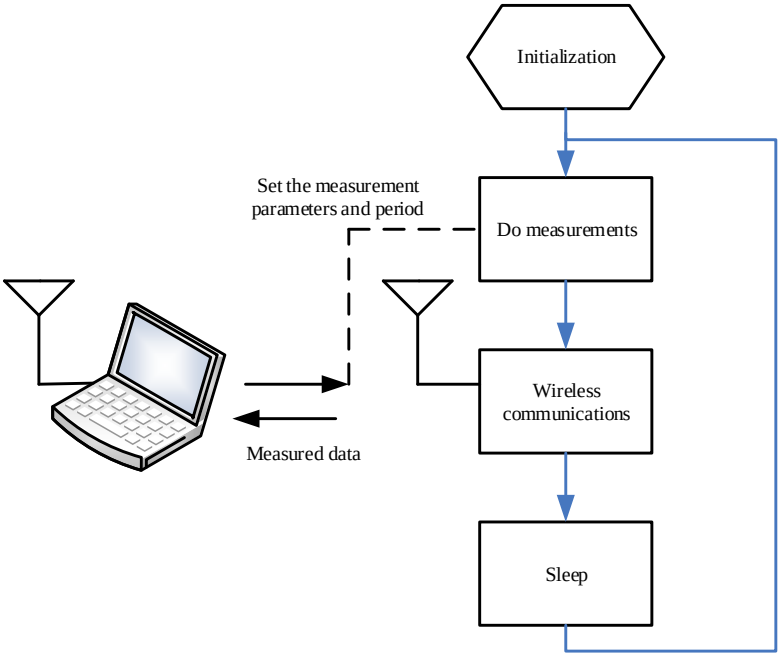

Figure 3.29: Work procedure of the micro-controller.

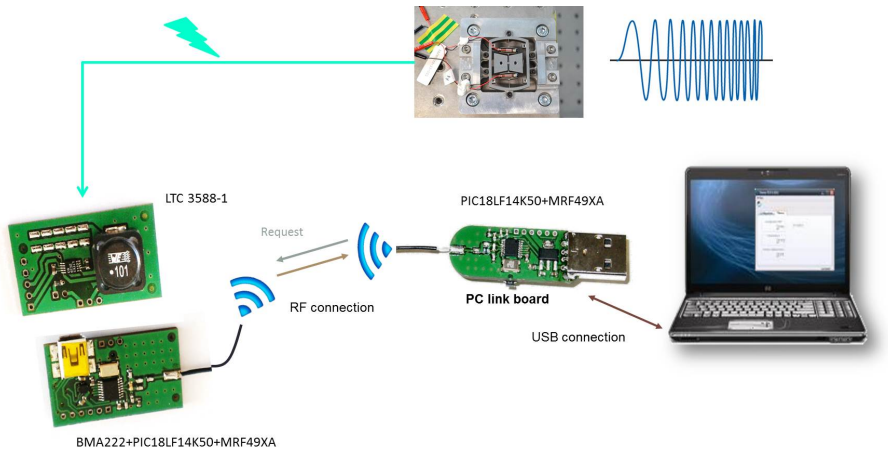

Figure 3.30: Demonstration platform of the autonomous sensor node.

Demonstration platform

In cooperation with the information process center (a computer with the wireless communication module), an autonomous measurement system is demonstrated in figure 3.30. The mono-block BSM generator is placed on a shaker providing the vibration excitation. Converted electric energy then passes through the power conditioning circuit for storage and regulation. After that, the regulated voltage is used for powering the energy consuming unit. The measurement parameters such as the required information and sampling period are configured using the lab-top computer and passed to the autonomous sensor node through wireless communications. Meanwhile, the acquired information is sent to the laptop from the sensor node.

In order to study the wideband properties of the mono-block generator when used for the autonomous sensor node, the demonstration platform is tested over a large frequency range. Figure 3.31(a) shows the stored voltage and output voltage of the power conditioning unit with a $6m/s^2$ excitation at 33.4Hz. It can be found that the enable threshold for the output is 4V and the disable threshold is 3V as the output is set to 2.5V. With the measurement and transmission period fixed at 8s, the sensor node lasts more than 230s then shuts down for 190s. As the stored voltage is accumulated increasingly until it has exceeded the enable threshold, the sensor node starts to work again. By comparing the work and the shutdown time, it is calculated that the duty cycle of the sensor node is about 60%.

When the excitation frequency is increased to 39.4Hz, the harvested power is also increased. The results in figure 3.31(b) show that it is enough to support the sensor node to work normally all the time. If the excitation frequency is further raised to 50.4Hz as presented in figure 3.31(c), the stored voltage keeps on growing since the harvested energy is more than the amount consumed.

Noted that the measurements in many applications are performed every 10 minutes or more, it can be concluded that the mono-block BSM generator is validated for the power supply for wideband excitations. Reliable performance for complex and variable environments can be expected for the sensor node with the proposed generator.

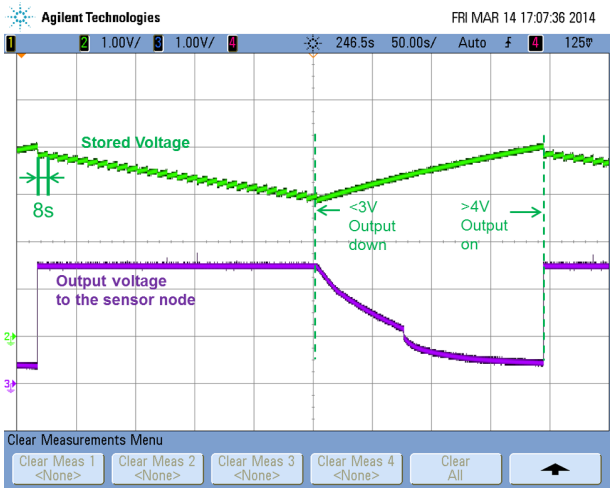

(a)

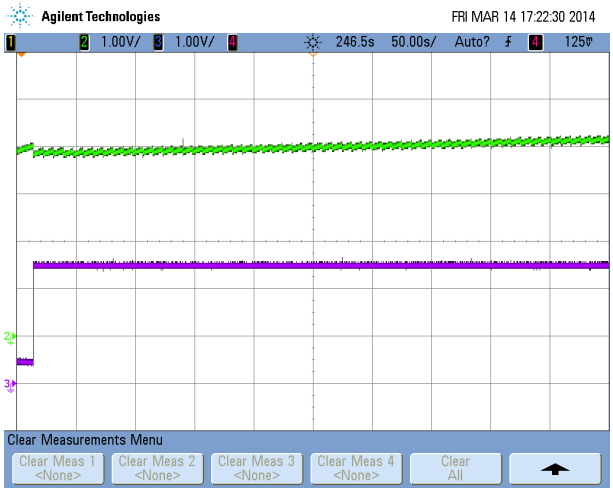

(b)

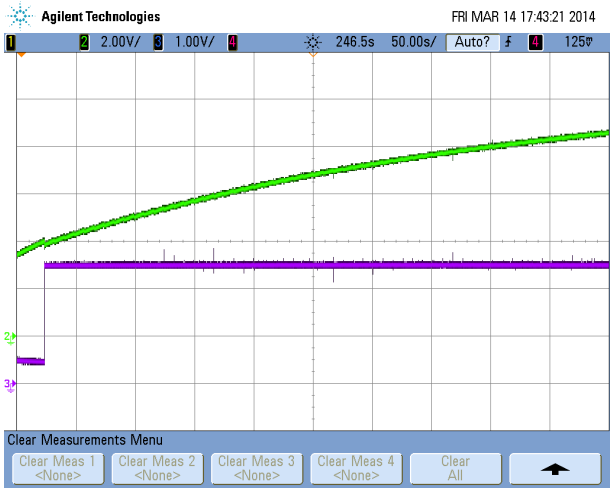

(c)

Figure 3.31: Stored and supplied voltage at different excitation frequencies: (a) 33.4Hz; (b) 39.4 Hz; (c) 50.4 Hz.

3.7 Figure of merit for the wideband generators

In order to make comparisons with other nonlinear generators for wideband energy harvesting in the literature, a figure of merit has to be proposed. Undoubtedly, the most important properties of the nonlinear generators are the bandwidth and the available power. In the light of the different testing conditions and masses for capturing the vibration energy, the proposed figure should take into account all this issues to provide fair evaluations. Therefore, the following NPBP (Normalized Power Bandwidth Product) figure is suggested:

$$NPBP = \frac{P_{av}}{P_{lim}}\frac{\Delta f}{f_c}Q_m = \frac{P_{av}}{\frac{M\gamma^2 Q_m}{16\pi f_c}}\frac{\Delta f}{f_c}Q_m = \frac{16\pi \Delta f P_{av}}{M\gamma^2} \tag{3.12}$$

where Δf is the bandwidth defined by the effective frequency range, P_{av} represents the power averaged over the bandwidth, f_c is the center frequency of the bandwidth, M is the inertial mass of the generator, γ is the acceleration amplitude of the excitation, Q_m is the quality factor and P_{lim} is the available maximum peak power of the linear generator with the same excitation, center frequency, mass and mechanical quality factor.

The NPBP figure contains a triple meaning: normalized power, normalized bandwidth and quality factor. It gives the indication that a good generator should be well designed for maximizing the synthesis of these three terms. Since the nonlinear generators have distinct responses for different excitations, the determination of the bandwidth and the average power is a little different from the linear generators. However, a general strategy is suggested to be used here.

Chirp excitation case:

When subjected to chirp excitations, due to the special hysteresis feature of the nonlinear generator, the bandwidth needs to be analyzed for the forward and reverse sweep respectively as shown in figure 3.32. For the forward sweep, the harvested peak power (P_{kF}, f_{kF}) can be found from the power responses. Next, two half peak-power points {($P_{kF}/2$, f_{LF}) and ($P_{kF}/2$, f_{HF}), $f_{LF} < f_{kF} \leqslant f_{HF}$} are determined. For the reverse sweep, three corresponding parameters {($P_{kR}/2$, f_{LR}) and ($P_{kR}/2$, f_{HR}), $f_{LR} < f_{kR} \leqslant f_{HR}$} can be found. Then the bandwidth is defined as $\Delta f = f_{HF} - f_{LR}$ with the center frequency $f_c = (f_{HF} + f_{LR})/2$. This definition is to cover the favorable range for both forward and backward sweep responses. Although the presented example is for a bistable generator, these definitions are also applicable for the monostable hardening or softening generators.

With the bandwidth determined, the average power for the effective band can be calculated as:

$$P_{av} = \frac{1}{\Delta f}\int_{f_{LR}}^{f_{HR}} P_R(f)p_1(f) + P_F(f)p_2(f)df \tag{3.13}$$

in which $P_R(f)$ and $P_F(f)$ are the reverse and forward power response separately. Considering that the forward and reverse responses represent two possible motion solutions of the generator, the final motion is determined by the initial condition. Then the probability for each response can be determined by the basin of attraction at the specific frequency with the excitation fixed and the probability distribution of the initial conditions. In equation (3.13), $p_1(f)$ denotes the probability for the reverse sweep and $p_2(f)$ is the probability for the forward sweep.

For simplifications, it is assumed that $p_1(f) = p_2(f) = 1/2$. As a further step, the power curve is approximated with some linear segments (red dashed lines) as shown in

Table 3.2: Comparison of the nonlinear literature generators

Reference	Mechanism	P_{av} (mW)	Δf (Hz)	f_c (Hz)	Mass (g)	Volume (cm^3)	γ (m/s^2)	$\Delta f/f$	Q_m	NPBP
[117]	Picewise	9.36	3	16.5	47	27.38	9.8	0.182	18.9	0.312
[112]	Hardening	15.025	5.5	26.25	80		4.98	0.21	44	2.073
[132]	Bistable	72.42	3.2	5.2	35.6	130.7	10	0.615	3.63	3.271
[110]	Hardening	0.288	3.8	29.4	10		1	0.128	150	5.5
[109]	Hardening	0.128	1.3	15.45	7.4		3	0.084	18.2	0.126
	Softening	0.098	3.6	12.4	7.4		3	0.29	15	0.268
[127]	Bistable	0.196	2.75	12.625	5.3	19	10	0.218	50	0.0514
Macro BSM	Bistable	2.834	15.99	19.44	45.8	48	3	0.646	31.45	5.53
Mono-block BSM	Bistable	0.544	37.48	47.16	9	5.46	6	0.795	35.9	3.157
[108]	Hardening		2.9	9.55	29.5		8.4	0.303	4.35	
[124]	Bistable	10.61	4.5	11.5		40	19.6	0.391		
[119]	Piecewise									
	(d=1.8)		8.8	33.1	0.72		9.8	0.266		
	(d=2.2)		6.9	32.05	0.72		9.8	0.215		
	(d=2.6)		5.2	31	0.72		9.8	0.168		
[113]	Hardening		250	1225				0.204		
[144]	Bistable (Oneside: softening, 150V bias)		545	697.5			9.68	0.781		
[120]	Hardening	0.242	23.25	74.625		9.9	14	0.312		
	Bistable	0.449	23.5	54.25		9.9	14	0.433		
[118]	Piecewise		10	37			6	0.27		

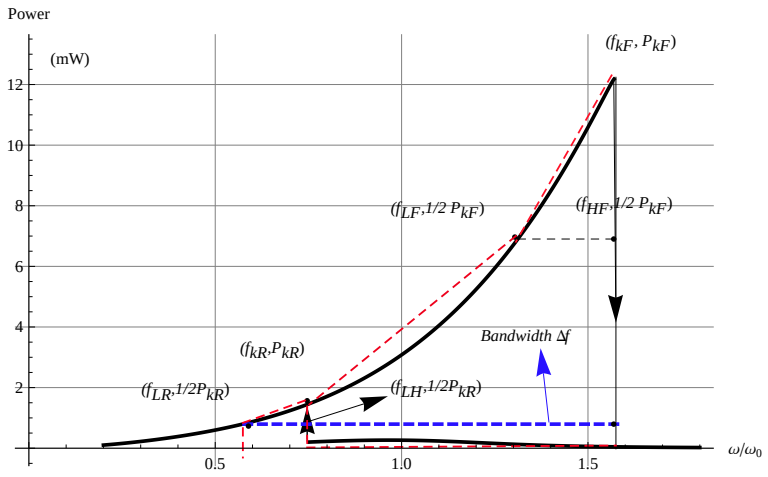

Figure 3.32: Bandwidth definition and average power approximation for the bistable generator.

figure 3.32. If the power is less than $1/2$ min(P_{kF}, P_{kR}), it is considered as zero with the approximation of horizontal lines. Then the average power is expressed:

$$P_{av} = \frac{1}{2\Delta f}(\frac{3}{2}P_{kR}(f_{HR} - f_{LR}) + \frac{1}{2}(\frac{1}{2}P_{kF} + P_{kR})(f_{kF} - f_{LR}) + \frac{3}{4}P_{kF}(f_{HF} - f_{LF})) \quad (3.14)$$

for the hardening and bistable generator or

$$P_{av} = \frac{1}{2\Delta f}(\frac{3}{4}P_{kR}(f_{HR} - f_{LR}) + \frac{1}{2}(\frac{1}{2}P_{kR} + P_{kF})(f_{HF} - f_{kR}) + \frac{3}{2}P_{kF}(f_{HF} - f_{kF})) \quad (3.15)$$

for the softening generator.

It is worth of note that this approximation is only effective for the negligible error induced by the linear approximation. When the power curve is not suitable for the linear approximation, other method needs to be used.

Single harmonic excitation case:

In this case, the excitation frequency is changed step by step and the result for each step is not related to the others. The test for each step is started from zero initial condition, which is different from the sweep cases. The bandwidth is defined by the points $\{(P_k,\ f_k)$ $,(P_k/2,\ f_L)$ and $(P_k/2,\ f_H)$, $f_L < f_k \leqslant f_H\}$ with P_k representing the peak power and f_L, f_k, f_H representing the corresponding frequency positions. Then the average power is calculated as:

$$P_{av} = \frac{1}{\Delta f}\int_{f_L}^{f_H} P(f)df \quad (3.16)$$

The similar strategy can be also applicable for the band-limited noise excitation.

Table 3.2 lists some literature generators with the calculated NPBP figure. The two BSM generator prototypes are also listed for comparison. Some parameters of the generators in the literature are estimated from responses curve in the article so that the results may be not very precise. However, it shows that the figure of merit offers a tool for the evaluation of the performance of nonlinear generators. All the results are obtained for the nonlinear generators in the case of chirp excitations.

3.8 Conclusion and prospect

Based on the good description of the model, the optimization of the BSM generator on ϵ and ω_0 is feasible. A strategy is proposed and applied to both chirp and noise excitations, providing useful information on the relationship between the performance and a few design parameters. The best performance comes from the optimal potential curve which is the combined action of ϵ and ω_0.

To have a reliable and optimal design, there are some key considerations to be taken into account. Some realistic constraints about the design are discussed. For the critical part of the hinges, investigations are performed to obtain the required properties of low rotational stiffness and high allowed rotation angle. With the strategy applied, a mono-block generator is proposed. It is demonstrated that the miniaturized design is capable of providing power for the sensor node over a large frequency band. Comparisons are made with the literature nonlinear generators using the new figure of merit NBPB. It is shown that the mono-block design of the BSM generator possesses some of the best performance for accounting the power and bandwidth simultaneously.

Considering that the results are obtained for the limited displacement and the non-optimal coupling level, it is expected that better performance can be achieved with the well set pre-stress condition of the piezoelectric materials and the introduced elastic stoppers for higher frequency and excitation applications.

4

Combination of the OSECE circuit and the BSM generator

Contents

4.1 Introduction

A VEH includes two parts: the generator and the interface circuit for energy extraction and storage. For the former, it consists of the mechanical structure and the electromechanical transducer as the BSM generator. For the latter, the simplest circuit is just the load resistor as has been discussed for the BSM macro generator in chapter 2. The resistor draws the converted electric energy from the electromechanical transduction parts and consumes it directly without storage. However, the utilized energy occupies a really small ratio of the total available energy in many cases [2].

Accordingly, improvements on the VEHs focus on the following two aspects: the mechanical structure and the interface circuit. The proposed BSM generator which aims at increasing the operation band belongs to the improvements on the structure. Meanwhile, the optimization of the energy extraction and storage circuit is the other important subject. According to former investigations, it is validated that the BSM generator has the desired properties for wideband energy harvesting with a load resistor. Better performance is expected if a proper extraction technique is applied.

For the piezoelectric vibration energy harvesting, many nonlinear switching harvesting techniques are developed to increase the harvested power, such as the SSHI [3, 4], SECE [5], OSECE [7]. It is shown that these nonlinear circuits can significantly increase the harvested power compared to the standard circuit, especially in the case of low electromechanical coupling coefficient [2, 79, 80, 81].

In view of the high efficiency of the nonlinear switching harvesting techniques and the wideband property of the bistable harvesters, optimized performances are believed to be obtained if these two techniques are combined. Chen et al. recently discussed the application of SSHI circuit to a bistable cantilever beam harvester based on a work cycle analysis [145]. It has shown that, compared with the standard circuit, the SSHI strategy can significantly increase the harvested power whenever the excitation frequency is away from the maximum response frequency. However, these results were obtained for one sweep excitation with a given constant electromechanical coupling coefficient. Consequently, further investigations are needed to provide a more detailed understanding of the benefits of bistable harvester with advanced nonlinear switching harvesting techniques.

In this chapter, several interface circuits are introduced and compared. Because of its easy operation and high performance, the newly developed OSECE circuit is selected and used with the BSM bistable generator. The performance is investigated and compared with the BSM generator with the standard circuit. In order to perform thorough comparisons between OSECE and the standard circuit for the BSM generator, the harvested power of the two circuits are evaluated for different levels of electromechanical coupling coefficients and two types of excitations. Finally, a new self-powered BSMOS harvester with the mechanical switches instead of the electronic switches in the OSECE circuit is proposed and discussed.

4.2 Interface circuits for piezoelectric energy harvesting

In order to select the proper interface circuit for the BSM generator, investigations are performed for several of the most used circuits. Considering the complex dynamics of the BSM generator, these circuits are studied in the case of linear generators for the purpose of simplifications. The electromechanical model for the linear piezoelectric generator is presented in figure 4.1.

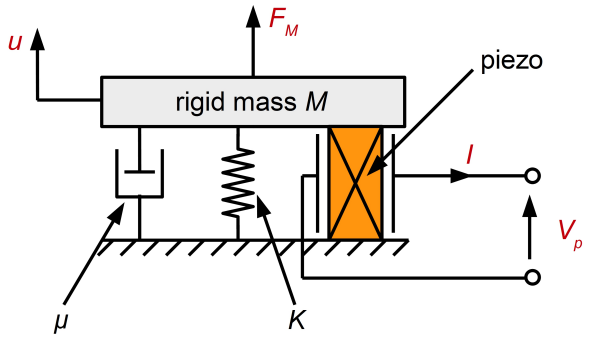

Figure 4.1: Electromechanical model for the linear piezoelectric generator.

The governing equation is written as:

$$\begin{cases} F_M = M\ddot{u} + \mu\dot{u} + Ku + \alpha V_p \\ I = \alpha\dot{u} - C_0\dot{V}_p \end{cases} \tag{4.1}$$

where α is the piezoelectric force factor, C_0 is the capacitance of the piezoelectric element and other parameters are defined in figure 4.1. The properties of the concerned circuits are studied in the following using this model.

4.2.1 AC circuit

The AC circuit is the simplest way to get the energy from the transducer components as shown in figure 4.2(a). A resistive load which plays the roles of energy extraction and consuming is directly connected to the piezoelectric component. The equivalent circuit is plotted in figure 4.2(b).

For the sinusoidal vibration with constant displacement amplitude u_M, the power harvested by the load resistor R_L is expressed as [146]:

$$P_{uac} = \frac{1}{2}\frac{\omega^2\alpha^2 R_L u_M^2}{1 + (R_L C_0\omega)^2} \tag{4.2}$$

where ω is the excitation frequency.

When the excitation force F_M is constant, then we have a new expression with u_M solved from equation (4.1):

$$P_{fac} = \frac{1}{2}\frac{\omega^2\alpha^2 R_L F_M^2}{1 + (R_L C_0\omega)^2}\frac{1}{(K - M\omega^2 + \frac{\omega^2\alpha^2 R_L^2 C_0}{1 + (R_L C_0\omega)^2})^2 + (\mu\omega + \frac{\omega\alpha^2 R_L}{1 + (R_L C_0\omega)^2})^2} \tag{4.3}$$

It can be inferred that the power is related to the load value and the coupling coefficient. The current from the transducer is divided into two paths for the intrinsic capacitance and the load separately. Therefore, the ratio of the extracted energy is determined by the impedance proportion between R_L and C_0. Without additional components, there is no electric energy loss in the AC circuit. Although the AC circuit is not suitable for most real applications, it is often used as a method for evaluating the performance of the generator.

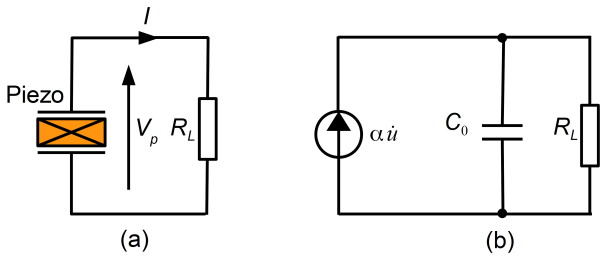

Figure 4.2: (a) AC standard circuit; (b) Equivalent model.

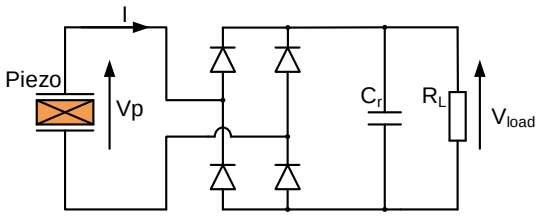

Figure 4.3: Standard circuit.

4.2.2 Standard circuit

The standard circuit deriving from the idea of converting AC to DC is composed of a rectifier and a filtering capacitance. Figure 4.3 and figure 4.4 show the circuit and the corresponding waveform.

When V_p is below V_{load}, the piezoelectric transducer is open-circuited and no current goes to the load. As V_p increases with the displacement u until it exceeds V_{load}, converted electric energy is supplied to load. Once u reaches the maximum value and starts to decrease towards the other direction, the transducer becomes open-circuited again until V_p reaches -V_{load}.

According to the force and charge balance described in the model, the power for the

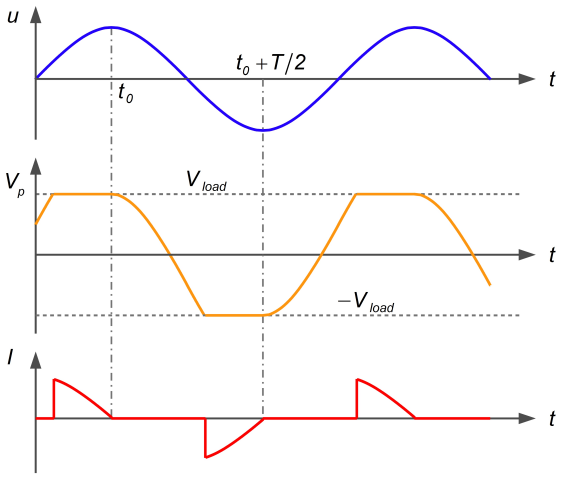

Figure 4.4: Waveform of the standard circuit for a sinusoidal vibration.

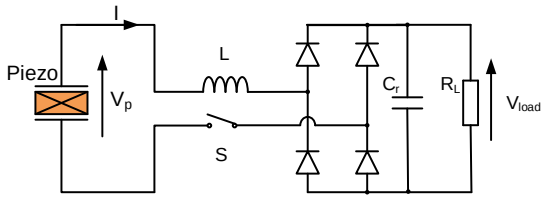

Figure 4.5: Serial-SSHI circuit.

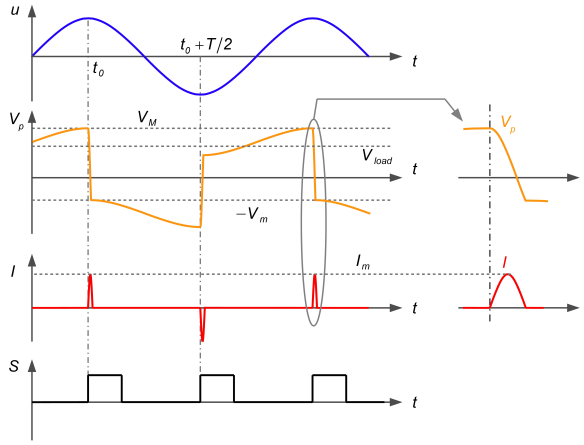

Figure 4.6: Waveforms of the serial-SSHI circuit.

sinusoidal vibration is then calculated as [7]:

$$P_{ustd} = \frac{V_{load}^2}{R_L} = \frac{\omega^2 \alpha^2 R_L u_M^2}{(\frac{\pi}{2} + R_L C_0 \omega)^2} \tag{4.4}$$

$$P_{fstd} = \frac{\alpha^2 R_L F_M^2}{(\frac{\pi}{2} + R_L C_0 \omega)^2} \frac{1}{(\mu + \frac{2\alpha^2 R_L}{(\pi/2 + R_L C_0 \omega)^2})^2} \tag{4.5}$$

Equation (4.4) and equation (4.5) represent the constant displacement case and the constant excitation force case at the resonance frequency respectively.

The standard circuit is simple and capable of providing the DC power. However, a large portion of electric energy is not extracted as can be seen in figure 4.4. The power output from the piezoelectric elements is only available when $|V_p|$ is above V_{load}. The rest of electric energy returns to the system. It is a critical issue for the low coupling level generators in which the harvested energy only occupies a small ratio of the total available energy. Besides, additional energy loss on the rectifier is introduced, which is especially not to be neglected in the case of low piezoelectric voltage.

4.2.3 Serial-SSHI circuit

To enhance the harvested power and fully utilize the converted electric energy, a nonlinear synchronous switching technique based on an inductor has been proposed by Guyomar et al. [3], named as SSHI. It includes two types of realizations, serial-SSHI and parallel-SSHI. Figure 4.5 is the schematic of serial-SSHI while figure 4.6 shows the waveforms of this circuit.

The working principle is illustrated as follows. When the switch is open, the piezoelectric element is disconnected from the load and V_p increases with the displacement u until the maximum voltage point V_M and the maximum displacement u_M are reached at the same time. Then S is closed and a LC oscillation process is started. The electric energy flows through the rectifier to the load from the piezoelectric component. Some of the energy is stored in C_r for powering the load while some is returned to the piezoelectric component in the form of the reversed voltage -V_m. Generally, V_m is less than V_{load} and then V_p decreases with u from $-V_m$ towards the negative direction in the open-circuited condition due to the rectifier. Before $|V_p|$ reaches V_{load}, S is opened to isolate the piezoelectric element from the load. As V_p and u arrive at the negative extreme, S is closed and another voltage inversion is started again.

The relationship between V_p, V_{load} and V_m is written as follows:

$$V_m - V_{load} = -(V_M - V_{load})e^{-\pi/(2Q_i)} \tag{4.6}$$

$$V_M = -V_m + \frac{\alpha u_M}{2C_0} \tag{4.7}$$

$$V_{load} \int_{t_0}^{t_0+T/2} Idt = C_0(V_m + V_M)V_{load} = \frac{\pi}{\omega R_L}V_{load}^2 \tag{4.8}$$

where Q_i is the qualify factor of the LC oscillation. The load voltage is solved to be:

$$V_{load} = \frac{2\alpha u_M \omega R_L(1 + e^{-\pi/(2Q_i)})}{\pi(1 - e^{-\pi/(2Q_i)}) + 2\omega R_L C_0(1 + e^{-\pi/(2Q_i)})} \tag{4.9}$$

Then the power expressions are deduced as:

$$P_{SSHI} = \frac{V_{load}^2}{R_L} \tag{4.10}$$

which can be used directly for the constant displacement case. For the constant force case at the resonance frequency, u_M needs to be calculated from the following equation based on the energy balance [2]:

$$F_M = \omega\mu u_M + \frac{V_{load}^2}{R_L u_M} + \frac{C_0(V_M - V_{load})^2}{2\pi u_M}(1 - e^{-\pi/(2Q_i)}) \tag{4.11}$$

Compared to the AC and standard circuits, the serial-SSHI technique presents the improvement on the utilization of the converted electric energy. Except for the energy extracted for the load, the residual energy is preserved on the piezoelectric elements in the form of the inverted voltage. This effect can be considered as a method of increasing the coupling level in some sense. With the inverted voltage as a bias voltage, the ratio of the converted electric energy on the total electromechanical energy is enlarged for the same displacement. The performance is greatly improved for the low coupling cases.

The switching strategy is relatively simple that S is only necessary to be closed at the positive or negative maximum displacement position and opened before V_p exceeds V_{load}. No exact operation of opening the switch is required. However, the performance is greatly influenced by the circuit quality factor which is determined by the energy loss within the rectifier and the inductor. More important, the power varies for different load situations.

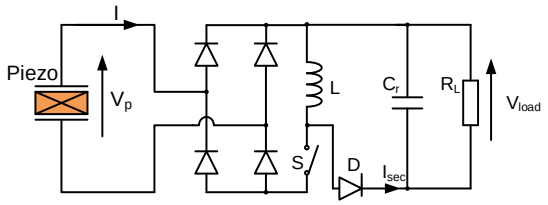

Figure 4.7: SECE circuit.

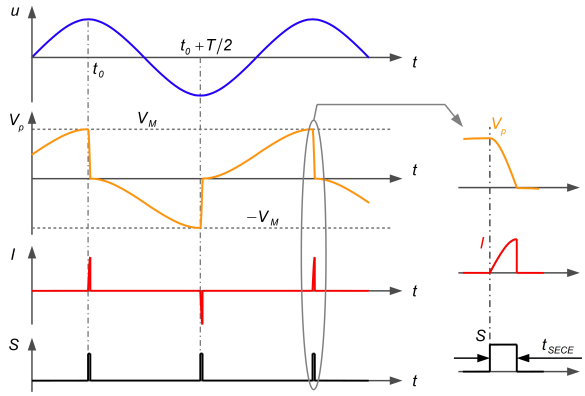

Figure 4.8: Waveforms of the SECE circuit.

4.2.4 SECE circuit

In order to develop an interface circuit which is independent on the load, the SECE technique is proposed by Lefeuvre et al. [5]. The circuit and the waveforms are shown in figure 4.7 and figure 4.8.

The piezoelectric element is firstly disconnected from the load with the switch S opened. As the displacement increases, the piezoelectric voltage climbs to the maximum position V_M. At this point, S is closed and a LC oscillation begins. After a quarter of the LC oscillation period t_{SECE}, all the electric energy is stored in the inductor L. Then S is opened, forcing all the energy to be transferred from L to the load. Meanwhile, V_p jumps to zero and begins to moving towards $-V_M$ with the decreasing displacement. Once the negative maximum position is reached, S is closed and another new LC oscillation starts again.

For each switch, the transferred energy is calculated as:

$$E_{SECE} = \frac{1}{2}LI_M^2 = \frac{1}{2}L(\sqrt{\frac{C_0}{L}}V_M e^{-\frac{\pi}{4Q_i}})^2 = \frac{1}{2}C_0V_M^2 e^{-\frac{\pi}{2Q_i}} \tag{4.12}$$

Since V_p always starts from zero and changes in the open-circuited condition, then we have:

$$V_M = 2\frac{\alpha}{C_0}u_M \tag{4.13}$$

The power is deduced as:

$$P_{uSECE} = E_{SECE}\frac{\omega}{\pi} = \frac{2\alpha^2\omega}{\pi C_0}e^{-\frac{\pi}{2Q_i}}u_M^2 \tag{4.14}$$

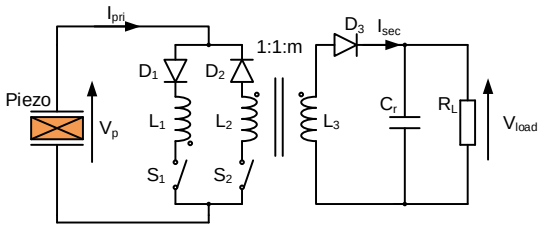

Figure 4.9: OSECE circuit.

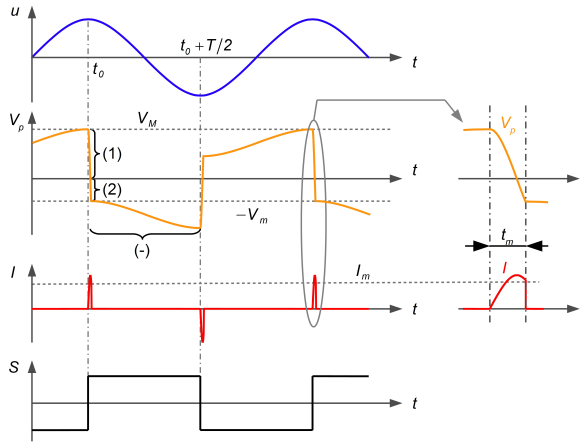

Figure 4.10: Waveforms of the OSECE circuit.

for the constant displacement case and

$$P_{fSECE} = \frac{2\alpha^2 e^{-\frac{\pi}{2Q_i}}}{\pi C_0 \omega} \frac{F_M^2}{(\mu + \frac{4\alpha^2}{\pi C_0 \omega})} \tag{4.15}$$

for the constant force case at the resonance frequency.

As seen in the expressions, the power is not dependent on the load. This favorable feature makes the SECE circuit suitable for different load situations and capable of providing a robust performance. Meanwhile, all the converted energy are transferred to the load, which can improve the energy utilization for low coupling cases.

However, in some sense, the precise control requirement of the switching strategy hinders the applications of the SECE technique and the self-powered realization too. In addition, the performance is also affected by the circuit quality factor as the serial-SSHI circuit.

4.2.5 OSECE circuit

Figure 4.9 presents the OSECE circuit developed by us at the SYMME laboratory. It is based on the SECE circuit with a simpler switching operation strategy [7]. In this circuit, a fly-back transformer is used instead of the inductor so that a unified ground is obtained for the piezoelectric element and the load. Two switches are in place of the single switch configuration in the SECE circuit.

The OSECE waveforms are presented in figure 4.10. The switch signal S is applied to two switches at the same time while S_1 and S_2 are closed for positive and negative

driving signal separately. At first, the piezoelectric element is placed in the open-circuited status with S_1 opened and S_2 closed. V_p increases with the displacement until V_M and u_M is reached. Then the switching signal is toggled so that S_1 is closed and S_2 is opened. A transient LC oscillation is started. For the process indicated by (1) in the figure, all the electric energy is stored to the transformer without going to the load because the voltage on L_3 is negative and blocked by D_3. For the moment, the current I_{pri} gets the maximum value while V_p equals zero. After that, the circuit enters process (2). The piezoelectric element is charged by L_1 along the reversed direction. As soon as V_p arrives at $-V_m = V_{load}/m$ so that the voltage on L_3 is greater than V_{load}, all the remain energy on the transformer is transferred to the load. Next, the circuit enters phase (-) in which V_p decreases with the displacement towards the negative peak. Then, the switching driving signal is toggled and another inversion transient process begins.

For each switching process, the transferred energy is:

$$E_{OSECE} = \frac{1}{2}L_1 I_m^2 = \frac{1}{2}L_2 I_m^2 \tag{4.16}$$

where I_m is the current of L_1 (L_2) with S_1 (S_2) closed as marked in the figure 4.10. It can be calculated by:

$$I_m = \sqrt{\frac{C_0}{L_1}} V_M \sin(\omega_I t_m) e^{-\frac{\omega_I t_m}{2Q_i}} \tag{4.17}$$

in which t_m is the lasting time of the LC oscillation. It is determined by the value of V_M and V_{load}:

$$-V_M \cos(\omega_I t_m) e^{-\frac{\omega_I t_m}{2Q_i}} = V_m = \frac{V_{load}}{m} (\pi/2 < \omega_I t_m < \pi) \tag{4.18}$$

The followed bracketed in-equation means that the LC oscillation lasts for more than a quarter but less than a half of the LC period $2\pi\sqrt{L_1 C_0}$.

The power is expressed as:

$$P = \frac{V_{load}^2}{R_L} = \frac{\omega}{\pi} E_{OSECE} \tag{4.19}$$

Considering the half excitation period between two switches, the piezoelectric component is open-circuited, thus:

$$V_M - V_m = 2\frac{\alpha}{C_0} u_M \tag{4.20}$$

Then V_{load} can be calculated:

$$\begin{cases} V_{load} = -\dfrac{2m\alpha}{C_0} \dfrac{\cos(\omega_I t_m) e^{-\frac{\omega_I t_m}{2Q_i}}}{1 + \cos(\omega_I t_m) e^{-\frac{\omega_I t_m}{2Q_i}}} u_M \\ \omega_I t_m = \arctan(-m\sqrt{\dfrac{2\pi}{R_L C_0 \omega}}) + \pi \end{cases} \tag{4.21}$$

Substituting equation (4.21) into equation (4.19), the power can be estimated for the constant displacement case.

For the constant force case at the resonance frequency, u_M can be solved with the model:

$$u_M = \frac{F_M}{\mu\omega + \frac{4\alpha^2}{\pi C_0}\frac{1-\cos(\omega_I t_m)e^{-\frac{\omega_I t_m}{2Q_i}}}{1+\cos(\omega_I t_m)e^{-\frac{\omega_I t_m}{2Q_i}}}} \tag{4.22}$$

Then the power expressions for these two cases are written as:

$$P_{uOSECE} = \frac{2\alpha^2\omega}{\pi C_0}\frac{\sin^2(\omega_I t_m)e^{-\frac{\omega_I t_m}{Q_i}}}{(1+\cos(\omega_I t_m)e^{-\frac{\omega_I t_m}{2Q_i}})^2}u_M^2 \tag{4.23}$$

$$P_{fOSECE} = \frac{2\alpha^2\omega}{\pi C_0}\frac{\sin^2(\omega_I t_m)e^{-\frac{\omega_I t_m}{Q_i}}}{(1+\cos(\omega_I t_m)e^{-\frac{\omega_I t_m}{2Q_i}})^2}\frac{F_M^2}{(\mu\omega + \frac{4\alpha^2}{\pi C_0}\frac{1-\cos(\omega_I t_m)e^{-\frac{\omega_I t_m}{2Q_i}}}{1+\cos(\omega_I t_m)e^{-\frac{\omega_I t_m}{2Q_i}}})^2} \tag{4.24}$$

There are some major improvements for the OSECE circuit compared with the SECE circuit. Only one diode in the primary side decreases the energy loss and increases the circuit quality which positively affects the circuit performance. The use of the transformer provides a sharing ground for the piezoelectric element and the load which facilitates the self-powered realization. More important, the switching strategy is greatly simplified as the switches are only required to be opened or closed at the exact extreme points. Besides, the inverted voltage preserved on the piezoelectric element can increase the coupling level as explicated in the serial-SSHI technique. The harvested power can be increased for low coupling cases while the low load dependence inherited from SECE is preserved to some extent. However, the performance is still related to the quality factor of circuit [7].

4.2.6 Comparison of several circuits

To have a sound knowledge of these circuits, it is proposed to compare the performance for the same conditions. Generally, there are two most concerned properties for the interface circuit: maximum available power and the dependency on the load impedance.

Apart from the excitation amplitude and the load, it can be found from the aforementioned power expressions that the power is related to the coupling level k^2 and the damping of the mechanical structure represented by the mechanical quality factor Q_m. As suggested in Arroyo's work [88], the product k^2Q_m is a good evaluation of the generator's characteristics. Figure 4.11 shows the maximum available power (all load values and excitation frequencies taken in consideration) for the generators with different k^2Q_m values with the same excitation force F_M. In the figure, the results are normalized by the maximum power of the standard circuit without loss included. For the nonlinear circuits, a high circuit quality factor Q_i is assumed (Q_i =20).

The nonlinear techniques have much better performance than the AC and standard circuits when k^2Q_m is small. As explicated in the former sections, nonlinear circuits are capable of fully utilize the converted electric energy thus providing higher efficiency for

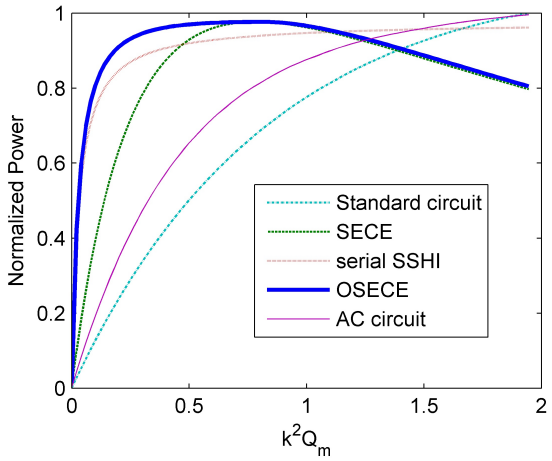

Figure 4.11: Normalized maximum available power for several circuits.

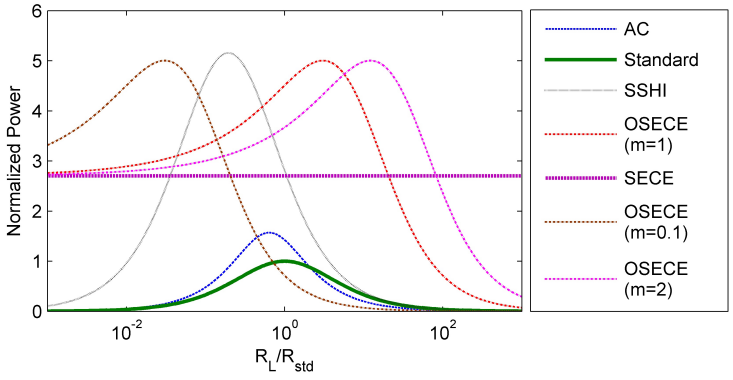

Figure 4.12: Normalized harvested powers under constant vibration amplitude (Q_i=4)

these low k^2Q_m cases. Especially for the serial-SSHI and the OSECE circuit, the harvested energy is raised quickly because of the increasing coupling effect from the voltage inversion.

As k^2Q_m increases, the maximum available power first increases then approaches a constant value for the AC, standard and serial SSHI circuits. For a generator with a given Q_m, when the coupling level is increased, the converted electric energy for the same displacement is raised too. However, as the coupling level reaches a considerable value, the damping from the harvested power is relevant, which suppresses the obtained displacement response and decreases the converted energy in the same time. In the end, an optimal balance is achieved so that the maximum power is limited to $F_M^2/(8\mu)$ [89] for $k^2Q_m > \pi$ with the proper load selected. However, for the OSECE and SECE, the maximum power declines when k^2Q_m is higher than 1. Under this condition, these two circuits bring too much damping without the ability of achieving the optimal balance between the damping and the harvested energy. It is due to the lack of the scheme which is able to return the converted electric energy to the mechanical structure as the other three circuits.

For the second concerned property of the impedance dependence, the comparison results are plotted in figure 4.12 for the constant displacement case. All the power is normalized by the maximum power of the standard circuit obtained at its optimal load value $R_{std} = \pi/(2\omega_0 C_0)$. Much better performance is obtained for the nonlinear techniques in the constant displacement vibration case since the damping from the circuits is excluded. As we can see, the performances of AC, standard and serial SSHI have strong dependence on the load while the SECE circuit is not influenced at all. For the OSECE circuit, it is not as good as the SECE circuit but still has low impedance dependence which is further improved by increasing the value of m. Meanwhile, more power is harvested with OSECE circuit for a wide load range than with SECE circuit.

After the investigations about these circuits, a proper interface circuit has to be selected for the BSM generator. The considerations to be accounted for are listed as follows:

- High harvested power;
- Simple switching strategy;
- Low impedance dependence;
- Feasibility of the self-powered realization.

As a result, the OSECE circuit is believed to be the best choice. Although the performance in the high k^2Q_m cases is not as good as others, it is superior for the low k^2Q_m values which are more common for the generators. More important, the simple switching strategy brings great convenience for the application and the OSECE approach which is less dependent on the load than SSHI appears to be more relevant in the case of a wideband oscillator. Indeed, under wideband vibrations, the output impedance of the generator is varying and low impedance dependence will ensure more stable and reliable performances.

4.3 Changing coupling level with a serially connected capacitance

To have a good understanding of the new technique that combines the BSM generator and the OSECE circuit, it is recommended to study the performance under the conditions of different coupling levels.

For the piezoelectric components with only electric energy input, the coupling coefficient k^2 is defined as the ratio between the produced mechanical energy E_m and the total energy

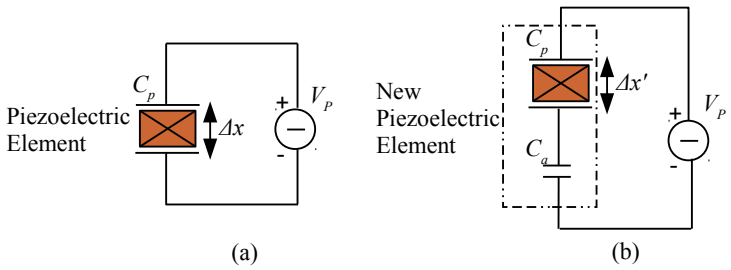

Figure 4.13: Schematic of adding a serially connected capacitance.

(mechanical energy E_m + electric energy E_e): $k^2 = E_m/(E_m + E_e)$. When the voltage V_p is applied to the piezoelectric component as shown in figure 4.13(a), E_m and E_e are obtained as:

$$E_m = \frac{1}{2}K\Delta x^2 = \frac{1}{2}K(\frac{\alpha V_p}{K})^2 = \frac{\alpha^2 V_p^2}{2K} \tag{4.25}$$

$$E_e = \frac{1}{2}C_p V_p^2 \tag{4.26}$$

where Δx is the deformation of the piezoelectric element. Then k^2 can be expressed as a function of the piezoelectric force factor (α) and the system capacitance ($C_0 = C_p$) as given in table 2.2.

To investigate the performance of the BSM harvester for different k^2, it is difficult to prepare a lot of devices with different coupling levels. Instead, a device with high k^2 is used along with an additional serially connected capacitance to decrease k^2 from high to low coupling levels. Considering that a new piezoelectric element composed of the same piezoelectric component with an additional capacitance C_a is applied with voltage V_p as shown in figure 4.13(b):

$$E_m = \frac{1}{2}K\Delta x'^2 = \frac{\alpha^2 V_p^2}{2K}(\frac{C_a}{C_p + C_a})^2 \tag{4.27}$$

$$E_e = \frac{1}{2}\frac{C_p C_a}{C_p + C_a}V_p^2 \tag{4.28}$$

$$k^2 = \frac{E_m}{E_m + E_e} = \frac{(\frac{\alpha C_a}{C_p + C_a})^2}{(\frac{\alpha C_a}{C_p + C_a})^2 + K\frac{C_p C_a}{C_p + C_a}} = \frac{\alpha_1^2}{\alpha_1^2 + KC_0} \tag{4.29}$$

where $\alpha_1 = C_a\alpha/(C_p + C_a)$ is the piezoelectric force factor for this new piezoelectric device and $C_0 = C_p C_a/(C_p + C_a)$ is the new system capacitance.

The serial capacitance changes the piezoelectric force factor and the total capacitance. With this method, k^2 can be tuned to a desired lower value from a high coupling level. Another common method to change the electromechanical coupling level is to add a parallel connected capacitance. It has the same effect as the proposed way of adding a serial capacitance. However, the serial connection which presents small system capacitance is good for increasing the quality factor of the OSECE circuit thus enhancing the energy harvesting efficiency. Since a BSM device with high coupling level is required here, the macro BSM generator ($k^2 = 0.0684$) in chapter 2 is used in the following investigations. In

addition, the miniaturized prototype had not been prepared yet when we were performing the followed experimental investigations. Therefore, all the results in this chapter are obtained used the macro BSM prototype.

4.4 BSM generator with OSECE

Figure 4.14 shows the model of the BSM generator with the OSECE circuit. As can be found in the figure, the piezoelectric components are serially connected instead of the parallel connection in chapter 2. The variation is to enhance the quality factor of the circuit with small capacitance for the LC oscillation. Meanwhile, the piezoelectric voltage is also doubled so that the ratio of the energy loss on the diodes is decreased.

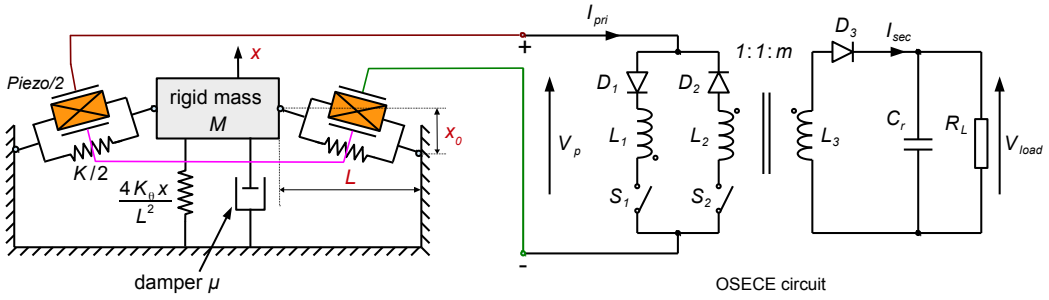

Figure 4.14: BSM generator with OSECE circuit.

The simulation waveforms of the generator and the circuit are plotted in figure 4.15 for a 19.2Hz sinusoidal excitation with the amplitude of 4m/s^2 which is applied to the BSM generator to ensure the inter-well motions. The upper half plot represents the cut-out waveforms of the mass displacement (x_0 and $-x_0$ are the two stable equilibrium positions) and the strain of the piezoelectric transducers while the bottom half is the voltage waveforms of the OSECE circuit. In this case, periodic inter-well motions are obtained.

Similar to the case when using for linear generators, the operations of the OSECE circuit are as follows: At time t_0, the switch S_1 is open and S_2 is closed, the piezoelectric voltage V_p is increasing with the strain in open-circuit situation until reaching V_M where the strain arrives at its positive apex, then S_1 is closed and S_2 is opened inducing a LC transient oscillation for energy transfer. When the inversed voltage reaches -$V_m = -V_{load}/m$, the remaining energy in the transformer is transferred to the load. After that time, V_p decreases with the strain until the negative minimum strain position ($x = 0$ and $V_p = -V_M$), S_1 is opened and S_2 is closed. Another voltage inversion process starts. It is clear that the switches are operated at the exact time when V_p and the strain are at the extreme values and kept unchanged until the next V_p extreme point. It is interesting to notice that the switches are operated four times for one inter-well motion period because the strain period is half the displacement period in the BSM bistable harvester architecture, which is a special feature compared to the more usual linear oscillator case.

For each switching operation, the energy extracted from the piezoelectric element can be expressed as:

$$E_p = \frac{1}{2}C_0(V_M^2 - V_m^2) = \frac{1}{2}C_0(V_M^2 - V_{load}^2/m^2) \tag{4.30}$$

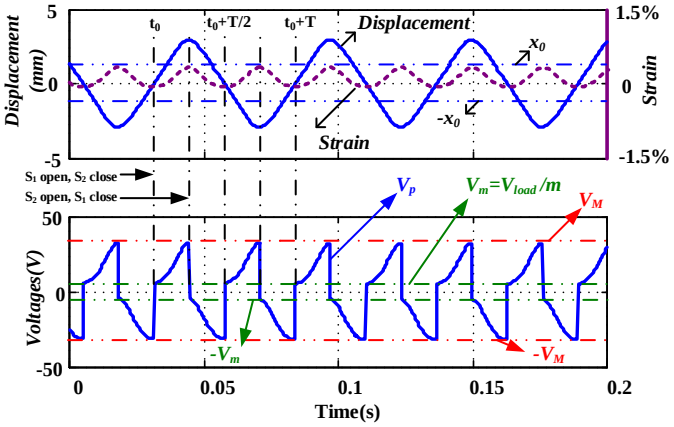

Figure 4.15: Simulation waveforms of the BSM bistable harvester with OSECE circuit.

During a time period T_p the average power consumed by the load is:

$$P = \frac{1}{T_p}\int_0^{T_p} \frac{V_{load}^2}{R_L} dt \tag{4.31}$$

Supposing that the number of the switching times during T_p is denoted n, the extracted average power P_e is then:

$$P_e = \sum_{i=1}^{n} E_p(i)/T_p \tag{4.32}$$

If T_p is large enough so that the energy stored in the load capacitance can be neglected or the energy harvested is balanced by the power consumed under stable state, the energy transfer efficiency of the OSECE circuit is defined as the following equation:

$$\eta = \frac{P}{P_e} \tag{4.33}$$

For the ideal case, $\eta = 1$. In real application, however, energy losses have to be expected as indicated by [7]. They are related to:

- The quality factor of the LC circuit and the transformer efficiency;
- The full-bridge rectifier;
- The series resistance in the secondary winding;
- The secondary diode.

Therefore, the efficiency is usually less than 100% for real applications.

4.5 Testing environment

With the same BSM generator and experimental instrument devices introduced in chapter 2, the testing system configuration is plotted in figure 4.16. Since the BSM generator's parameters may drift with the time and vary with the configuration, identifications are performed again. The results are shown in table 4.1. The turn ratio m of the transformer

Parameter	Value	Parameter	Value
M(g)	45.8	L(mm)	33
K(N/m)	3.9e5	x_0(mm)	1.3
C_p(μF)	0.59	α(N/m)	0.26
μ(Ns/m)	0.22	R(kΩ)	3.84
K_θ (Nm/rad)	0.03		

Table 4.1: Parameters for the BSM generator with identifications done again after disassembling and reassembling.

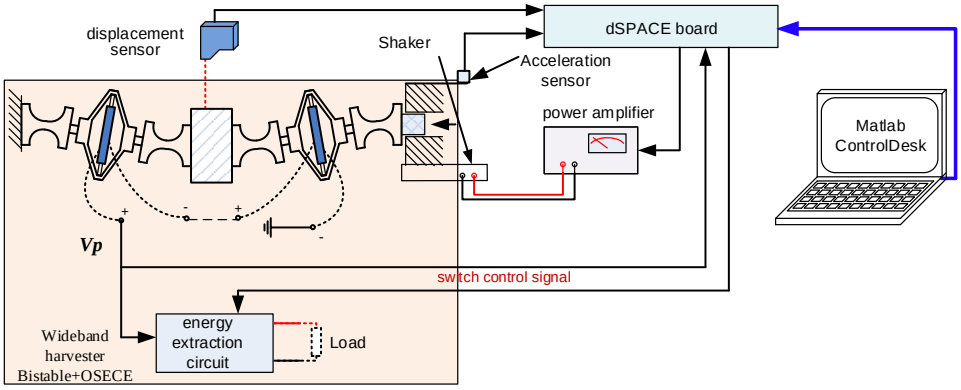

Figure 4.16: Testing system for the BSM generator with the OSECE circuit.

in the OSECE circuit is 0.94. The characteristic frequency is measured to 18.2 Hz (114.35 rad/s) which is in good accordance with the model. In the proposed device, the system capacitance C_0 is the total capacitance of the piezoelectric elements (C_p) and a serially connected capacitance (C_a) such as $C_0 = C_pC_a/(C_p + C_a)$. By doing this, the electromechanical coupling coefficient can be purposely tuned. It is worthy of note that the given values for α and k^2 in table 4.1 are obtained in the case of no additional capacitance ($C_0 = C_p$).

The piezoelectric and the load voltages are sampled by the dSpace board. According to the piezoelectric voltage signal, the switches in the OSECE circuit are operated at the proper extreme voltage points. Considering that there are a lot of frequency components in the motions of the bistable harvester, especially for the noise excitations, the waveforms of the piezoelectric voltage are complex. Therefore, the switches may be triggered on local extrema rather than on the major extrema, which lowers the performance [147]. In the experiment, a dedicated strategy is introduced to stop the switching operation if the piezoelectric voltage is less than the average RMS value for a short period of 0.02s. This time constant is approximately the piezoelectric strain period of the inter-well motions at the natural frequency ω_0. An experimental cut-out waveform of the piezoelectric voltage V_p used for explicating the switching strategy is shown in figure 4.17. The piezoelectric voltage RMS value V_{pRMS} for 0.02s is also plotted in dashed lines. As can be seen in figure 4.17, whenever the voltage extrema are less than V_{pRMS}, the switching process is not triggered.

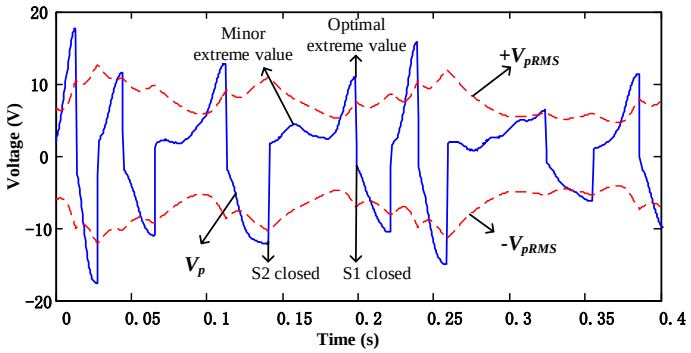

Figure 4.17: Cut-out experimental waveform of the piezoelectric voltage ($k^2 = 0.044$, 4Hz-20Hz band-limited noise, RMS 3.5$\mathrm{m/s^2}$).

4.6 Numerical and experimental investigations

As previously pointed out, the aim of this work is to investigate the best performance obtained using the combination of the OSECE circuit and the bistable harvester for different electromechanical coupling coefficients and excitations. By connecting an additional serial capacitance C_a to the piezoelectric elements, the electromechanical coupling coefficient can be tuned to the desired lower value. Regarding the excitations, both chirp and band-limited noise are used for tests. The performance of the BSM generator with the standard circuit is also studied for comparison.

4.6.1 Determination of the best impedance point

In order to perform comparisons between the OSECE and the standard techniques, the optimal impedances of the two techniques need to be sought (even if the effect of the impedance on the harvested power is low in the case of the OSECE approach). However, to limit the total test time (each test requires a 20 minutes run), the optimal load resistance was not systematically determined for every different excitation and electromechanical coupling coefficient k^2.

The system is subjected to a forward sweep excitation ($4\mathrm{m/s^2}$, 4Hz-44Hz) and $k^2 = 0.016$ for several impedances. The excitation amplitude is selected to let the favorable inter-well motions happen in all tested configurations. The average power of the whole sweep process of each circuit is shown as in figure 4.18 where the resistive load is normalized according the standard resistance R_{std} (equation 4.34) corresponding to the classical impedance matching strategy for the standard interface circuit. It is clear that the OSECE has lower impedance dependence than standard circuit. The optimal load resistances are selected for the standard circuit as $R_{L1} = R_{std}$ and for the OSECE circuit as $R_{L2} = R_{std}/10$. This impedance matching strategy is applied to all the following cases.

$$R_{std} = \frac{\pi}{2C_0\omega_0} \tag{4.34}$$

4.6.2 Simulink model

Because of the complex dynamics of the BSM generator, it is difficult to have a good prediction of the results with the analytical model. Therefore, a common substituted method is to use the numerical simulations while Matlab/Simulink is chosen here.

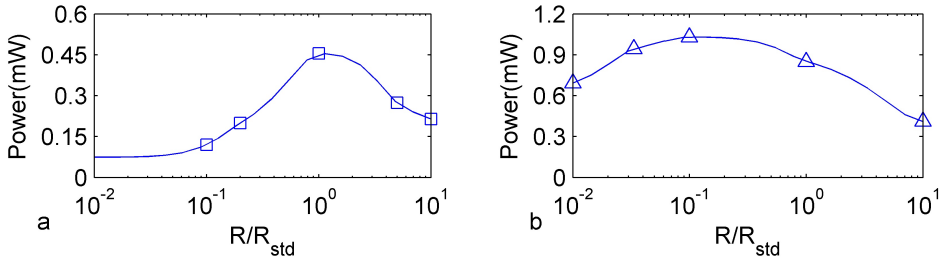

Figure 4.18: Experimental power vs load impedance:(a) standard circuit; (b)OSECE circuit.

Figure 4.19 and figure 4.20 pictures the schematic models developed for the BSM generator with the OSECE and the standard circuits in the Simulink environment. It is simple for the standard circuit but more complex for the OSECE circuit. The most critical parts are the switching signal generation and the energy transfer modules. By introducing a proper extreme detecting scheme, the switches avoid useless switching operations and achieve better energy extraction as exemplified in figure 4.17. The efficiency is included in the energy transfer module to make the numerical investigations keep pace with the experimental testing.

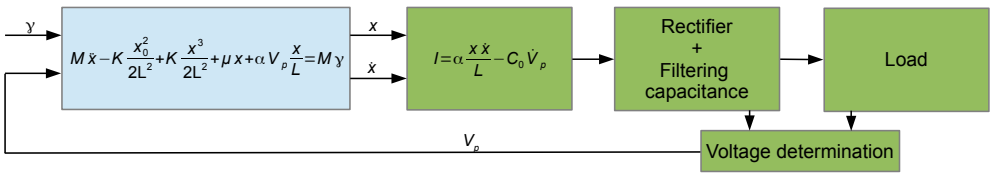

Figure 4.19: Simulink model of the BSM generator with the standard circuit.

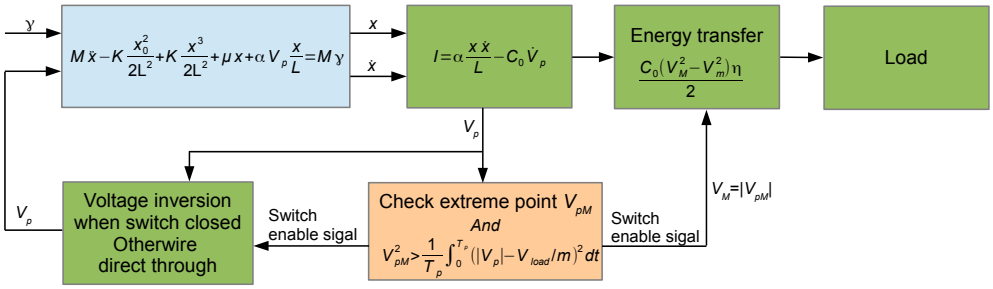

Figure 4.20: Simulink model of the BSM generator with the OSECE circuit.

4.6.3 Chirp excitations

A good strategy to appraise the desired wideband property is using the chirp excitations to investigate the performance of bistable harvester with standard and OSECE circuits. The amplitude 4m/s^2 and sweep rate 0.05Hz/s are determined for obtaining periodic inter-well motions for all tested cases. The average power over the swept frequency range (4Hz-44Hz) is compared for the two techniques. Both experimental and numerical investigations are performed. Simulations are performed using Matlab/Simulink. Considering the electrical energy losses mentioned before, the efficiency used for OSECE simulation is

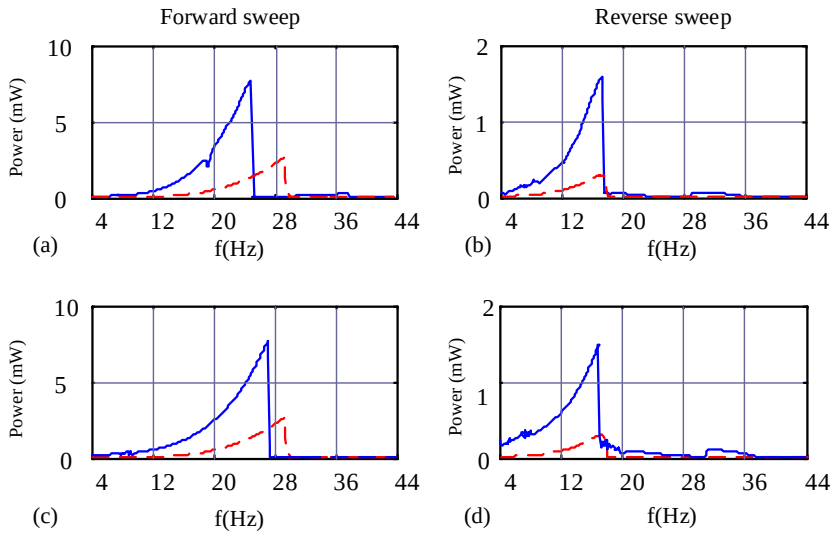

Figure 4.21: Experimental (a, b) and numerical (c, d) harvested power for $k^2 = 0.0137$. Solid line: OSECE circuit; Dashed line: standard circuit.

obtained from experimental results, as shown in figure 4.25. The energy loss in the diodes using the standard circuit is also included in the simulations aiming for fair comparisons.

Figure 4.21 shows the experimental and associated numerical harvested powers using the OSECE in the case of a low coupling ($k^2 = 0.0137$). The power response is obtained from equation (4.31) for T_p=2s. Comparing the forward and reverse sweeps power responses, a typical nonlinear hysteresis phenomenon can be observed. The maximum value is 7.7mW at 24.9Hz for forward sweep and 1.6mW at 17.3Hz for reverse sweep. This discrepancy is due to a BSM generator hardening effect when the excitations are strong enough to maintain periodic inter-well motions. As it is the case for nonlinear oscillator showing a hardening stiffness, higher responses are obtained for forward sweeps as shown in figure 4.21.

The power harvested by the BSM generator with standard circuit is also presented for comparison in figure 4.21. More power is harvested using OSECE for both forward and reverse sweep over the whole frequency range, except the small area when the power drops from the maximum point earlier for the OSECE technique than for the standard technique because of the stronger damping effect of OSECE. This damping is associated to: the energy extracted to the load in the one hand and the remained piezoelectric voltage after the switching process in the other hand. This remained piezoelectric voltage keeps the non-extracted energy for the next switching process so that the harvesting efficiency is boosted, especially in low coupling cases.The introduced high piezoelectric counterforce is the result of the electromechanical interaction from the piezoelectric voltage which leads to suppressing the motions of the BSM generator.

When the sweep excitation frequency is away from the natural frequency of the generator, the response is not sensitive to the damping effect of the OSECE circuit and is similar to a constant displacement response. In this situation, more power is extracted and harvested by the OSECE circuit as shown in figure 4.21. The same is true for the reverse sweep response which represents the lowest energy solution of the bistable generator for this excitation amplitude. However, as the forward sweep frequency approaches the natural frequency, the OSECE's damping prevents the motion to increase further. Therefore,

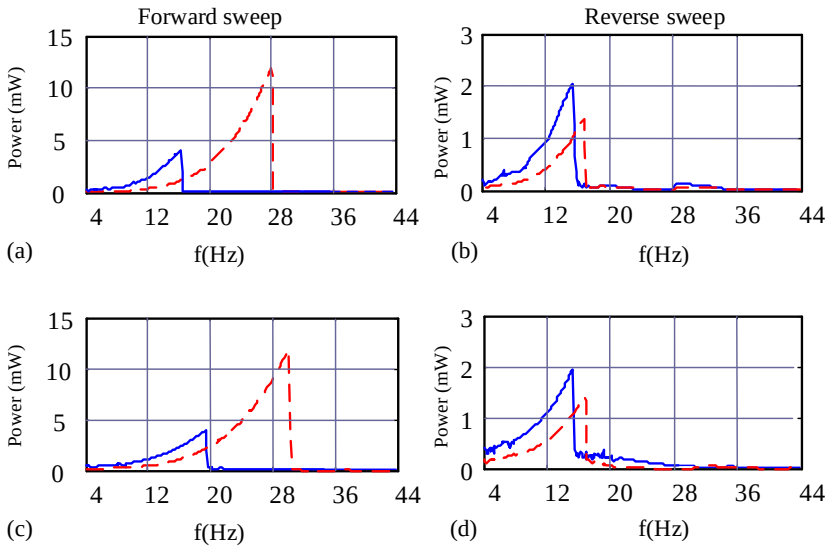

Figure 4.22: Experimental (a, b) and numerical (c, d) harvested power for $k^2 = 0.0684$. *Solid line: OSECE circuit; Dashed line: standard circuit.*

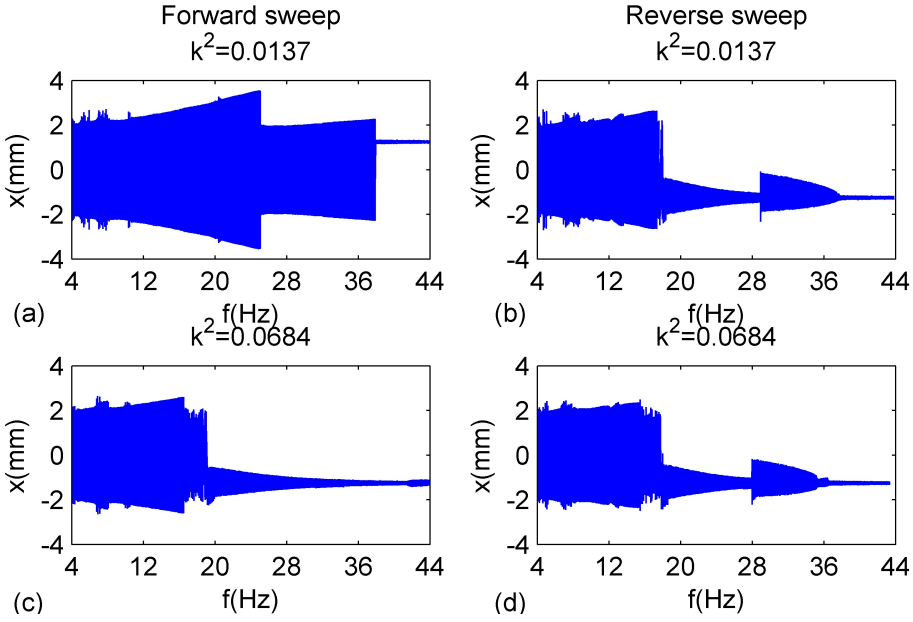

Figure 4.23: Experiment displacement responses of the BSM harvester with OSECE circuit for $k^2 = 0.0137$ *and* $k^2 = 0.0684$.

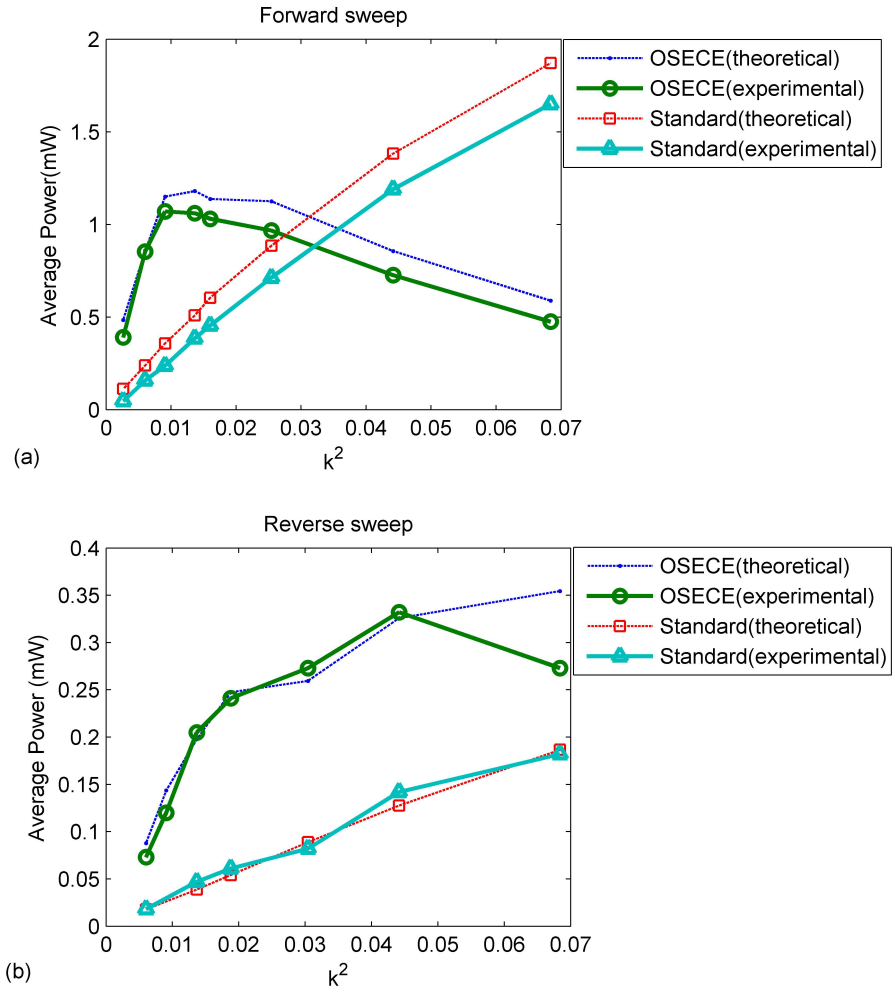

Figure 4.24: Average harvested power versus k^2 for chirp excitation ($4\mathrm{m/s^2}$, 4-44Hz, 0.05Hz/s): (a) forward sweep; (b) reverse sweep.

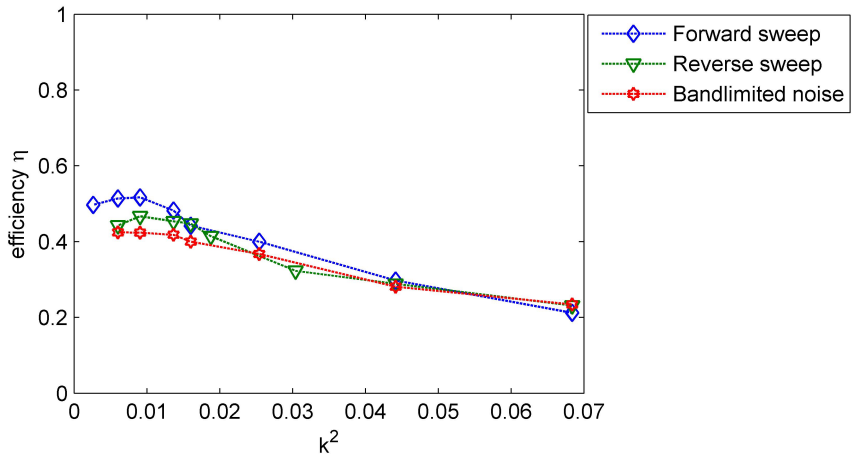

Figure 4.25: Efficiency of the OSECE circuit for different k^2 cases.

the BSM generator's power response drops from the maximum value earlier for OSECE circuit than for standard circuit.

The average power of the OSECE technique over the whole frequency range is 1.06mW (forward sweep) and 0.205mW (reverse sweep) while the value of the standard technique is 0.385mW (forward sweep) and 0.047mW (reverse sweep). These values are calculated using equation (4.31) with T_p representing the whole sweep time for each experiment.

When the electromechanical coupling coefficient is increased to a larger value $k^2 = 0.0684$, the harvested power is shown in figure 4.22. In this high coupling case, the damping effect of the OSECE circuit is more obvious since higher k^2 means stronger electromechanical interaction, thus higher piezoelectric counterforce with the same voltage. The displacement response shown in figure 4.23 clearly demonstrates this increased damping effect with the coupling coefficient. For forward sweep, the inter-well motion ends at the much smaller frequency of 19Hz ($k^2 = 0.0684$) compared with the 38Hz for low coupling ($k^2 = 0.0137$). However, when the excitation frequency is smaller than the frequency at the maximum power point of the OSECE for the forward sweep case as well as the reverse sweep case, the OSECE technique is always better than the standard circuit. It can be related to the less sensitivity of the bistable harvester to the damping in these situations.

In the case of $k^2 = 0.0684$, the average power of the OSECE technique is 0.475mW (forward sweep) and 0.273mW (reverse sweep) while the value of the standard technique is 1.65mW (forward sweep) and 0.182mW (reverse sweep).

The wideband property is validated in figure 4.21 and figure 4.22. The estimated half-power bandwidth of the BSM generator with OSECE circuit in different cases is calculated as follows: 4.32Hz (forward sweep) and 3.5Hz (reverse sweep) for $k^2 = 0.0137$; 3.2Hz (forward sweep) and 3.35Hz (reverse sweep) for $k^2 = 0.0684$. The obtained bandwidth is much larger than for the equivalent linear generator whose bandwidth is about 1Hz for a natural frequency of about 18Hz and a mechanical quality factor of $Q_m = 23.8$. Moreover, better power responses over the low frequency range are also exhibited. The overall consistencies between the experimental and numerical results validates that the BSM generator and the OSECE circuit performance are well predicted by the model which can be used for design and optimization.

The tests have been performed again for several value of k^2, the average power values are plotted in figure 4.24. It is clear that the OSECE shows much better performance for low k^2 cases for both forward and reverse sweep excitations. The power enhancing effect of the OSECE circuit is superior to its damping effect. As k^2 increases, the OSECE induced damping effect increases and exceeds the optimal value. This optimal value is a function of ξ. In these situations, the motion of the BSM generator is over damped. Therefore, the standard circuit gets more power for forward sweep excitations when k^2 is high enough. It is similar to the linear case [7].

By calculating the product k^2Q_m for the BSM generator, it is found that the performance of the combination of the BSM generator and the OSECE technique starts to decrease from $k^2Q_m = 0.33$ ($k^2 = 0.0137$, $Q_m = 23.8$) which is much smaller than the theoretical prediction $k^2Q_m = 1$ obtained in the linear case. It is because the efficiency of the OSECE circuit in this case is not 100% . The same phenomenon is also observed for linear generators [7].

However, for the reverse sweep excitations, the OSECE technique always gets more favorable results since the damping of the OSECE has less influence on the motions. The power increases with the coupling level except for the last experimental result.

As already mentioned, some energy loss factors limit the efficiency of the OSECE

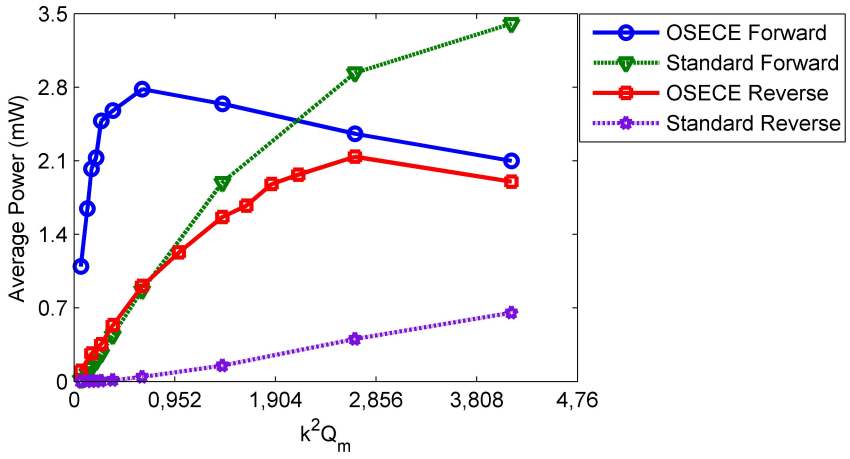

Figure 4.26: Average harvested power comparison between OSECE and standard circuits for $\eta = 1$ by simulation.

circuit. To account for these losses, the efficiency of the OSECE technique has been also evaluated considering the extracted and harvested powers for each experiment (T_p equals the whole sweep time). The results are given in figure 4.25. As k^2 increases, the efficiency decreases because the energy loss is swiftly increased due to the LC circuit quality factor decrease. A second cause is the growing ratio between the diode threshold voltage and the load voltage. Since k^2 is changed by the added serial capacitance, the total capacitance increases with k^2. As a result, the piezoelectric voltage and the load impedance decrease due to the capacitance rising, which makes the load voltage falls. The ratio between the diode forward voltage and the load voltage is then increased, leading to lower efficiency. The measured experimental efficiencies are used in the models so the numerical harvested average power curves are close to the experimental results as can be seen in figure 4.24.

Because the OSECE circuit electronic components were not optimized in this experiment, the efficiency of the device is bounded to about 50% (figure 4.25). To provide a prospective potential of the OSECE technique, the average power with 100% efficiency by simulation is plotted in figure 4.26 versus the product of k^2 and the same mechanical quality factor Q_m. In the ideal case, the performance for the forward sweep declines from the value around $k^2 = 0.04$ corresponding to $k^2 Q_m = 0.952$, close to 1. In the meantime, it is concluded according to the figure that even better performance could be expected by lowering the losses in the magnetic coil, which would require a dedicated and optimized design of the transformer, and by reducing the proportion of the diode voltage to the load voltage.

4.6.4 Band-limited noise excitations

As another typical type of excitation, the band-limited noise is also chosen to test the bistable harvester with OSECE and standard circuits. The band-limited noise is defined here as an ideal white noise passing through a second order 4Hz-20Hz band pass Butterworth filter, RMS 3.5m/s^2 ·

Figure 4.27 shows the transient and average power obtained from the experiment for the two techniques with the same excitation. As we can see, the OSECE presents a much better performance than the standard circuit. An average power of 0.352mW is obtained for the standard technique while the OSECE gets 0.595mW. The power increase is boosted by 69%.

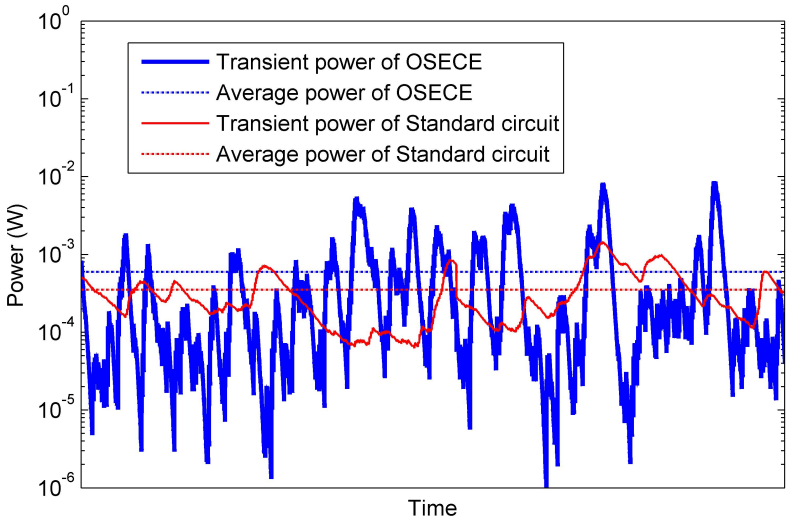

Figure 4.27: Transient and average power comparison between the OSECE circuit and the standard circuit for the band-limited noise ($k^2 = 0.0684$).

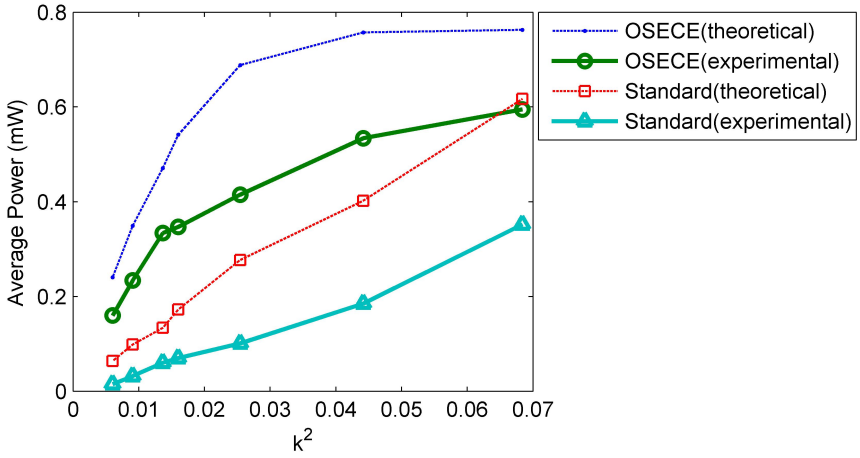

Figure 4.28: Average harvested power of the OSECE and the standard circuit for the bandlimited noise excitation.

To include the influence of the coupling coefficient, the experimental and numerical average powers are obtained for several k^2 values as shown in figure 4.28. The OSECE technique appears to be superior to the standard technique for all cases which is similar to the reverse sweep excitations. For the band-limited noise excitations which contain a wide spectrum, most of the excitation frequencies are away from the natural frequency. As a result, the power-increasing property of the OSECE technique for these excitation parts produces more drastic effects than the overall damping factor.

The simulation results are not exactly consistent with the experimental measurements. However, the same trends between two techniques are validated. Since the harvested power is calculated by the filtered output voltage of the interface circuit, the spectrum information of the harvested power is lost. Therefore, the bandwidth of the BSM generator with OSECE circuit for the band-limited noise excitation case cannot be easily provided. However, the wideband property has been validated in chapter 3 with a pure resistor as the load.

4.7 Self-powered OSECE with mechanical switches for the BSM generator with stoppers

To fulfill the autonomous requirement of the generator, it is quite simple for the standard circuit. However, for the nonlinear interface techniques which need to detect the voltage peak and operate the switches properly, self-powered realization is a key issue.

Lallart et al. [148] developed a PKD (peak detector) circuit for the SSHI circuit while Liang and Liao [149] analyzed and discussed it in details. Some other self-powered approaches such as zero-crossing detector [150] and digital control technique [151] were also proposed. A similar PKD was developed for the OSECE circuit by us [152]. These self-powered techniques take advantages of additional electronic or transduction components to detect the proper voltage extreme and drive the electronic switches accordingly. Recently, Giusa et al. [153] proposed a new approach of RMSHI (Random Mechanical Switching Harvesting on Inductor) based on the SSHI technique using mechanical switches. It needs less electronic parts and shows a zero voltage threshold. However, it is difficult for the mechanical switches to be closed and opened at the proper time to obtain high harvested power. More recently, we successfully used stoppers as mechanical switches for the OSECE circuit on a piezoelectric cantilever beam [154].

For the proposed combination of OSECE circuit and the BSM generator, the PKD developed by us [152] based on the linear generator is still applicable. As an alternative solution, a self-powered approach with a new mechanical switch structure is proposed specially for the BSM generator and the OSECE circuit in this thesis. The switching strategy of the OSECE technique is simple which makes it suitable to replace the electronic approach by a mechanical one. Using mechanical switches, less electronic components are to be used and the electronic energy loss is expected to be reduced. This self-powered approach is applied to a new structure BSMOS (BSM Oscillator with Stoppers).

As we know, beside the bistable generators, introducing stoppers to a linear structure to design a piece-wise oscillator can also allow the bandwidth to be extended at least for the forward sweep [115, 118, 116, 119]. The BSMOS structure aims at capitalizing on the advantages of the two nonlinear techniques (bistability and stoppers) at the same time. The purpose of the stoppers is dual: to obtain a broader bandwidth than the BSM oscillator alone and to be part of the self-powered approach. Besides, the stoppers provide limitations of the structure displacement when over-high excited, and can therefore prevent potential damages. As a result, a self-powered bistable harvester with wider bandwidth can be achieved. The performance of this self-powered BSMOS structure is studied the-

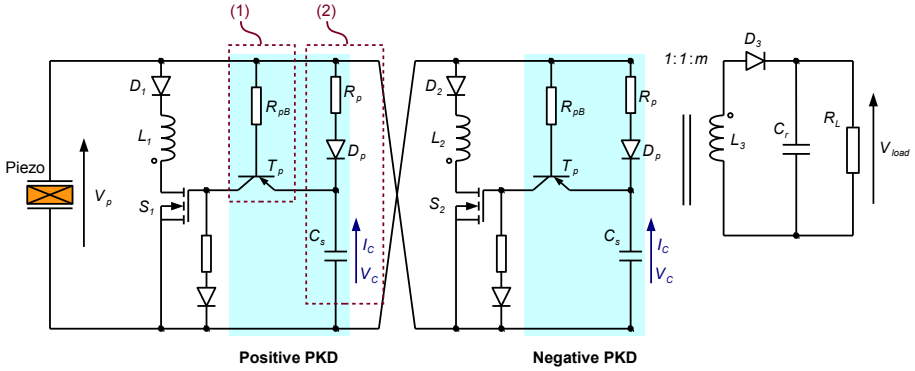

Figure 4.29: Self-powered OSECE circuit [152].

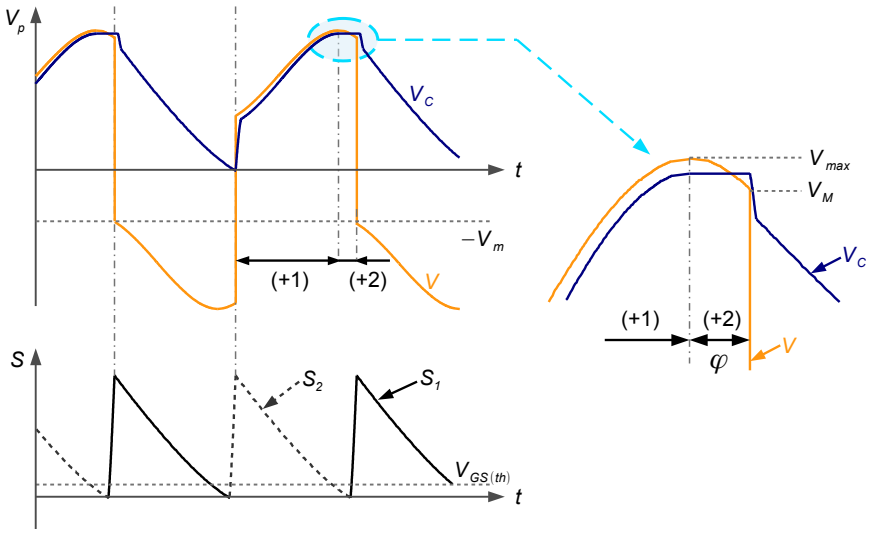

Figure 4.30: Waveforms for the self-powered OSECE circuit [152].

oretically and validated experimentally. Results are compared with the BSM generator using standard circuit.

4.7.1 Self-powered OSECE with an electronic approach

As indicated in former discussions, the performance of the standard circuit is not satisfactory for the low electromechanical coupling cases while OSECE has shown special advantages. It presents a simple switching operation strategy and high harvested power. Moreover, it shows low impedance dependence while only one ground in the circuit makes it easy to be self-powered. Figure 4.29 shows the self-powered OSECE circuit realized with electronic components. Two PKD circuits are added in the original circuit for controlling the switches S_1 (positive PKD) and S_2 (negative PKD) separately.

According to the working principle introduced before, S_1 and S_2 need to be closed and opened alternatively at the proper extrema positions. In the self-powered circuit, it is done by the PKD which is composed of two parts: (1) the comparator and (2) the envelope detector. The envelope detector preserves the voltage peak over a specific period which is determined by the value of R_p and C_s, while the comparator compares the piezoelectric voltage value with the preserved peak. As V_p drops from the peak for the threshold of the Base-Emitter transistor junction (peak detected), T_p is turned on then S_1 or S_2 is driven

to closed by the C_s. At the same time, C_s is discharged so that the switches are opened after a short time. The time is long enough to accomplish the LC transient process.

The waveforms of the self-powered circuit are plotted in figure 4.30. It can be seen that there is a phase lag between the switching signal and the peak of V_p. This phase lag is due to the voltage threshold to turn on the transistor T_p. As discussed in [152], the influence of the phase lag on the harvested power is varied according to the coupling level.

Since the power consumption on the PKD circuits occupies an appreciable portion of the harvested power, the efficiency is decreased. However, better performance is obtained when compared with the standard circuit in the low coupling cases.

Except for the electronic self-powered approach, another approach using mechanical structure to realize the switching operation has been studied to a great extend in the literature [154, 153]. Based on this idea, a novel BSMOS structure with mechanical switches instead of the electronic switch is introduced in the following.

4.7.2 BSMOS structure

As shown in figure 4.31, the proposed BSMOS structure includes three parts: a BSM oscillator, a mechanical switch structure and two stoppers. The BSM oscillator is composed of two piezoelectric components and a central inertial mass connected with flexible hinges. The piezoelectric materials are electrically connected in series.

To realize an autonomous harvester, a double-pole, single-throw mechanical switch structure is introduced into the BSM oscillator. An electrode support is fixed between the flexible hinge and one of the piezoelectric components and follows the rotational motion of the latter. Two separated copper electrodes (the center electrode and the side electrode) are carved. When the moving electrodes part swings with the hinge, the static electrode part is electrically connected to the moving center electrode when the mass cross the zero position and to the moving side electrode when the mass arrives at a given positive or negative displacement. By doing this, the electrical connection is made on and off alternately and the electrodes act as synchronized switches. Moreover, two identical elastic stoppers are symmetrically arranged at the two sides of the mass. When the displacement is large enough to let the mass contact a stopper, the additional stiffness from the stopper presents a more obvious hardening effect than the single BSM oscillator. Then the bandwidth can be increased in some excitation cases. Figure 4.31(b) and table 4.2 define the parameters of the system. In order to get a clear view of the structure configuration, the mechanical switch component is removed in figure 4.31(b).

From a modeling point of view, two springs are used to account for the stoppers. The mechanical potential energy of the BSM oscillator is written as the sum of equation (2.2) and equation (2.3).For the stoppers, the potential is:

$$U_s = \frac{1}{2}K_s(x-d)^2H(x-d) + \frac{1}{2}K_s(x+d)^2H(-x-d) \tag{4.35}$$

where $H(x)$ is the Heaviside function.

Then the total potential energy of the BSMOS structure $U = U_1 + U_2 + U_s$ is plotted and compared with the BSM oscillator in figure 4.32. It is clear that the stoppers bring supplementary stiffness to the BSM oscillator as the potential increases more quickly when the displacement is larger than the stopper position d. Neglecting the mass of the hinges, the mechanical structure and piezoelectric components, the kinetic energy of the system is:

$$T = \frac{1}{2}M\dot{x}^2 \tag{4.36}$$

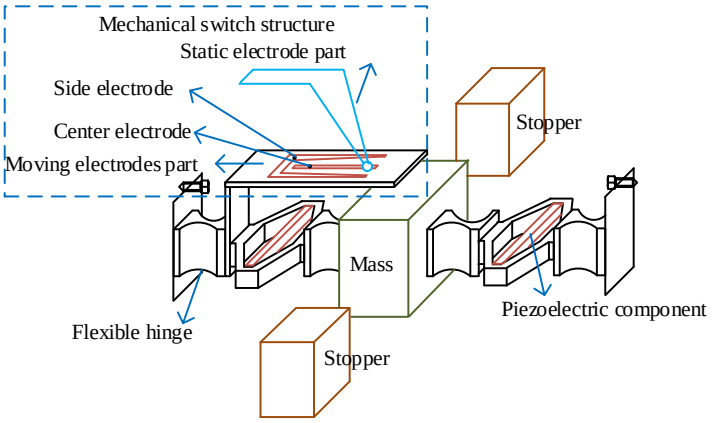

(a)

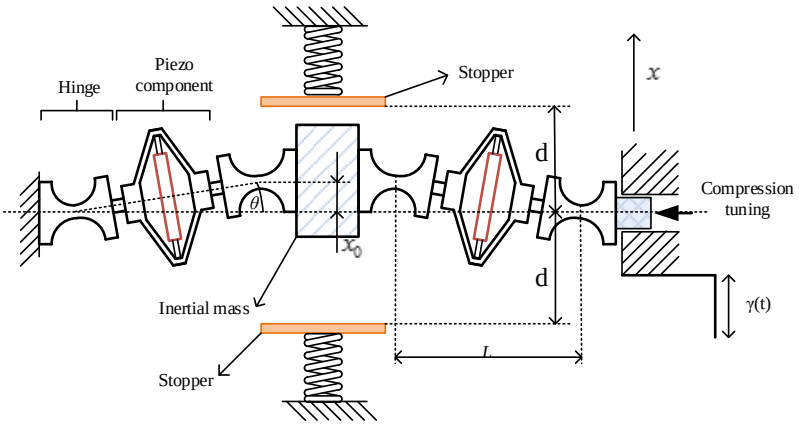

(b)

Figure 4.31: BSMOS structure: (a) 3D schematic plot (with mechanical switches); (b) 2D schematic view (without mechanical switches).

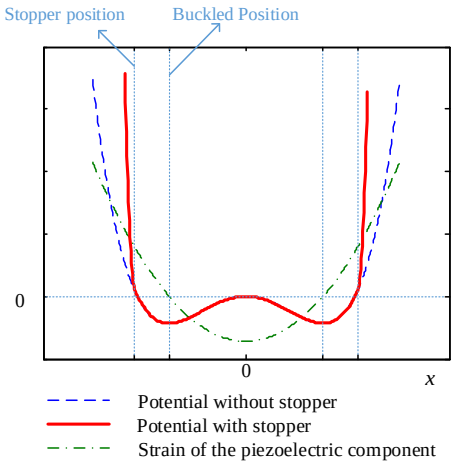

Figure 4.32: Potential of the BSMOS structure and related strain of the piezoelectric element .

Definition of Parameters	Symbol	Value
Mass	M	42 g
Horizontal Distance between two adjacent rotary centers	L	33 mm
Stiffness of one piezoelectric spring	$K/2$	0.195 N/μm
Damping coefficient	μ	0.42 N/(m/s)
Stiffness of the stoppers	K_s	2334 N/m
Distance between the stoppers and the center	d	1.85 mm
Capacitance	C_0	0.154 μF
Piezoelectric force factor	α	0.034 N/V
Initial buckled position	x_0	1.85 mm
Transformer turn ratio	m	0.94

Table 4.2: Definitions of the BSMOS generator parameters

Normalized parameters and variables	Symbol	Definition
Buckling level	ϵ	x_0/L
Electromechanical coupling coefficient	k^2	$\alpha^2/(\alpha^2 + KC_0)$
Mechanical damping coefficient	ξ	$\mu/(2\epsilon\sqrt{KM})$
Characteristic angular frequency	ω_0	$\epsilon\sqrt{K/M}$
Stopper position	ϵ_s	d/L
Stopper damping coefficient	ξ_s	$\mu_s/(2\sqrt{K_sM})$
Characteristic frequency for stopper stiffness	ω_s	$\sqrt{K_s/M}$
Normalized displacement	$\bar{L}$	x/L
Normalized excitation	$\bar{\gamma}$	γ/L
Normalized voltage	$\bar{V}$	$V_p/(\alpha x_0/C_0)$
Normalized current	$\bar{I}$	$I/(\alpha x_0)$
Normalized power	$\bar{P}$	$P/(ML^2)$

Table 4.3: Normalized parameters and variables of the BSMOS generator.

Applying the Euler-Lagrange approach to the device:

$$\frac{d}{dt}\left(\frac{\partial \Pi}{\partial \dot{x}}\right) - \frac{\partial \Pi}{\partial x} = M\gamma - \alpha V_p \frac{x}{L} - \mu_0 \dot{x} - \mu_s \dot{x}(H(x-d) + H(-x-d)) \tag{4.37}$$

where $\Pi = T - U$ is the Lagrangian function, the second term of the right side is the piezoelectric force, the third term is the damping force of the BSM oscillator and the last two terms are damping effects induced by the stoppers. The shock energy dissipation between the mass and the stoppers is included in the damping. Then we have:

$$\begin{aligned} M\ddot{x} + K\left(1 - \frac{l_0}{\sqrt{L^2+x^2}}\right)x + 4K_\theta \frac{x^2}{L^2} = M\gamma - (\mu_s \dot{x} + K_s(x-d))H(x-d) \\ -(\mu_s \dot{x} + K_s(x+d))H(-x-d)) - \mu_0 \dot{x} - \alpha V_p \frac{x}{L} \end{aligned} \tag{4.38}$$

Considering the electric charge balance, the governing equations are written as follows ($x << L$):

$$\begin{cases} M\gamma = M\ddot{x} - \dfrac{K}{2L^2}(l_0^2 - L^2 - \dfrac{8K_\theta}{K})x + \dfrac{Kx^3}{2L^2} + (\mu_s \dot{x} + K_s(x-d))H(x-d) \\ \qquad +(\mu_s \dot{x} + K_s(x+d))H(-x-d)) + \mu_0 \dot{x} + \alpha V_p \dfrac{x}{L} \\ \\ I = \alpha \dfrac{x\dot{x}}{L} - C_0 \dot{V}_p \end{cases} \tag{4.39}$$

in which x_0 defines the initial equilibrium position of the BSM generator (see equation 2.7).

Using the parameters defined in table 4.3, normalized equations can be written as:

$$\begin{cases} \bar{\gamma} = \ddot{\bar{x}} - \dfrac{1}{2}\omega_0^2 \bar{x} + \dfrac{1}{2}\dfrac{\omega_0^2}{\epsilon^2}\bar{x}^3 + (\omega_s^2(\bar{x} - \epsilon_s) + 2\xi_s\omega_s\dot{\bar{x}})H(\bar{x} - \epsilon_s) + 2\xi\omega_0\dot{\bar{x}} \\ \qquad +(\omega_s^2(\bar{x} + \epsilon_s) + 2\xi_s\omega_s\dot{\bar{x}})H(-\bar{x} - \epsilon_s) + \dfrac{k^2}{1-k^2}\dfrac{\omega_0^2\bar{x}}{\epsilon}\bar{V} \\ \\ \bar{I} = \dfrac{\bar{x}\dot{\bar{x}}}{\epsilon} - \dot{\bar{V}} \end{cases} \tag{4.40}$$

In addition to the four critical dimensionless parameters (ϵ, ξ, ω_0, k^2) of the BSM oscillator, there are three new parameters defining the stopper characteristics (ϵ_s, ξ_s, ω_s).

4.7.3 Self-powered OSECE circuit with mechanical switches

Figure 4.33 shows the self-powered OSECE circuit with the mechanical switch structure to be used with the BSMOS structure.

On the moving part of the mechanical switch structure, there are two separate electrodes which are related to the strain evolution of the piezoelectric element. With reference to the strain curve in figure 4.31, the center electrode lets the mechanical switch S_{1m} close at the minimum strain position ($x = 0$) in place of the electronic switch S_1 while the side electrode are meant to connect with the static electrode as a mechanical switch S_{2m} in place of S_2 at fixed positive strain positions related to the displacement maximal amplitude. To adapt the different displacement amplitude for varied excitation strengths, the chosen carved geometry makes the space between the center and the side electrodes varies along the electrode while the static electrode part can be moved horizontally and placed

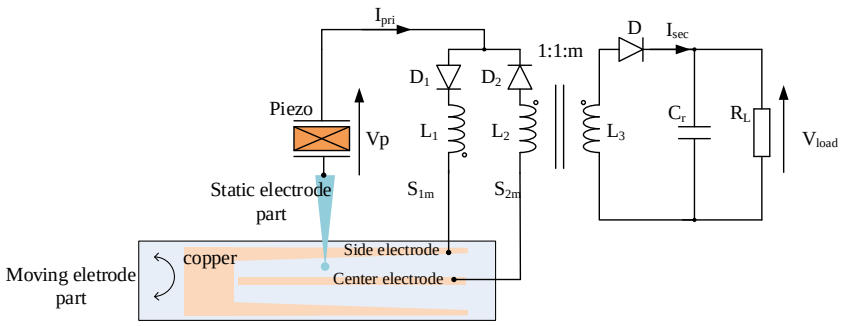

Figure 4.33: Self-powered OSECE with the mechanical switch structure.

at the desired position. In this way, the closed position for the mechanical switch S_{2m} (the side electrode connecting with the static electrode) can be tuned to a certain displacement amplitude. This mechanical switch is especially suitable for the BSM oscillator considering its relatively flat displacement response over a broad frequency range. Reliable mechanical switching is expected once the closed position of S_{2m} is determined according to the displacement amplitude.

In the BSMOS structure, the performance of the self-powered OSECE with a mechanical switch structure can be further improved with the stoppers. When the motions are large enough to touch the stoppers, the displacement is restricted to an almost constant value which simplifies the operation of the mechanical switches. Moreover, it is a good choice to tune the static electrode position to let the mechanical switch S_{2m} close at the stopper position which makes the mechanical switching easier and reliable. No peak detection actions are required since the maximal displacement is about the stopper position where the mechanical switches are to be closed. In the following investigations, this configuration is performed for all simulations and experiments.

4.7.4 Experimental and numerical results

To investigate the performance of the self-powered BSMOS generator, a prototype device has been fabricated and tested. As shown in figure 4.34, the BSMOS structure is composed of three parts: the BSM oscillator, the mechanical switch structure and the stoppers.

Over the BSM oscillator, the moving electrode part is fixed to one of the four flexible hinges through a rectangular aluminum beam, on which the printed circuit board with the moving electrodes is attached. The static electrode can be tuned and fixed on the base in the horizontal direction. To ensure reliable connections and reduce the friction of the mechanical switches, the static electrode is made of the soft probe structure with a smooth steel ball welded at the tip end. Then this soft spring structure is welded with a copper beam which can be deformed to control the contact pre-stress between the static electrode and moving electrode parts.

Two symmetrical springs at the two sides of the BSM oscillator are used as stoppers. Springs are selected to reduce the shock dissipation. The distance between the two stoppers can be easily set using screws. For comparison and simplification purposes, the mechanical switch is adjusted to let S_{2m} closed at the stopper positions for all investigations, as mentioned above.

The structure parameters are shown in table 4.2. The stiffness of the piezoelectric

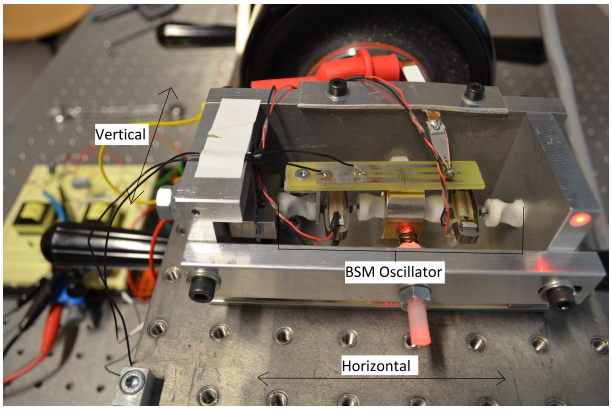

(a)

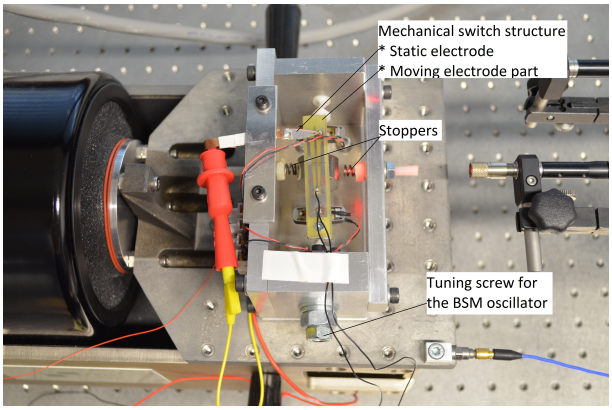

(b)

Figure 4.34: Experimental prototype of the proposed BSMOS generator: (a) Side view; (b) Top view.

components are measured under short-circuit condition while the piezoelectric force factor α is obtained under open-circuit condition. The damping of the BSM oscillator is measured in the small excitation case with the half-bandwidth method. By fitting the simulation to the experimental results, the damping of the stoppers is determined while the spring stiffness coefficient is known through dedicated static experiments. As indicated in the former sections, the power extracted from the electromechanical structure by the OSECE circuit is not totally transferred to the load. Owing to the energy loss of the electronic components such as the transformer and the diodes, the efficiency (the ratio of the power consumed by the load to the extracted power) is limited. As shown in the previous work, the optimal performance of the OSECE technique is obtained for low coupling cases. It is interesting to investigate the performance of the self-powered BSMOS generator which uses the OSECE technique for the same situation. Therefore, the coupling coefficient is decreased to a lower value by connecting an additional capacitance (C_a=0.208 μF) in series with the piezoelectric element. The corresponding values of α and C_0 are shown in table 4.2. Besides, the OSECE efficiency is also improved with higher LC circuit quality factor for the smaller capacitance.

As presented in the previous work of Liu [116] and Soliman [115], the stoppers impose a stiffness-hardening effect on the original oscillator so that it is capable of increasing the bandwidth for the forward sweep excitations. However, for the reverse sweep, no benefit is exhibited (reverse sweep with or without stoppers would lead to similar bandwidth). The high-energy orbit is obtained in the forward case while the low-energy orbit can be

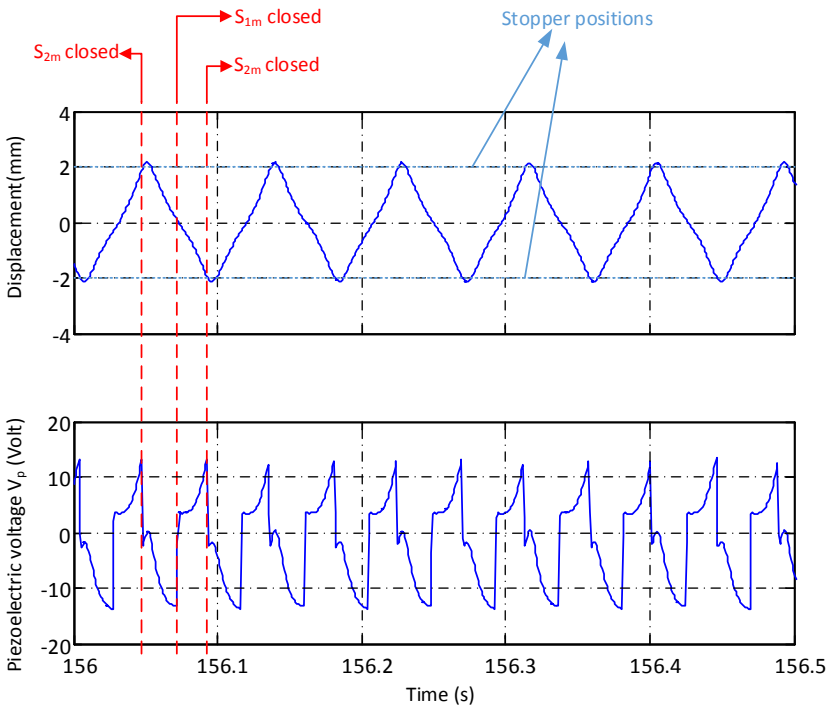

Figure 4.35: Experimental waveforms of the self-powered BSMOS generator ($d = 2mm$).

jumped to the high-energy orbit by changing the initial condition or applying a short and strong impact [128]. For that reason, in this chapter, the performance for the forward excitation only is investigated. Moreover, excitation amplitude of the BSM oscillator has to be sufficient to ensure the favorable inter-well motions (mass jumps from one equilibrium position to another). Compared to the intra-well motions around one buckled equilibrium position, the inter-well motions can generate more power, as shown in chapter 2. Large amplitude inter-well motions are also required for impacting the stoppers. A forward sweep excitation of 5m/s^2 , 5-45Hz is used, ensuring these requirements to be fulfilled.

Figure 4.35 shows the cut-out experiment waveforms of the self-powered BSMOS generator at 12.3Hz with $d = 2mm$. As can be seen, when the mass has crossed the center positions and moves towards a stopper, the piezoelectric elements are maintained in open circuit so the voltage increases with the strain; once the mass hits the stopper, the mechanical switch S_{2m} is closed and the voltage is reversed. Since the stopper is not rigid, the mass displacement is not stopped immediately and the stopper is slightly compressed. As a result, the piezoelectric voltage presents small fluctuations after the inversion. Then the mass is bounded back and moves to the other side while the piezoelectric voltage decreases with the strain. As it crosses the center position, the mechanical switch S_{1m} is closed and the piezoelectric voltage is reversed again at the minimum strain position. Then, the mass moves to the opposite stopper.

It can be seen that the self-powered OSECE circuit with mechanical switch works well while the stoppers limit the displacement to an almost constant value to cooperate with the mechanical switch and help to reduce the voltage fluctuation.

The displacement responses of the proposed self-powered BSMOS generator are plotted in figure 4.36 with two different stopper positions $d = 2mm$ and $d = 1.85mm$. The response of the BSM oscillator with the standard circuit and no stopper is also plotted for

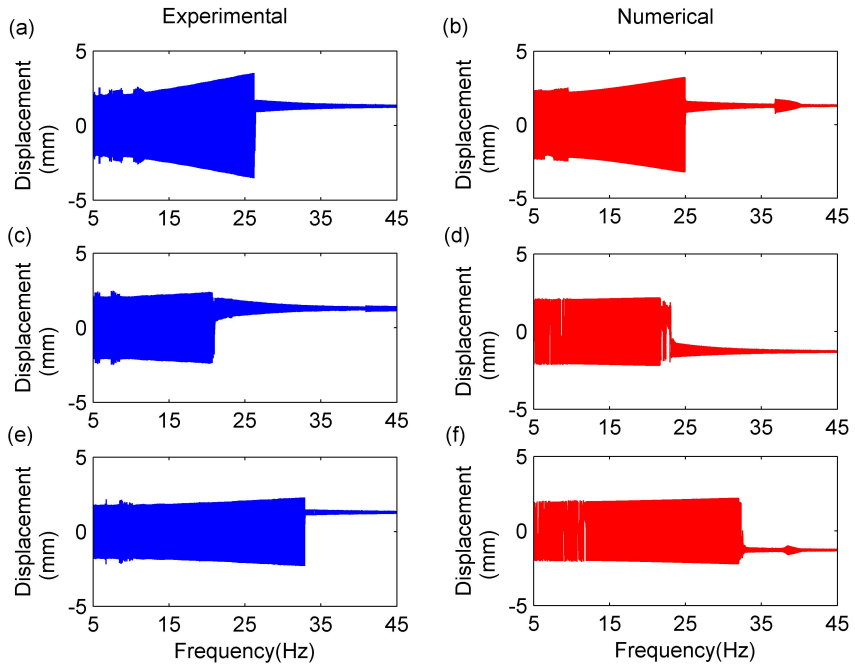

Figure 4.36: Displacement responses of the BSM oscillator with the standard circuit and the self-powered BSMOS generator for a forward sweep excitation: (a, b) BSM oscillator with the standard circuit; (c, d) BSMOS generator with $d = 2mm$; (e, f) BSMOS generator with d=1.85mm.

comparison. For the stoppers position set as $d = 2mm$, the useful band of the inter-well motions is not increased since the damping is large as estimated to be μ_s=5.46 N/(m/s). The large damping is thought to come from the shock and the polymer tape which is used to fix the springs. It is all the more significant as d is large and the spring deformation is small. However, as the stoppers distance is reduced ($d = 1.85mm$), the inter-well motion range is greatly enlarged (5-33Hz compared with 5-27Hz for the BSM oscillator). The damping is measured to decrease to μ_s=1.91 N/(m/s) as the energy loss on the shock and the tape represents a smaller fraction compared to the mechanical energy stored in the springs. The study shows that the damping of the stoppers appears to be a critical point for the performance of the self-powered BSMOS generator. However, the bandwidth increasing effect of the stoppers is demonstrated for bistable generators.

A power gain is also obtained as shown in figure 4.37. The average power over the whole forward sweep process is 0.235mW for the self-powered BSMOS generator while it is only 0.156mW for the BSM oscillator with the standard circuit under the same damping condition. The load for the standard circuit is determined with the matching strategy $R = \pi/(2\omega_0 C_p)$. Considering that the OSECE technique is weakly sensitive to the impedance, the load resistor value is arbitrarily selected to be 10 kΩ. Since the OSECE has not been optimized yet for the efficiency (the calculated efficiency is only around 60%), more power is expected to be reached with dedicated effort to improve the efficiency of the OSECE circuit. Further optimizations have to be made on the transformer and the diodes.

To verify the model, the simulation results using the model in Matlab/Simulink are presented in figure 4.36 and figure 4.37. They are in good accordance with the experimental results, meaning that the model is valid. The inter-well motions end at 32Hz for the simulation and 32.7Hz for the experiment in the case of $d = 1.85mm$ while the experimental maximal power is 1.13mW, close to the simulation value 1.24mW.

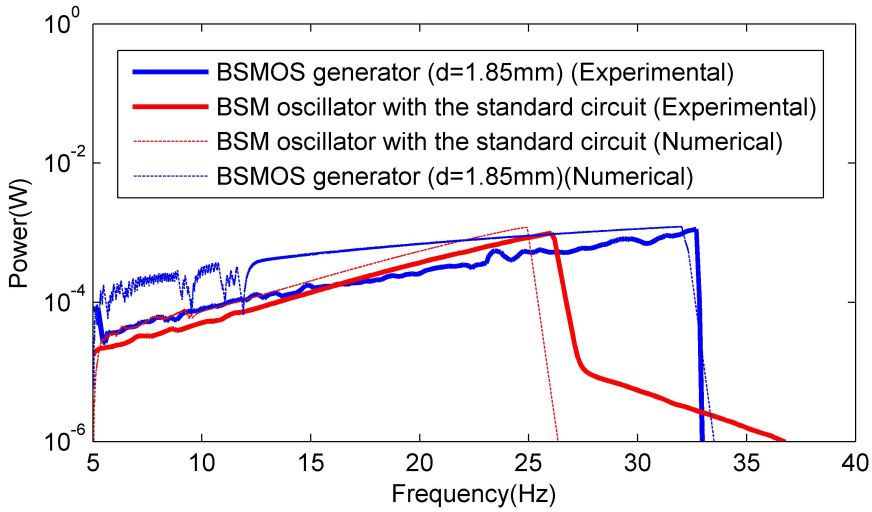

Figure 4.37: Harvested power comparison of the self-powered BSMOS generator ($d = 1.85mm$) and the BSM oscillator with the standard circuit for a forward sweep excitation.

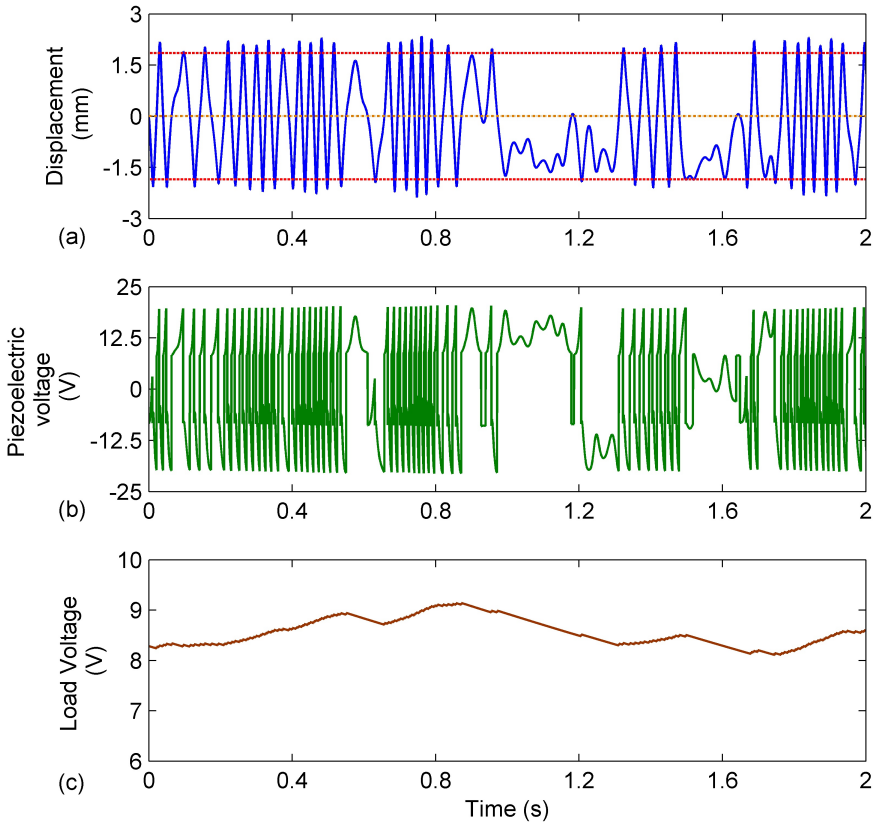

Figure 4.38: Cut-out waveforms of the BSMOS structure for a bandlimited noise excitation by simulation.

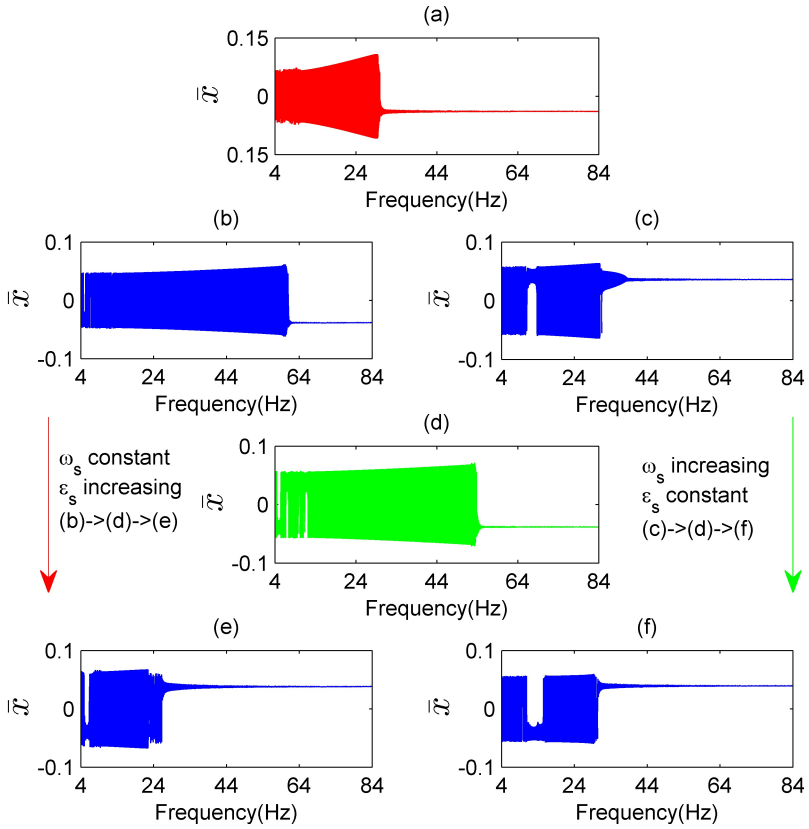

Figure 4.39: Displacement responses of the BSM and BSMOS generators for a forward sweep excitation. (a) BSM generator with standard circuit. (b-f) BSMOS generators with self-powered OSECE circuit: (b) $\omega_s = 8.5\omega_0$, $\epsilon_s = 1.1\epsilon$; (c) $\omega_s = 6\omega_0$, $\epsilon_s = 1.35\epsilon$; (d) $\omega_s = 8.5\omega_0$, $\epsilon_s = 1.35\epsilon$; (e)$\omega_s = 8.5\omega_0$, $\epsilon_s = 1.6\epsilon$; (f) $\omega_s = 11\omega_0$, $\epsilon_s = 1.35\epsilon$.

With the validated model, the effectiveness of the proposed approach is also numerically studied for the random excitation case. Figure 4.38 presents the cut-out waveforms of the displacement and the voltage obtained for a band-limited noise (cut-off frequency 30Hz) with the BSMOS structure. In order to ensure that the mechanical switches operate normally, the RMS value of the excitation is set to 6m/s^2 which is enough to make the mass capable of contacting the stoppers and the center electrodes frequently. The load resistor is set the same as before. As found in figure 4.38, the switching operations are performed well when the mass reaches the stopper positions (the upper and the bottom dashed line in figure 4.38(a)) and the center electrode position (the center dashed line). Stable load voltage is obtained as shown in figure 4.38(c) even though the energy extraction operations are not performed in the small displacement range. It can be inferred that the BSMOS approach is suitable for random excitations which are large enough to trigger the mechanical switch (x_0 can be tuned to achieve this feature for relatively low excitations) .

4.7.5 Discussion and optimization

Since the performance of the self-powered BSMOS structure is dependent on the stopper parameters, more numerical investigations are conducted. The simulations are performed with the normalized model described by equation (4.40) to provide a generic evaluation of the BSMOS structure independently of its dimensions. The relationship between the performance and the parameters are discussed and the optimal parameters are found out.

In order to explain the properties of the proposed new structure with stoppers and

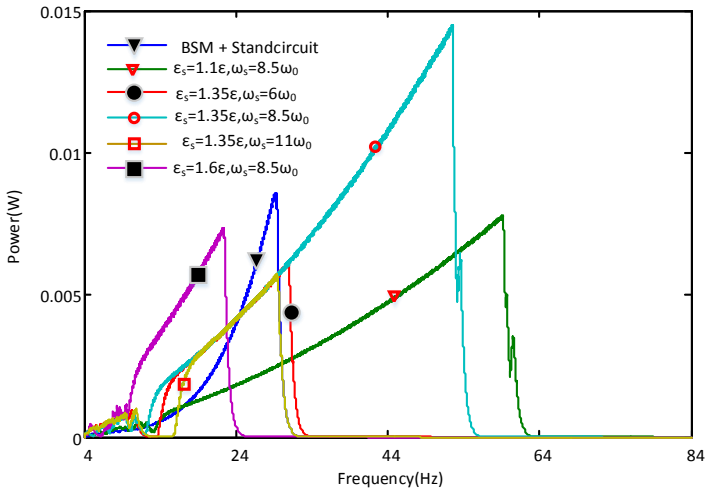

Figure 4.40: Harvested power for the proposed self-powered BSMOS generator and the BSM generator with the standard circuit.

mechanical switch, comparisons are made between the self-powered BSMOS generator and the BSM generator with the standard circuit. For the same BSM oscillator, three additional parameters (ϵ_s, ξ_s, ω_s) account for the stoppers as shown in equation (4.40).

Since the damping of the stoppers is difficult to predetermine, it is better to investigate the optimal parameters (ϵ_s, ω_s) first for a fixed damping value. Figure 4.39 shows the displacement responses of the self-powered BSMOS generator with different stopper parameters (ϵ_s, ω_s) for a 4Hz – 84Hz forward sweep, with an acceleration level corresponding to 4m/s^2 $\cdot$ The parameters of the BSM oscillator are set as $\epsilon = 0.394$, $\omega = 120$, $k^2 = 0.0684$ and $\xi = 0.021$, while the damping of the stoppers is assumed as $\xi_s = 1.5\xi$. The normalizing parameter $L = 33mm$ is set according to the BSM prototype. The response of the BSM generator with the standard circuit is also plotted for reference.

As can be seen in the figure 4.39(b)(d)(e), the inter-well motion range, which represents the useful band, decreases as the stopper positions deviate the initial buckled position (ϵ_s : $1.1\epsilon \rightarrow 1.6\epsilon$) while the stopper stiffness characteristic frequency ω_s is kept constant. The possible reason is that the damping induced by the mechanical structure and the energy extraction circuit lessens as the displacement limited by the stopper gets smaller.

The useful band increases and then declines with the stopper stiffness ω_s as shown in figure 4.39(c)(d)(f) when ϵ_s is maintained at a constant value of 1.35ϵ. It can be inferred that there is an optimal stiffness for the stoppers that leads to the broadest band with the stopper positions fixed.

As the stiffness continues increasing, there is a rapid and large velocity change due to the effect of the stoppers, which breaks the continuity of the forward motions. In this case, no stable inter-well motion solution can be obtained for the forward higher excitation frequencies and the inter-well motions quickly stop. By comparing figure 4.39(b-f) with figure 4.39(a), it is easy to observe that the bandwidth enhancement does not happen for all cases.

The power responses using equation (2.10) are shown in figure 4.40, using the same value of L and M as for the experimental generator. The results of the self-powered BSMOS generator is obtained with the efficiency assumed to be 50%. This relevant value is selected according to experimental results which show that the efficiency is around 50% in most

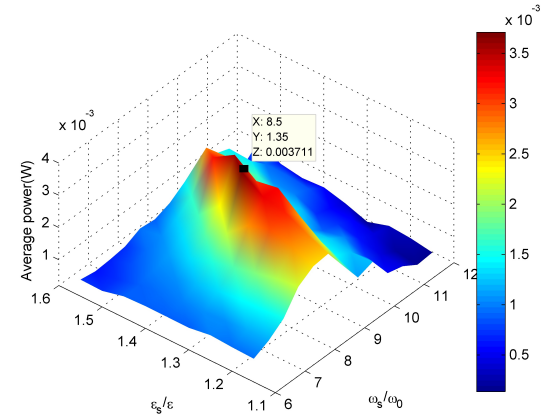

(a)

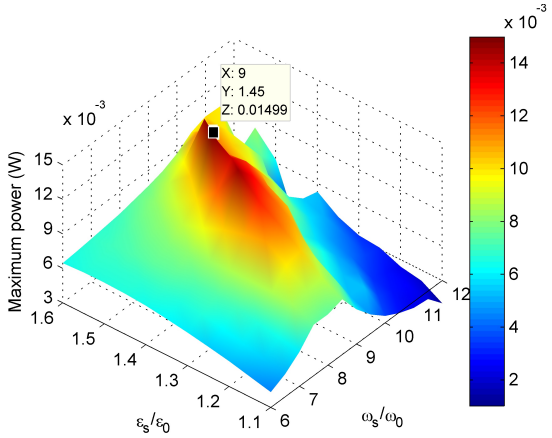

(b)

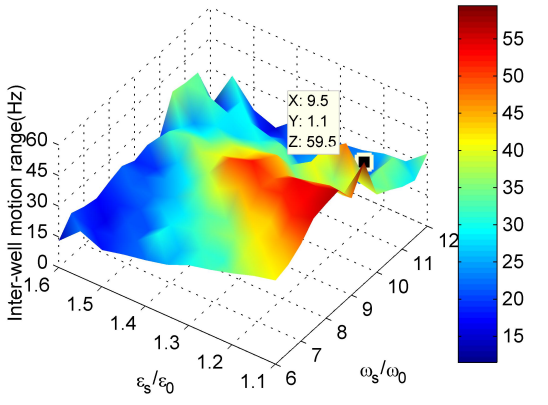

(c)

Figure 4.41: Performance of the self-powered BSMOS generator versus ϵ_s and ω_s: (a) Average harvested power; (b) Max power; (c) Inter-well motion range.

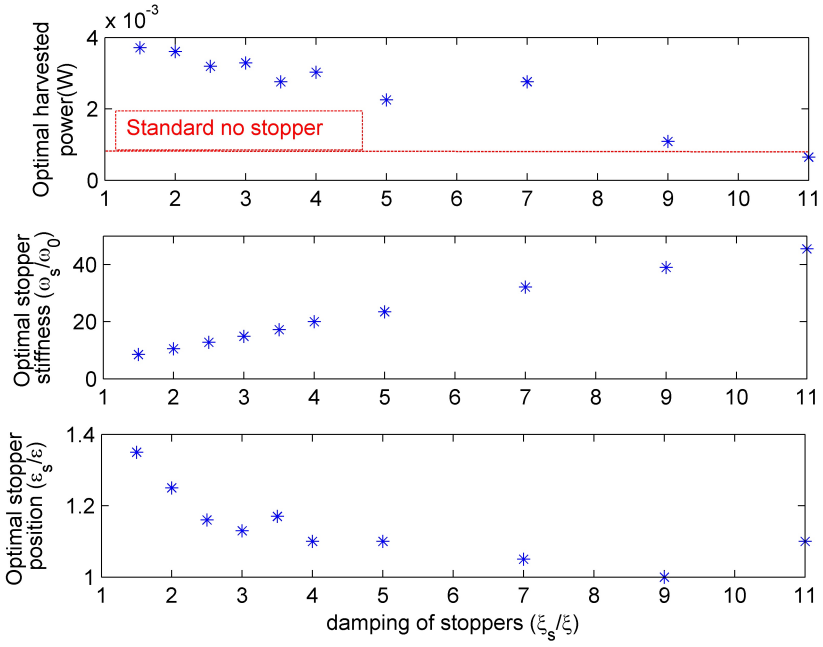

Figure 4.42: Optimal stopper parameter configurations for different ξ_s.

cases. The load values ($R = \pi/(2\omega_0 C_p)$) are determined for all cases by the proposed impedance matching strategy for the BSM generator with the standard circuit. The same load is also used in the OSECE cases. It is clear from figure 4.40 that the harvested power is increased if the proper stopper parameters are selected such as $\omega_s = 8.5\omega_0$, $\epsilon_s = 1.35\epsilon$.

To numerically find out the optimal parameters, multiple simulations are done with different ω_s and ϵ_s values and the average power of each simulation are evaluated and plotted in figure 4.41(a). Then the optimal parameters ($\omega_s = 8.5\omega_0$, $\epsilon_s = 1.35\epsilon$) corresponding to the maximal average harvested power is determined for the fixed stopper damping $\xi_s = 1.5\xi$.

When only the maximum transient power at the peak point of the displacement response is considered, the optimal configuration shown in figure 4.41(b) ($\omega_s = 9\omega_0$, $\epsilon_s = 1.45\epsilon$)is not the same as the best configuration accounted for average power. The reason is that the average power is not only related to the peak power but also the bandwidth.

Figure 4.41(c) plots the inter-well motion range information for the different parameter configurations. The whole frequency range is split into sections of 0.5Hz. Then the inter-motion range is the sum of the section where there are inter-well motions. As indicated in the former sections, the inter-motion range increases while the stopper positions approach the initial buckled position ϵ. Meanwhile, the parameters configuration which gives the maximum inter-well motion range does not coincide with the optimal configuration for the average power. It is in accordance with the results shown in 4.40, which further validates the compromise to be done for the average power, the max transient power and bandwidth.

The optimal parameters configuration $\omega_s = 8.5\omega_0$, $\epsilon_s = 1.35\epsilon$ is surprisingly not located in the range of smaller ϵ_s values which represent wider useful band. In fact, as ϵ_s decreases, the motions of the BSMOS generator are limited to smaller amplitudes and less power can be harvested since the strain is proportionately limited. Therefore, a tradeoff needs to be dealt with between the bandwidth and the harvested power.

Since the damping of the stoppers ξ_s is related to the chosen materials and the struc-

tures of the stoppers, it is necessary to investigate its influence on the performance. Therefore, we change ξ_s and find the optimal parameters (ϵ_s,ω_s) for each value. The max average power and the optimal parameter values are plotted versus ξ_s in figure 4.42. As expected, as the damping of the stoppers increases, the maximal average power decreases, the optimal stiffness increases and the optimal stopper position gets close to the equilibrium position. With higher ω_s and smaller ϵ_s, the deformation of the stoppers is reduced so that the damping loss is restricted. The average power of the BSM oscillator with the standard approach is plotted with the dashed line. As indicated in figure 4.42, the self-powered BSMOS structure has much better performance when the damping of the stoppers is small and the proper stiffness and positions are selected with careful design.

4.8 Conclusion

A wideband energy harvesting technique with bistable generator and nonlinear switching harvesting circuits is proposed to figure out the challenge of variable vibrations. After detailed analysis and comparisons between some common harvesting circuits, the OSECE technique is selected to be used with the BSM bistable generator to provide high efficiency energy scavenging. The performance is evaluated for a whole range of electromechanical coupling coefficients and different representative excitation cases with the standard circuit as a reference.

The simulation and experimental investigations show that the OSECE circuit can significantly enhance the harvested energy for low k^2 cases. When k^2 increases to high values, the OSECE circuit brings more damping to the BSM generator rather than the efficiency enhancing effect, leading to less harvested energy.

The situation is quite different for the reverse sweep and the band-limited excitations. For these cases in which the bistable generator behavior is not so sensitive to the damping, the performances of the OSECE technique are always superior to the standard circuit for the whole tested k^2 value range.

Considering that aiming at high k^2 implies more piezoelectric material cost and a high integration requirement, the value of most generators is usually low for common applications. Moreover, the real excitation is more likely similar to the noise signals. As a result, the OSECE technique is to be chosen instead of the standard circuit, especially for the excitation cases in which the damping effect has low influence. Besides, the OSECE circuit is not fully optimized in the experiment. With extra dedicated efforts to improve the efficiency, especially with an optimally designed transformer instead of the use of commercial transformers, the performance is expected to be improved. The combination of bistable generators and OSECE technique has a good prospect for wideband and high efficient energy harvesting.

Then, an autonomous BSMOS generator is proposed with two improvements: the self-powered OSECE circuit with the mechanical switches and the stoppers. The former one is a new self-powered approach for the OSECE circuits with the BSM generator. Compared with the self-powered electronic technique with the PKD circuit, it needs fewer components so that the energy loss on the PKD circuit and the electronic switches is avoided. Introducing stoppers to the BSM oscillator is also another important modification. The hardening effect of the stoppers is capable of further increasing the bandwidth (in the case of forward sweep) by contrast to the BSM oscillator. Therefore, an autonomous wideband generator with very good performance is obtained.

The model of this new BSMOS generator is obtained and the normalizations are also done to provide general and useful information for design and scaling. The model has been

Approaches	Advantages	Drawbacks
BSM+Standard circuit	Simple; Self-powered; Good performance in high electromechanical coupling and output voltage cases	Load dependence; Poor performance in low coupling and low output voltage cases
BSM+OSECE	Simple switching strategy; High performance in low coupling cases; Weak load dependence	Self-powered circuit required; High Q circuit required; Decreased performance at high coupling cases
BSMOS	Bandwidth further enlarged; Self-powered; Performance improved in some cases; Weak load dependence	Excitation strength constraint; Strong dependency on both structure configuration and excitations; High Q circuit required

Table 4.4: Comparison between the harvesting approaches.

compared with experimental results and shows good correlation.

Better performance is also theoretically and experimentally observed for the BSMOS generator compared with the BSM oscillator with the standard circuit. Further discussions and optimizations have been performed. The relationship between the performance and the stopper parameters have been investigated especially. Using the optimal parameters and minimizing the damping of the stoppers, a new prototype could reach better performance.

To have an overall idea about the investigated harvesting approaches with the BSM generator in this thesis, table 4.4 shows the advantages and drawbacks of each method. It is suggested to select the proper harvesting method according to the specific application environment and the BSM generator parameters.

Conclusions

Vibration energy harvesting is one of the most promising technologies among the large number of potential renewable energy solutions. Early investigations are focused on linear resonance structures which are intended to pick up the excitation peak frequency to get the maximum available energy with the quasi-stationary excitation assumption. Some conventional transduction methods are developed such as piezoelectric, electromagnetic, electrostatic etc.. The efforts generally aim at decreasing the structural damping, increasing the electromechanical coupling level, minimizing the volume and optimizing the interface circuit.

The idea of developing wideband vibration harvesters comes from the fact that the environmental vibrations are usually varying and depending on different conditions. The variability of the vibrations makes it questionable to provide stable and sufficient power output with linear generators. To figure out this issue, wideband harvesters are brought to light. With detailed literature studies, several typical approaches to widen the operation bandwidth are presented in this thesis, including resonance tuning structures, multi-modal oscillators, frequency-up-conversion mechanisms, and nonlinear generators. Compared with other branches of the nonlinear generators such as monostable softening or hardening oscillators and piecewise structures, the bistable generator is especially interesting for its good performance at both low and high frequency range. According to the architectures, the bistable generators are able to be classified into two main categories: buckling effects and magnetic interactions.

The bistable structures using buckling effects have some advantages in the miniaturization and power density. Some very common examples are the buckled beams and plates, for which the complexities of model and the susceptibilities of the fabrications and the boundary conditions hinder the optimization and design of these structures. Therefore, a novel bistable generator which can be simplified with the buckled-spring-mass architecture is proposed and studied. It is simple and compact with two piezoelectric transducers, an inertial mass and four flexible hinges united together. With the model developed and normalized, the harmonic analytical method is performed to obtain the initial idea of the relationship between the performance and the parameters. Based on the analysis, a macro BSM prototype of decimeter scale is fabricated and tested. Experimental and numerical investigations with the chirp and noise excitations show that the proposed BSM generator has much better performance than the linear equivalent one regarding the operation band. The performance is especially superior when the characteristic frequency of both BSM and linear generators are higher than the band-limited noise excitation range. Comparisons are made between the BSM prototype and some literature generators. A power density of 3.7 $\mu W/cm^3$ by normalizing the excitation to $10m/s^2$ is obtained, which is shown to be among the best performance.

It is also validated that experimental results have good consistency with the theoretical results predicted by the model. The complex nonlinear dynamics of the BSM generator are also investigated with the bifurcation map and the spectrum method from the experimental and simulated view. A strange attractor of this structure is observed in both the experiment

and the simulation, which further proves the accuracy of the model. In order to achieve better performance from the high-energy inter-well motions, the initial conditions are a key factor.

Using the developed model, optimizations have been performed on the critical parameters to get the best performance. The optimization strategy is proposed with the detail operations concluded. Applying the corresponding procedure, an optimal parameter configuration can be found for a specific excitation. It is explicated for the typical chirp and noise excitations. The influence of the parameters is also discussed. Moreover, it is shown that the shape of the BSM generator's potential curve including the barrier's height and width plays a critical role on the available power.

Besides the general parameter optimization, some compulsory design considerations need to be taken into account, such as volume and safety constraints. Special discussions are devoted to the hinges which are also critical parts for the determination of the maximum available displacement. Following the optimization and additional design procedures, a mono-block miniaturized BSM generator is fabricated with the volume of 5.46 cm^3. The performance is studied with chirp signals, band-limited noises and a replicated excitation from a driving car wheel. Prospective application potentials are confirmed through the tests. An autonomous wireless monitoring and communication demonstration platform is designed to show the wideband operation capability.

Moreover, a NPBP figure of merit is proposed for making fair comparisons between the developed wideband generators. Power and bandwidth are included in a single index which facilitates the evaluation of the generator.

As the other important aspect of the energy harvester, the interface circuits have made great advancements. By comparing several common energy extraction methods, the OSECE circuit is selected to work with the BSM generator. This new approach is meant to enhance the harvested energy over a wide frequency range by taking the advantages of the two. It is shown that the combination of two advance technologies brings some obvious advantages over the combination of the BSM generator and the standard circuit. The performance is investigated for varied electromechanical coupling levels with different excitations. A Simulink model is also developed and validated with the experimental results. The damping from the extraction circuit is thoroughly analyzed. When the interface circuit exerts less damping on the generator in the low coupling cases, the harvested power is always better for the new approach since more energy can be extracted with the OSECE technique. It is especially obvious at the low-frequency range where the BSM generator is not sensitive to the damping. This point is also shown for the reverse sweep and band-limited noise cases. For the cases of high coupling level and forward sweep, the performance gets worse because of the lack of mechanism to tune the extract energy to match the mechanical damping.

In the end, mechanical switches and stoppers are introduced into the BSM generator and the OSECE circuit to present a novel self-powered approach. Instead of the conventional self-powered solution with electronic circuits, the mechanical switch method requires less components and leads to less energy loss. Meanwhile, the existence of the stoppers is able to effectively further extension of the operation bandwidth by capitalizing the advantages of the piecewise and the BSM structures. The proposed method is validated with experimental and numerical investigations. With proper configurations, the performance is shown to be improved for the BSM generator with stand circuit. Optimizations and discussions are done to study the optimal potential of the BSMOS generator.

Although a well designed BSM centimeter generator has been fabricated, there are

still several points to be improved, especially about the coupling level and the protection stoppers. Better performance for the BSM generator and its derived BSMOS structure are predictable with these future works to be done.

Bibliography

[1] Emmanuelle Arroyo. *Récupération d'énergie à partir des vibrations ambiantes: dispositif électromagnétique et circuit électronique d'extraction synchrone*. PhD thesis, Université de Savoie, 2012.

[2] E Lefeuvre, A Badel, C Richard, L Petit, and D Guyomar. A comparison between several vibration-powered piezoelectric generators for standalone systems. *Sensors and Actuators A: Physical*, 126(2):405–416, 2006.

[3] D Guyomar, A Badel, E Lefeuvre, and C Richard. Toward Energy Harvesting Using Active Materials and Conversion Improvement by Nonlinear Processing. *IEEE transactions on ultrasonics, ferroelectrics, and frequency control*, 52(4):584–595, 2005.

[4] A Badel, D Guyomar, E Lefeuvre, and C Richard. Efficiency enhancement of a piezoelectric energy harvesting device in pulsed operation by synchronous charge inversion. *Journal of Intelligent Materials Systems and Structures*, 16:889–901, 2005.

[5] E. Lefeuvre. Piezoelectric Energy Harvesting Device Optimization by Synchronous Electric Charge Extraction. *Journal of Intelligent Material Systems and Structures*, 16(10):865–876, 2005.

[6] M Lallart, L Garbuio, L Petit, C Richard, and D J Guyomar. Double synchronized switch harvesting (DSSH): a new energy harvesting scheme for efficient energy extraction. *IEEE transactions on ultrasonics, ferroelectrics, and frequency control*, 55(10):2119–2130, 2008.

[7] Y Wu, A Badel, F Formosa, W Liu, and A E Agbossou. Piezoelectric vibration energy harvesting by optimized synchronous electric charge extraction. *Journal of Intelligent Material Systems and Structures*, 24(12):1445–1458, 2012.

[8] L Tang, Y Yang, and CK Soh. Toward broadband vibration-based energy harvesting. *Journal of Intelligent Material Systems and structures*, 21(18):1867, 2010.

[9] J Twiefel and H Westermann. Survey on broadband techniques for vibration energy harvesting. *Journal of Intelligent Material Systems and Structures*, 24(11):1291–1302, 2013.

[10] E S Leland and P K Wright. Resonance tuning of piezoelectric vibration energy scavenging generators using compressive axial preload. *Smart Materials and Structures*, 15:1413–1420, 2006.

[11] S Roundy and Y Zhang. Toward self-tuning adaptive vibration based microgenerators. In *Proc. of SPIE Vol.5649*, volume 5649, pages 373–384, 2005.

[12] V R Challa, M G Prasad, Y Shi, and F T Fisher. A vibration energy harvesting device with bidirectional resonance frequency tunability. *Smart Materials and Structures*, 17(1):015035, 2008.

[13] S M Shahruz. Design of mechanical band-pass filters for energy scavenging. *Journal of Sound and Vibration*, 292:987–998, 2006.

[14] H Xue, Y Hu, and Q Wang. Broadband piezoelectric energy harvesting devices using multiple bimorphs with different operating frequencies. *IEEE transactions on ultrasonics, ferroelectrics, and frequency control*, 55:2104–2108, 2008.

[15] Y Tadesse and S Priya. Multimodal Energy Harvesting System: Piezoelectric and Electromagnetic. *Journal of Intelligent Material Systems and Structures*, 20(5):625–632, 2008.

[16] M Pozzi and M Zhu. Plucked piezoelectric bimorphs for energy harvesting applications. In Ulrich Schmid, José Luis Sánchez-Rojas, and Monik Leester-Schaedel, editors, *Proc. of SPIE Vol.8066*, volume 8066, page 806616, 2011.

[17] R Ramlan, M J Brennan, B R Mace, and I Kovacic. Potential benefits of a non-linear stiffness in an energy harvesting device. *Nonlinear Dynamics*, 59(4):545–558, 2009.

[18] M F Daqaq, R Masana, A Erturk, and D Dane Quinn. On the Role of Nonlinearities in Vibratory Energy Harvesting: A Critical Review and Discussion. *Applied Mechanics Reviews*, 66(4):040801, 2014.

[19] R L Harne and K W Wang. A review of the recent research on vibration energy harvesting via bistable systems. *Smart Materials and Structures*, 22(2):023001, 2013.

[20] S P Pellegrini, N Tolou, M Schenk, and J L Herder. Bistable vibration energy harvesters: A review. *Journal of Intelligent Material Systems and Structures*, 24(11):1303–1312, 2013.

[21] A Masuda, A Senda, T Sanada, and A Sone. Global stabilization of high-energy response for a Duffing-type wideband nonlinear energy harvester via self-excitation and entrainment. *Journal of Intelligent Material Systems and Structures*, 24(13):1598–1612, 2013.

[22] I Neri, F Travasso, R Mincigrucci, H Vocca, F Orfei, and L Gammaitoni. A real vibration database for kinetic energy harvesting application. *Journal of Intelligent Material Systems and Structures*, 23(18):2095–2101, 2012.

[23] http://www.ti.com.

[24] D Dunn-Rankin, E M Leal, and D C Walther. Personal power systems. *Progress in Energy and Combustion Science*, 31(5-6):422–465, 2005.

[25] S Cho and C B Yun. Smart wireless sensor technology for structural health monitoring of civil structures. *Steel Structures*, 8:267–275, 2008.

[26] L Ruiz-Garcia, L Lunadei, P Barreiro, and J I Robla. A review of wireless sensor technologies and applications in agriculture and food industry: state of the art and current trends. *Sensors (Basel, Switzerland)*, 9(6):4728–50, 2009.

[27] L M Oliveira and J J Rodrigues. Wireless Sensor Networks: a Survey on Environmental Monitoring. *Journal of Communications*, 6(2):143–151, 2011.

[28] J G Ko, C Lu, and M B Srivastava. Wireless sensor networks for healthcare. *Proceedings of the IEEE*, 98(11):1947–1960, 2010.

[29] W Shen, Y Lei, L Hu, and Y Wang. Feasibility of Output-Only Modal Identification Using Wireless Sensor Network: A Quantitative Field Experimental Study. *International Journal of Distributed Sensor Networks*, 2012:560161, 2012.

[30] D Wanless. Securing our future health: Taking a long term view. Technical report, HM Treasury, U.K, 2002.

[31] A Flowerday and R Smith. Lessons learnt from long-term chronic condition monitoring. In *Proc. 1st Int. Workshop Wearable Implantable Body Sensor Netw.*, page 48, 2004.

[32] A Darwish and A E Hassanien. Wearable and implantable wireless sensor network solutions for healthcare monitoring. *Sensors*, 11(6):5561–95, 2011.

[33] J P Lynch. A Summary Review of Wireless Sensors and Sensor Networks for Structural Health Monitoring. *The Shock and Vibration Digest*, 38(2):91–128, 2006.

[34] J A Paradiso and T Starner. Energy scavenging for mobile and wireless electronics. *Pervasive Computing, IEEE*, 4:18–27, 2005.

[35] P D Mitcheson, E M Yeatman, G K Rao, A S Holmes, and T C Green. Human and Machine Motion for Wireless Electronic Devices. *Proceedings of the IEEE*, 96(9):1457–1486, 2008.

[36] J Sauerbrey, D Schmitt-Landsiedel, and R Thewes. A 0.5 V 1 µW successive approximation ADC. *IEEE J. Solid-State Circuit*, 38:1261–1265, 2003.

[37] S P Beeby, M J Tudor, and N M White. Energy harvesting vibration sources for microsystems applications. *Measurement Science and Technology*, 17(12):R175–R195, 2006.

[38] L Zuo and X Tang. Large-scale vibration energy harvesting. *Journal of Intelligent Material Systems and Structures*, 24(11):1405–1430, 2013.

[39] http://www.fujitsu.com.

[40] S Roundy, P K Wright, and J Rabaey. A study of low level vibrations as a power source for wireless sensor nodes. *Computer Communications*, 26(11):1131–1144, 2003.

[41] V Leonov and R J M Vullers. Thermoelectric generators on living beings. In *Proceedings of the 5th European Conference on Thermoelectrics*, pages 47–52, 2007.

[42] E M Yeatman. Advances in power sources for wireless sensor nodes. In *Proceedings of the International Worshop Wearable and Implantable Body Sensor Networks*, pages 20–21, 2004.

[43] http://www.thorlabs.de/tutorials/tables2.cfm?

[44] O Puscasu, S Monfray, J Boughaleb, P J Cottinet, D Rapisarda, E Rouvière, G Delepierre, C Maître, F Boeuf, D Guyomar, and T Skotnicki. Flexible bimetal and piezoelectric based thermal to electrical energy converters. *Sensors and Actuators A: Physical*, 2014.

[45] D Avirovik, A Kumar, R J Bodnar, and S Priya. Remote light energy harvesting and actuation using shape memory alloy-piezoelectric hybrid transducer. *Smart Materials and Structures*, 22(5):052001, 2013.

[46] A Erturk and G Delporte. Underwater thrust and power generation using flexible piezoelectric composites: an experimental investigation toward self-powered swimmer-sensor platforms. *Smart Materials and Structures*, 20(12):125013, 2011.

[47] X Wang, C L Pan, Y B Liu, and Z H Feng. Electromagnetic resonant cavity wind energy harvester with optimized reed design and effective magnetic loop. *Sensors and Actuators A: Physical*, 205:63–71, 2014.

[48] S Roundy and P K Wright. A piezoelectric vibration based generator for wireless electronics. *Smart Materials and Structures*, 13(5):1131–1142, 2004.

[49] A Erturk and D J Inman. On Mechanical Modeling of Cantilevered Piezoelectric Vibration Energy Harvesters. *Journal of Intelligent Material Systems and Structures*, 19(11):1311–1325, 2008.

[50] P Glynne-Jones, S P Beeby, and White N W. Towards a piezoelectric vibration powered microgenerator. *IEE Proceedings-Science, Measurement and Technology*, 148(2):68–72, 2001.

[51] Q C Guan, B Ju, J W Xu, Y B Liu, and Z H Feng. Improved strain distribution of cantilever piezoelectric energy harvesting devices using H-shaped proof masses. *Journal of Intelligent Material Systems and Structures*, 24(9):1059–1066, 2013.

[52] J W Xu, W W Shao, F R Kong, and Z H Feng. Right-angle piezoelectric cantilever with improved energy harvesting efficiency. *Applied Physics Letters*, 96(15):152904, 2010.

[53] S Basrour and B Charlot. Design and fabrication of piezoelectric micro power generators for autonomous microsystems. In *IEEE DTIP*, pages 299–302, 2005.

[54] Y B Jeon, J H Jeong, R Sood, and S G Kim. Mems power generator with transverse mode thin film pzt. *Sensors and Actuators A: Physical*, 122(1):16–22, 2005.

[55] H Liu, C Lee, T Kobayashi, C J Tay, and C Quan. A new S-shaped MEMS PZT cantilever for energy harvesting from low frequency vibrations below 30Hz. *Microsystem Technologies*, 18(4):497–506, 2012.

[56] K A Cook-Chennault, N Thambi, and A M Sastry. Powering MEMS portable devices-a review of non-regenerative and regenerative power supply systems with special emphasis on piezoelectric energy harvesting systems. *Smart Materials and Structures*, 17(4):043001, 2008.

[57] N S Shenck and J A Paradiso. Energy scavenging with shoe-mounted piezoelectrics. *IEEE Micro*, 21(3):30–42, 2001.

[58] H A Sodano, G Park, D J Leo, and D J Inman. Use of piezoelectric energy harvesting devices for charging batteries. In *Proc. SPIE 10th Annual Int. Symp. on Smart Structures and Materials*, page 101–108, 2003.

[59] L Mateu and F Moll. Appropriate charge control of the storage capacitor in a piezoelectric energy harvesting device for discontinuous load operation. *Sensors and Actuators A: Physical*, 132:302–310, 2006.

[60] B Yang and K S Yun. Piezoelectric shell structures as wearable energy harvesters for effective power generation at low-frequency movement. *Sensors and Actuators A: Physical*, 188:427–433, 2012.

[61] A K Bonsi. Fatigue of piezoelectric beams used in vibration energy harvesting. Master's thesis, McGill University, 2010.

[62] C B Williams and R B Yates. Analysis of a micro-electric generator for microsystems. *Sensors and Actuators A: Physical*, 52:8–11, 1996.

[63] C B Williams, C Shearwood, M A Harradine, P H Mellor, T S Birch, and R B Yates. Development of an electromagnetic micro-generator. *IEE Proceedings - Circuits, Devices and Systems*, 148(6):337, 2001.

[64] P Glynne-Jones, S P Tudor, M Jand Beeby, and N M White. An electromagnetic, vibration-powered generator for intelligent sensor systems. *Sensors and Actuators A: Physical*, 110:344–349, 2004.

[65] E Arroyo, A Badel, and F Formosa. Energy harvesting from ambient vibrations: Electromagnetic device and synchronous extraction circuit. *Journal of Intelligent Material Systems and Structures*, 24(16):2023–2035, 2013.

[66] D Spreemann, B Folkmer, and Y Manoli. Comparative study of electromagnetic coupling architectures for vibraton energy harvesting devices. In *Proceedings of PowerMEMS*, pages 257–260, 2008.

[67] C T Pan and T T Wu. Development of a rotary electromagnetic microgenerator. *Journal of Micromechanics and Microengineering*, 17(1):120–128, 2007.

[68] D Marioli, E Sardini, and M Serpelloni. Electromagnetic Generators Employing Planar Inductors for Autonomous Sensor Applications. In *Procedia Chemistry*, volume 1, pages 469–472. Elsevier B.V., 2009.

[69] S P Beeby, M J Tudor, Koukharenko E, White N M, T O'Donnell, C Saha, S Kulkarni, and S Roy. Micromachined silicon generator for harvesting power from vibration. In *Proc. Transducers*, pages 780–783, 2005.

[70] S Meninger, J O Mur-Miranda, R Amirtharajah, A P Chandrakasan, and J H Lang. Vibration-to-electric energy conversion. *IEEE Transactions on Very Large Scale Integration (VLSI) Systems*, 9(1):64–76, 2001.

[71] R Amirtharajah and A P Chandrakasan. A micropower programmable DSP using approximate signal processing based on distributed arithmetic. *IEEE Journal of Solid-State Circuits*, 39(2):337–347, 2004.

[72] T Sterken, P Fiorini, K Baert, G Borghs, and R Puers. Novel design and fabrication of a mems electrostatic vibration scavenger. In *Power MEMS Conference*, pages 18–21, 2004.

[73] Y Arakawa, Y Suzuki, and N Kasagi. 2004. In *PowerMEMS Conference*, pages 187–190, 2004.

[74] F Peano and T Tambosso. Design and optimisation of a mems electret-based capacitive energy scavenger. *Journal of Microelectromechanical Systems*, 14(3):429–435, 2005.

[75] X Dai, Y Wen, P Li, J Yang, and G Hang. Modeling, characterization and fabrication of vibration energy harvester using Terfenol-D/PZT/Terfenol-D composite transducer. *Sensors and Actuators A: Physical*, 156(2):350–358, 2009.

[76] Feng-Ru Fan, Zhong-Qun Tian, and Zhong Lin Wang. Flexible triboelectric generator. *Nano Energy*, 1(2):328–334, March 2012.

[77] Yannan Xie, Sihong Wang, Simiao Niu, Long Lin, Qingshen Jing, Yuanjie Su, Zhengyun Wu, and Zhong Lin Wang. Multi-layered disk triboelectric nanogenerator for harvesting hydropower. *Nano Energy*, 6:129–136, 2014.

[78] G K Ottman. Optimized piezoelectric energy harvesting circuit using step-down converter in discontinuous conduction mode. *IEEE Transactions on Power Electronics*, 18(2):1988–1994, 2003.

[79] Y C Shu, I C Lien, and W J Wu. An improved analysis of the SSHI interface in piezoelectric energy harvesting. *Smart Materials and Structures*, 16:2253–2264, 2007.

[80] J Liang and W H Liao. Energy flow in piezoelectric energy harvesting systems. *Smart Materials and Structures*, 22(5):015005, 2011.

[81] I C Lien, Y C Shu, W J Wu, S M Shiu, and H C Lin. Revisit of series-SSHI with comparisons to other interfacing circuits in piezoelectric energy harvesting. *Smart Materials and Structures*, 19(12):125009, 2010.

[82] Hui Shen, Jinhao Qiu, Hongli Ji, Kongjun Zhu, and Marco Balsi. Enhanced synchronized switch harvesting: a new energy harvesting scheme for efficient energy extraction. *Smart Materials and Structures*, 19(11):115017, 2010.

[83] M Lallart and D Guyomar. Piezoelectric conversion and energy harvesting enhancement by initial energy injection. *Applied Physics Letters*, 97(1):014104, 2010.

[84] P D Mitcheson, T C Green, and E M Yeatman. Power processing circuits for electromagnetic, electrostatic and piezoelectric inertial energy scavengers. *Microsystem Technologies*, 13(11-12):1629–1635, 2007.

[85] X Cao and W J Chiang. Electromagnetic energy harvesting circuit with feedforward and feedback DC-DC PWM boost converter for vibration power generator system. *IEEE Transactions on Power Electronics*, 22(2):679–685, 2007.

[86] E Arroyo and A Badel. Electromagnetic vibration energy harvesting device optimization by synchronous energy extraction. *Sensors and Actuators A: Physical*, 171(2):266–273, 2011.

[87] S Beeby and N M White. *Energy harvesting for autonomous systems*. Artech House, 2010.

[88] E Arroyo, A Badel, F Formosa, Y Wu, and J Qiu. Comparison of electromagnetic and piezoelectric vibration energy harvesters: model and experiments. *Sensors and Actuators A: Physical*, 183:148–156, 2012.

[89] E Lefeuvre, A Badel, C Richard, and D Guyomar. High Performance Piezoelectric Vibration Energy Reclamation. In *SPIE Vol.5390*, volume 5390, pages 379–387, 2004.

[90] V R Challa, M G Prasad, and F T Fisher. Towards an autonomous self-tuning vibration energy harvesting device for wireless sensor network applications. *Smart Materials and Structures*, 20(2):025004, 2011.

[91] C Eichhorn, F Goldschmidtboeing, Y Porro, and P Woias. A piezoelectric harvester with an integrated frequency-tuning mechanism. In *Power MEMS*, pages 45–48, 2009.

[92] M Ferrari, V Ferrari, M Guizzetti, D Marioli, and A Taroni. Piezoelectric multifrequency energy converter for power harvesting in autonomous microsystems. *Sensors and Actuators A: Physical*, 142:329–335, 2008.

[93] I C Lien and Y C Shu. Array of piezoelectric energy harvesting by the equivalent impedance approach. *Smart Materials and Structures*, 21(8):082001, 2012.

[94] V R Challa, M G Prasad, and F T Fisher. A coupled piezoelectric-electromagnetic energy harvesting technique for achieving increased power output through damping matching. *Smart Materials and Structures*, 18(9):095029, 2009.

[95] Z Yang and J Yang. Connected vibrating piezoelectric bimorph beams as a wide-band piezoelectric power harvester. *Journal of Intelligent Material Systems and Structures*, 20:569–574, 2009.

[96] T Galchev, H Kim, and K Najafi. Non-Resonant Bi-stable Frequency-increased power scavenger from low-frequency ambient vibration. In *IEEE Transducers 2009*, pages 632–635, 2009.

[97] P Pillatsch, E M Yeatman, and A S Holmes. A scalable piezoelectric impulse-excited energy harvester for human body excitation. *Smart Materials and Structures*, 21(11):115018, 2012.

[98] T Galchev, H Kim, and K Najafi. Micro power generator for harvesting low-frequency and nonperiodic vibrations. *Journal of Microelectromechanical Systems*, 20(4):852–866, 2011.

[99] T Galchev, E E Aktakka, and K Najafi. A Piezoelectric Parametric Frequency Increased Generator for Harvesting Low-Frequency Vibrations. *Journal of Microelectromechanical Systems*, 21(6):1311–1320, 2012.

[100] Q C Tang, Y L Yang, and X Li. Bi-stable frequency up-conversion piezoelectric energy harvester driven by non-contact magnetic repulsion. *Smart Materials and Structures*, 20:125011, 2011.

[101] L Gu and C Livermore. Impact-driven, frequency up-converting coupled vibration energy harvesting device for low frequency operation. *Smart Materials and Structures*, 20(4):045004, 2011.

[102] D G Lee, G P Carman, D Murphy, and C Schulenburg. Novel Micro Vibration Energy Harvesting Device using Frequency Up Conversion. In *International Solid-State Sensors, Actuators and Microsystems Conference*, pages 871–874. Ieee, 2007.

[103] H Kulah and Kl Najafi. Energy scavenging from low-frequency vibrations by using frequency up-conversion for wireless sensor applications. *IEEE Sensors Journal*, 8(3):261–268, 2008.

[104] L Moro and D Benasciutti. Harvested power and sensitivity analysis of vibrating shoe-mounted piezoelectric cantilevers. *Smart Materials and Structures*, 19(11):115011, 2010.

[105] M Renaud, P Fiorini, R van Schaijk, and C van Hoof. Harvesting energy from the motion of human limbs: the design and analysis of an impact-based piezoelectric generator. *Smart Materials and Structures*, 18(3):035001, 2009.

[106] A Triplett and D D Quinn. The Effect of Non-linear Piezoelectric Coupling on Vibration-based Energy Harvesting. *Journal of Intelligent Material Systems and Structures*, 20(16):1959–1967, 2009.

[107] S C Stanton, A Erturk, B P Mann, and D J Inman. Nonlinear piezoelectricity in electroelastic energy harvesters: Modeling and experimental identification. *Journal of Applied Physics*, 108(7):074903, 2010.

[108] B P Mann and N D Sims. Energy harvesting from the nonlinear oscillations of magnetic levitation. *Journal of Sound and Vibration*, 319:515–530, 2009.

[109] S C Stanton, C C McGehee, and B P Mann. Reversible hysteresis for broadband magnetopiezoelastic energy harvesting. *Applied Physics Letters*, 95(17):174103, 2009.

[110] G Sebald, H Kuwano, D Guyomar, and B Ducharne. Experimental Duffing oscillator for broadband piezoelectric energy harvesting. *Smart Materials and Structures*, 20(10):102001, 2011.

[111] G Sebald, H Kuwano, D Guyomar, and B Ducharne. Simulation of a Duffing oscillator for broadband piezoelectric energy harvesting. *Smart Materials and Structures*, 20(7):075022, 2011.

[112] D Barton, S Burrow, and L Clare. Energy Harvesting From Vibrations With a Nonlinear Oscillator. *Journal of Vibration and Acoustics*, 132(2):021009, 2010.

[113] A Hajati and S G Kim. Ultra-wide bandwidth piezoelectric energy harvesting. *Applied Physics Letters*, 99(8):083105, 2011.

[114] S D Nguyen and E Halvorsen. Nonlinear springs for bandwidth-tolerant vibration energy harvesting. *Journal of Microelectromechanical Systems*, 20(6):1225–1227, 2011.

[115] M S M Soliman, E M Abdel-Rahman, E F El-Saadany, and R R Mansour. A wideband vibration-based energy harvester. *Journal of Micromechanics and Microengineering*, 18(11):115021, 2008.

[116] H Liu, C Lee, T Kobayashi, C J Tay, and C Quan. Investigation of a MEMS piezoelectric energy harvester system with a frequency-widened-bandwidth mechanism introduced by mechanical stoppers. *Smart Materials and Structures*, 21(3):035005, 2012.

[117] K Ashraf, M H Md Khir, J O Dennis, and Z Baharudin. A wideband, frequency up-converting bounded vibration energy harvester for a low-frequency environment. *Smart Materials and Structures*, 22(2):025018, 2013.

[118] H Liu, C Lee, T Kobayashi, C J Tay, and C Quan. Piezoelectric MEMS-based wideband energy harvesting systems using a frequency-up-conversion cantilever stopper. *Sensors and Actuators A: Physical*, 186:242–248, 2012.

[119] L Dhakar, H Liu, F E H Tay, and C Lee. A new energy harvester design for high power output at low frequencies. *Sensors and Actuators A: Physical*, 199:344–352, 2013.

[120] Ravindra Masana and Mohammed F. Daqaq. Relative performance of a vibratory energy harvester in mono- and bi-stable potentials. *Journal of Sound and Vibration*, 330(24):6036–6052, November 2011.

[121] F Cottone, L Gammaitoni, H Vocca, M Ferrari, and V Ferrari. Piezoelectric buckled beams for random vibration energy harvesting. *Smart Materials and Structures*, 21:035021, 2012.

[122] A J Sneller, P Cette, and B P Mann. Experimental investigation of a post-buckled piezoelectric beam with an attached central mass used to harvest energy. *Proceedings of the Institution of Mechanical Engineers, Part I: Journal of Systems and Control Engineering*, 225(4):497–509, 2011.

[123] L V Blarigan, P Danzl, and J Moehlis. A broadband vibrational energy harvester. *Applied Physics Letters*, 100(25):253904, 2012.

[124] A F Arrieta and P Hagedorn. A piezoelectric bistable plate for nonlinear broadband energy harvesting. *Applied Physics Letters*, 97:104102, 2010.

[125] F Cottone, H Vocca, and L Gammaitoni. Nonlinear Energy Harvesting. *Physical Review Letters*, 102(8):080601, 2009.

[126] M Ferrari, V Ferrari, M Guizzetti, B Andò, S Baglio, and C Trigona. Improved energy harvesting from wideband vibrations by nonlinear piezoelectric converters. *Sensors and Actuators A: Physical*, 162(2):425–431, 2010.

[127] Samuel C Stanton, Clark C Mcgehee, and Brian P Mann. Nonlinear dynamics for broadband energy harvesting : Investigation of a bistable piezoelectric inertial generator. *Physica D*, 239(10):640–653, 2010.

[128] A Erturk and D J Inman. Broadband piezoelectric power generation on high-energy orbits of the bistable Duffing oscillator with electromechanical coupling. *Journal of Sound and Vibration*, 330(10):2339–2353, 2011.

[129] M Ferrari, M Baù, M Guizzetti, and V Ferrari. A single-magnet nonlinear piezoelectric converter for enhanced energy harvesting from random vibrations. *Sensors and Actuators A: Physical*, 172(1):287–292, 2011.

[130] B Andò, S Baglio, N Dumas, L Latorre, P Nouet, and C Trigona. Nonlinear mechanism in MEMS devices for energy harvesting applications. *Journal of Micromechanics and Microengineering*, 20(12):125020, 2010.

[131] B Andò, S Baglio, F Maiorca, and C Trigona. Analysis of two dimensional, wideband, bistable vibration energy harvester. *Sensors and Actuators A: Physical*, 202:176–182, 2013.

[132] B P Mann and B A Owens. Investigations of a nonlinear energy harvester with a bistable potential well. *Journal of Sound and Vibration*, 329(9):1215–1226, 2010.

[133] Gi-Woo Kim and Jaehwan Kim. Compliant bistable mechanism for low frequency vibration energy harvester inspired by auditory hair bundle structures. *Smart Materials and Structures*, 22(1):014005, 2013.

[134] R L Harne, M Thota, and K W Wang. Bistable energy harvesting enhancement with an auxiliary linear oscillator. *Smart Materials and Structures*, 22(12):125028, 2013.

[135] N Cohen, I Bucher, and M Feldman. Slow-fast response decomposition of a bi-stable energy harvester. *Mechanical Systems and Signal Processing*, 31:29–39, 2012.

[136] E Halvorsen. Fundamental issues in nonlinear wide-band vibration energy harvesting. *Physical review E*, 87:042129, 2013.

[137] S M Jung and K S Yun. Energy-harvesting device with mechanical frequency-up conversion mechanism for increased power efficiency and wideband operation. *Applied Physics Letters*, 96(11):111906, 2010.

[138] S C Stanton, B A M Owens, and B P Mann. Harmonic balance analysis of the bistable piezoelectric inertial generator. *Journal of Sound and Vibration*, 331(15):3317–3327, 2012.

[139] Ali H Nayfeh and Dean T Mook. *Nonlinear oscillations*. John Wiley & Sons, 2008.

[140] S P Beeby, R N Torah, M J Tudor, P Glynne-Jones, T O'Donnell, C R Saha, and S Roy. A micro electromagnetic generator for vibration energy harvesting. *Journal of Micromechanics and Microengineering*, 17(7):1257–1265, July 2007.

[141] www.cedrat-technologies.com.

[142] A H Nayfeh and S A Emam. Exact solution and stability of postbuckling configurations of beams. *Nonlinear Dynamics*, 54(4):395–408, 2008.

[143] Y Zhang, F Zhang, and Y Shakhsheer et al. A batteryless 19 W MICS/ISM-band energy harvesting body sensor node soc for EXG applications. *IEEE Journal of Solid-State Circuits*, 48(1):199–213, 2013.

[144] S D Nguyen, E Halvorsen, and I Paprotny. Bistable springs for wideband microelectromechanical energy harvesters. *Applied Physics Letters*, 102(2):023904, 2013.

[145] D Chen, Y Yand Vasic, Y P Liu, and F Costa. Study of a piezoelectric switching circuit for energy harvesting with bistable broadband technique by work-cycle analysis. *Journal of Intelligent Material Systems and Structures*, 24(2):180–193, September 2012.

[146] A Badel. *Récupération d'énergie et contrôle vibratoire par éléments piézoélectriques suivant une approche non linéaire*. PhD thesis, Université de Savoie, 2005.

[147] D Guyomar and A Badel. Nonlinear semi-passive multimodal vibration damping: An efficient probabilistic approach. *Journal of Sound and Vibration*, 294:249–268, 2006.

[148] M Lallart, E Lefeuvre, C Richard, and D Guyomar. Self-powered circuit for broadband, multimodal piezoelectric vibration control. *Sensors and Actuators A: Physical*, 143(2):377–382, 2008.

[149] J Liang and W H Liao. Improved design and analysis of self-powered synchronized switch interface circuit for piezoelectric energy harvesting systems. *IEEE Transactions on Industrial Electronics*, 59(4):1950–1960, 2012.

[150] Y Y Chen, D Vasic, F Costa, W J Wu, and C K Lee. A self-powered switching circuit for piezoelectric energy harvesting with velocity control. *The European Physical Journal Applied Physics*, 57(3):30903, 2012.

[151] S Shimose, K Makihar, and J Onoda. Comparison of analog and digital self-powered systems in multimodal vibration suppression. *Smart Materials Research*, 2012.

[152] Y Wu, A Badel, F Formosa, W Liu, and A Agbossou. Self-powered optimized synchronous electric charge extraction circuit for piezoelectric energy harvesting. *Journal of Intelligent Material Systems and Structures*, January 2014.

[153] F Giusa, A Giuffrida, C Trigona, A R. Andò, Band Bulsara, and S Baglio. "Random Mechanical Switching Harvesting on Inductor": A novel approach to collect and store energy from weak random vibrations with zero voltage threshold. *Sensors and Actuators A: Physical*, 198:35–45, 2013.

[154] Y Wu, A Badel, F Formosa, W Liu, and A Agbossou. Nonlinear vibration energy harvesting device integrating mechanical stoppers used as synchronous mechanical switches. *Journal of Intelligent Material Systems and Structures*, 2014.

[155] S A Emam and A H Nayfeh. Postbuckling and free vibrations of composite beams. *Composite Structures*, 88(4):636–642, 2009.

List of publications

International journals

[1] W Q Liu, A Badel, F Formosa, Y P Wu, A Agbossou and Nabil Bencheickh, A wideband integrated piezoelectric bistable generator: experimental performances evaluation and potential for real environmental vibrations, Journal of Intelligent Material Systems and structures, 2014. Doi: 10.1177/1045389X14546660.

[2] W Q Liu, F Formosa, A Badel, Y P Wu and A Agbossou, Self-powered nonlinear harvesting circuit with mechanical switches for a bistable generator with stoppers, Sensors and Actuators A: Physical, 216, 106-115, 2014.

[3] Y Wu, A Badel, F Formosa, W Liu and A Agbossou, Self-powered optimized synchronous electric charge extraction circuit for piezoelectric energy harvesting, Journal of Intelligent Material Systems and structures, 2014. Doi: 10.1177/1045389X13517315.

[4] Y Wu, A Badel, F Formosa, W Liu and A Agbossou, Nonlinear vibration energy harvesting device integrating mechanical stoppers used as synchronous mechanical switches, Journal of Intelligent Material Systems and structures, 2014. Doi: 10.1177/1045389X14533437.

[5] Y Wu, A Badel, F Formosa, W Liu and A E Agbossou, Piezoelectric vibration energy harvesting by optimized synchronous electric charge extraction, Journal of Intelligent Material Systems and structures, 24 (12), 1445-1458, 2013.

[6] W Q Liu, A Badel, F Formosa, Y P Wu and A Agbossou, Wideband energy harvesting using a combination of an optimized synchronous electric charge extraction circuit and a bistable harvester, Smart Materials and Structures, 22(12), 125038, 2013.

[7] W Q Liu, A Badel, F Formosa, Y P Wu and A Agbossou, Novel piezoelectric bistable oscillator architecture for wideband vibration energy harvesting, Smart Materials and Structures, 22(3), 035013, 2013.

International conferences with activities

[8] W Q Liu, A Badel, F Formosa, Y P Wu and A Agbossou, Design and optimization of a novel bistable power generator for autonomous sensor nodes, Design, Test, Integration and Packaging of MEMS/MOEMS (DTIP), 2013 Symposium on, Barcelona, Spain.

[9] W Q Liu, A Badel, F Formosa, Y P Wu and A Agbossou, Integrated bistable generator for wideband energy harvesting with optimized synchronous electric charge extraction circuit, Journal of Physics: Conference Series, 476, PowerMEMS2013, London, British.

[10] Y Wu, A Badel, F Formosa, W Liu and A Agbossou, Two self-powered energy harvesting interfaces based on the optimized synchronous electric charge extraction technique, Journal of Physics: Conference Series, 476, PowerMEMS2013, London, British.

[11] Y Wu, A Badel, F Formosa, W Liu and A Agbossou, Vibration Energy Extraction Circuit Optimization by Optimized Synchronous Electric Charge Extraction and Its

Self-powered Circuit, The 23rd International Conference on Adaptive Structures and Technologies ICAST 2012, Nanjing, China.

National conference

[12] W Q Liu, A Badel, F Formosa, Y P Wu, A Agbossou and N Becncheikh, Integrated bistable generator for wideband vibration energy harvesting, Journées nationales sur la récupération et le stockage d'énergie, April 2014, Annecy le vieux, France.

List of Tables

List of Figures

A

Double buckled beam

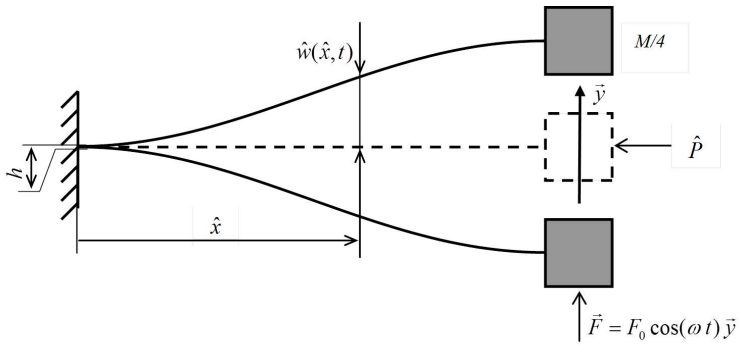

Figure A.1: Quarter geometry of the symmetric post-buckled structure.

A.1 Geometry description

Figure 2.1 shows the general scheme of the bistable energy harvester device with the main geometrical parameters defined. A rigid frame holds two staked clamped straight beams with an inertial mass linked to the central part of each beam. By doing this, the mass is forced to move along the $\vec{y}$ axis and prevent any parasitic rotational motion. Hence, an electromagnetic transducer structure is thought to be integrated along the motion axis. As an alternative transduction mechanism, piezoelectric patches can be added to the beam.

A.2 Analytical model

This part details the mathematical strategy to represent the behavior of the system. It is assumed that the external excitation is represented by the movement of a rigid frame which enclosed the movable device (see figure 2.1). Moreover the effect of this excitation on the beams is negligible with respect to the effect of the central inertial mass.

Because of the symmetric properties, it can be simplified to a quarter of the structure as shown in figure A.1 . The governing equation of such a buckled beam is [142]:

$$m\frac{\partial^2\hat{w}}{\partial\hat{t}^2} + EI\frac{\partial^4\hat{w}}{\partial\hat{x}^4} + \hat{P}\frac{\partial^2\hat{w}}{\partial\hat{x}^2} - \frac{1}{2}\frac{EA}{L}\frac{\partial^2\hat{w}}{\partial\hat{x}^2}\int_0^L(\frac{\partial\hat{w}}{\partial\hat{x}})^2 d\hat{x} = 0 \tag{A.1}$$

$$\begin{aligned} \hat{w}_{|\hat{x}=0} &= 0 \\ \frac{\partial\hat{w}}{\partial\hat{x}}_{|\hat{x}=0} &= 0 \\ \frac{\partial\hat{w}}{\partial\hat{x}}_{|\hat{x}=L} &= 0 \\ EI\frac{\partial^3\hat{w}}{\partial\hat{x}^3}_{|\hat{x}=L} &= \frac{M}{4}(\frac{\partial^2\hat{w}}{\partial\hat{t}^2}_{|\hat{x}=L} + \frac{\partial^2\hat{u}}{\partial\hat{t}^2}) - \frac{\hat{C}}{4}\frac{\partial\hat{w}}{\partial\hat{x}}_{|\hat{x}=L} \end{aligned} \tag{A.2}$$

In which, m is the mass per unit of length of the beam, E, I and A are young modulus, quadratic moment and area respectively. $\hat{P}$ stands for the compression force which leads to the initial buckling of the structure.M is the mass of the central ballast and $\hat{C}$ is a linear damping associated to the electromechanical converter. $\hat{u}$ is the displacement of the frame.

In a more convenient way, we choose to express the non-dimensional equilibrium equation for the beam setting:

$$x = \frac{\hat{x}}{L}\ t = \hat{t}\sqrt{\frac{mL^4}{EI}}\ w = \frac{\hat{w}}{r}\ P = \hat{P}\frac{L^2}{EI} \tag{A.3}$$

where r is the gyration radius defined as $r = \sqrt{I/A} = 2\sqrt{3}h$ in the case of a rectangular cross section.

Therefore, equations (A.1) and (A.2) are written again as:

$$\frac{\partial^2 w}{\partial t^2} + \frac{\partial^4 w}{\partial x^4} + P\frac{\partial^2 w}{\partial x^2} - \frac{1}{2}\frac{\partial^2 w}{\partial x^2}\int_0^1 (\frac{\partial w}{\partial x})^2 dx = 0 \tag{A.4}$$

$$\begin{aligned} w_{|x=0} &= 0 \\ \frac{\partial w}{\partial x}_{|x=0} &= 0 \\ \frac{\partial w}{\partial x}_{|x=1} &= 0 \\ \frac{\partial^3 w}{\partial x^3}_{|x=1} &= \alpha_M(\frac{\partial^2 w}{\partial t^2}_{|x=1} + \frac{\partial^2 u}{\partial t^2}) - c\frac{\partial w}{\partial x}_{|x=1} \end{aligned} \tag{A.5}$$

in which $\alpha_M = M/(4mL)$ is the inertial mass to total beam mass ratio, and $c = CL(mEI)^{-1/2}/4$. Noting that if P equals $P_c = 4\pi^2$ (the Euler critical force for boundary conditions associated to the problem), any first mode buckled configuration can be defined as:

$$w_b = \frac{1}{2}b(1 - \cos(\pi x)) \tag{A.6}$$

for which $b = 4(P - P_c)^{-1/2}/\pi$.Consequently, the solution of Equations (A.4) and (A.5) can be expressed using equation (A.6) as:

$$w(x,t) = w_b(x) + v(x,t) \tag{A.7}$$

Using equation (A.7) and substituting the expression of P, equations (A.4) and (A.5) can be also written as:

$$\begin{aligned} &\frac{\partial^2 v}{\partial t^2} + \frac{\partial^4 v}{\partial x^4} + \pi^2\frac{\partial^2 v}{\partial x^2} - \frac{1}{2}\frac{\partial^2 v}{\partial x^2}\int_0^1 (\frac{\partial v}{\partial x})^2 dx - \frac{1}{2}b\pi\frac{\partial^2 v}{\partial x^2}\int_0^1 \sin(\pi x)\frac{\partial v}{\partial x}dx \\ &-\frac{1}{4}b\pi^2\cos(\pi x)\int_0^1 (\frac{\partial v}{\partial x})^2 dx - \frac{1}{4}b^2\pi^3\cos(\pi x)\int_0^1 \sin(\pi x)\frac{\partial v}{\partial x}dx = 0 \end{aligned} \tag{A.8}$$

$$\begin{aligned} v_{|x=0} &= 0 \\ \frac{\partial v}{\partial x}_{|x=0} &= 0 \\ \frac{\partial v}{\partial x}_{|x=1} &= 0 \\ \frac{\partial^3 v}{\partial x^3}_{|x=1} &= \alpha_M(\frac{\partial^2 v}{\partial t^2}_{|x=1} + \frac{\partial^2 u}{\partial t^2}) - c\frac{\partial v}{\partial x}_{|x=1} \end{aligned} \tag{A.9}$$

A.3 Modal analysis

Modal discretization is used to simplify the previous model defined by equations (A.8) and (A.9). The linear vibration mode shapes are obtained by dropping nonlinear and

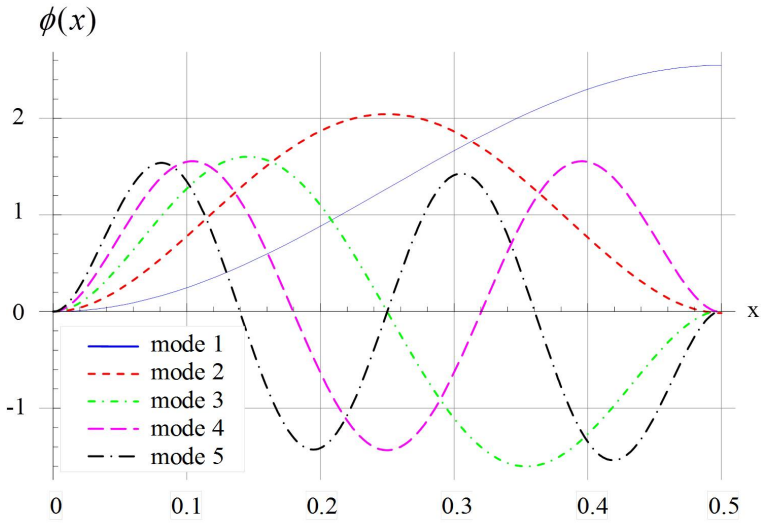

Figure A.2: Modal shape for modes 1 to 5 and $b = 1$.

damping terms. Seeking for the harmonic solutions $v(x,t) = \phi(x)e^{-j\omega t}$, the mode shapes are solutions of the followed equilibrium with the boundary conditions satisfied:

$$-\omega^2\phi + \frac{d^4\phi}{dx^4} + \pi^2\frac{d^2\phi}{dx^2} - \frac{1}{4}b^2\pi^3\cos(\pi x)\int_0^1 \sin(\pi x)\frac{d\phi}{dx}dx = 0 \tag{A.10}$$

$$\begin{aligned} \phi_{|x=0} &= 0 \\ \frac{d\phi}{dx}_{|x=0} &= 0 \\ \frac{d\phi}{dx}_{|x=1} &= 0 \\ \frac{d^3\phi}{dx^3}_{|x=1} &= -\alpha_M\omega^2\phi_{|x=1} \end{aligned} \tag{A.11}$$

Following the approach of Emam and Nayfeh [155, 142] the solution can be expressed as:

$$\phi(x) = c_1\sin(s_1x) + c_2\cos(s_1x) + c_3\sinh(s_2x) + c_4\cosh(s_2x) + c_5\cos(\pi x) \tag{A.12}$$

in which $s_{1,2} = \sqrt{\frac{1}{2}(\pm\pi^2 + \sqrt{\pi^4 + 4\omega^2})}$.

The eigenvalue problem can then be obtained from the substitution of equation (A.12) into equations (A.10) and (A.11). The natural frequencies ω_i and corresponding mode shapes $\phi_i(x)$ at a given buckling level b are then evaluated. As an example, figure A.2 shows the first 5 modes for $b = 1$.

Figure A.3 shows the evolution of the first three frequencies as a function of b and α_M. The buckling amplitude has a drastic hardening effect on the first and third frequencies (figure A.3(a)). As expected, the more the central mass, the less the first mode frequency (figure A.3(b)), the second and third mode frequencies are not affected by the central mass value.

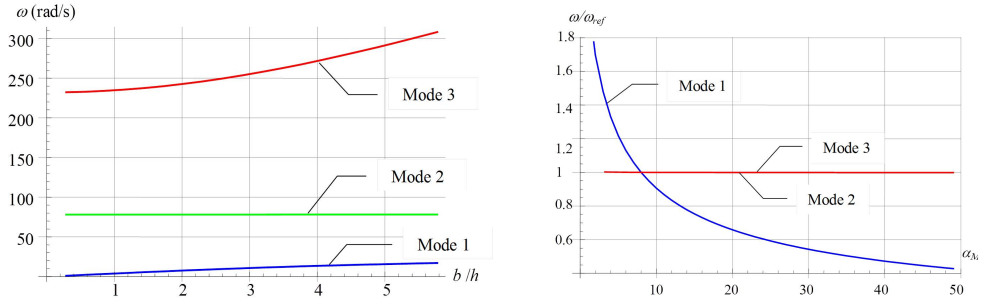

(a) (b)

Figure A.3: (a) Evolution of the natural frequencies with respect to b to h ratio for $\alpha_M = 18$; (b) Evolution of the natural frequencies with respect to α_M for $b = 1$ (ω_{ref} obtained at $\alpha_M = 18$).

A.4 Problem discretization

The linear vibration mode shapes are used as basis for the discretization strategy and normalized such that:

$$\int_0^1 \phi_i \phi_j dx + \alpha_M \phi_i(1)\phi_j(1) = \delta_{ij} \tag{A.13}$$

δ_{ij} is the Kronecker delta function such as $\delta_{ij} = 1$ if $i = j$ and $\delta_{ij} = 0$ if not.

According to the Galerkin discretization method, the solution of equations (A.8) and (A.9) is written as:

$$v(x,t) = \sum_{i=1}^{N} q_i(t)\phi_i(x) \tag{A.14}$$

By doing this, equations (A.8) and (A.9) become the set of N differential equations:

$$\begin{aligned} \ddot{q}_i + 2\omega_i(\xi_i + \xi_{li}\phi_i(1)^2)\dot{q}_i + \omega_i^2 q_i - 2b \sum_{j,k=1}^{N} A_{ijk} q_j q_k \\ - \sum_{j,k,l=1}^{N} B_{ijkl} q_j q_k q_l = F_i \end{aligned} \tag{A.15}$$

in which, ξ_i is the modal damping coefficient of mode i, $\xi_{li} = c/(2\omega_i)$ the damping effect of the electromechanical converter.

Coefficients A_{ijk}, B_{ijkl} and F_i are defined as:

$$\begin{aligned} A_{ijk} = \frac{1}{8}\pi^2 \int_0^1 \phi_i(x)\cos(\pi x)dx \int_0^1 \frac{d\phi_j}{dx}\frac{d\phi_k}{dx}dx \\ + \frac{1}{4}\pi \int_0^1 \phi_i(x)\frac{d_j^{\phi}}{dx^2}dx \int_0^1 \frac{d\phi_k}{dx}\sin(\pi x)dx \end{aligned} \tag{A.16}$$

$$B_{ijkl} = \frac{1}{2}\pi \int_0^1 \phi_i(x)\frac{d_j^{\phi}}{dx^2}dx \int_0^1 \frac{d\phi_k}{dx}\frac{d\phi_l}{dx}dx \tag{A.17}$$

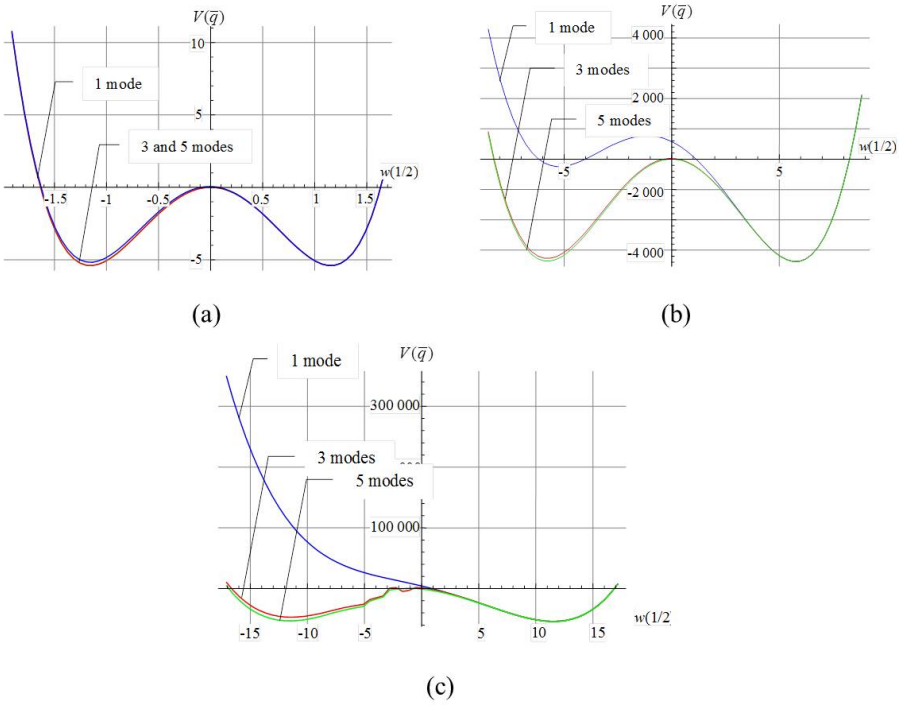

Figure A.4: Energetic potential: (a) $b/h = 1$;(b) $b/h = 5$;(c) $b/h = 10$.

$$F_i = \alpha_M \frac{d^2}{dt^2}\phi_i(1) \tag{A.18}$$

For the single mode model, the simplified equation is:

$$\ddot{q}_1 + 2\omega_1(\xi_1 + \xi_{l1}\phi_1(1)^2)\dot{q}_1 + \omega_1^2 q_1 - 2bA_{111}q_j q_1^2 - B_{1111}q_1^3 = F_1 \tag{A.19}$$

It is worthy of note that using the new variable

$$\bar{q} = q + \frac{2}{3}b\frac{A_{111}}{B_{1111}} \tag{A.20}$$

and noting that the coefficients A_{111} and B_{1111} are negative, the equilibrium equation equation A.19 is the Duffing equation:

$$\begin{aligned}\ddot{\bar{q}}_1 + 2\omega_1(\xi_1 + \xi_{l1}\phi_1(1)^2)\dot{\bar{q}}_1 + (\omega_1^2 + \frac{4}{3}b^2\frac{A_{111}}{B_{1111}})\bar{q}_1 - B_{1111}\bar{q}_1^3 \\ = F_1 + \frac{2}{3}b\frac{A_{111}}{B_{1111}} + \frac{8}{9}b^3\frac{A_{111}^3}{B_{1111}^2} - B_{1111}(\frac{2}{3}b\frac{A_{111}}{B_{1111}})^3\end{aligned} \tag{A.21}$$

The associated elastic energy potential is therefore:

$$V(\bar{q}) = \frac{1}{2}(\omega_1^2 + \frac{4}{3}b^2\frac{A_{111}}{B_{1111}})\bar{q}_1^2 - \frac{1}{4}B_{1111}\bar{q}_1^4 \tag{A.22}$$

The energetic potential is evaluated as a function of the buckling level and the number of modes to study the effect of the number of modes used for the discretized model. The accuracy of the potential shape from the discretized equations using single and multi-mode approximations will be used to determine the number of modes that needs to be retained in the dynamic analysis for different buckling levels.

Parameter	Symbol	Value	Parameter	Symbol	Value
Young modulus	E	210 Gpa	Inertial mass	M	7.8 g
Density	ρ	7800 kg/m^3	Mass per unit length	m	5.46 g/m
Height	H	10 mm	Cross section	A	0.7 mm^2
Length	L	15 mm	Quadratic momentum	I	2.85e-4 mm^4
Width	W	10 mm	Gyration radius	r	2.02e-2 mm
Thickness	h	0.07 mm	Total length	L_{tot}	20 mm

Table A.1: Parameters for the NLBO beam generator.

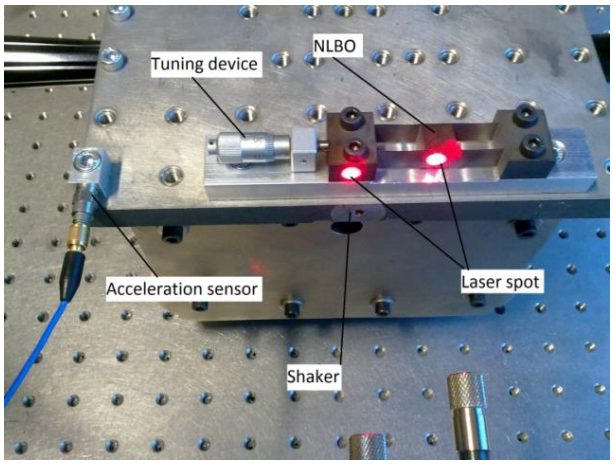

Figure A.5: Fabricated prototype of the beam NLBO.

Figure A.4 plots the energetic potential for various buckling level b for a single, three and five degree of freedom models. It shows the evolution of $V(\bar{q})$ for various buckling configuration. For small buckling level (figure A.4(a)), the potential is symmetrical and clearly exhibits the two stable wells. However, as b increases, the symmetry is loss and the positive stable well becomes preponderant (figure A.4(b) and (c)).

For $b = 1$ (figure A.4(a)) a single mode discretization model is able to account for the symmetrical shape of the bistable oscillator. As the buckling level increases, significant discrepancies between the single mode model and the 3 and 5 modes models can be seen especially for the lower stable and central unstable positions (figure A.4(b)). Adding more modes in the discretization improves the solution. Providing that the maximal deflection of the beam is bounded to about 15 times its thickness, 5 modes model will be used hereafter to represent the dynamic behaviour of the structure.

A.5 Experimental Analysis

Figure A.5 shows the fabricated NLBO (Non-Linear Bistable beam Oscillator) attached to a shaker. The prototype NLBO is produced from a whole piece of steel material. Four screws are used to fix the device after tuning to the desired buckling level. The parameters are shown in table A.1.

Considering that most energy harvesters are used in an environment with relatively low excitation frequencies (usually less than 100Hz), the characteristic frequency of the

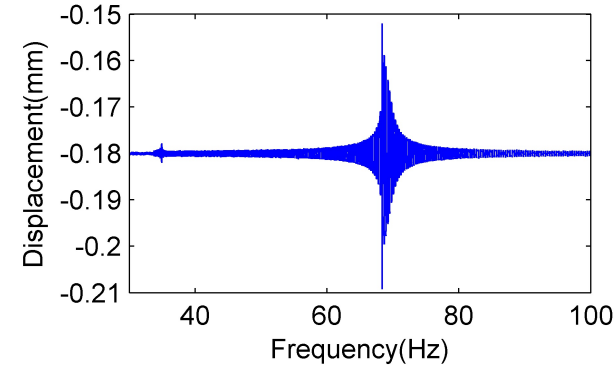

(a)

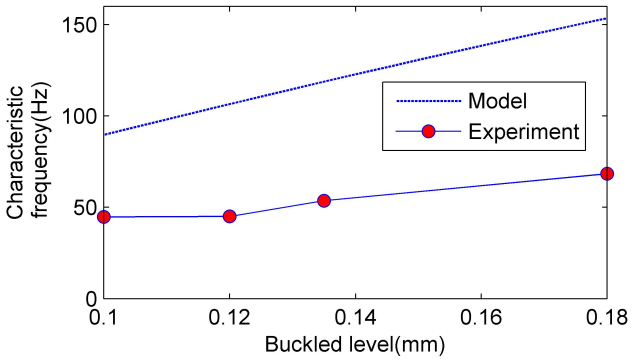

(b)

Figure A.6: (a) Displacement response of the NLBO with a buckled level of 0.18mm for excitation amplitude 0.05$\mathrm{m/s^2}$ *; (b) Characteristic frequency of the NLBO versus the buckled level.*

bi-stable energy harvester are selected to be placed in this range to get good responses by tuning the buckled level. Linear responses in the vicinity of the initial stable buckled position are obtained when the excitations is very small. In order to investigate the relationship between the initial buckled level y_0 and the characteristic frequency, several tests are performed for different buckled configurations with a very small amplitude forward sweep excitation. Figure A.6 shows an example of the response and the measured characteristic frequency. As expected, the displacement response of the NLBO is similar to a linear oscillator while the characteristic frequency increases with the buckling level. However, the measured characteristic frequency is very different from the model prediction as shown in the figure A.6(b).

Since the most attractive properties of the NLBO come from the nonlinear response, the inter-well motions especially, the performance is investigated for stronger excitations. A NLBO system can exhibit complex and large differences responses when submitted to slightly different excitations, though it is meaningful and prospective to study the effect of a frequency sweep at some typical constant acceleration amplitude. Moreover, it allows the estimation of the frequency range broadening and provides a mean of comparison with former works. Therefore, the response of the system when submitted to sweep harmonic base excitations with a slowly varying frequency (30Hz-150Hz, 0.1Hz/s) is studied here. Two different amplitudes ($5\mathrm{m/s^2}$, $10\mathrm{m/s^2}$) are applied to the NLBO with the buckled level set to 0.18mm. The forward and reverse responses are shown in figure A.7

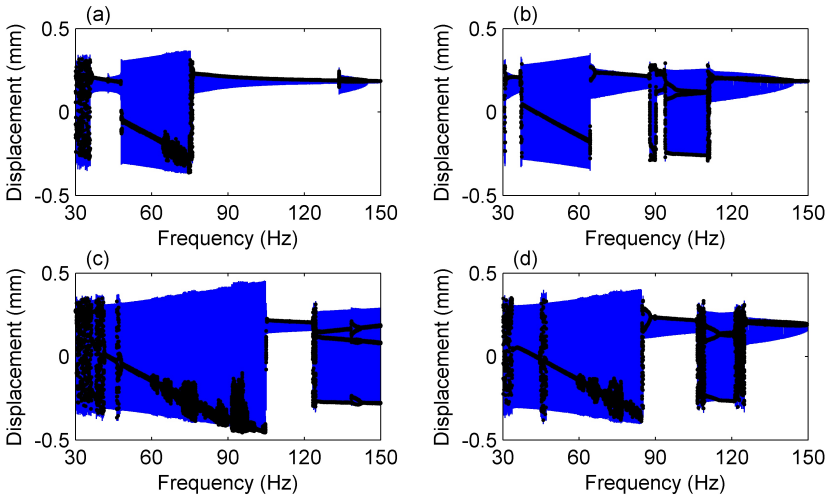

Figure A.7: Experimental displacement responses of the NLBO (buckled level, 0.18mm): (a) Forward sweep, 5$\mathrm{m/s^2}$ *; (b) Reverse sweep, 5*$\mathrm{m/s^2}$ *; (c) Forward sweep, 10*$\mathrm{m/s^2}$ *; (d) Reverse sweep, 10*$\mathrm{m/s^2}$ *.*

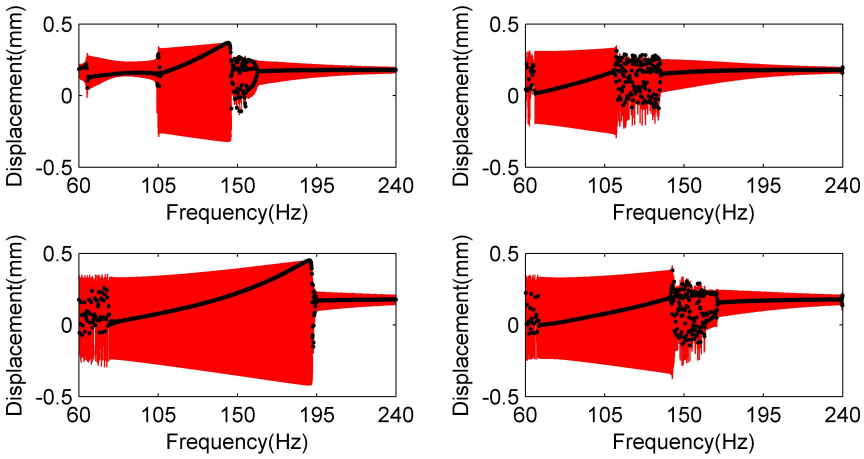

Figure A.8: Theoretical displacement responses of the NLBO (buckled level, 0.18mm): (a) Forward sweep, 30$\mathrm{m/s^2}$ *; (b) Reverse sweep, 30*$\mathrm{m/s^2}$ *; (c) Forward sweep, 50*$\mathrm{m/s^2}$ *; (d) Reverse sweep, 50*$\mathrm{m/s^2}$ *.*

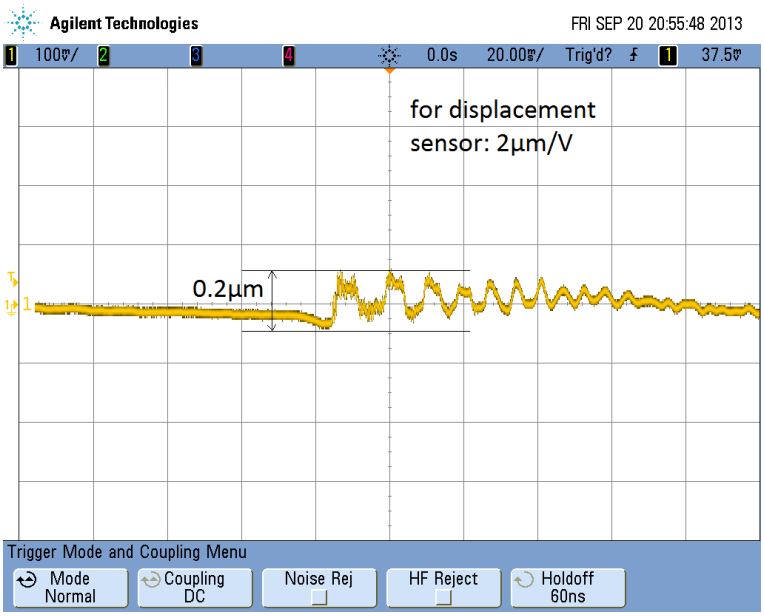

Figure A.9: Axial transient response when the beam changes from one stable position to the other.

The black dots in the figure represent the Poincaré section which indicates the type of the motion (chaotic or periodic). The relationship between the frequency of the response and the excitation frequency is exhibited if the motion is periodic. As it is seen in figure A.7(a)(b), the mass crosses the potential saddle at the zero position frequently for an excitation of 5m/s^2 · The inter-well motions are observed for the forward sweep (30Hz-35Hz and 47Hz-75Hz) and reverse sweep (37Hz-64Hz and 94Hz-111Hz). These inter-well motions bring large displacement responses which are desired for energy harvesting. As a result, the useful frequency bandwidth is greatly enlarged compared with the linear case. Band broadening effects are more obvious when the acceleration amplitude increases to 10m/s^2 · The inter-well motions are exhibited over almost the whole frequency sweep range as shown in Fig.A.7(c)(d). It proves that the NLBO can effectively overcome the narrow band limitation on the linear oscillator.

However, with the same buckled level 0.18mm, the predicted resonance frequency is 153Hz which is much higher than the experimental value. To have the similar inter-well motion as obtained in the experimental, the theoretical required excitation is also much stronger. Figure A.8 shows the simulation results with the excitations of $30\ \text{m/s}^2$ and $50\ \text{m/s}^2$. It is inferred that the theoretical potential barrier is much higher than expected.

A possible explanation is the imperfect boundary condition: the beam is not clamped and fixed rigidly. There exists the axial motion ($\hat{x}$ direction) which is not to be neglected. Therefore, a static test is performed to observe this motion. When the mass is pushed from one stable position to the other, the displacement at one axial end is measured. The transient response in figure A.9 validates the existence of the axial motion. Although this axial motion is pretty small, the effect on the dynamics of the NLBO under investigating cannot be neglected and needs to be taken into consideration in the modeling analysis.

Therefore, the imperfect boundary conditions are required to be included. The finite element method is proposed to investigate the problem. Nevertheless, it is not to be discussed here. This investigation shows that the model for the buckled beam is easy to be influenced by the boundary conditions. As a result, it is difficult to have a precise model to predict the dynamics of the buckled beam, which might place limitations on the design

and optimization of this kind of generator.